MRI Applications for Transplantation: Organ Preservation Techniques and Pre-Transplant Ex-Vivo Viability Assessment and Improved Phosphorus Magnetic Resonance Spectroscopic Imaging using Accelerated non-Fourier Reconstruction Techniques, and Artificial Intelligence

Songeon, Julien

UNIVERSITÉ DE GENÈVE
Groupe de Physique Appliquée

FACULTÉ DES SCIENCES
Professeur J.-P. Wolf

Département de Radiologie
et d'Informatique Médicale

FACULTÉ DE MÉDECINE
Professeur F. Lazeyras

MRI Applications for Transplantation: Organ Preservation Techniques and Pre-Transplant Ex-Vivo Viability Assessment *and* Improved Phosphorus Magnetic Resonance Spectroscopic Imaging using Accelerated non-Fourier Reconstruction Techniques, and Artificial Intelligence

THÈSE

présentée à la Faculté des Sciences de l'Université de Genève
pour obtenir le grade de Docteur ès Sciences, mention Physique

par

Julien SONGEON
de
Nyon (Vaud)

Thèse n°5741

GENÈVE
Atelier d'impression ReproMail
2023

UNIVERSITÉ
DE GENÈVE
FACULTÉ DES SCIENCES

DOCTORAT ÈS SCIENCES, MENTION PHYSIQUE

Thèse de Monsieur Julien SONGEON

intitulée :

«MRI Applications for Transplantation: Organ Preservation Techniques and Pre-Transplant Ex-Vivo Viability Assessment and Improved Phosphorus Magnetic Resonance Spectroscopic Imaging using Accelerated non-Fourier Reconstruction Techniques, and Artificial Intelligence»

La Faculté des sciences, sur le préavis de Monsieur F. LAZEYRAS, professeur associé et directeur de thèse (Faculté de médecine, Département de Radiologie et d'Informatique Médicale), Monsieur J.-P. WOLF, professeur ordinaire et codirecteur de thèse (Groupe de physique appliquée), Monsieur W. BOGNER, professeur (Department of Biomedical Imaging and Image-guided Therapy, Medical University of Vienna, Vienna, Austria) et Monsieur A. LONGCHAMP, docteur (Service de Chirurgie Vasculaire, Faculté de Biologie et Médecine, Université de Lausanne), autorise l'impression de la présente thèse, sans exprimer d'opinion sur les propositions qui y sont énoncées.

Genève, le 30 juin 2023

Thèse - 5741 -

Le Doyen

N.B. - La thèse doit porter la déclaration précédente et remplir les conditions énumérées dans les "Informations relatives aux thèses de doctorat à l'Université de Genève".

"Deep in the human unconscious is a pervasive need for a logical universe that makes sense. But the real universe is always one step beyond logic."

- Frank Herbert, *Dune*

ACKNOWLEDGEMENTS

This thesis represents 4 years of work that I would characterize as instructive, captivating, and enjoyable. The passage of time seemed to be swift, as the pace of research never appeared to have slowed down during these years. Although I could probably dedicate an entire chapter to expressing my gratitude and recounting the pleasures of my doctoral studies, I will keep my acknowledgement brief. Nevertheless, I hope that my deep appreciation will appear evident in the concise words that follow on this page.

I would like to expressing my gratitude to my research group, start by my mentors: Professor François Lazeyras, Dr. Antoine Klauser, and Dr. Sébastien Courvoisier. You have not only taught me about MR physics, biology, and programming, but also provided me with full overview into every aspect of research. I am truly grateful for the opportunity to work in your group, which provided the best work environment that any doctoral student could hope for. I have learned an enormous amount about a wide range of topics, thanks to your guidance and support. I wish François a good retirement! To the last group member and fellow PhD student Oscar, I would like to express my sincere appreciation for the enjoyable experience of working alongside you. Our engaging meetings, coffee breaks, and lunch discussions were always thought-provoking and informative. It was a pleasure to collaborate with you.

I wish to extend my thanks to Dr. Alban Longchamp, Thomas Agius, Raphael Ruttimann, Jean Pierre Giliberto for the enjoyable and productive collaboration on our shared research. Working with you has been a great pleasure, and I have gained valuable insights into the fields of biology and medicine. I appreciate the time we spent together.

A special appreciation to Professor Jean-Pierre Wolf, for agreeing to co-supervise me, enabling my journey of academic research and pursuing my passion for physics. Additionally, I am grateful for the opportunity to serve as a teaching assistant for the physics courses.

I particularly wish to express my heartfelt gratitude to to Professor Anna Sfyrla, with whom I had the privilege of working as a teaching assistant. Teaching general physics was a rewarding experience, and I am grateful for your trust in me and your invaluable guidance, which helped me improve my teaching skills significantly. I am immensely grateful for the opportunity you gave me to also deliver magistral lectures, which I found to be a highly enjoyable experience.

I would like to express my appreciation to the members of the jury, namely Professor Wolfgang Bogner, Professor Jean-Pierre Wolf, Dr. Alban Longchamp, and Professor François Lazeyras, for their time and efforts in evaluating this work.

I would like to present my deeply thank to the extended group of the CIBM, namely Professor Rares Salomir, Michel Kocher, Pauline, Orane and Yacine, and Marie Louise. Our time spent together has been a source of great enjoyment, and I am grateful for the stimulating discussions, good advice, fond memories, and companionship that we have shared over the years.

To my family, Christophe, Fadia, Laure, Roland, Irène, George and Cosette, for their love and limitless patience throughout my academic pursuit. Despite not fully grasping the concepts of physics, you have listened to me talk about it for the last decade and provided me with endless encouragement to continue on this journey. Your constant support and understanding have been the foundation of my success, and I am forever grateful for all that you have done for me.

To my dear friends, Amaury, Camille, Damien, David, Elisa, Florian, Hugo, José, Kiara, Marie, Mathieu L., Mathieu P., Nicolas, Rebecca, Théo, Yannick, for being incredible individuals with whom I have shared countless moments of joy, laughter, and occasional serious discussions. From memorable parties to dinners and much more, our time together has been nothing short of amazing.

Above all, I wish to express my deepest gratitude to my fiancée and future wife Leslie. Since I met you, my life has become significantly brighter, and your support has been my constant source of strength and motivation. Your attentive listening, constructive criticism, and invaluable advice have played an integral role in bringing this thesis to fruition. I am immensely grateful for your unwavering presence in my life, and I look forward to a bright and promising future together. My final expression of gratitude goes to my faithful partner in crime, Nemesis, who has been by my side during the last years of my thesis. Your presence has undoubtedly improved my quality of life, and your unconditional love and watchful gaze have been a constant source of comfort and motivation. Thank you for your companionship and devotion.

ABSTRACT

The field of transplantation currently faces a significant challenge of organ shortage. In Switzerland, the number of patients waiting for transplantation surpasses 1435, while only 342 transplants were performed in 2022, amounting to a mere 20% of the number of waiting patients. To address this problem, marginal donors, extended-criteria donors (ECD), and donation after circulatory death (DCD) donors are being considered as alternative sources. However, the utilization of such donors is limited by the absence of a reliable and non-invasive method for evaluating kidney viability. Phosphorus magnetic resonance spectroscopy (^{31}P-MRS) is a non-invasive technique that can detect high-energy phosphate metabolites in the kidney and provide insight into its energetic metabolism. This technique can identify several crucial metabolites, which may serve as significant biomarkers for graft viability. Due to its non-invasive nature, ^{31}P-MRS represents a promising approach for monitoring mitochondrial function and predicting graft viability. The objective of this project is to implement the proposed methodology in actual clinical scenarios, with the aim of enhancing kidney preservation and improving ^{31}P-MRSI into a practical approach for evaluating organ viability.

^{31}P-MRSI is currently limited by lengthy acquisition times and lower relative sensitivity compared to proton spectroscopy (^{1}H), which requires larger voxel size to achieve acceptable signal-to-noise ratio (SNR). Analysis of MRS data is achieved through fitting algorithms that demand considerable computing time and have poor performance for quantifying low SNR spectra. To overcome these limitations, we have developed deep learning techniques based on convolutional neural networks for the analysis, quantification, and reconstruction of measured spectra. The proposed methodology encompasses the full pipeline, including the creation of simulated datasets for training purposes, several networks with various applications such as metabolite concentration quantification, spectral parameter estimation, and baseline correction. To address the issue of lengthy acquisition times, the study investigates the potential of a reconstruction acceleration technique that combines compressed sensing with low-rank and total generalized variation regularization approaches to accelerate and enhance the acquisition process. The CS-LR framework developed in this thesis features a new approach that employs distinct random undersampling patterns for each k-space average to avoid the suppression of identical points, thus facilitating greater k-space coverage without altering the acceleration factor.

Our research on organ preservation and viability assessment focused around three main themes. Firstly, the study outlines the experimental setup utilized for evaluating kidney viability. This involves a pneumatically-driven hypothermic pulsatile perfusion (HPP) system composed of non-magnetic materials that is compatible with MRI technology. The HPP system was fully developed at Geneva University Hospital (HUG) and is the only MR-compatible system worldwide capable of conducting both MRI and ^{31}P-MRS acquisition while accommodating organ recovery procedures. The second aspect of our research is the investigation of sub-normothermic preservation at 22 °C in contrast to hypothermic preservation at 4 °C. Thirdly, we investigated the administration of hydrogen sulfide (H_2S) through the injection of NaHS. This approach aims to decrease oxygen and adenosine triphosphate (ATP) consumption in isolated perfused kidneys, reduce inflammation, and enhance renal function following an ischemia-reperfusion injury.

RESUME

Le domaine de la transplantation fait face à un problême significatif de pénurie d'organes. En Suisse, le nombre de patients en attente d'une transplantation dépasse 1435, alors que seulement 342 transplantations sont réalisées en 2022, soit seulement 20%. Pour résoudre ce problème, des donneurs marginaux, des donneurs à critères étendus (ECD) et des donneurs décédés après arrêt circulatoire (DCD) sont considérés comme des sources alternatives. Cependant, l'utilisation de tels donneurs est limitée par l'absence d'une méthode fiable et non invasive pour évaluer la viabilité du rein. La spectroscopie par résonance magnétique au phosphore (^{31}P-MRS) est une technique non invasive qui peut détecter certains métabolites énergétiques cellulaires du rein. Cette technique peut identifier plusieurs métabolites cruciaux, qui peuvent servir de biomarqueurs significatifs pour la viabilité de la greffe. En raison de sa nature non invasive, ^{31}P-MRS représente une approche prometteuse pour déterminer la fonction mitochondriale et prédire la viabilité de la greffe. L'objectif de ce projet est de mettre en œuvre la méthodologie proposée dans des scénarios cliniques réels, dans le but d'améliorer la préservation du rein et d'améliorer l'approche ^{31}P-MRSI pour évaluer la viabilité des organes avant transplantation.

^{31}P-MRSI est actuellement limité par des temps d'acquisition longs et une sensibilité relative inférieure par rapport à la spectroscopie proton (^{1}H), qui nécessite des tailles de voxel plus grandes pour atteindre un rapport signal sur bruit (SNR) acceptable. L'analyse des données MRS est obtenue par des algorithmes d'ajustement qui demandent un temps de calcul considérable et ont une faible performance pour quantifier les spectres à faible SNR. Pour surmonter ces limites, nous avons développé des techniques d'intelligence artificielle basées sur des réseaux de neurones convolutifs (CNN) pour l'analyse, la quantification et la reconstruction des spectres mesurés. La méthodologie proposée englobe la création de données simulées à des fins d'entraînement, plusieurs réseaux de neurones avec diverses applications telles que la quantification de la concentration de métabolites, l'estimation de paramètres spectraux et la correction de la ligne de base. Pour résoudre le problème des temps d'acquisition longs, l'étude examine le potentiel d'une technique d'accélération et de reconstruction qui combine l'acquisition comprimée (Compressed Sensing) avec des approches de régularisation à bas rang (Low Rank) et de variation totale généralisée (TGV) pour améliorer le processus d'acquisition. Le cadre CS-LR développé dans cette thèse présente une nouvelle approche qui utilise des motifs de sous-échantillonnage aléatoires distincts pour chaque mesure de l'espace k afin d'éviter la suppression de points identiques, facilitant ainsi une plus grande couverture de l'espace de Fourier sans altérer le facteur d'accélération.

Notre recherche sur la préservation et l'évaluation de la viabilité des organes a porté sur trois principaux sujets. Tout d'abord, nous avons mis au point la configuration expérimentale utilisée pour évaluer la viabilité rénale. Cela implique un système de perfusion pulsatile hypothermique (HPP) à commande pneumatique composé de matériaux non magnétiques, qui est compatible avec la technologie d'IRM. Le système HPP a été entièrement développé à l'Hôpital universitaire de Genève (HUG) et est le seul système compatible avec l'IRM au monde capable de réaliser à la fois l'IRM et l'acquisition ^{31}P-MRS tout en permettant les procédures de régénération de l'organe. Le deuxième aspect de notre recherche concerne l'étude de la préservation sub-normothermique à 22 °C par rapport à la préservation hypothermique à 4 °C. Enfin, le troisième sujet de notre recherche se concentre sur l'administration de sulfure d'hydrogène (H_2S) par injection de NaHS. Cette approche vise à réduire la consommation d'oxygène et d'adénosine triphosphate (ATP) dans les reins perfusés isolés, à réduire l'inflammation et à améliorer la fonction rénale après une lésion d'ischémie-reperfusion.

PUBLICATIONS

Peer Reviewed Publications:

1. Alban Longchamp, Antoine Klauser, **Julien Songeon**, Thomas Agius, Antonio Nastasi, Raphael Ruttimann, Solange Moll, Raphael Meier, Leo Buhler, Jean-Marc Corpataux, and François Lazeyras. "Ex Vivo Analysis of Kidney Graft Viability Using 31P Magnetic Resonance Imaging Spectroscopy." In *Transplantation.* 2020 Sep;104(9):1825-1831.

2. **Julien Songeon**, Sébastien Courvoisier, Lijing Xin, Thomas Agius, Oscar Dabrowski, Alban Longchamp, François Lazeyras, Antoine Klauser. "In-Vivo Magnetic Resonance ^{31}P-Spectral Analysis With Neural Networks: 31P-SPAWNN" In *Magnetic Resonance in Medicine* 2023; 89: 40- 53.
    - The publication has been chosen as the MRM Highlights pick for the month of January 2023 because it demonstrated exemplary reproducible research practices.

* *Co-first authors*

3. Thomas Agius*, **Julien Songeon***, Antoine Klauser, Grégoire Longchamp, Florent Allagnat, Raphael Ruttimann, Raphael Meier, Julijana Ivaniesevic, James F Markmann, Korkut Uygun, Leo Buhler, Christian Toso, Jean-Marc Corpataux, François Lazeyras, Alban Longchamp. "Sub-Normothermic Ex-Vivo DCD Porcine Kidney Perfusion Improves Energy Metabolism: Analysis using ^{31}P Magnetic Resonance Spectroscopic Imaging." In *Transplantation Direct* 8(10):p e1354, October 2022.

4. Thomas Agius, **Julien Songeon**, Antoine Klauser, Grégoire Longchamp, Florent Allagnat, Raphael Ruttimann, Raphael Meier, Julijana Ivaniesevic, James F Markmann, Korkut Uygun, Leo Buhler, Christian Toso, Jean-Marc Corpataux, François Lazeyras, Alban Longchamp. "Sodium Hydrosulfide (NaHS) Treatment During Porcine Kidney Ex-Vivo Perfusion and Transplantation". Manuscript accepted for publication in *Transplantation Direct.*

5. Oscar Dabrowski, Sébastien Courvoisier, Jean-Luc Falcone, Antoine Klauser, **Julien Songeon**, Michel Kocher, Bastien Chopard, and François Lazeyras. "Choreography Controlled (ChoCo) brain MRI artifact generation for labeled motion-corrupted datasets". In *Physica Medica*, 102, 2022, 79-87.

Publications under review:

1. **Julien Songeon**, Sébastien Courvoisier, Thomas Agius, Oscar Dabrowski, Alban Longchamp, François Lazeyras, Antoine Klauser. "Improved Phosphorus MRSI acquisition through Compressed Sensing Acceleration combined with Low-Rank Reconstruction". Manuscript submitted for publication in *Magnetic Resonance in Medicine.*

CONFERENCES

Abstracts:

1. **Julien Songeon**, Sébastien Courvoisier, Antoine Klauser, Alban Longchamp, Jean-Marc Corpataux, Leo Buhler, and François Lazeyras. "31P Magnetic Resonance Spectroscopy analyzed and quantified by Convolutional Neural Network (CNN)". *Proceedings of the 2020 Annual Meeting of the International Society for Magnetic Resonance in Medicine (ISMRM Online).*

2. **Julien Songeon**, Thomas Agius, Antoine Klauser, Grégoire Longchamp, Raphael Ruttimann, Jean-Marc Corpataux, Alban Longchamp, François Lazeyras. "Sub-Normothermic Ex-Vivo DCD Porcine Kidney Perfusion Improves Energy Metabolism: Analysis using ^{31}P-MRSI." *Proceedings of the 2022 Annual Meeting of the International Society for Magnetic Resonance in Medicine (ISMRM London).*

3. **Julien Songeon**, Sébastien Courvoisier, Lijing Xin, Thomas Agius, Oscar Dabrowski, Alban Longchamp, François Lazeyras, Antoine Klauser. "^{31}P-MRS Analysis with Neural Network: 31P-SPAWNN." *International Magnetic Resonance Spectroscopy Workshop - MRS 2022 Lausanne.*

4. **Julien Songeon**, Sébastien Courvoisier, Oscar Dabrowski, François Lazeyras, Antoine Klauser. "Kidney transplant monitoring by ^{31}P-MRSI and analysis by neural network." *BBL-CIBM-FCBG Research day 2022 Geneva.*

5. Thomas Agius, **Julien Songeon**, Antoine Klauser, Antonio Nastasi, Raphael Ruttimann, Raphael Meier, Leo Buhler, Florent Allagnat, Jean-Marc Corpataux, François Lazeyras, and Alban Longchamp. "Hydrogen sulfide (H2S) reduces oxygen and ATP consumption in the isolated perfused pig kidney." *Abstracts of the 108th Annual Swiss Congress of Surgery (2021 Online)*

6. Alban Longchamp, Antoine Klauser, Thomas Agius, **Julien Songeon**, Antonio Nastasi, Raphael Ruttimann, Raphael Meier, Leo Buhler, Florent Allagnat, Jean-Marc Corpataux, and François Lazeyras. "Ex vivo analysis of graft viability using 31P magnetic resonance imaging spectroscopy." *Abstracts of the 108th Annual Swiss Congress of Surgery (2021 Online)*

7. Oscar Dabrowski, Sébastien Courvoisier, Jean-Luc Falcone, Antoine Klauser, **Julien Songeon**, Michel Kocher, Bastien Chopard, and François Lazeyras.. "Temporally improved volume registration by data driven subvolume interpolation of simultaneous multislice EPI time series." *Proceedings of the 2022 Annual Meeting of the International Society for Magnetic Resonance in Medicine (ISMRM London).*

8. Oscar Dabrowski, Sébastien Courvoisier, Jean-Luc Falcone, Antoine Klauser, **Julien Songeon**, Michel Kocher, Bastien Chopard, and François Lazeyras. "Choreography Controlled (ChoCo) by synchronized video for motion artifact reproducibility and dataset generation." *Proceedings of the 2022 Annual Meeting of the International Society for Magnetic Resonance in Medicine (ISMRM London).*

CONTENTS

LIST OF FIGURES

LIST OF TABLES

ACRONYMS AND PHYSICAL CONSTANTS

ACRONYMS

AI	Artificial Intelligence
ADP	Adenosine Diphosphate
AMP	Adenosine Monophosphate
ATP	Adenosine Triphosphate
BW	Bandwidth
CNN	Convolutional Neural Network
CS	Compressed Sensing
CSS	Cold Static Storage
CSDA	Chemical Shift Displacement Artifact
CSI	Chemical Shift Imaging
DCD	Donation after Circulatory Death
DGF	Delay Graft Function
DFT	Discrete Fourier Transform
DIFT	Discrete Inverse Fourier Transform
DL	Deep Learning
ECD	Extended-Criteria Donor
ESRD	End-Stage Renal Disease
FID	Free Induction Decay
FOV	Field of View
FT	Fourier Transform
GD	Gradient Descent
GPC	Glycerol phosphorylcholine
GPE	Glycerol phosphorylethanolamine
H_2S	Hydrogen Sulfide
HBD	Heart Beating Donor
HPP	Hypothermic Pulsatile Perfusion
IFT	Inverse Fourier Transform

IRI	Ischemia/Reperfusion Injury
LR	Low Rank
LRD	Living Related-Donor
ML	Machine Learning
MLP	Multilayer Perceptron
MP	Membrane phospholipids
MRI	Magnetic Resonance Imaging
MRS	Magnetic Resonance Spectroscopy
MRSI	Magnetic Resonance Spectroscopic Imaging
NAD+/NADH	Nicotinamide adenine dinucleotide oxidized/reduced
NaHS	Sodium Hydrosulfide
NMR	Nuclear Magnetic Resonance
PCh	Phosphorylcholine
PCr	Phosphocreatine
PDE	Phosphodiesters
PE	Phosphorylethanolamine
Pi	Inorganic phosphate
PME	Phosphomonoester
PReLU	Parametric Rectified Linear activation Unit
ppm	Parts-per-million
PSF	Pointspread Function
RF	Radio-frequency
ReLU	Rectified Linear activation Unit
ROI	Region of Interest
ROS	Reactive oxygen species
SGD	Stochastic Gradient Descent
SNR	Signal to Noise Ratio
TGV	Total Generalized Variation
TV	Total Variation
VOI	Volume of Interest

PHYSICAL CONSTANTS AND MATHEMATICAL NOTATION

B_0	Static magnetic field [T]
B_1	Magnetic radiofrequency field [T]
G	Magnetic field gradient strength $[T \cdot m^{-1}]$
γ	Gyromagnetic ratio $[rad \cdot s^{-1} \cdot T^{-1}]$
γ	$\gamma/2\pi$ $[s^{-1} \cdot T^{-1}]$
$\hat{H}$	Hamiltonian
$\hbar$	Reduced Planck constant: $1.054 \cdot 10^{-34}\,J \cdot s$
k_B	Boltzmann constant: $1.3806 \cdot 10^{-23}\,J \cdot K^{-1}$
T_1	Longitudinal relaxation time [s]
T_2	Transverse relaxation time [s]
$T_2^\star$	Effective Transverse relaxation time [s]
TE	Echo time [s]
TI	Inversion Time [s]
TR	Repetition time [s]
$\mathbf{x}$	A vector
$\mathbf{X}$	A matrix
x^i	A component i of a vector $\mathbf{x}$
X^i	A component ij of a matrix $\mathbf{X}$
$\mathbf{X}^T$	Transpose of the matrice $\mathbf{X}$
$\mathbf{X}^H$	Hermitian transpose of the matrice $\mathbf{X}$

1

INTRODUCTION

"Not all those who wander are lost."

- J.R.R. Tolkien, *The Fellowship of the Ring*

Contents

Magnetic Resonance Imaging (MRI) is a relatively new technique in the applied sciences, with its beginnings traced back to the paper by Lauterbur and Mansfield in 1973 [1, 2]. The development of MRI is the result of numerous discoveries made in the 20^{th} century. The starting point would be the discovery of spin and the development of quantum mechanics [3, 4], as well as the Larmor precession of the spins when exposed to a magnetic field. Another crucial discovery was nuclear magnetic resonance (NMR) by Prucell [5], and Bloch [6–8] in 1945; and more specifically with in 1966 with the introduction of pulsed NMR combined with Fourier transform by Ernst and Anderson [9], in combination to the discovery of the Zeeman effect [10] and Rabbi oscillation [11]. The discovery and evolution of superconducting magnets also made a significant contribution to the creation of the MRI machine, allowing for the production of static magnetic fields of the order of Tesla. Despite being a relatively young discipline in the realm of applied sciences, with only 50 years of history, MRI is a well-known and widely used clinical tool for medical applications. The method has several advantages, the most significant being that MRI is non-ionizing and non-invasive due to the nature of magnetic field physics. The ability of the MR machine to image soft tissues in the human body and metabolic processes therein has led to its strong position in biomedical science applications. MRI has the potential to provide in-vivo insight into the physiology of human body functions. An additional valuable feature of the MR system is the ability to investigate metabolism via magnetic resonance spectroscopy (MRS). Protons within identical nuclei of different molecules are subject to slightly different magnetic fields, even in the presence of identical external magnetic fields. In other words, various chemical compounds have slightly different local magnetic fields, leading to the local excitation frequency being shifted to distinct values first observed by Proctor and Yu in 1949 [12]. By applying position-dependent magnetic fields in addition to the static magnetic field, the reconstruction the spatial distribution of nuclear spins in the form of an image can be achieved, utilizing a method called magnetic resonance spectroscopic imaging (MRSI). The pioneering report of in-vivo proton NMR measurements dates back to 1985, when Bottomley reported such measurements on a rat brain [13]. The application of multidimensional NMR has facilitated the study of biological macromolecules and enabled the determination of the 3D structure of proteins in an aqueous environment, thereby providing an alternative to X-ray crystallography.

The concept of transplantation can be traced back to pictorial representations from the 13^{th} century [14]. However, modern transplantation is attributed to Theodor Kocher, who performed the first successful thyroid transplant in 1883 [15]. At the beginning of the 20^{th} century, the problem of rejection was first identified by Alexis Carrel [16], while Georg Schöne discovered

that the body's own immune system was responsible for rejection [17]. The contemporary era of transplantation may be deemed to have commenced in the early 1950s with two significant breakthroughs. The first of these was the description by Peter Medawar of actively acquired immunological tolerance in rats, which paved the way for an improved understanding of transplant immunology [18]. The second was the performance of the first successful kidney transplantation between identical twin brothers by Joseph Murray [19]. These two groundbreaking accomplishments laid the foundation for the development of transplantation as a therapeutic option for patients with end-stage organ failure. Prior to 1970, the therapeutic options for patients diagnosed with end-stage renal disease (ESRD) were extremely limited. At that time, only a few dialysis facilities existed, leading to only a small number of patients receiving regular dialysis. Kidney transplantation was in its nascent stages of development as a viable therapeutic option, and transplant immunology and immunosuppressive therapy were also in their infancy. Consequently, a diagnosis of chronic renal failure was once considered a death sentence. Dialysis treatment, though it provided some relief, often left patients feeling unwell with persistent constitutional symptoms of fatigue and malaise. Despite better anemia management, progressive cardiovascular disease, peripheral and autonomic neuropathy, and bone disease were common. However, the availability of renal transplantation therapy has improved drastically since it became covered by the extend Medicare in the United States. Nowadays, renal transplantation is theoretically available to all those who require it, even if it may not always be feasible in practice [20]. Currently, the field of transplantation is grappling with a significant shortage of viable organs. In the United States, it is estimated that around 100000 patients are awaiting kidney transplantation, while only 18000 procedures are carried out each year [21]. Similarly, in Switzerland, there are 1435 patients on the waiting list with only 342 kidney transplants performed annually [22]. As a possible solution, marginal donors are being considered. However, the use of such donors is limited by the lack of a reliable and non-invasive method for assessing kidney viability.

Phosphorus magnetic resonance spectroscopy (^{31}P-MRS) is a non-invasive technique that can detect high-energy phosphate metabolites in the kidney and provide insight into its energetic metabolism [23]. This technique enables the detection of several metabolites, including adenosine triphosphate (ATP), inorganic phosphates (Pi), phosphomonoesters (PME) containing cell membrane precursors such as phosphocholine, phosphoethanolamine, and ATP precursors such as adenosine monophosphate (AMP). The PME/Pi intensity ratio measured during cold storage prior to transplantation is an important biomarker for graft viability [24]. Viable cells should be able to rephosphorylate AMP to ATP, especially when the reserve is abundant. Additionally, degradation of phospholipids in cell membranes is reflected by a reduction of PME and an increase of phosphodiester [25]. Thus, monitoring the PME level provides information on both cell membrane integrity and AMP storage. The non-invasive nature of ^{31}P-MRS makes it a promising approach for monitoring mitochondrial function and predicting graft viability. This project aims to apply the technique in real clinical situations to improve kidney preservation and ^{31}P-MRS (shorter acquisition time and more sensitive metabolite detection). Ultimately, we hope that the use of marginal donors can be extended, and that MR-related techniques will be an accurate, non-invasive way to evaluate kidney outcomes following transplantation.

1.1 CONTRIBUTIONS

1.1.1 *Improving ^{31}P-MRSI with Artificial Intelligence*

The analysis of MR spectra is commonly performed through fitting algorithms. Multiple software packages, such as LCModel or AMARES, are traditionally used to analyze and quantify the measured spectra. Both algorithms rely on prior knowledge, in the form of a basis set of each resonance. However, these methods have limitations, including long computation times, particularly for multi-voxel magnetic resonance spectroscopic imaging (MRSI) measurements, and difficulties in quantifying low signal-to-noise ratio (SNR) spectra. In the context of assessing the viability of kidneys prior to transplantation using ^{31}P-MRSI measurements, there is a need for a fast computation analysis that can handle the inherent low sensitivity of phosphorus metabolites.

In order to address this need, we developed deep learning methods using convolutional neural networks to analyze, quantify, and reconstruct the measured spectra. We developed the full pipeline, including the generation of simulated datasets for training the networks, multiple networks with different applications, such as quantification of metabolite concentrations, spectral parameter estimation, and baseline estimation. We also developed a method for reconstructing the spectra using the physical model with the estimated parameters, for the purpose of spectrum plotting. We demonstrated that the deep learning model performs similarly to the fitting software LCModel, and even outperforms it at low SNR. The new model meets expectations for fast computation time and has the potential to provide improved analysis and quantification of ^{31}P-MRSI spectra for the assessment of kidney viability prior to transplantation.

1.1.2 *Improving ^{31}P-MRSI with Compress Sensing Acceleration and Low Rank Reconstruction*

Fourier-based methods have been instrumental in MRI, but they require complete sampling of k-space, along with other specific requirements. This approach imposes constraints on acquisition, which can be time-consuming and clinically impractical, especially when evaluating organs for transplantation or ensuring patient comfort. Moreover, the inherent low SNR in ^{31}P-MRSI can result in the use of multiple acquisition averages as compensation, leading to prolonged scan times. Alternative approaches, such as non-Fourier-based techniques, propose reconstruction methodologies that frame the reconstruction process as an optimization problem. Compressed sensing (CS) is a notable example of such methods that has garnered significant attention due to its ability to reduce scanning time while preserving superior image quality. Low-rank (LR) reconstruction has been shown to be particularly advantageous for applications that require improved SNR, as it can effectively denoise the reconstructed images.

To address the challenges encountered in phosphorus spectroscopy, we investigated the potential of an acceleration reconstruction method that combines compressed sensing with low-rank and total generalized variation regularization approaches to enhance the acquisition process. We developed the framework of the CS-LR methods, which includes a novel approach of using distinct random undersampling patterns for each k-space average to prevent the suppression of identical points, thereby enabling greater k-space coverage without altering the acceleration factor. The effectiveness of these methods was evaluated using healthy volunteers' brain data and ex-vivo perfused kidney. We demonstrated that the methods significantly improved the SNR while preserving spectral and spatial quality, even when the acquisition was accelerated threefold. Furthermore, the metabolite peak linewidth remained constant at all acceleration factors, and anatomical information could be recovered from signal attenuation.

1.1.3 *Applications for Transplantation: Organ Preservation Techniques and Pre-Transplant Ex-Vivo Viability Assessment*

Transplantation plays a vital role in the medical field, particularly for end-stage diseases where it may be the sole option for survival. However, the number of patients awaiting transplantation far exceeds the availability of organs, particularly in the case of end-stage renal disease. The limited availability of these organs necessitates that many patients rely on dialysis or face poor survival rates, incurring costs that can be up to 10 times higher than transplantation. To address this scarcity, the donor pool has been expanded beyond standard-criteria donors to include extended-criteria donors (ECD) and donation after circulatory death (DCD) donors, commonly referred to as marginal donors. Despite these efforts, the use of marginal donors is hindered by their poor outcomes. A significant challenge in the use of organs from marginal donors is the lack of reliable non-invasive methods for assessing their viability. Marginal organs are particularly vulnerable to ischemia-reperfusion injury, which can occur following the restoration of blood flow to previously ischemic tissues.

The present study on organ preservation and viability assessment is part of two thesis projects. This thesis focuses on the assessment of organ viability using a multi-modal MRI approach, including imaging of the organs, assessment of kidney perfusion via contrast medium injection, and phosphorus metabolic assessment via ^{31}P-MRSI. The other part of the project was conducted by Thomas Agius as part of his Biology thesis. He was responsible for performing the same research using kidney biopsies and analyzing histological scores. He also managed the surgical aspect of the research, including administration of the preservation product and management of the different experimental models.

Our research on organ preservation and viability assessment focused on three main areas. Firstly, we presented the experimental setup used for evaluating kidney viability. This involved a pneumatically-driven hypothermic pulsatile perfusion (HPP) system that is made of non-magnetic materials and is compatible with MRI technology. The system was fully developed at the Geneva University Hospital (HUG) and is the only MR-compatible system in the world that can perform both MRI and ^{31}P-MRS acquisition while being compatible with organ recovery procedures. Our research was carried out using porcine kidneys and we were successful in detecting ischemia-reperfusion damage. We found that the descending slope of gadolinium perfusion elimination was correlated with histological damage scores. The second subject of our research was the investigation of sub-normothermic preservation at 22 °C compared to hypothermic preservation at 4 °C. Our study showed that perfusing kidney grafts at 22 °C resulted in increased production of high-energy phosphorus metabolites and minimized ischemia-reperfusion injury during transplantation, when compared to 4 °C perfusions. We observed differences in the sub-normothermic preservation versus hypothermic preservation are strongly correlated with the histological score that measures cellular damage. The third subject of our investigation focused on the administration of hydrogen sulfide (H_2S) through the injection of NaHS, which aimed to reduce oxygen and ATP consumption in isolated perfused kidneys, diminish inflammation, and improve renal function following an ischemia-reperfusion injury. Our findings indicated that H_2S administration did not result in significant reductions in ischemia-reperfusion injuries or improvements in kidney metabolism. Furthermore, no significant difference was observed in renal artery injection of H_2S or auto-transplantation in terms of histological lesions or cortical/medullary kidney perfusion. As such, our study suggests that the use of NaHS for H_2S treatment does not significantly enhance renal graft function in porcine kidneys.

1.2 OUTLINE OF THE THESIS

The present thesis is structured as follows: The initial Part will present a comprehensive overview of the theoretical concepts of magnetic resonance imaging and magnetic resonance spectroscopy, divided into three chapters. Chapter 2 will begin with a discussion on nuclear physics, elucidating the application of quantum theory in describing spin, and further expounding on the equations of particle evolution in a magnetic field. The signal emission will be discussed, with particular attention given to spin excitation and relaxation. Subsequently, Chapter 3 will describe the signal emitted from the excitation and acquisition techniques. The chapter will introduce Faraday's law of signal induction, which enables signal measurement, and then present a few general acquisition methods. The chapter will conclude with a discussion on encoding principles, including the Fourier domain acquisition and the use of an external gradient magnetic field to encode multi-dimensional images. Chapter 4 will address another aspect of MR techniques, magnetic resonance spectroscopy . The chapter will introduce the theory of molecule resonances, incorporating electron shielding (chemical shift) and spin coupling (J-coupling). In addition, it will elaborate on localization spectroscopy and multi-voxel spectroscopy, with the goal of introducing magnetic resonance spectroscopic imaging (MRSI). The second part of the chapter will focus on phosphorus spectroscopy, beginning with an overview of the biology of relevant phosphorus molecules observed and the physiological functions of said molecules.

The second part of this thesis will explore the topic of Artificial Intelligence (AI). Chapter 5 will present an overview of machine learning (ML) and deep learning (DL), with a focus on Convolutional neural networks (CNNs). The chapter will provide all the necessary components to support the discussion in Chapter 6, which is a published article presenting a novel analysis tool for phosphorus spectroscopy that utilizes CNNs. The framework aims to enhance the analysis of phosphorus spectroscopy by providing faster computing analysis and robustness in low signal situations.

The third part of the thesis will concentrate on acquisition and reconstruction techniques. Chapter 7 will revisit k-space encoding and provide a more detailed explanation of Fourier sampling and transformation. The chapter will also discuss the advantages and the need for developing alternative non-Fourier reconstruction methods. This chapter will concentrate on two techniques, namely, compressed sensing (CS) and low rank (LR) that enable faster acquisition and improved reconstruction. Chapter 8 will present a paper currently under review that details the development of an enhancement of phosphorus spectroscopic acquisition using the combination of compressed sensing acceleration and low rank reconstruction.

The fourth part of this thesis is dedicated to the application of ex-vivo phosphorus magnetic resonance spectroscopic imaging in transplantation. Chapter 9 will introduce the field of transplantation and its relevance to this study. Chapter 10 will present a published article that demonstrates the feasibility of assessing and quantifying phosphorus metabolites ex-vivo in kidney grafts, and highlights the correlation between warm ischemia injuries and ATP levels. In Chapter 11, a published article will be presented that discusses the benefits of subnormothermic temperatures for organ preservation compared to cold storage. Finally, Chapter 12 will present a paper accepted for publication on the potential benefits of Sodium Hydrosulfide (H_2S) for kidney protection before transplantation.

The fifth and final part of this thesis will provide a summary of the presented work and additional discussions. It will also outline the future research directions in this field.

Part I

GENERAL OVERVIEW: FROM ELEMENTARY PARTICLES PHYSICS TO MAGNETIC RESONANCE IMAGING AND SPECTROSCOPY

2

PHYSICS OF THE MRI : AN OVERVIEW

"To a physicist, beauty means symmetry and simplicity. If a theory is beautiful, this means it has a powerful symmetry that can explain a large body of data in the most compact, economical manner."

- Michio Kaku, *Parallel Worlds: A Journey through Creation, Higher Dimensions, and the Future of the Cosmos*

Contents

2.1 INTRODUCTION

Magnetic resonance imaging (MRI) is the application of nuclear magnetic resonance (NMR), which was originally named nuclear magnetic resonance imaging. NMR involves the use of a magnetic field and radio-frequency pulses to study the magnetic properties of a sample. The nucleons (protons and neutrons) within the atomic nucleus of certain atoms have the capability to absorb radio-frequency energy, resulting in the creation of a transverse magnetization. This magnetization can then return to its initial state, inducing a signal in the process. The key element in this process is spin, which is a fundamental quantum property of particles. Spin is not straightforward to describe, the most generic explanation is that it can be thought of as the angular momentum of an orbiting object in the classical world. However, particles are not in orbit and therefore they do not have a classical counterpart.

The discovery of spin took place at the beginning of the 20th century, when the foundations of quantum theory were being established. In 1922, the Stern-Gerlach experiment demonstrated that angular momentum was quantized [26]. A few years later, in 1925, George Uhlenbeck and Samuel Goudsmit presented their theory of electron spin [3], the same year that Wolfgang Pauli introduced the Pauli exclusion principle [27]. These discoveries indicated that the electron had an additional degree of freedom and that two electrons could not occupy the same quantum state. Paul Dirac further developed the theory of spin in quantum mechanics in 1930 [4], and Pauli extended it to all elementary particles in 1940 [28]. In addition to the development of quantum spin, two other discoveries have had a significant impact on the field of NRM. The first is the Zeeman effect [10], which describes the splitting of the energy levels of electrons in the presence of a static magnetic field as a function of their spin value. The second is the Rabi cycle [11], which refers to the induction of state transitions between two energy levels in an electron using time-varying fields.

Quantum physics theories are not necessary to comprehend and explain the physics and principles of MRI. While they may be presented using classical theories to increase understanding, it would be a shame to pass up the chance to delve into the quantum world and its marvels. Therefore, this chapter will use quantum mechanics to derive the principles of MRI, in tribute to the elegance and beauty of the equations.

2.2 PHYSICS OF ELEMENTARY PARTICLE

2.2.1 *Symmetries*

In physics, symmetry implies the invariance under some transformation. A symmetrical transformation allows us to change our perspective without altering the possible outcomes of an experiment [29]. This leads to one of the most fundamental theorems in theoretical physics: Noether's theorem, which states that every differentiable symmetry of the action has a corresponding conservation law. In quantum physics, the most significant group of symmetry is the Poincaré group, named after Henri Poincaré. This group includes the symmetry of translation in space-time, rotational symmetry, and symmetry under a boost. The last two symmetries form the Lorentz group together. This group has six generators $J^{\mu\nu}$, with a pair of anti-symmetric indices (μ, ν) [30]. These generators can be rearranged into two spatial vectors, one of which is

The Boost is the Lorentz transformation which connects the inertial reference frame of two bodies.

$$J^i = \frac{1}{2}\epsilon^{ijk}J^{jk}. \tag{2.1}$$

The J^i vector is the angular momentum. Since the Poincaré group is a Lie group and its algebra is the Lie algebra as well, we can write the relation between the angular momentum component as follow

$$[J^i, J^j] = i\hbar\epsilon^{ijk}J^k. \tag{2.2}$$

The subgroup of the Lorentz group that describes rotations is the $SU(2)$ group. It has the unique property of acquiring a negative sign under a 2π rotation and is only periodic under a 4π rotation. This means that the solution to equation (2.2) includes both half-integer and integer spin. The $SU(2)$ representation is labelled with an index j that takes the values $0, 1/2, 1, 3/2, 2$, ... and determines the possible values of the states. The index-j has $2j + 1$ dimensions, and each state within it is labeled j_z, which ranges from $-j$ to j in integer steps [31]. The fundamental representation of $SU(2)$ is $j = 1/2$, on which the J^i are represented as

$$J^i = \frac{1}{2}\hbar\sigma^i, \tag{2.3}$$

where the σ^i are the Pauli matrices

$$\sigma^x = \begin{pmatrix} 0 & 1 \\ 1 & 0 \end{pmatrix}, \quad \sigma^y = \begin{pmatrix} 0 & -i \\ i & 0 \end{pmatrix}, \quad \sigma^z = \begin{pmatrix} 1 & 0 \\ 0 & -1 \end{pmatrix}. \tag{2.4}$$

Angular momentum can be further divided into two components: orbital momentum $L^{\mu\nu}$ and spin $S^{\mu\nu}$ with $J^{\mu\nu} = L^{\mu\nu} + S^{\mu\nu}$. While $L^{\mu\nu}$ is independent of the representation used, $S^{\mu\nu}$ depends on the specific representation. In contrast, $L^{\mu\nu}$ depends on spatial coordinates, while $S^{\mu\nu}$ does not. Therefore they commute $[L^{\mu\nu}, S^{\mu\nu}] = 0$ and both satisfy the angular momentum commutations relations given in equation (2.2).

2.2.2 *Spin*

Spin is a fundamental intrinsic property of particles and does not have a counterpart in the classical world. For example, an electron has a spin of $1/2$ (an index-s of $1/2$). Following the same rule as the angular momentum, a one-half spin has two possible s_z states: spin up with

$s_z = +1/2$ and spin down with $s_z = -1/2$. The spin is commonly represented using braket notation.

$$|\uparrow\rangle = \begin{pmatrix} 1 \\ 0 \end{pmatrix} \text{ spin up}, \qquad |\downarrow\rangle = \begin{pmatrix} 0 \\ 1 \end{pmatrix} \text{ spin down}. \tag{2.5}$$

The spin operator S^i is derived from the generator $S^{\mu\nu}$ in the same way as angular momentum. For a one-half spin, it is represented as follows.

$$S^i = \frac{1}{2}\hbar\sigma^i. \tag{2.6}$$

In this representation, the spin up and spin down are eigenvector with eigenvalues of $\pm\frac{1}{2}\hbar$, respectively. Since the spin is a physical quantity that can be measured, the spin operator S^i is an observable.

2.2.3 *Schrödinger's equation*

In non-relativistic quantum mechanics, particles are described by wave functions. A general wave function can be written as

$$|\Psi(\mathbf{x}, t)\rangle = e^{\frac{-i\hat{H}t}{\hbar}} |\Psi(\mathbf{x})\rangle . \tag{2.7}$$

The function is decomposed into $|\Psi(\mathbf{x})\rangle$, the initial state, and $e^{\frac{-i\hat{H}t}{\hbar}}$, the time evolution operator. The latter preserves the inner product between vectors in the Hilbert space. The Schrödinger equation describes the time evolution of the wave in the presence of a specified potential energy $\hat{V}(\mathbf{x}, t)$. The time-dependent Schrödinger equation is

The inner product is the binary operation $\langle\cdot|\cdot\rangle$ that associates vectors and returns a scalar.

$$\hat{H} |\Psi(\mathbf{x}, t)\rangle = i\hbar\frac{d}{dt} |\Psi(\mathbf{x}, t)\rangle . \tag{2.8}$$

If the potential $\hat{V}(\mathbf{x}, t)$ in the Hamiltonian $\hat{H}$ does not depend explicitly on t, the wave function can be separated as shown in equation (2.7). $|\Psi(\mathbf{x})\rangle$ now satisfies the time-independent Schrödinger equation.

$$\hat{H} |\Psi(\mathbf{x})\rangle = \left[-\frac{\hbar^2}{2m}\nabla^2 + \hat{V}\right] |\Psi(\mathbf{x})\rangle . \tag{2.9}$$

The equation describes stationary waves that have a solution of $\hat{H} |\Psi(\mathbf{x})\rangle = E |\Psi(\mathbf{x})\rangle$, where E is the energy of the particle and the eigenvalue associated with the eigenvector Ψ. Like the spin, the Hamiltonian is an observable.

2.2.4 *Particle in a magnetic field*

In the context of MRI, we are interested in the evolution of in a particle in a magnetic field [32, 33]. In the classical world, the magnetic moment describes the intensity of a magnetic object and is calculated by multiplying a current value over an enclosed surface. In quantum physics, charged particles have a magnetic moment due to their spin, known as spin magnetic moment. For a particle of charge q, mass m and spin $1/2$ the spin magnetic moment is

$$\boldsymbol{\mu} = g\frac{q}{2m}\boldsymbol{S} \tag{2.10}$$

$$= \gamma\boldsymbol{S}. \tag{2.11}$$

The g-factor of the electron is the most accurate measured value in physics, with an accuracy of 15 decimal places.

The constant g, called g-factor, is intrinsic to each particle, and γ is the gyromagnetic ratio ($rad \cdot s^{-1} \cdot T^{-1}$). The g-factor and, by extension, the gyromagnetic ratio, can be extend to nuclei, atomes, and even molecules. This is particularly useful because MRI probes the nuclei of atomes of molecules.

Let us consider a constant magnetic field in the form $\mathbf{B} = B_0\hat{z}$. The potential energy of this magnetic field is given by

$$V = -\boldsymbol{\mu} \cdot \mathbf{B} = -\gamma S^z B_0 \tag{2.12}$$

If we consider the specific case of a particle at rest with no kinetic energy, the first term of equation (2.9) becomes zero. Thus, the equations is now written as

$$\begin{aligned} \hat{H}\,|\Psi(\mathbf{x})\rangle &= -\gamma \hat{S}^z B_0\,|\Psi(\mathbf{x})\rangle && (2.13)\\ &= -\gamma \frac{1}{2}\hbar\sigma^z B_0\,|\Psi(\mathbf{x})\rangle && (2.14)\\ &= E\,|\Psi(\mathbf{x})\rangle && (2.15) \end{aligned}$$

The equation (2.13) is known as the Zeeman Hamiltonian. Calculating of the spin observable $\hat{S}^z$ on the wave function in the equation (2.13) gives its eigenvalue $1/2\hbar\sigma^z$. It is useful to define $\omega_0 = \gamma B_0$, because ω_0 has the dimension of a frequency. The two solution for the energy eigenvalues obtained in equation (2.15) are

This definition of ω_0 is the standard in NMR, but quantum mechanics books will often define it as $\omega_0 = -\gamma B_0$.

$$\begin{cases} E_+ = -\frac{1}{2}\hbar\omega_0 & \text{Spin parallel } (s_z = +1/2) \\ E_- = +\frac{1}{2}\hbar\omega_0 & \text{Spin anti-parallel} (s_z = -1/2) \end{cases} \tag{2.16}$$

Thus, the difference of energy is $\Delta E = E_- - E_+ = \hbar\omega_0$. This energy difference can be associated with the absorption or the emission of a photon during the transition between one state to another. The frequency ω_0 is the Larmor precession frequency, which will be discussed in the following section. The Figure 1 shows the Zeeman effect of the energy splitting in a magnetic field.

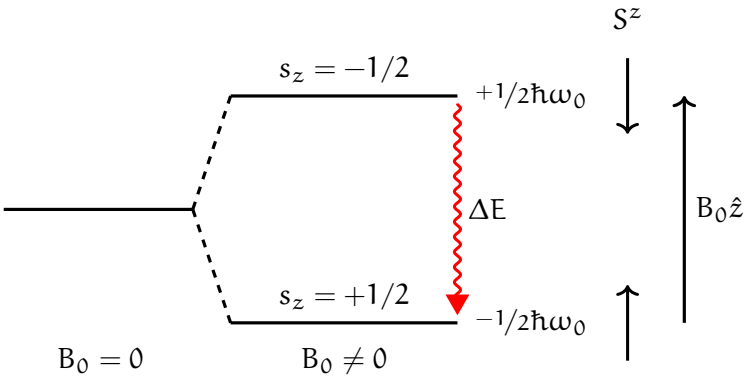

Figure 1: Zeeman effect of the energy splitting in a constant magnetic field B_0. In a situation with no magnetic field ($B_0 = 0$), particles in the same quantum state with opposite spin have the same energy level. When they are immersed in a magnetic field ($B_0 \neq 0$) these two particles are now be at a different energy level. The spin that will align with the magnetic field will have the lowest energy.

It is possible to give the Hamiltonian of equation (2.13) a matrix representation (2.5).

$$\hat{H} = -\gamma \hat{S}^z B_0 = \begin{pmatrix} -\frac{1}{2}\hbar\omega_0 & 0 \\ 0 & +\frac{1}{2}\hbar\omega_0 \end{pmatrix} \tag{2.17}$$

The two states, spin up and spin down, in equation (2.5) being the two possible states for $|\Psi(\mathbf{x})\rangle$ and the eigenfunctions of $\hat{H}$ and $\hat{S}^z$. The wave function $|\Psi(\mathbf{x}, t)\rangle$ can be simplified to $|\Psi(t)\rangle$ because we neglect any dependence on the orbital or translational motion of the particle. Thus, $|\Psi(\mathbf{x}, t)\rangle$ can be written as the sum of the solutions:

$$\begin{aligned} |\Psi(t)\rangle &= \sum_{s_z} c_{s_z} |\Psi(\mathbf{x})\rangle_z \, e^{\frac{-iE_z t}{\hbar}} && (2.18) \\ &= c_+ e^{-iE_+ t/\hbar} |\uparrow\rangle + c_- e^{-iE_- t/\hbar} |\downarrow\rangle && (2.19) \end{aligned}$$

The constants c_+ and c_- are complex coefficients which must satisfy $|c_+|^2 + |c_-|^2 = 1$. With the same argument as before, the position $\mathbf{x}$ does not appear in this equation either.

2.2.5 *Precession*

We can represent the wave function as a unit vector in spherical coordinate. The solution for the coefficients can be written in terms of the polar angles as $c_+ = \cos\left(\frac{\theta}{2}\right) e^{-i\phi/2}$ and $c_- = \sin\left(\frac{\theta}{2}\right) e^{i\phi/2}$. Thus the eigenfunction becomes

$$|\Psi(t)\rangle = \cos\left(\frac{\theta}{2}\right) e^{-i(\phi_0 - \omega_0 t)/2} e^{-iE_+ t/\hbar} |\uparrow\rangle + \sin\left(\frac{\theta}{2}\right) e^{i(\phi_0 - \omega_0 t)/2} e^{-iE_- t/\hbar} |\downarrow\rangle \tag{2.20}$$

In this representation, it is clear that the magnetic field induces a phase shift proportional to time for the two spin states. Over time, the angles evolution are $\theta(t) = \theta$ and $\phi(t) = \phi_0 - \omega_0 t$, meaning that the angle of the vector along the z-axis (the direction of the magnetic field B_0) remains constant while it revolves around the axis with a velocity of ω_0. This is the Larmor precession. From there, we can calculate the expectation values for the spin magnetic moment. For the three dimensions of the vector $\boldsymbol{\mu}$ in the equation (2.11), we obtain

$$\begin{aligned} \langle \mu^x \rangle &= \gamma \langle \Psi(t)| S^x |\Psi(t)\rangle && (2.21) \\ &= \frac{\gamma\hbar}{2} \sin(\theta) \cos(\phi_0 - \omega_0 t) && (2.22) \\ \langle \mu^y \rangle &= \gamma \langle \Psi(t)| S^y |\Psi(t)\rangle && (2.23) \\ &= \frac{\gamma\hbar}{2} \sin(\theta) \sin(\phi_0 - \omega_0 t) && (2.24) \\ \langle \mu^z \rangle &= \gamma \langle \Psi(t)| S^z |\Psi(t)\rangle && (2.25) \\ &= \frac{\gamma\hbar}{2} \cos(\theta) && (2.26) \\ & && (2.27) \end{aligned}$$

The equations for the three expected values behave like the classical components of angular momentum. The negative sign in front of the ω_0 in the $(\hat{x} - \hat{y})$ plane describes a clockwise precession around the magnetic field direction. A counter-clockwise precession will occur for negative γ values.

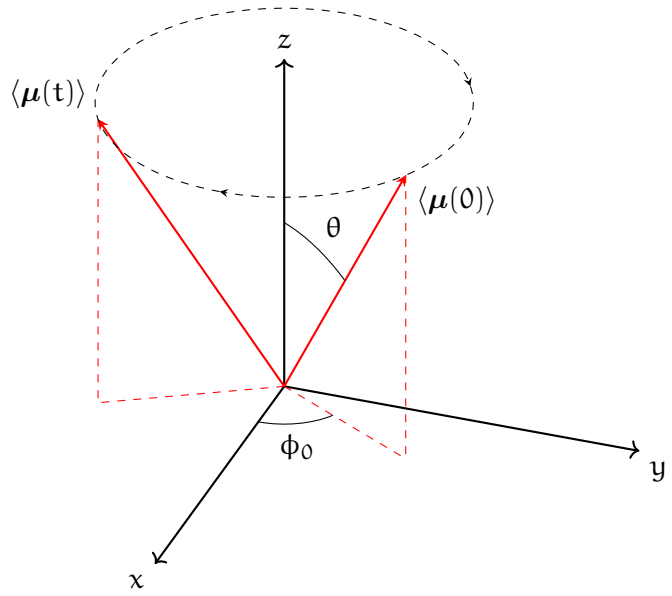

Figure 2: The precession of the expectation values of $\boldsymbol{\mu}$ in the presence of a magnetic field in the z-direction [32].

2.2.6 *Thermal equilibrium*

In the absence of a magnetic field, the atoms of a macroscopic system are all in their ground state, as thermal excitation would require a temperature of around 10^4 K. When immersed in a magnetic field, each atom switches to one of the available discrete energy levels. The macroscopic system acquires a magnetization $\mathbf{M}$ either in the direction of the magnetic field (paramagnetic) or opposite to it (diamagnetic). For paramagnetic atoms, the spin will either align itself with the magnetic field and thus minimize its energy, or use thermal contact to gain energy and move to the higher energy state. The situation is the opposite for diamagnetic atoms. If the distance between the atoms is large, we can neglect the magnetic moment interaction and consider each atom independently. For a system with N particles ($\gg 1$) at equilibrium temperature T, the Hamiltonian of the system is expressed as follow [34].

$$H = \sum_{i}^{N} -\boldsymbol{\mu_i} \cdot \mathbf{B} = \sum_{i}^{N} -\mu_i^z \cdot B_0 \tag{2.28}$$

Using the Boltzmann statistics, we can describe the probability of having the system in a state λ with energy E_λ is

$$P_\lambda = \frac{1}{Z} e^{-E_\lambda / k_b T} \tag{2.29}$$

with the associated partition function

$$Z = \sum_{(\lambda)} e^{-E_\lambda / k_b T} \tag{2.30}$$

As we previously assumed that each atom is independent, the partition function Z is the factorisation of the partition function of each atom $Z = z^N$. For a single atome with spin $1/2$, the partition function becomes the sum of the contribution of the two spin states.

$$z = \sum_{\lambda=-1/2}^{1/2} e^{-E_\lambda/k_b T} \tag{2.31}$$

$$z = \mathrm{tr}\left(e^{-\gamma \frac{1}{2}\sigma^z \hbar B_0/k_b T}\right) \tag{2.32}$$

$$= 2\cosh\left(\frac{\gamma\hbar B_0}{2k_b T}\right) \tag{2.33}$$

The equilibrium magnetization can be derive from the partition function, over the total volume.

$$M_0 = k_b T \frac{\partial \ln(Z)}{\partial B_0} \tag{2.34}$$

$$= \frac{N\gamma\hbar}{2}\tanh\left(\frac{\gamma\hbar B_0}{2k_b T}\right) \tag{2.35}$$

In the context of MRI, the magnetic field is considered low compared to the temperature with $\hbar B_0 \ll k_b T$. We can make the approximation $\frac{\gamma\hbar B_0}{2k_b T} \ll 1$ and therefore $\tanh(x) \approx x$. Thus the magnetization along the magnetic field then becomes

$$M_0 \simeq \frac{N(\gamma\hbar)^2 B_0}{4k_b T} \tag{2.36}$$

We can see from the equation (2.36) that the magnetization M_0 depends on the magnetic field B_0 and the gyromagnetic ratio γ as well. The relationship is linear with the magnetic field, which implies that the signal is enhanced at a higher field. The proportionality between M_0 and γ^2 expresses that isotopes with high resonance frequencies generate a stronger signal. The magnetization is also inversely proportional to the temperature T, so it could be improved by lowering the temperature, but it is unrealistic for in-vivo application. Other factors, such as the sample volume and noise, will also affect sensitivity.

ISOTOPE	SPIN	GYROMAGNETIC RATIO $\frac{\gamma}{2\pi}$ $[10^{-6} \cdot s^{-1} \cdot T^{-1}]$	RELATIVE SENSITIVITY
^{1}H	1/2	42.576	1.00
^{2}H	1	6.536	$1.45 \cdot 10^{-6}$
^{3}He	1/2	−32.434	$5.75 \cdot 10^{-7}$
^{13}C	1/2	10.705	$1.76 \cdot 10^{-4}$
^{14}N	1	3.078	$1.00 \cdot 10^{-3}$
^{15}N	1/2	−4.316	$3.86 \cdot 10^{-6}$
^{17}O	5/2	−5.774	$1.08 \cdot 10^{-5}$
^{19}F	1/2	40.053	$8.34 \cdot 10^{-1}$
^{23}Na	3/2	11.268	$9.27 \cdot 10^{-2}$
^{31}P	1/2	17.235	$6.65 \cdot 10^{-2}$
^{39}K	3/2	1.989	$4.75 \cdot 10^{-4}$
^{129}Xe	1/2	−11.777	$5.71 \cdot 10^{-3}$

Table 1: NMR properties of the most commonly studied isotopes in MRI. The relative sensitivity is calculated with the NMR sensitivity and the natural abundance of the isotope N.

2.3 PHYSICS OF THE MRI

2.3.1 *Physics of the Proton*

The contribution of quarks's spin to the spin of the nucleon is close to zero, this discovery is known as the proton spin crisis.

In MRI, the goal is to probe the nucleus of an atom. A nucleus is made up of protons and neutrons, each of which is composed of up quarks and down quarks. Although the contributions of each component are deeply non-trivial, it follows that protons and neutrons both have convenient one-half spins. Protons and neutrons make up the nucleus of atoms, and the spin of a nucleus can be described using the nuclear shell model. Each type of nucleus (proton or neutron) fills energy layers of its own type in a similar way to how atomic orbitals are filled with electrons.

In general, MRI is described using the physics of protons, which are the only component of the hydrogen nucleus, the most abundant atom in the universe. They are also the most abundant atom in the human body, as the body is made up of about 60% water (H_2O). However, for other atoms, such as those listed in Table 1, both protons and neutrons are involved. The proton has a g-factor of $g_p = +5.585$ while the neutron has a g-factor of $g_n = -3.826$. The spin of an atom can be roughly explained by the fact that there is an odd number of at least one of the two types of nuclei. The negative value of the neutron g-factor explains the negative values of gyromagnetic ratios in Table 1. In the following sections, the physics of MRI will be presented using the simple case of proton physics.

2.3.2 *Bloch equations*

To obtain the equation of motion that will describe the evolution of the magnetization over time, we must use the Heisenberg representation. In the Heisenberg representation, the physical state $|\Psi(\mathbf{x})\rangle$ is fixed in time, while observables evolve in time. In contrast, in Schrödinger's representation, the operators of the system are constant, and the quantum states evolve in time. Observables, such as the magnetic moment $\boldsymbol{\mu}$, satisfy:

$$\frac{d\boldsymbol{\mu}(t)}{dt} = \frac{i}{\hbar}\left[\hat{H}, \boldsymbol{\mu}\right] \tag{2.37}$$

The operation $[\cdot,\cdot]$ is the commutator, such that $[a,b] = ab - ba$.

To compute the commutator, we use $\boldsymbol{\mu} = \gamma \boldsymbol{S}$ and $\hat{H} = -\boldsymbol{\mu}\cdot\mathbf{B} = -\gamma \boldsymbol{S}\cdot\mathbf{B}$. The derivation of the equation (2.37) becomes:

$$\begin{aligned}
\frac{d\boldsymbol{\mu}}{dt} &= \frac{i}{\hbar}\left[-\gamma \boldsymbol{S}\cdot\mathbf{B}, \gamma \boldsymbol{S}\right] && (2.38)\\
&= \frac{-i\gamma^2}{\hbar}\left[\boldsymbol{S}\cdot\mathbf{B}, \boldsymbol{S}\right] && (2.39)\\
&= \frac{-i\gamma^2}{\hbar}\left(\boldsymbol{S}\left[\mathbf{B}, \boldsymbol{S}\right] + \left[\boldsymbol{S}, \boldsymbol{S}\right]\mathbf{B}\right) && (2.40)
\end{aligned}$$

For only one of the three components, the derivation continues as:

$$\begin{aligned}
\left(\frac{d\mu}{dt}\right)_i &= \frac{-i\gamma^2}{\hbar}\left(S_j\left[B_j, S_i\right] + \left[S_j, S_i\right]B_j\right) && (2.41)\\
&= \frac{-i\gamma^2}{\hbar}\left[S_j, S_i\right]B_j && (2.42)\\
&= \frac{-i\gamma^2}{\hbar} i\hbar\epsilon^{jik} S_k B_j && (2.43)\\
& && (2.44)
\end{aligned}$$

It is obvious to see that the first terms of equation (2.41) is 0 as B_j and S_i commute.

$$= \frac{-i\gamma^2}{\hbar} i\hbar(\boldsymbol{S} \times \boldsymbol{B})_i \tag{2.45}$$
$$= \gamma(\boldsymbol{\mu} \times \boldsymbol{B})_i \tag{2.46}$$

An observant reader will recognize the classical Bloch equations for NMR and free induction decay.

$$\frac{d\mathbf{M}(t)}{dt} = \gamma \mathbf{M}(t) \times \mathbf{B}(t) \tag{2.47}$$

The original formula for single proton magnetization $\boldsymbol{\mu}(t)$ has been expanded to include volume magnetization $\mathbf{M}(t)$. The static field is oriented in the $\hat{z}$ direction, as indicated by $\mathbf{B_0} = B_0\hat{z}$. The remaining components of the field are derived from a radio-frequency field $\mathbf{B_1}$, which will be explained in the subsequent section. The equation (2.47) can be further developed in

$$\frac{dM_x(t)}{dt} = \gamma M_y(t)B_0 - \gamma M_z(t)B_{1,y} \tag{2.48}$$
$$\frac{dM_y(t)}{dt} = \gamma M_z(t)B_{1,x} - \gamma M_x(t)B_0 \tag{2.49}$$
$$\frac{dM_z(t)}{dt} = \gamma M_x(t)B_{1,y} - \gamma M_y(t)B_{1,x} \tag{2.50}$$

2.3.3 *Radio-frequency Spin tipping*

To generate an NRM signal, the net magnetization must be rotated in the transverse plane, as stated in reference [32]. This is achieved by applying a radio-frequency (RF) pulse in conjunction with the existing static field. For this discussion, the static field will be assumed to be oriented in the z direction and the transverse plane will be the $(\hat{x} - \hat{y})$ plane. The purpose of the B_1 field is to 'tip' the net magnetization in the transverse plane. The two fields are

$$\mathbf{B_0} = \begin{pmatrix} 0 \\ 0 \\ B_0 \end{pmatrix} \quad \text{and} \quad \mathbf{B_1}(t) = \begin{pmatrix} B_1 \cos(\omega t) \\ -B_1 \sin(\omega t) \\ 0 \end{pmatrix} \tag{2.51}$$

B_1 is define as a circularly polarised field. In this case, the rotation is defined as left-handed polarization, but the direction of rotation should actually follow the gyromagnetic precession direction of the excited isotope. For isotopes with negative gyromagnetic values, as shown in Table 1, the B_1 field must be right-handed polarized. Thus, the total field is the sum of the static field and the RF pulse:

Left-handed polarised B_1 field will produce a counter-clockwise motion of the net magnetization in Figure 3.

$$\mathbf{B_{tot}}(t) = \mathbf{B_0} + \mathbf{B_1}(t) \tag{2.52}$$

The new potential of the field is now given with the total magnetic field $V = -\boldsymbol{\mu} \cdot \mathbf{B}_{tot}$. The equation (2.13) can be used again with the new potentiel, to obtain the new Hamiltonian.

$$\hat{H} = -\boldsymbol{\mu} \cdot \mathbf{B}_{tot} \tag{2.53}$$
$$= -\gamma \left[\hat{S}^x B_1 \cos(\omega t) - \hat{S}^y B_1 \sin(\omega t) + \hat{S}^z B_0\right] \tag{2.54}$$
$$= -\frac{\hbar\gamma}{2} \left[B_1 \left(\sigma^x \cos(\omega t) - \sigma^y \sin(\omega t)\right) + \sigma^z B_0\right] \tag{2.55}$$

Since the two fields are orthogonal, we can compute them independently. The first and second components give

$$-\frac{\hbar\gamma B_1}{2}\left[\sigma^x\cos(\omega t)-\sigma^y\sin(\omega t)\right] = -\frac{\hbar\omega_1}{2}\begin{pmatrix}0 & e^{i\omega t}\\ e^{-i\omega t} & 0\end{pmatrix} \tag{2.56}$$

In equation (2.56), we used the Larmor frequency identity $\omega_1 = \gamma B_1$. The third components of equation (2.55) gives back the result obtained in the equation (2.17). Thus we can sum the two equations to express the Hamiltonian.

$$\hat{H} = -\frac{\hbar\omega_1}{2}\begin{pmatrix}0 & e^{i\omega t}\\ e^{-i\omega t} & 0\end{pmatrix} - \frac{\hbar\omega_0}{2}\begin{pmatrix}1 & 0\\ 0 & -1\end{pmatrix} \tag{2.57}$$

$$= -\frac{\hbar}{2}\begin{pmatrix}\omega_0 & \omega_1 e^{i\omega t}\\ \omega_1 e^{-i\omega t} & -\omega_0\end{pmatrix} \tag{2.58}$$

The time dependent Schrödinger equation can now be written as follow

$$i\hbar\frac{d}{dt}|\Psi(t)\rangle = \hat{H}|\Psi(t)\rangle \tag{2.59}$$

$$i\hbar\frac{d}{dt}|\Psi(t)\rangle = -\frac{\hbar}{2}\begin{pmatrix}\omega_0 & \omega_1 e^{i\omega t}\\ \omega_1 e^{-i\omega t} & -\omega_0\end{pmatrix}|\Psi(t)\rangle \tag{2.60}$$

In the same way as in the previous section, we can write the wave function as a sum of its quantum states $|\Psi(t)\rangle = a_+(t)|\uparrow\rangle + a_-(t)|\downarrow\rangle$. The coefficients are now time dependent. Because of its matrix form, equation (2.60) produce 2 differential equations.

$$\begin{cases} i\hbar\dfrac{da_+(t)}{dt} = -\dfrac{\hbar\omega_0}{2}a_+(t) - \dfrac{\hbar\omega_1}{2}e^{i\omega t}a_-(t)\\ i\hbar\dfrac{da_-(t)}{dt} = \dfrac{\hbar\omega_0}{2}a_-(t) - \dfrac{\hbar\omega_1}{2}e^{-i\omega t}a_+(t)\end{cases} \tag{2.61}$$

It is convenient to move from the laboratory frame to the rotating reference frame. Such a transformation can be expressed using a rotation matrix $R(t)$.

$$\left|\tilde{\Psi}(t)\right\rangle = R(t)|\Psi(t)\rangle \tag{2.62}$$

$$= e^{i\omega t\hat{S}^z/\hbar}|\Psi(t)\rangle \tag{2.63}$$

The new wave function can be written as $\left|\tilde{\Psi}(t)\right\rangle = b_+(t)|\uparrow\rangle + b_-(t)|\downarrow\rangle$. The new coefficients are defined as $b_\pm(t) = e^{\pm i\omega t/2}a_\pm(t)$. The differentials equations now become

$$\begin{cases} i\dfrac{db_+(t)}{dt} = -\dfrac{\Delta\omega}{2}b_+(t) - \dfrac{\omega_1}{2}b_-(t)\\ i\dfrac{db_-(t)}{dt} = \dfrac{\Delta\omega_0}{2}b_-(t) - \dfrac{\omega_1}{2}b_+(t)\end{cases} \tag{2.64}$$

We expressed the difference between the Larmor frequency and the rotation of the reference frame as $\Delta\omega = \omega - \omega_0$. This leads to a transformation of the hamiltonian as well.

$$\hat{\tilde{H}} = -\frac{\hbar}{2}\begin{pmatrix} -\Delta\omega & \omega_1 \\ \omega_1 & \Delta\omega \end{pmatrix} \tag{2.65}$$

In this representation, $\hat{\tilde{H}}$ does not depend explicitly on time. Thus, the solution of equation (2.15) an be computed explicitly and gives the two energy levels.

$$\begin{cases} E_+ = -\frac{1}{2}\hbar\sqrt{\Delta\omega^2 + \omega_1^2} \\ E_- = +\frac{1}{2}\hbar\sqrt{\Delta\omega^2 + \omega_1^2} \end{cases} \tag{2.66}$$

It is noteworthy that the angular frequency can be expressed as the effective field $\sqrt{\Delta\omega^2 + \omega_1^2} = |\gamma \mathbf{B_{eff}}|$. An interesting property to consider is the Rabi's transition formula, which calculates the probability of transitioning between energy states. If the initial energy state is set to the aligned configuration with $|\Psi(0)\rangle = |\uparrow\rangle$, the transition rate

$$P_{\uparrow\downarrow}(t) = |\langle\downarrow|\Psi(t)\rangle|^2 \tag{2.67}$$

$$= \frac{\omega_1^2}{\Delta\omega^2 + \omega_1^2} \sin\left(\sqrt{\Delta\omega^2 + \omega_1^2}\frac{t}{2}\right)^2 \tag{2.68}$$

The probability will oscillate between 0 and $\frac{\omega_1^2}{\Delta\omega^2+\omega_1^2}$. For values with $\Delta\omega \gg \omega_1$, the probability of transition remains close to zero. On the other hand, when $\Delta\omega = 0$ ($\omega_0 = \omega$), the transition amplitude oscillates between 0 and 1.

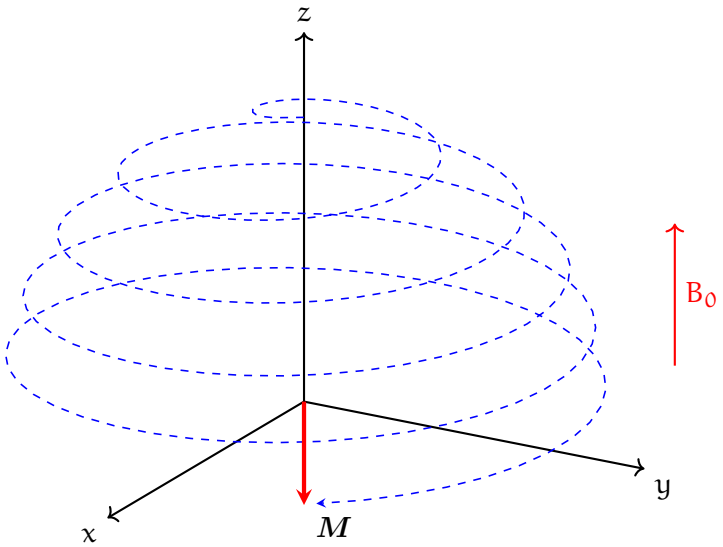

Figure 3: Precession of the net magnetization tipped into the transverse plane with a right-handed $\mathbf{B_1}$ radio-frequency pulse. Inspired from [32].

After the excitation pulse ends, the system returns to its initial equilibrium state, in which the populations of spins are distributed according to the Boltzmann distribution and there are no coherences in the system. This return to the initial state is referred to as relaxation, and it is characterized by two processes: longitudinal relaxation and transverse relaxation. The former process is solely involved in the transition from the excited state to the equilibrium state, while the latter process is related to the loss of coherence in the system.

2.3.4 *T1 longitudinal relaxation*

Longitudinal relaxation is a spin-lattice relaxation process in which the excited particles transfer their energy to the surrounding lattice and return to the equilibrium state. This relaxation results in the regrowth of magnetization along the direction of the static magnetic field. Consider a simple system of N particles with no interactions between them. From equation (2.19), the probability of finding a nucleus in the state $|\uparrow\rangle$ is $|c_+^2|$, and the probability of finding it in the state $|\downarrow\rangle$ is $|c_-^2|$. For a two-state spin system, the populations of particles in each state, $n_\uparrow$ and $n_\downarrow$, can be written as

$$n_\uparrow = \sum_i^N P_i(\uparrow) \tag{2.69}$$

$$n_\downarrow = \sum_i^N P_i(\downarrow). \tag{2.70}$$

Additionally, the statement "proportional to" indicates that the magnetization will scale with a constant factor.

The summation is performed over $P_i(\uparrow)$ and $P_i(\downarrow)$, which represent the probability of finding particle i in one of the two states. The z-magnetization is directly proportional to the difference between the two population states, $M_z \propto n_\uparrow - n_\downarrow$. For theoretical purpose, we can assume that the magnetization is equal to the difference of population, $M_z = n_\uparrow - n_\downarrow$. The probability of transition is given by perturbation theory [35].

$$W_{i\to f} = \frac{2\pi}{\hbar} |\langle f| V |i\rangle|^2 \, \delta(E_f - E_i) \tag{2.71}$$

The energies E_f and E_i are the energies E_+ and E_-, respectively, for a transition from the low-energy state to the high-energy state, and vice versa. A decrease in spin energy is accompanied by an increase in lattice energy due to the conservation of energy. The indices i and j represent the initial and final states, respectively, between $|\uparrow\rangle$ and $|\downarrow\rangle$, or vice versa. We can express the transition from one population to the other as

$$\text{rate of transition from } |\uparrow\rangle \text{ to } |\downarrow\rangle = W_{\uparrow\to\downarrow}(n_\uparrow - n_\uparrow^{eq}) \tag{2.72}$$

$$\text{rate of transition from } |\downarrow\rangle \text{ to } |\uparrow\rangle = W_{\downarrow\to\uparrow}(n_\downarrow - n_\downarrow^{eq}) \tag{2.73}$$

From here, only the first order of the perturbation will be further considered. Particles transitioning from state $|\uparrow\rangle$ to $|\downarrow\rangle$ will decrease the population of $n_\uparrow$ and increase the population of $n_\downarrow$, with the changes being relative to the equilibrium. Thus, the change in rate is

$$\frac{dn_\uparrow}{dt} = W_{\downarrow\to\uparrow}(n_\downarrow - n_\downarrow^{eq}) - W_{\uparrow\to\downarrow}(n_\uparrow - n_\uparrow^{eq}) \tag{2.74}$$

$$\frac{dn_\downarrow}{dt} = W_{\uparrow\to\downarrow}(n_\uparrow - n_\uparrow^{eq}) - W_{\downarrow\to\uparrow}(n_\downarrow - n_\downarrow^{eq}) \tag{2.75}$$

As previously stated, the magnetization is assumed to be equal to the difference in populations. Therefore, the variation in magnetization is equal to the variation in the difference of populations.

$$\begin{aligned}
\frac{dM_z(t)}{dt} &= \frac{d(n_\uparrow - n_\downarrow)}{dt} && (2.76)\\
&= 2W_{\downarrow\to\uparrow}(n_\downarrow - n_\downarrow^{eq}) - 2W_{\uparrow\to\downarrow}(n_\uparrow - n_\uparrow^{eq}) && (2.77)\\
&= -2W_{\downarrow\to\uparrow}\left[(n_\uparrow - n_\uparrow^{eq}) - (n_\downarrow - n_\downarrow^{eq})\right] && (2.78)\\
&= -2W_{\downarrow\to\uparrow}\left[(n_\uparrow - n_\downarrow) - (n_\uparrow^{eq} - n_\downarrow^{eq})\right] && (2.79)\\
&= -2W_{\downarrow\to\uparrow}\left[M_z - M^{eq}\right] && (2.80)
\end{aligned}$$

The integration of both side of equation (2.80) is given by

$$dM_z(t) = (M_z(0) - M^{eq})e^{-t/T_1} + M^{eq} \quad (2.81)$$

We can identify $-2W_{\downarrow\to\uparrow}$ as the spin-relaxation decay rate and write $2W_{\downarrow\to\uparrow} = 1/T_1$. T_1 is the experimental spin-lattice relaxation time. The equation (2.50) can be rewritten as follow.

$$\frac{dM_z(t)}{dt} = -\frac{M_z(t) - M^{eq}}{T_1} \quad (2.82)$$

2.3.5 *T2 transverse relaxation*

Transverse relaxation is a spin-spin relaxation process in which the spins precessing in the transverse plane interact with each other, accumulating phase shift that leads to a loss of the coherence. Unlike the longitudinal relaxation, transverse relaxation does not involve any energy loss as there is no energy state transition. The transverse dipolar relaxation for a two-spin system can be calculated [36]. In the transverse plane, the derivation can be performed using the transverse component of the angular momentum. The derivation will be presented with respect to the $\hat{x}$-axis, but it is entirely symmetrical to the $\hat{y}$-axis. We first need to write the eigenvector.

$$\begin{cases} |+\rangle = \frac{1}{\sqrt{2}}(|\uparrow\rangle + |\uparrow\rangle) & \text{and} \\ |-\rangle = \frac{1}{\sqrt{2}}(|\uparrow\rangle - |\uparrow\rangle) \end{cases} \quad (2.83)$$

In a similar way to equation (2.6), the eigenfunction and eigenvalues are

$$\begin{aligned}
\mu^x |\pm\rangle &= \gamma S^x |\pm\rangle && (2.84)\\
&= \pm\frac{\gamma\hbar}{2} |\pm\rangle && (2.85)
\end{aligned}$$

For this two spin system we will have the two spin operators, one for each spins that will be labelled 1 or 2. The expected values of the two operators are

$$\begin{aligned}
\langle S_1^x \rangle &= (n_{++} - n_{-+}) + (n_{+-} - n_{--}) && (2.86)\\
\langle S_2^x \rangle &= (n_{++} - n_{+-}) + (n_{-+} - n_{--}) && (2.87)\\
& && (2.88)
\end{aligned}$$

Similarly to equation 2.77, the variation of magnetization in time is proportional to the variation of spin population. For the $\hat{x}$-axis, we get

$$\frac{d}{dt}\langle S^x\rangle(t) = \frac{d}{dt}\left(\langle S_1^x\rangle + \langle S_2^x\rangle\right)(t) \tag{2.89}$$

Following the same derivation as the previous section, we can obtain the following solution

$$\frac{d}{dt}\langle S^x\rangle(t) = -(2W_1 + 2W_2)[\langle S^x\rangle - \langle S^{x,eq}\rangle] \tag{2.90}$$

W_1 is the transition of only one of the two spin from a state to another with the other spin constant, and W_2 the transition probability of the two spins in the same state towards the same state. It follows that $(2W_1 + 2W_2) = 1/T_2$. We can write again the equations (2.48) and (2.49) as follow.

$$\frac{dM_{xy}(t)}{dt} = -\frac{M_{xy}(t)}{T_2} \tag{2.91}$$

Dipolar relaxation is one of the relaxation processes; other factors that contribute to T_2 include the presence of macromolecules and cross-relaxation.

Cross-relaxation refers to the transition of both spins from a state $|+,-\rangle$ to a state $|-,+\rangle$, or vice versa. There is no loss of energy, but there is a loss of coherence due to the change in angular momentum.

2.3.6 *T2' and T2⋆*

In the context of MRI, additional phase shift can occur due to magnetic field inhomogeneities. These modify the resonance frequencies around the Larmor frequency, leading to additional loss of coherence in the sample that reduces the magnetization in the transverse plane. The time constant for this effect is T_2', and the time constant that account for both transverse relaxation effect is $T_2^\star$.

$$\frac{1}{T_2^\star} = \frac{1}{T_2} + \frac{1}{T_2'} \tag{2.92}$$

It is evident from the equation that the observed (or apparent) $T_2^\star$ decays faster than the natural T_2. Although the observe relaxation is $T_2^\star$, T_2' is reversible and some sequences are designed to rephase the spins in order to measure the true T_2. T_1 and T_2 are determined by the chemical environment and are therefore specific to different tissues. Table 2 shows exemple of relaxation parameters values for different body tissues.

	MAGNETIC FIELD			
	1.5 T		3 T	
Tissue type	T_1 (ms)	T_2 (ms)	T_1 (ms)	T_2 (ms)
Brain Grey Matter (GM)	1188 ± 69	95 ± 8	1820 ± 114	99 ± 7
Brain White Matter (WM)	656 ± 16	72 ± 4	1084 ± 45	69 ± 3
Blood	1540 ± 23	290 ± 30	1932 ± 85	275 ± 50
Fat	343 ± 37	58 ± 4	382 ± 13	68 ± 4
Kidney Cortex	966 ± 58	87 ± 4	1142 ± 154	76 ± 4
Kidney Medula	1412 ± 58	85 ± 11	1545 ± 142	81 ± 8

Table 2: Exemple of relaxation parameters T_1 and T_2 values for different field strength and different body tissues [37].

The solution to the equation (2.82) and (2.91) are

$$M_x(t) = e^{-t/T_2}(M_x(0)\cos(\omega_0 t) + M_y(0)\sin(\omega_0 t)) \quad (2.93)$$
$$M_y(t) = e^{-t/T_2}(M_y(0)\cos(\omega_0 t) - M_x(0)\sin(\omega_0 t)) \quad (2.94)$$
$$M_z(t) = e^{-t/T_1}M_z(0) + (1 - e^{-t/T_1})M_0 \quad (2.95)$$

It is possible to write the magnetization in the transverse plan with the contribution of both $M_x(t)$ and $M_y(t)$ as follow. This definition will be useful for the next chapter.

$$M_\perp(t) = M_{xy}(t) \quad (2.96)$$
$$= e^{-t/T_2}|M_\perp(0)|e^{-i(\omega_0 t - \phi_0)} \quad (2.97)$$

Figure 4 shows an exemple of relaxation trajectory for a magnetization that following a 90° excitation pulse. Figure 5a and Figure 5b illustrate the decay of the transverse magnetization with the t_2 value constant, and the regrowth of the longiitudinal magnetization with the constant value T_1.

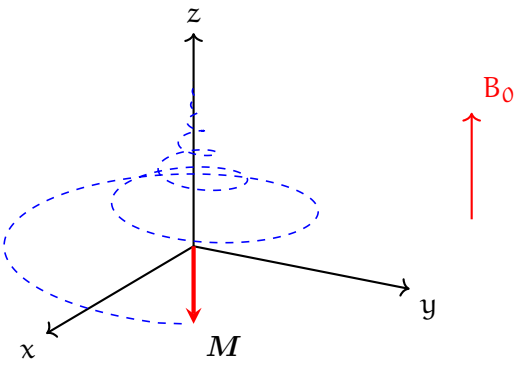

Figure 4: Relaxation trajectory of the magnetization vector, with the regrowth of the longitudinal magnetization and the decay of the transverse component [32].

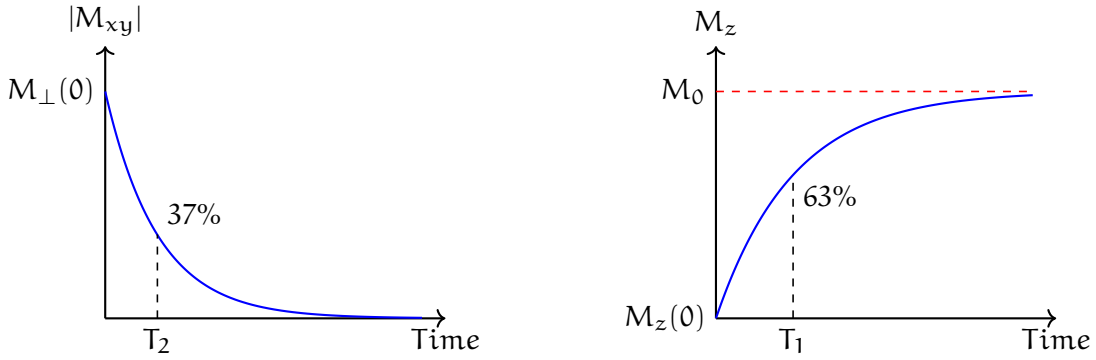

Figure 5: (a) Decay of the transverse magnetization from its initial value $M_\perp(0)$. (b) Regrowth of the longitudinal magnetization from the initial magnetization $M_z(0)$ to the equilibrium value M_0 [32].

3

MAGNETIC RESONANCE IMAGING

"Nature flies from the infinite; for the infinite is imperfect, and nature always seeks an end."

"We, on the other hand, must take for granted that the things that exist by nature are, either all or some of them, in motion which is indeed made plain by induction."

- Aristotle, *Complete Works of Aristotle Volume 1*

Contents

3.1 INTRODUCTION

The previous chapter explained how a magnetic field can induce magnetization in nuclei through the Zeeman effect and how MRI can use radio-frequency pulses to induce rotation of the magnetization around the direction of the static field. To measure a signal, another law of electromagnetism is necessary: Faraday's law of induction. Faraday's law states that *Whenever (and for whatever reason) the magnetic flux through a loop changes, an electromotive force (emf) will appear in the loop* [10]. It is the spin's magnetic flux that generates an electromotive force by rotating after the excitation pulse. The MR signal is then detected using an RF coil placed near the sample. The form of the current generated in the coil contains all the relevant information. This chapter will discuss the physics behind electromagnetic induction and the sequence schemes used to measure the induction signal. It will also describe the frequency domain in which the signal is acquired and how MR images can be obtained from it.

3.2 NUCLEAR MAGNETIC RESONANCE SIGNAL

3.2.1 *Faraday induction*

The magnetic flux must first be defined in order to define the emf. The flux is defined as the integration of the magnetic field through a closed surface. For MRI, the closed surface in the coil area.

$$\Phi = \int_{\text{coil area}} \mathbf{B} \cdot d\mathbf{S} \tag{3.1}$$

This equation can then be used to define the emf. The negative sign in front of the derivative means that the current created will induce a magnetic field which will oppose the change of that received.

$$\varepsilon = -\frac{d}{dt}\Phi \tag{3.2}$$

In order to compute the integral of equation (3.1), it is necessary to use the Stockes theorem because the magnetic field $\mathbf{B}$ is currently unknown. The theorem states that the integral of the curl of the vector field over some surface is equal to the line integral of the vector field around the boundary of the surface.

$$\int_{\Sigma} (\nabla \times \mathbf{A}) \cdot d\mathbf{S} = \oint_{\partial\Sigma} \mathbf{A} \cdot d\Gamma \tag{3.3}$$

This equation does not define the magnetic vector potential uniquely because it can be modify with the addition of curl-free components that will vanish and lead to the same observed magnetic field. This is known as gauge invariance.

To perform the theorem, the magnetic field can be defined as the curl of the magnetic vector potential $\mathbf{A}$ as follow $\mathbf{B} = \nabla \times \mathbf{A}$. Now that the magnetic field is define with a magnetic vector potential, the effective current density can also be define $\mathbf{J} = \nabla \times \mathbf{M}(\mathbf{r}, t)$. This leads to the expression of the magnetic vector potential with the

$$\mathbf{A}(\mathbf{r}) = \frac{\mu_0}{4\pi} \int_{\Omega \subset \mathbb{R}^3} \frac{\nabla' \times \mathbf{M}(\mathbf{r}', t)}{|\mathbf{r} - \mathbf{r}'|} d\mathbf{r}' \tag{3.4}$$

The magnetic flux equation (3.1) can be further developed using newly obtained equations (3.3) and (3.4).

$$\Phi = \oint_{\partial\Sigma} \left[\frac{\mu_0}{4\pi} \int_{\Omega \subset \mathbb{R}^3} \frac{\nabla' \times \mathbf{M}(\mathbf{r}', t)}{|\mathbf{r} - \mathbf{r}'|} d\mathbf{r}' \right] \cdot d\Gamma \tag{3.5}$$

$$= \int_{\Omega \subset \mathbb{R}^3} \mathbf{M}(\mathbf{r}', t) \left[\nabla' \times \left(\frac{\mu_0}{4\pi} \oint_{\partial\Sigma} \frac{d\Gamma}{|\mathbf{r} - \mathbf{r}'|} \right) \right] d\mathbf{r}' \tag{3.6}$$

$$= \int_{\Omega \subset \mathbb{R}^3} \mathbf{M}(\mathbf{r}', t) \cdot \mathbf{B}^{\text{received}}(\mathbf{r}') \cdot d\mathbf{r}' \tag{3.7}$$

The bracket in equation (3.6) can be rewrite in simple form as $\mathbf{B}^{\text{received}}(\mathbf{r}') = \mathbf{B}(\mathbf{r}')/I$, with I as the current in the loop. This makes $\mathbf{B}^{\text{received}}(\mathbf{r}')$ being the magnetic field per unit of current that is produced in the coil at a given point. With this last equation, the emf can be written in function of the magnetization and the received field by the RF coil.

$$\varepsilon = -\frac{d}{dt} \int_{\Omega \subset \mathbb{R}^3} \mathbf{M}(\mathbf{r}', t) \cdot \mathbf{B}^{\text{received}}(\mathbf{r}') \cdot d\mathbf{r}' \tag{3.8}$$

The electromotive force is produced by the magnetization $\mathbf{M}$ as well as the received magnetic field $\mathbf{B}^{\text{received}}$. The emf is implicitly dependent on the transmitted magnetic field $\mathbf{B}_1$ with the magnetization of the sample.

3.2.2 *Magnetization signal*

The magnetic resonance is based on the detection of the electromotive force signal. The measured signal only have a proportionality relationship to the emf signal, because the strict equality depends on others factor, like amplifier gain, can affect the amplitude of the signal. The measured signal $s(t)$ is given by

$$s(t) \propto -\frac{d}{dt} \int_{\Omega \subset \mathbb{R}^3} \mathbf{M}(\mathbf{r}, t) \cdot \mathbf{B}^{\text{received}}(\mathbf{r}) \cdot d\mathbf{r} \tag{3.9}$$

The magnetization depends on time, whereas the received magnetic field only depends on spatial coordinates. Using its linearity property, the integral can be decomposed into its three coordinate components. The values of the magnetization from the previous chapter, equations (2.93 - 2.95), can be extended to include dependency on spatial coordinates. The equations for the transverse plane and the longitudinal plane are

$$M_\perp(\mathbf{r},t) = e^{-t/T_2(\mathbf{r})} M_\perp(\mathbf{r},0) e^{-i(\omega_0 t - \phi_0(\mathbf{r}))} \tag{3.10}$$

$$M_z(t) = e^{-t/T_1(\mathbf{r})} M_z(0) + (1 - e^{-t/T_1(\mathbf{r})}) M_0 \tag{3.11}$$

By taking the derivative with respect to time, the following three factors will be brought outside the integral: $1/T_2(\mathbf{r})$, $1/T_1(\mathbf{r})$, and ω_0. In MRI, operating at magnetic fields on the order of tesla, the Larmor frequency ω_0 is at least four orders of magnitude greater than the other two values. Therefore, we can neglect them, which eliminates the longitudinal component from the integral with ω_0 being the prefactor of the transverse magnetization. It is useful to express the received magnetic field in terms of a transverse component as well. From a laboratory perspective, the received magnetic field is $\mathbf{B}^{\text{received}}(\mathbf{r}) = B_\perp(\mathbf{r}) e^{i\theta_B(\mathbf{r})}$ with θ_B the angle in the transverse plane. The approximated signal is now

$$s(t) \propto \omega_0 \int_{\Omega \subset \mathbb{R}^3} e^{-t/T_2(\mathbf{r})} e^{-i(\omega_0 t - \phi_0(\mathbf{r}) + \theta_B(\mathbf{r}))} M_\perp(\mathbf{r},t) \cdot B_\perp(\mathbf{r}) \cdot d\mathbf{r} \tag{3.12}$$

The replacement of T_2 to $T_2^\star$ can be made with the presence of inhomogeneity in a sample.

3.2.3 *Demodulation of the signal*

From a practical standpoint, analog-to-digital converters are not fast enough to digitize signals in the RF range. In addition, noise can be induced by electronics at the Larmor frequency, leading to artifacts. To measure the signal, demodulation is applied to convert the high frequencies into low frequencies, which still contain the modulated information from the frequency range in the field of view. Demodulation involves multiplying the signal by a sinusoid or cosinusoid with a frequency $\omega_0 + \delta\omega$ near to the Larmor frequency. Physically, demodulation is a transformation from the laboratory to the rotating reference frame. Mathematically, we can express demodulation as

$$\text{demodulation} \propto \text{sinusoid} \cdot \text{signal} \tag{3.13}$$

$$\propto \sin(\omega_0 t + \delta\omega t) \cdot \sin(\omega_0 t + \phi_0 - \theta_B) \tag{3.14}$$

$$\propto \frac{1}{2}\left[\cos(\delta\omega t - \phi_0 + \theta_B) - \cos(2\omega_0 t + \delta\omega t + \phi_0 - \theta_B)\right] \tag{3.15}$$

In a second step, a low-pass filter is applied on the data to remove the high frequency.

$$\text{demodulation and low-pass filter} \propto \frac{1}{2}\cos(\delta\omega t - \phi_0 + \theta_B) \tag{3.16}$$

$$\propto \frac{1}{2}\,\mathrm{Re}(e^{i(\delta\omega t - \phi_0 + \theta_B)}) \tag{3.17}$$

The same demodulation can be achieved with a cosinusoid which gives

$$\text{demodulation and low-pass filter} \propto \frac{1}{2}\sin(\delta\omega t - \phi_0 + \theta_B) \tag{3.18}$$

$$\propto \frac{1}{2}\,\mathrm{Im}(e^{i(\delta\omega t - \phi_0 + \theta_B)}) \tag{3.19}$$

The equations (3.17) and (3.19) are referred as the real channel and the imaginary channel. Thus, the signal can be see as a sum of the real and imaginary channel demodulated signals. Defining the reference frequency $\Omega = \omega_0 + \delta\omega$ used for signal demodulation, the signal becomes

$$s(t) \propto \omega_0 \int_{\Omega \subset \mathbb{R}^3} e^{-t/T_2^\star(\mathbf{r})} e^{i((\Omega-\omega(\mathbf{r}))t+\phi_0(\mathbf{r})-\theta_B(\mathbf{r}))} M_\perp(\mathbf{r},t) \cdot B_\perp(\mathbf{r}) \cdot d\mathbf{r} \tag{3.20}$$

The precession frequency is now also dependent on the spatial position $\omega(\mathbf{r}) = \omega_0 + \Delta\omega(\mathbf{r})$, the reason for this will be detailed in the Section 3.4. The received signal described in equation (3.20) is dependent on the sample's magnetic properties, but it is also determined by the different magnetic field applications. Section 3.3 will describe the application of different RF pulses to probe the T_1, T_2, and $T_2^\star$ parameters. Section 3.4 will describe the concept of gradient fields to create a spatial variation of the static magnetic field for multidimensional acquisition.

3.3 ACQUISITION SCHEME

The measured signal by the coil is determined by the properties of the sample, but it is also affected by the choice of RF excitation pulses. Previously, we discussed the use of a 90° RF pulse that flips the magnetization M_0 in the transverse plane. However, the application of different pulses, such as an additional 180° pulse, can create an echo of the signal. By applying the 180° pulse followed by the 90° pulse, it is possible to suppress the signal from certain tissues in the sample and measure the signal from the remaining parts. For simplicity, we will assume that the sample is homogenous, resulting in a constant Larmor frequency of $\omega(\mathbf{r}) = \omega_0$. We will also assume that the phases, direction of the received field, and demodulation Ω are space-independent. This leads to the following equation

$$s(t) \propto \omega_0 e^{-t/T_2^\star} e^{i(-\omega_0 t+\phi_0-\theta_B)} \int_{\Omega \subset \mathbb{R}^3} M_\perp(\mathbf{r},t) \cdot B_\perp(\mathbf{r}) \cdot d\mathbf{r} \tag{3.21}$$

3.3.1 *FID*

The Free Induction Decay (FID), shown on the Figure 6, is a measurement process that involves an initial radio-frequency (RF) pulse that flips the magnetization of the sample in the transverse plane, followed by data acquisition with an analog-to-digital converter (ADC). The sequence is then repeated cyclically, with a single repetition referred to as the repetition time T_R. During data acquisition, the signal is sampled at discrete intervals of Δt, with a total of N points being measured. The total measurement time is given by $T_s = T_r \cdot \Delta t(N-1)$.

The Figure 6 also presents an example of signal that can be measured with the FID.l is at a maximum immediately after the RF pulse and decays exponentially over time, with the rate of decay being characterized by the $T_2^\star$ relaxation time. The signal exhibits oscillations with an exponential envelope.

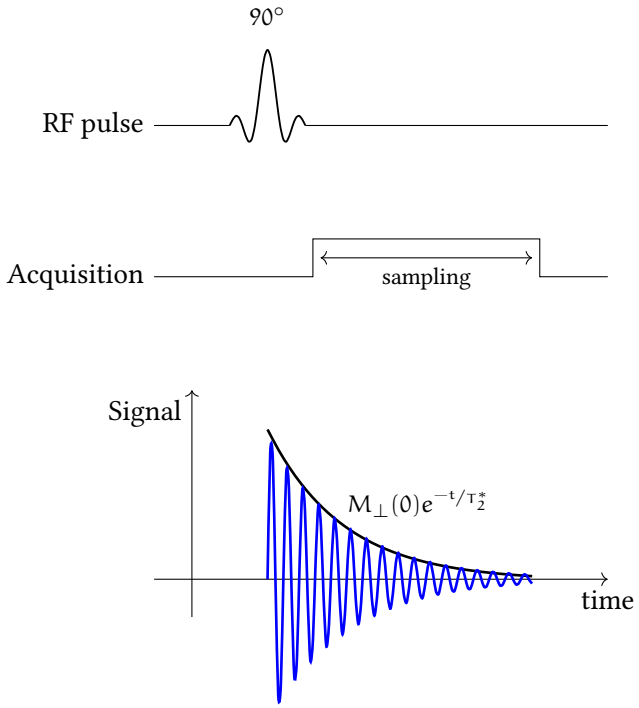

Figure 6: FID sequence with a single TR. The top of the figure presents a scheme of the sequence and the bottom an example of measurable signal [32]. In the figure a truncated sinc is displayed for the RF pulse, however, the pulse shape may have other shapes such as a rectangle, known also as "hard pulse".

3.3.2 *Spin Echo*

As presented in the Section 2.3.6, the $T_2^\star$ relaxation consists of two relaxation constants. One reflects the effect of magnetic field inhomogeneity (T_2') and the other is due to molecular interaction (T_2). While T_2 is irreversible, T_2' is reversible and a substantial part of the transverse magnetization can be recovered by using a Spin Echo. The spin echo effect was discovered by Erwin Hahn [38], and is illustrated on Figure 7 with the sequence diagram and an example of signal observed. The sequence starts with an excitation RF pulse followed by a second pulse with double the amplitude of the first one after a time τ. The second pulse, also known as the refocusing pulse, reverses the dephasing to create an echo. After the first pulse, the phase will evolve as followed

$$\phi(\mathbf{r},t) = -\gamma\Delta B_\perp(\mathbf{r})t, \quad 0 < t < \tau \tag{3.22}$$

The phase reaches $\phi(\mathbf{r},\tau) = -\gamma\Delta B_\perp(\mathbf{r})\tau$ before the second pulse is applied. Following the refocusing, spins that had accumulated negative phases will now have a positive phase and vice versa. Thus the phase becomes $\phi(\mathbf{r},\tau) = \gamma\Delta B_\perp(\mathbf{r})\tau$. The evolution continues as

$$\phi(\mathbf{r},t) = \gamma\Delta B_\perp(\mathbf{r})\tau - \gamma\Delta B_\perp(\mathbf{r})(t-\tau), \quad \tau < t \tag{3.23}$$
$$= -\gamma\Delta B_\perp(\mathbf{r})(t-2\tau) \tag{3.24}$$

It is clear from this equation that the phase will be zero at a time $t = 2\tau$, which we define as the echo time T_E. As shown in Figure 7, the signal will regenerate after the second pulse and reach a maximum at the echo time. The maximum amplitude of the echo will be lower than the initial maximum of the signal, representing the T_2 decay. The Spin Eco sequence can be

Refocusing is applied at intervals of $(2n+1)\tau$.

performed with multiple refocusing pulses at 2τ intervals, with data acquisition in between, to fully sample the T_2 envelope decay.

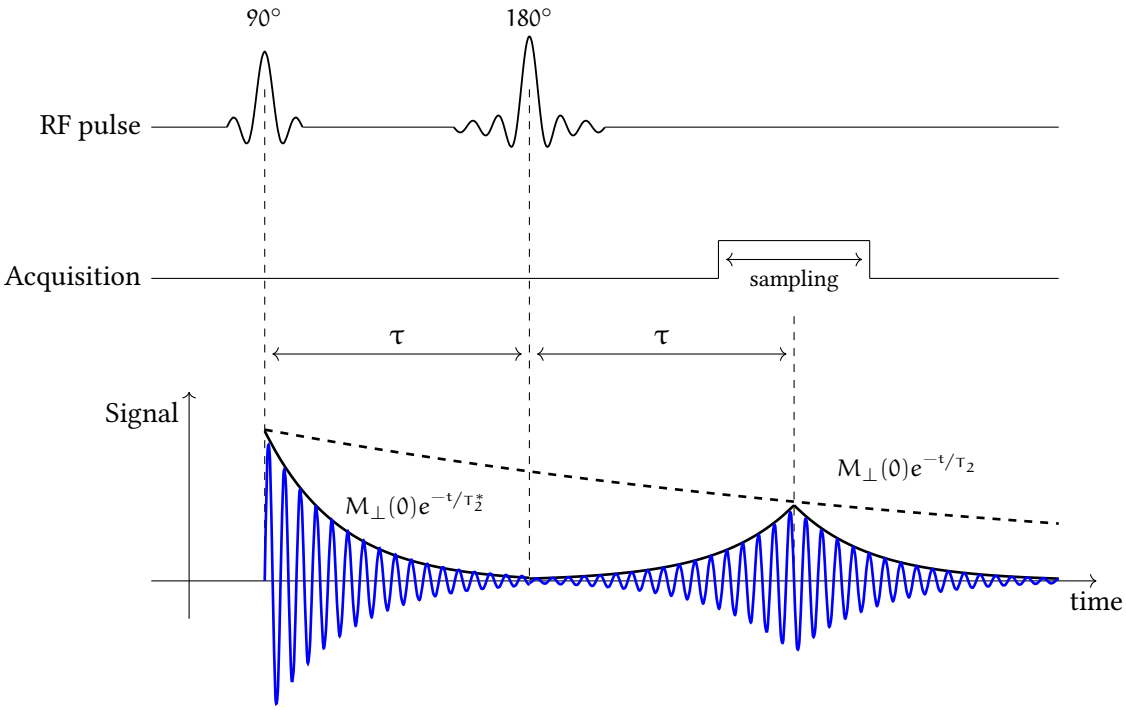

Figure 7: Spin Echo sequence diagram with an example of signal. An excitation pulse is first applied followed by a refocusing pulse after a time τ, creating an echo of the signal at a time 2τ. The signal decrease between the initial excitation and the echo is the T_2 decay [32].

3.3.3 *Inversion Recovery*

The previous sequences allow the measurement of the sample's T_2 and $T_2^\star$ constants. The third relaxation constant, T_1, cannot be directly probed because the generated signal is in the transverse plane and T_1 is in the longitudinal axis. However, T_1 can still be estimated using the inversion recovery sequence, which is shown in Figure 8. The sequence begins with a 180° pulse that flips the spins to the negative longitudinal magnetization $M_z(0) = -M_0$. Using the equation (2.95),The evolution of the magnetization can be described with

$$\begin{aligned} M_z(t) &= e^{-t/T_1}M_z(0) + (1-e^{-t/T_1})M_0, \quad 0 < t < T_I && (3.25)\\ &= -e^{-t/T_1}M_0 + (1-e^{-t/T_1})M_0 && (3.26)\\ &= (1-2e^{-t/T_1})M_0 && (3.27) \end{aligned}$$

A second pulse is then applied after a time interval T_I, called the inversion time, followed by data acquisition. Unlike the previous sequences, this sequence is repeated with the second pulse applied at different T_I. Figure 8 shows a diagram of the evolution of the absolute magnetization over time. The second pulse acts as the excitation pulse, and the resulting signal is acquired. If the pulse is applied at the exact time when the longitudinal magnetization is zero, there will be no spins to excite, and therefore no signal will be produced. Using equation (2.97), the transverse magnetization at the time of the second pulse application can be calculated

$$\begin{aligned} M_\perp(t) &= |M_\perp(T_I)| \cdot e^{-(t-T_I)/T_2}e^{-i(\omega_0(t-T_I)-\phi_0)}, \quad T_I < t && (3.28)\\ &= |(1-2e^{-T_I/T_1})M_0| \cdot e^{-(t-T_I)/T_2}e^{-i(\omega_0(t-T_I)-\phi_0)} && (3.29) \end{aligned}$$

The transverse magnetization, and therefore the acquired signal, depends on the inversion time according to $(1 - 2e^{-T_I/T_1})$. The transverse magnetization becomes zero if the inversion pulse is applied at the exact time of $T_I = T_1 \ln(2)$. By repeating the sequence with different values of T_I, it is possible to determine T_1 when the measured signal is zero.

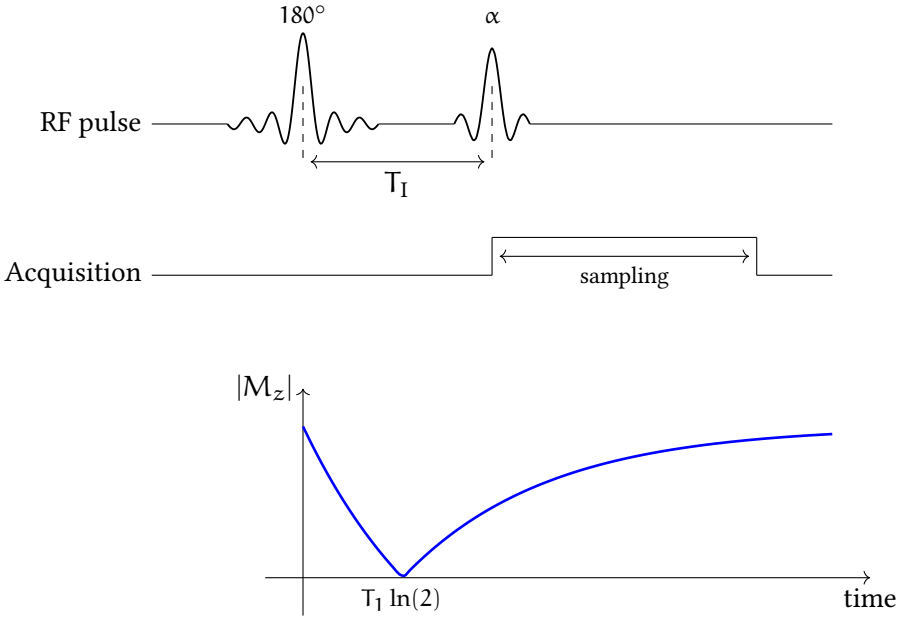

Figure 8: Inversion recovery sequence with example of transverse magnetization evolution. The magnetization is tipped to the negative equilibrium magnetization, and the longitudinal magnetization will be null after a time $T_1 \ln(2)$. Applying an excitation pulse α at this time will result in a null signal. The T_1 relaxation constant can be accurately measured with the repetition of the sequence [32].

This method is not limited to the measurement of T_1. Different body tissues have different longitudinal relaxation times, so they will not cancel at the same inversion time. Applying an inversion pulse to eliminate the signal from one tissue type allows the pure signal from a second body tissue to be measured.

3.4 K-SPACE

This chapter has introduced the magnetic induction produced in the coil by the excited sample and the signals created using different sequence schemes to measure the three relaxation times. While this material is sufficient for studying whole sample spectroscopy (which, as it happens, is the subject of the next chapter), it is not sufficient for imaging. MRI requires spatial information to produce images of the human body. In general, images are not about differentiating nuclei, but rather about spatially resolving the same nucleus, particularly hydrogen ^{1}H. To add a spatial dependence to the signal, the static field can be modified with a variable field along the three dimensions. The choice of variations is related to two other important concepts: k-space, the spin density distribution, and its relationship to the measured signal through the Fourier transform.

3.4.1 *Spin density*

In quantum mechanics, the spin density is the probability of finding a particle's spin in a given orientation (up or down) at a given spatial position. For MRI, this refers to the concentration of nuclei's spins that contribute to the magnetization M_0 in equation (2.36) within a unit of volume. It is possible to express the transverse magnetization as a function of the spin density.

$$M_\perp(\mathbf{r}, 0) = \frac{\rho_0(\mathbf{r})(\gamma\hbar)^2 B_0}{4k_b T} \tag{3.30}$$

For this section, we will use the previous equation (3.20) for the signal, with some convenient assumptions. For simplicity, the equation moves from proportionality to equality with the introduction of the constant Θ that includes the gain factor from the electronics, the relaxation, and the phase direction. We will also assume that the signal transmitted to the RF coils is uniform, so the initial magnetization phase, the directional phase, and the received field amplitude are independent of position. The reference frequency Ω is chosen to be equal to the Larmor frequency ω_0. The signal becomes

$$s(t) = \omega_0 \Theta B_\perp \int_{\Omega \subset \mathbb{R}^3} M_\perp(\mathbf{r}, 0) \cdot e^{i(\Omega t + \phi(\mathbf{r},0))} d\mathbf{r} \tag{3.31}$$

The magnetization phase is accumulating phases with time $\phi(\mathbf{r}, 0) = -\int_0^t \omega(\mathbf{r}, t')dt'$. The effective spin density can be define with the new constant $\rho(\mathbf{r}) = \omega_0 \Theta B_\perp M_\perp(\mathbf{r}, 0)$. The signal is now written in a simple equation

$$s(t) = \int_{\Omega \subset \mathbb{R}^3} \rho(\mathbf{r}) \cdot e^{i((\Omega - \omega(\mathbf{r},t))t + \phi(\mathbf{r},0))} d\mathbf{r} \tag{3.32}$$

The purpose of signal measurement will be to determine the spin density of the sample.

3.4.2 *Frequency encoding*

The maximum value of the gradient variation is much smaller than the value of the static field.

As mentioned at the beginning of this section, we can apply a linear gradient on the static field. that modifies the frequency resonance with respect to position. The linear gradient can be applied in all three directions. The field will now be express as

$$\mathbf{B}(\mathbf{r}, t) = \mathbf{B_0} + \mathbf{G}(t) \cdot \mathbf{r} \tag{3.33}$$

Thus, the gradient is define as the variation of the total field.

$$\mathbf{G}(t) = \nabla \mathbf{B}(\mathbf{r}, t) \tag{3.34}$$

The resonance frequency of the nuclei will now be dependent on the spatial position.

$$\omega(\mathbf{r}, t) = \omega_0 + \gamma \mathbf{G}(t) \cdot \mathbf{r} \tag{3.35}$$

Equation (3.35) is referred to as frequency encoding. In equation (3.31), we assumed that the spin density would have a field that is spatially independent. This assumption remains valid despite the variation of the static field in equation (3.33), because the applied gradient is on the

order of $mT \cdot m^{-1}$. The contribution of the gradient to the signal amplitude can therefore be neglected. However, the accumulating phase of the magnetization now becomes

$$\phi(\mathbf{r}, 0) = -\omega_0 t - \gamma \cdot \mathbf{r} \int_0^t \mathbf{G}(t')dt' \tag{3.36}$$

Since the reference frequency Ω is chosen to be equal to ω_0 in the equation (3.31), it will cancel out with the first term of the accumulated phase. We define the spatial frequency $\mathbf{k}(t)$ using $\gamma = \gamma/2\pi$ as

$$\mathbf{k}(t) = \gamma \int_0^t \mathbf{G}(t')dt' \tag{3.37}$$

By inserting the spatial frequency in the signal equation from (3.31), it can be written as

$$s(\mathbf{k}) = \int_{\Omega \subset \mathbb{R}^3} \rho(\mathbf{r}) \cdot e^{-2\pi i \mathbf{k} \cdot \mathbf{r}} d\mathbf{r} \tag{3.38}$$

We can see that the signal is the Fourier transform of the spin density of the sample, $s(\mathbf{k}) = \mathcal{F}\{\rho\}(\mathbf{r})$. $\mathbf{k}$ is referred to as k-space. It may not be immediately apparent, but according to the definition in equation (3.37), different gradient applications $\mathbf{G}$ result in different k-space positions. To recover the spin density position, we must perform an inverse Fourier transform of the signal.

$$\rho(\mathbf{r}) = \mathcal{F}^{-1}\{s\}(\mathbf{r}) \tag{3.39}$$

$$= \int_{\Omega \subset \mathbb{R}^3} s(\mathbf{k}) \cdot e^{2\pi i \mathbf{k} \cdot \mathbf{r}} d\mathbf{k} \tag{3.40}$$

The Fourier transform is a function that transforms complex functions from the kspace-time domain to the spatial-frequency domain. The frequency encoding modifies the resonance frequency with the application of the gradient, and the signal is acquired in k-space. Since data acquisition is performed with a finite number of points, k-space must be filled at equal intervals in order to perform the inverse Fourier transform. The Chapter 7 will go further into details on the Fourier transform. The next subsection will discuss techniques for applying gradients to cover k-space.

3.4.3 *Brief digression on the MRI coordinates system*

The following sections will discuss multi-dimensional acquisition. Since MRI is used for medical purposes, its coordinate system is based on the anatomical coordinate system. This system has three planes: transverse, sagittal, and coronal. The transverse plane is the $(\hat{x}\text{-}\hat{y})$ plane that divides the body into superior (head) and inferior (feet). The sagittal plane is the$(\hat{y}\text{-}\hat{z})$ plane that separates the body into left and right. And the coronal plane is the $(\hat{x}\text{-}\hat{z})$ plane that divides the anterior (front) from the posterior (back). The position of the patient during acquisition determines the coordinate system within the MRI.

The transverse plane can also be referred to as the axial plane.

Figure 9 shows an example of patient positioning with the corresponding coordinate system. In the figure, the patient is lying head-first supine, meaning they are lying with their back on the table, looking upwards and going head-first into the MRI. In this position, the $\hat{z}$ axis goes out of the MRI in the direction of the patient, the $\hat{y}$ axis goes upwards, and the $\hat{x}$ axis goes to the right when facing the MRI.

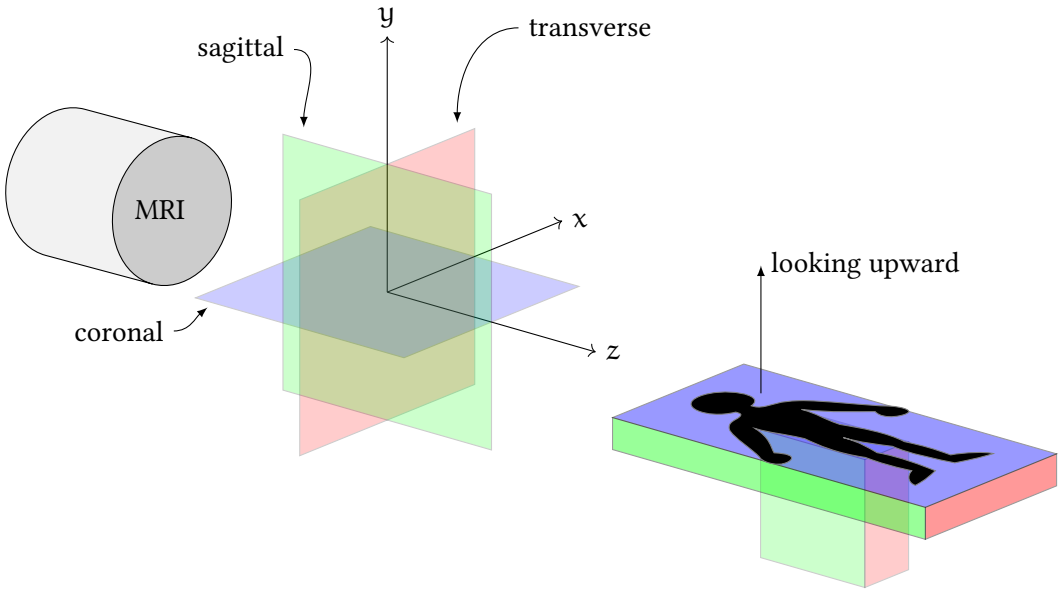

Figure 9: Example of anatomical coordinate system for a patient laying back on the table, looking upward and going head first inside the MRI. This specific position is called head first supine [32].

The Figure 10 present three images, with one for each plane orientation. Prior to the acquisition, the position of the patient inside the MRI needs to be registered in order to produce the same set of images in the same orientation regardless of the patient position on the table.

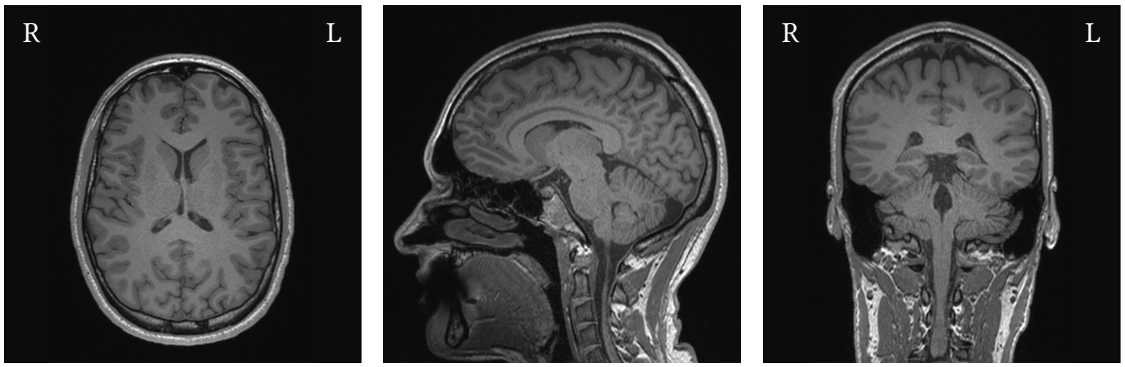

(a) Transverse (b) Sagittal (c) Coronal

Figure 10: Example of brain acquisition with a preview of the images obtained in the three anatomical planes. By conventions in radiology, images display the right side of the body on the left side of the image and vice versa for transverse and coronal planes. This orientation is achieved by reverting the $\hat{x}$ and $\hat{y}$ axes compared to the MRI coordinate system presented in the Figure 9.

3.4.4 *Gradient echo*

The application of a gradient will cause the FID signal to dephase. The gradient echo, similar to the spin echo, aims to rephase the signal for acquisition. The main difference between the two methods is that the gradient echo only rephases spins that were dephased by itself. Figure 11 illustrates an example of a gradient echo sequence. The sequence begins with an RF excitation pulse followed by the application of the gradient. The positions of the spins are frequency encoded by the application of a gradient for a duration of τ_{-}. This causes the signal to decay more rapidly. The dephasing caused by the first echo is:

$$\phi(\mathbf{r}, t) = +\gamma \mathbf{G} \cdot \mathbf{r}(t - t_1), \quad t_1 < t < t_2 \tag{3.41}$$

The second application of the gradient with inverse polarity and a duration $\tau_+ = 2\tau_-$ will form an echo. The phase becomes

$$\phi(\mathbf{r}, t) = +\gamma \mathbf{G} \cdot \mathbf{r}(t_2 - t_1) - \gamma \mathbf{G} \cdot \mathbf{r}(t - t_3), \quad t_3 < t < t_4 \tag{3.42}$$

It is easy to see that the phase will return to zero at $t = t_3 + t_2 - t_1$. This defines to the echo time T_E, the echo correspond to the vanishing of the gradient waveform $\int \mathbf{G}(t)dt = 0$. Choosing the second gradient to have a duration of twice the first will result in an echo at its center.

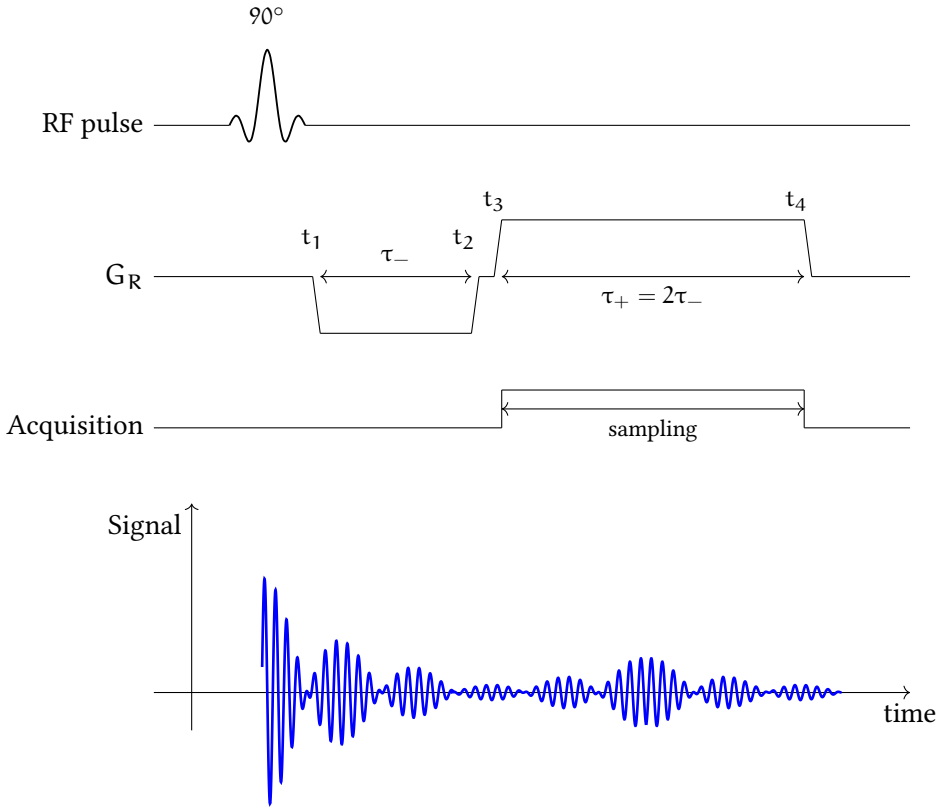

Figure 11: Gradient sequence scheme with the resulting signal. The first gradient will move the position in the k-space while causing an accelerated dephasing in the signal, and the second gradient will create an echo. The sampling of the data is performed during the second gradient [32].

In this example, the signal in k-space is acquired symmetrically and has bounds of $\mathbf{k_{max}}$ and $\mathbf{k_{min}}$, which are equal to $\pm\gamma \mathbf{G}(\tau_+/2)$, respectively. A k-space diagram of the acquisition would look like Figure 12. The initial position is at the center of k-space, the first gradient moves the position to the lower bound $\mathbf{k_{min}}$, and the second moves to the upper bound $\mathbf{k_{max}}$, covering the entire space.

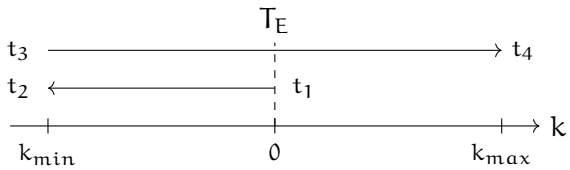

Figure 12: Example of motion in the k-space using the sequence from the Figure 11 [32].

From Figure 12, it is clear that we cover a line in k-space in a single TR. The direction in which the gradient moves in k-space during acquisition is called the "readout direction." Frequency encoding only requires one dimension. The spin echo variant of the gradient echo involves applying two gradients of the same polarity with a refocusing pulse in between. The first gradient moves the position in k-space to $\mathbf{k_{max}}$, and the refocusing pulse changes it to $\mathbf{k_{min}}$.

3.4.5 *Phase encoding*

The reading gradient can move along an axis to acquire data, but additional gradients are needed to move in k-space. In a Cartesian plane, frequency encoding can be attributed to the k_x dimension. The purpose of phase encoding is to move the reading direction along another axis. By applying phase encoding gradients after each pulse, the position in k-space will move along the second and/or third dimension. Figure 13 shows a 3D phase encoding sequence.

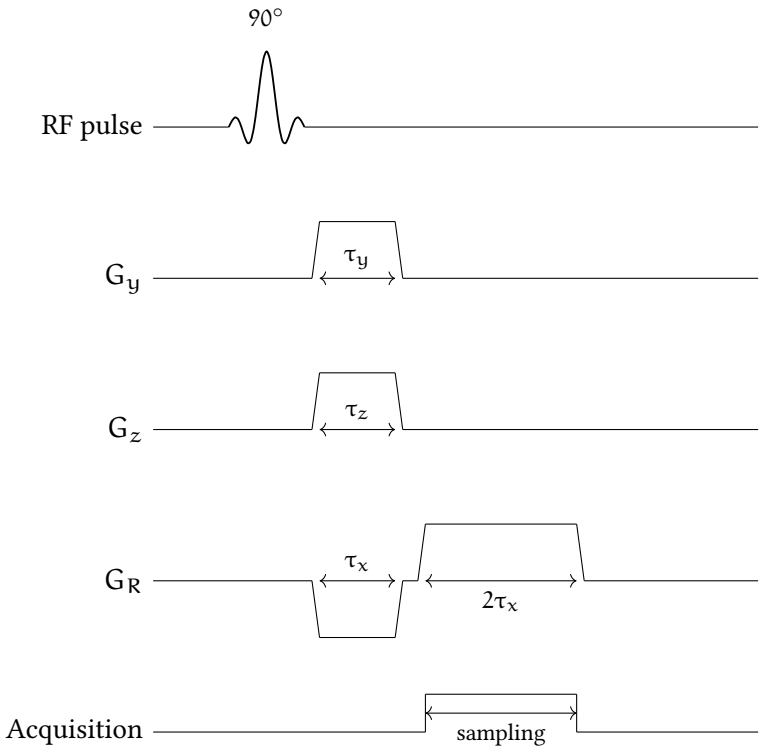

Figure 13: Phase encoding sequence scheme. The sequence has a reading gradient and two phase encoding gradients along the $\hat{y}$ and $\hat{z}$ direction. For a 2D sequence, only a single phase encoding gradient is needed. [32].

The sequence in Figure 13 starts with an excitation pulse, followed by two phase encoding gradients G_y and G_z and the first read gradient. Similar to Figure 12, the phase gradient moves the initial position from the center of k-space to a border of the k_x axis. The second read gradient is then applied along with the sampling of the signal. Measurements are not continuous as data are acquired in finite numbers. In the reading direction, k-space points are acquired at time steps Δt, with a continuous gradient application, resulting in an interval between two points of $\Delta k_x = \gamma G_x \Delta t$. For the orthogonal directions, gradients are applied with the same duration at each repetition but with different amplitudes, resulting in $\Delta k_y = \gamma \Delta G_y \tau_y$ and $\Delta k_z = \gamma \Delta G_z \tau_z$. The amplitude of the phase gradient is incremented at each repetition time. The phase gradient is usually depicted as shown in Figure 16.

The total acquisition time is equal to the number of lines acquired in the y and z directions and the repetition time to acquire a line in x, $T_{acq} = N_y N_z T_R$. The T_R for images is usually in the range of $10's$ ms, resulting in acquisitions that take a few minutes. Figure 14a and Figure 14b illustrate a conceptual example of k-space with the intervals between points in three dimensions and the data acquisition trajectory with phase and read gradients. In Figure 14b, we can see that the phase gradients move the position in single increments, while the read gradient travels through the entire k-space. In this example, only one of the two encoding gradients is applied at each repetition time. If both gradients were applied, the position would move diagonally.

It should be noted that Figure 14b is unrealistic as the read trajectory would be performed in the same direction and the position would return to the center of k-space between each repetition time (TR).

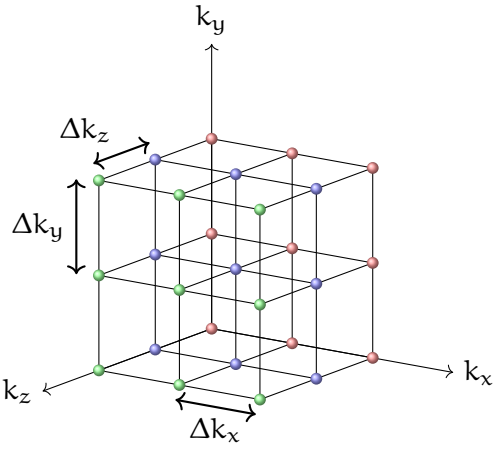

(a) Example of discrete k-space sampling.

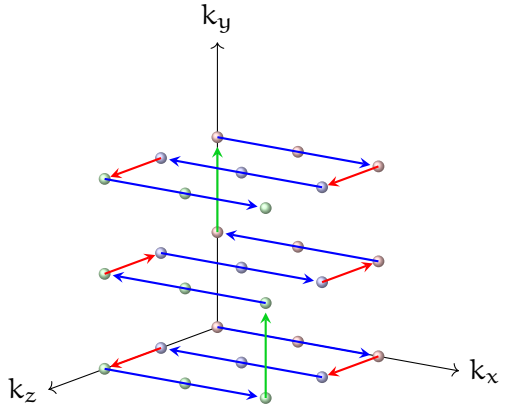

(b) Conceptual scanning scheme of the k-space sampling with two phase gradients and a read gradient.

Figure 14: A k-space coverage and sampling 3D example [32].

3.4.6 *Slice encoding*

Slice encoding is a technique used in 3D imaging to acquire data in "slices," or thin layers, along the third dimension. This technique can be used in a two-dimensional acquisition, where each slice is obtained individually, or in a three-dimensional acquisition, where a thicker slab is selected and further divided into thinner slices through encoding. The slice selection gradient is applied in conjunction with phase encoding and reading gradients. To perform slice selection, a linear gradient field is created along a particular direction and an RF pulse is applied to excite spins within a certain range of Larmor frequencies corresponding to the desired slice. The direction of the slice selection gradient will depend on the chosen anatomical coordinate system. For example, to obtain a transverse slice in the $(\hat{x}\text{-}\hat{y})$ plane, the slice gradient must be applied in the $\hat{z}$ direction.

The phase encoding gradient, as shown in Figure 16, is the standard representation used in textbooks.

Previously, equation (3.33) described the linear variation of the field with a linear gradient applied, and equation (3.35) described the resulting variation in resonance frequency. Figure 15 illustrates the linear gradient field variation along the $\hat{z}$ direction. To excite a slice with thickness Δz centered at position z_0, the RF pulse must have a bandwidth of excitation with a range of $\Delta\omega$ centered around the frequency $\omega(Z_0)$. The RF bandwidth is given by

$$\Delta\omega = \omega(z_0 + \frac{\Delta z}{2}) - \omega(z_0 - \frac{\Delta z}{2}) \tag{3.43}$$

$$= \gamma G_z \cdot \Delta z \tag{3.44}$$

Since the bandwidth and the gradient are the chosen values for the slice thickness selection, it is convenient to describe them in the other way around.

$$\Delta z = \frac{\Delta\omega}{\gamma G_z} \tag{3.45}$$

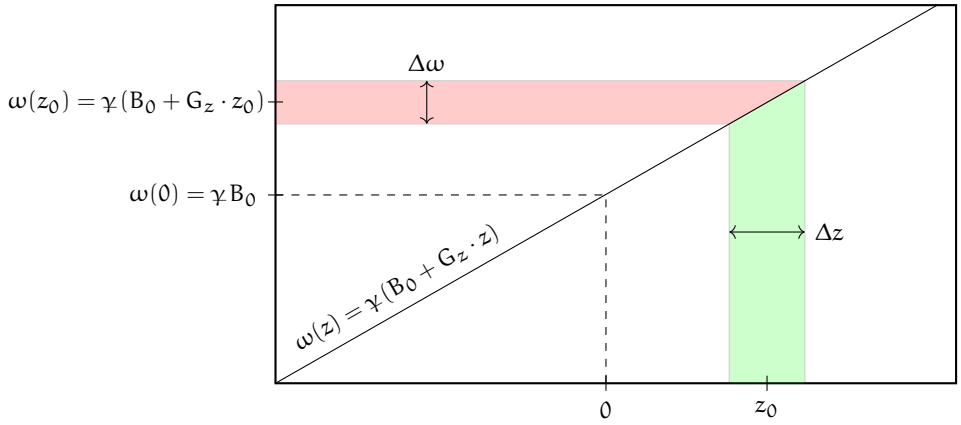

Figure 15: Schema of the evolution of the resonance frequency with the application of a linear gradient. The relation between the bandwidth selection $\Delta\omega$ and the corresponding excited slice thickness Δz is illustrated [32].

The purpose of slice selection is to uniformly excite a slice of a sample, but the gradients used can cause a loss of signal similar to that seen in gradient echo sequences. Figure 16 illustrates an example of a slice selection sequence acquisition.

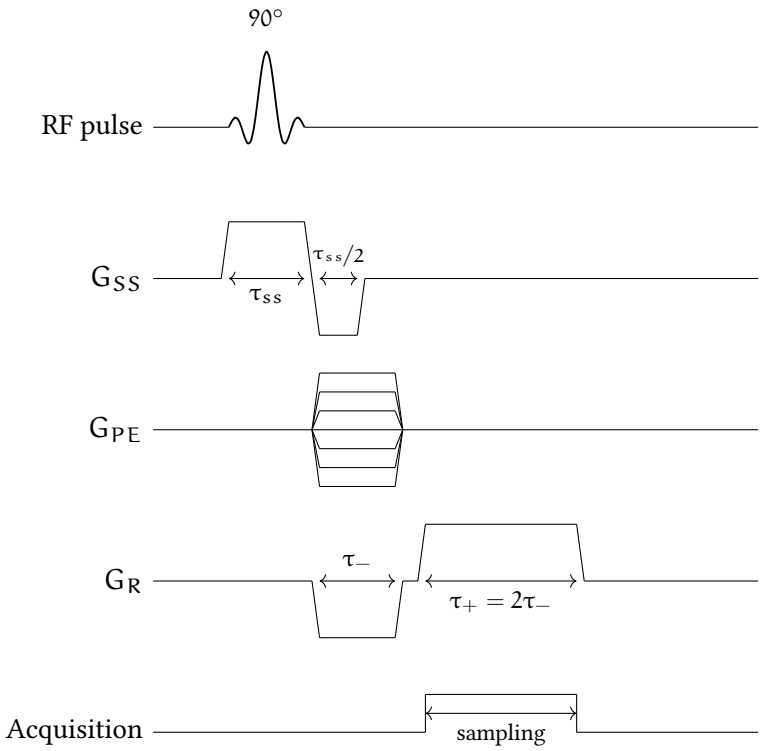

Figure 16: Slice selection acquisition scheme. The slice selection gradient is applied during the RF pulse, and then applied for half the time with inverse the polarity to compensate the signal loss created.[32].

The slice selection gradient is applied during the RF pulse, resulting in a loss of signal during this period. The gradient is then reversed after the RF pulse and applied for half the duration of the first one. As shown in Figure 16, the rephasing of the slice selection gradient, the phase encoding gradient, and the first lobe of the read gradient are all applied at the same time. The phase encoding gradient and slice selection gradient can be applied with a spin echo or a gradient echo.

4

PHOSPHORUS MAGNETIC RESONANCE SPECTROSCOPIC IMAGING

"The mystery of life isn't problem to solve, but a reality to experience "

- Frank Herbert *Dune*

Contents

4.1 INTRODUCTION

The previous chapter introduced the concepts of MR imaging, including the principle of magnetic induction and its application to obtain images of a sample with the spin density spatial distribution. Along with imaging, the application of spectroscopy has been developed for nuclear magnetic resonance (NMR) spectroscopy measurements. The application of NRM, known as the magnetic resonance spectroscopy (MRS), was first successfully implemented by Bloch and Purcell [39] in 1946, for which they were awarded the Nobel Prize in physics six years later. MRI is primarily used for imaging, while MRS is used to study the chemical composition of tissues. The signal obtain from MRS contains the information of the ensemble of all nuclear species whose Larmor frequency falls within the pulse spectrum. The goal was to measure the presence and concentration of these chemical species, and therefore the focus is on measuring the spectral composition rather than the spatial distribution. Both techniques can be combined in magnetic resonance spectroscopy imaging (MRSI), which measures the concentration of molecules and their spatial distribution.

Hydrogen magnetic resonance spectroscopy (^{1}H MRS) is the most commun application and field of research in MRS. ^{1}H MRS allows the study of the metabolism of specific hydrogen-containing biomolecules in living tissues. Hydrogen is the lightest atom and the most common in the human body, with 62% atomic presence and 10% contribution of the total body mass. Its prevalence result in a high contribution to the MR signal. In addition to the ^{1}H, research has expended to others nuclei notably carbon ^{13}C, fluorine ^{19}F, and phosphorus ^{31}P, with the later being of particular interest throughout the rest of this thesis.

Phosphorus magnetic resonance spectroscopic imaging (^{31}P MRSI) probs the metabolism of phosphorus-containing biomolecules. The isotope ^{31}P has a 100% natural abundance but has only 6.6% the sensitivity of the ^{1}H for an equal number of nuclei while having a 0.22% presence in the human body. ^{31}P MRS offers unique opportunities to probe cellular metabolism, as phosphorus-based metabolites are associated with the metabolic activity of the cell, and allow the measurement of biologically relevant information such as in-vivo pH and free magnesium levels (Mg^{2+}) [40–42]. Moreover, in contrast to ^{1}H MRS where the dominant water signal has to be suppressed to make the chemical compounds of interest detectable, ^{31}P MRS does not need any signal suppression solution. However, despite its many advantages, ^{31}P MRS also presents some challenges as the low sensitivity of the technique means that it may not be suitable for studying small or highly localized areas of the body.

This chapter will introduce the concepts MR spectroscopy, including the chemical shift and spin-spin coupling. The chapter will also cover single voxel and multi-voxel spectroscopy. In the second part of the chapter, the focus will shift to phosphorus biology and the relevant metabolites probed by ^{31}P MRS. As this thesis focuses on the phosphorus spectroscopy, only relevant topic will be discussed and topics such as water suppression will be omitted. The same applies to topics on data filtering, as the aim of this thesis is to use artificial intelligence to analyze unfiltered data.

4.2 MAGNETIC RESONANCE SPECTROSCOPY

In the previous chapter, Section 3.4.1 introduced the spin density equation (3.32) that describes the signal obtained from the excitation of a particular nuclear species in a sample, while the other species remain unexcited. For spectroscopy, the focus shifts to obtaining a signal from multiples nuclear species using a broad-band RF excitation pulse. The bandwidth of the receive filter must also be broadened to adapt to the resulting signal. The excited nucleus is sensitive to its molecular environment, where interaction with neighbouring nuclei and electrons will affect its Larmor frequency. The two dominant effects of these interactions are the chemical shift and the spin-spin coupling. These effects are highly dependent on the molecular structure of each substance, and as a result, each molecule will have its own unique resonance and therefore allowing the study of the biochemistry.

Single voxel spectroscopy involves the analysis of the chemical composition of a single voxel, as the name might suggest. This technique is commonly used to study specific areas of the body, such as the brain, liver, or heart. It allows for precise measurement of the chemical composition of a specific area, but does not provide information about the surrounding tissue. In contrast, multi-voxel spectroscopy involves the analysis of the chemical composition of multiple voxels at once. This technique is often used to study larger areas of the body, such as the entire brain or liver. It provides more detailed information about the chemical composition of the tissue, but comes with more challenges than single voxel spectroscopy.

4.2.1 *Chemical Shift*

Shielding effect is actually a special case of electric-field screening.

The chemical shift is the variation in the Larmor frequency of a nucleus due to the distribution of electrons in its environment. The effect of the electrons is known as shielding . This phenomenon occurs when the local field induced by the presence and movement of electrons modifies the magnetic field felt by the nucleus. The magnetic field felt by the nucleus $\mathbf{B}_{eff}$ will linearly differs from the static field $\mathbf{B}_0$, and can be describe by the following equation [43]. For a nuclear specie j, the effective magnetic field perceived is

$$\mathbf{B}_{eff}(j) = (1-\sigma_j)\mathbf{B}_0 \tag{4.1}$$

In this equation, σ_j is referred to the chemical shift value, which is a dimensionless constant [32]. The chemical shift can be either positive in the presence of a shielding or negative in a presence of anti-shielding. Thus, the larmor resonance frequency will be modify accordingly into

$$\omega_j = \gamma B_0(1-\sigma_j) \tag{4.2}$$

If we consider a larger sample with j different chemical compositions of spin densities N_j, the signal will be as follows

$$s(t) \propto \sum_j N_j e^{i\omega_j \gamma B_0 t} \tag{4.3}$$

The analysis is always performed on a finit number of chemical compound, which allow us to simply summed the chemicals instead of integrating them.

While the chemical shift is dimensionless, the frequency displacement can be express as $\omega_\sigma = -\sigma\gamma B_0$. This is explicitly depends on the field strength, meaning that it linearly increases with the field. This implies that molecular signature will also vary in its frequency resonance with variation in the static magnetic field. To enable comparison between spectroscopic analyses that are independent of the field, a new scale is needed. This scale is called parts per million (ppm) and is defined as follows:

$$\delta_{ppm} = \frac{\omega_j - \omega_{ref}}{\omega_{ref}} \cdot 10^6 \tag{4.4}$$

The ω_{ref} corresponds to the zero point of the axis. The reference is chosen by convention, for ^{1}H spectroscopy it is the signal of tetramethylsilane (TSM) and for ^{31}P it is the signal of phosphocreatine (PCr). The abscissa axis is inverted with the higher values appearing on the left and decreasing as you move to the right. Moving to the right on this axis corresponds to an increase in shielding, which reduces the effective magnetic field and results in a decrease in the resonance frequency and ppm values. Moving to the left on this axis corresponds to an increase in anti-shielding, which increases the resonance frequency and ppm values. The Figure 17 summaries the concept of parts per million (ppm).

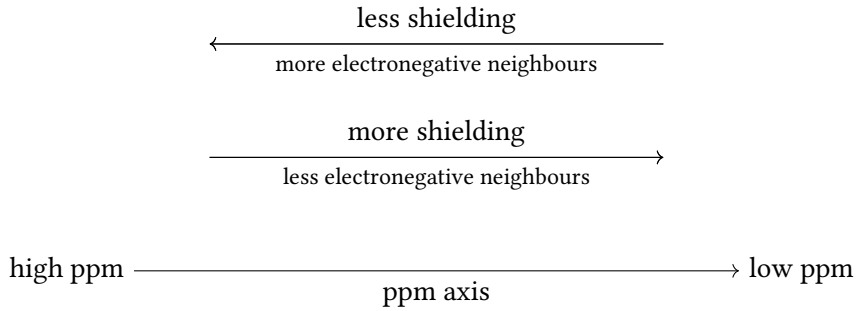

Figure 17: Ppm scale summerized [37].

4.2.2 *Spin-spin coupling*

J-coupling, also known as spin-spin coupling or scalar coupling, arises from the nuclear magnetic moments within a molecule affecting each other. This interaction is mediated by the electron cloud and cannot occur directly between the nucleus.The interaction can be represented as the sum of the multi-linear interaction, starting with the linear interaction between the spin and the static field. The Hamiltonian for this interaction can be expressed as follows [36]:

$$\hat{H}_0 = -\sum_k \gamma(1-\boldsymbol{\sigma}_k)\hat{\mathbf{S}}_k \mathbf{B}_0 \tag{4.5}$$

To formally describe the interaction, one should specify that $\boldsymbol{\sigma}$ is a tensor here.

The equation shows that the chemical shift previously described is the linear component of the Hamiltonian. The spin-spin coupling is the bilinear term interaction between the spins.

$$\hat{H}_J = \frac{2\pi}{\hbar} \sum_{k<l} \hat{\mathbf{S}}_k \mathbf{J}_{kl} \hat{\mathbf{S}}_l \tag{4.6}$$

In this equation, $\mathbf{J}_{kl}$ is the 3x3 coupling tensor between the spin k and the spin l [36, 44]. Adding the two component leads to the complete hamiltonian description.

$$\hat{H} = -\sum_k \gamma(1-\boldsymbol{\sigma}_k)\hat{\mathbf{S}}_k\mathbf{B}_0 + \frac{2\pi}{\hbar}\sum_{k<l}\hat{\mathbf{S}}_k\mathbf{J}_{kl}\hat{\mathbf{S}}_l \tag{4.7}$$

If we limit ourselves to a simple two $^1/_2$ spin system, the Hamiltonian will modify as follows. The spins operators must be transformed into 4x4 matrices. The right-hand side spin operator is transformed using the Kronecker product according to $\hat{S}_k^a = \hat{S}^a \otimes \mathbb{1}$ and the left-hand side spin operator is transform with $\hat{S}_l^a = \mathbb{1} \otimes \hat{S}^a$, with $a = \{x, y, z\}$. The coupling tensor can be separated into isotropic and anisotropic components, $\mathbf{J}_{kl} = \mathbf{J}_{kl}^{iso} + \mathbf{J}_{kl}^{aniso} = J_{kl}\mathbb{1} + \mathbf{J}_{kl}^{aniso}$. By averaging the coupling, we find that $J_{kl} = \frac{1}{3}\mathrm{tr}(\mathbf{J}_{kl}^{iso})$ and $\mathrm{tr}(\mathbf{J}_{kl}^{aniso}) = 0$. Additionally, the anisotropic contribution cannot be distinguished from direct dipolar contribution. Thus, in the context of high-resolution NRM, only the isotropic contribution is considered.

$$\hat{H} = -\gamma_1 B_0(1-\sigma_1)\hat{S}_1^z - \gamma_2 B_0(1-\sigma_2)\hat{S}_2^z + \frac{2\pi J_{12}}{\hbar}\hat{\mathbf{S}}_1\hat{\mathbf{S}}_2 \tag{4.8}$$

We can start by introducing a regime of weak coupling where the components in the $\hat{x}$ and $\hat{y}$ axes can be discarded, keeping only the components along the magnetic field. This coupling works for resonances where $\omega_0|\sigma_2 - \sigma_1| \gg \pi J_{12}$. Thus the Hamiltonian can be written as follow.

$$\hat{H} = -\gamma_1 B_0(1-\sigma_1)\hat{S}_1^z - \gamma_2 B_0(1-\sigma_2)\hat{S}_2^z + \frac{2\pi J_{12}}{\hbar}\hat{S}_1^z\hat{S}_2^z \tag{4.9}$$

Such hamiltonian can be written in as a matrix form, and simplify as well. Using equation (4.2), The matrix components are able to be simplify using $\omega_{avg} = \frac{\omega_1+\omega_2}{2}$ and $\Delta\omega = \omega_1 - \omega_2$. The matrix form of the Hamiltonian for weak coupling is

$$\hat{H} = \hbar\begin{pmatrix} -\omega_{avg} + \frac{\pi J_{12}}{2} & 0 & 0 & 0 \\ 0 & \frac{\Delta\omega - \pi J_{12}}{2} & 0 & 0 \\ 0 & 0 & \frac{-\Delta\omega - \pi J_{12}}{2} & 0 \\ 0 & 0 & 0 & \omega_{avg} + \frac{\pi J_{12}}{2} \end{pmatrix} \tag{4.10}$$

As the Hamiltonian is diagonal, it is trivial to obtain its energy level. Using the equation (2.15) with the set of spin arrangement $|+,+\rangle$, $|+,-\rangle$, $|-,+\rangle$, and $|-,-\rangle$.

$$E_{+,+} = -\hbar\omega_{avg} + \frac{1}{2}\hbar\pi J_{12} \tag{4.11}$$

$$E_{+,-} = \frac{1}{2}\hbar\Delta\omega - \frac{1}{2}\hbar\pi J_{12} \tag{4.12}$$

$$E_{-,+} = -\frac{1}{2}\hbar\Delta\omega - \frac{1}{2}\hbar\pi J_{12} \tag{4.13}$$

$$E_{-,-} = \hbar\omega_{avg} + \frac{1}{2}\hbar\pi J_{12} \tag{4.14}$$

With the Energy values, we can calculate the corresponding frequency of transition with $\Delta E = \hbar\omega$.

$$\omega_{(+,+)\to(+,-)} = \omega_1 - \pi J_{12} \tag{4.15}$$
$$\omega_{(+,+)\to(-,+)} = \omega_2 - \pi J_{12} \tag{4.16}$$
$$\omega_{(+,-)\to(-,-)} = \omega_2 + \pi J_{12} \tag{4.17}$$
$$\omega_{(-,+)\to(-,-)} = \omega_1 + \pi J_{12} \tag{4.18}$$
$$\omega_{(+,-)\to(-,+)} = \omega_1 - \omega_2 \tag{4.19}$$

With the equation (4.2), it is again possible write the transition frequencies in function of ω_0 and the chemical shifts of the two spins.

$$\omega_{(+,+)\to(+,-)} = \omega_0(1-\sigma_1) - \pi J_{12} \tag{4.20}$$
$$\omega_{(+,+)\to(-,+)} = \omega_0(1-\sigma_2) - \pi J_{12} \tag{4.21}$$
$$\omega_{(+,-)\to(-,-)} = \omega_0(1-\sigma_2) + \pi J_{12} \tag{4.22}$$
$$\omega_{(+,-)\to(-,-)} = \omega_0(1-\sigma_1) + \pi J_{12} \tag{4.23}$$
$$\omega_{(+,-)\to(-,+)} = \omega_0(\sigma_2 - \sigma_1) \tag{4.24}$$

Through further calculations with the evolution matrix, it is possible to show that the splitting between the two central peaks is $\frac{\omega_0|\sigma_2-\sigma_1|}{2\pi}$, and that the amplitudes of the two peaks are half the original one, while maintaining the conservation of the integral under the peaks. The intra-doublet peaks are separated by $2\pi J_{12}$. The multiplicity pattern with more than two identical nucleus will have $2n+1$ lines, where n is the number of neighbouring nuclei and the peak height intensity can be obtained from the Pascal's triangle [45]. Example of doublets and triplets will be observed in the second part of this chapter.

This result only holds for coupling where the chemical shift of the two spins is much greater than the spin-spin coupling. For strong coupling, the spin-spin coupling contribution from the $\hat{x}$ and $\hat{y}$ axes can no longer be neglected. From the equation (4.8), the matrix form of the strong coupling becomes

The $\hat{S}_1^x\hat{S}_2^x$ and $\hat{S}_1^y\hat{S}_2^y$ only contribute to anti-diagonal terms.

$$\hat{H} = \hbar \begin{pmatrix} -\omega_{avg} + \frac{\pi J_{12}}{2} & 0 & 0 & 0 \\ 0 & \frac{\Delta\omega - \pi J_{12}}{2} & \pi J_{12} & 0 \\ 0 & \pi J_{12} & \frac{-\Delta\omega - \pi J_{12}}{2} & 0 \\ 0 & 0 & 0 & \omega_{avg} + \frac{\pi J_{12}}{2} \end{pmatrix} \tag{4.25}$$

The Hamiltonian is no longer diagonal, and the calculation of the energy levels requires more computation. This results in the following energy levels:

$$E_{+,+} = -\hbar\omega_{avg} + \frac{1}{2}\hbar\pi J_{12} \tag{4.26}$$
$$E_{+,-} = \frac{1}{2}\hbar\sqrt{\Delta\omega^2 + 4\pi^2 J_{12}^2} - \frac{1}{2}\hbar\pi J_{12} \tag{4.27}$$
$$E_{-,+} = -\frac{1}{2}\hbar\sqrt{\Delta\omega^2 + 4\pi^2 J_{12}^2} - \frac{1}{2}\hbar\pi J_{12} \tag{4.28}$$
$$E_{-,-} = \hbar\omega_{avg} + \frac{1}{2}\hbar\pi J_{12} \tag{4.29}$$

With the energy levels, it is possible to calculate the transition frequency for the strong coupling.

$$\omega_{(+,+)\to(+,-)} = \omega_{avg} - \pi J_{12} + \frac{1}{2}\sqrt{\Delta\omega^2 + 4\pi^2 J_{12}^2} \tag{4.30}$$

$$\omega_{(+,+)\to(-,+)} = \omega_{avg} - \pi J_{12} - \frac{1}{2}\sqrt{\Delta\omega^2 + 4\pi^2 J_{12}^2} \tag{4.31}$$

$$\omega_{(+,-)\to(-,-)} = \omega_{avg} + \pi J_{12} - \frac{1}{2}\sqrt{\Delta\omega^2 + 4\pi^2 J_{12}^2} \tag{4.32}$$

$$\omega_{(-,+)\to(-,-)} = \omega_{avg} + \pi J_{12} + \frac{1}{2}\sqrt{\Delta\omega^2 + 4\pi^2 J_{12}^2} \tag{4.33}$$

$$\omega_{(+,-)\to(-,+)} = -\sqrt{\Delta\omega^2 + 4\pi^2 J_{12}^2} \tag{4.34}$$

From these equations, we can see that we can recover the weak coupling regime by neglecting the term $4\pi^2 J_{12}^2$ in the square root.

4.3 LOCALIZED SPECTROSCOPY

Unlocalized spectroscopy is a technique for exciting and recording signals from a whole sample. While this approach allows for the contribution of all chemical compounds, it has some drawbacks. Firstly, the signal measurement is highly dependent on the coil profile, so signals close to the coil will be more intense than those further away and the 3D volume extends only over the coil sensitivity area . Secondly, the signal can be contaminated by signals from other sources that are not of interest, such as the skull or fat tissue for the ^{1}H spectroscopy or from muscle for ^{31}P. Heterogeneity within the sample can also impair the data, causing resonances to be broader due to variation in local magnetic susceptibility between tissues, with potentially baseline distortion caused by lipid and water contamination. The difficulty to achieve a homogeneous static magnetic field within a large sample can reduce spectral resolution.

The signal intensity decreases with the distance squared r^2.

Localized spectroscopy allows for the analysis of a specific region of interest, resulting in narrower resonances and the ability to exclude unwanted resonances (and can also be used for lipid suppression in ^{1}H spectroscopy). This technique results in a more specific spatial characterization, but with a decrease in SNR due to the reduced excitation volume. MR localized spectroscopy involves defining a specific area of interest, or voxel, and measuring the chemical composition of that area. There are two types of localization spectroscopy: single voxel and multi-voxel spectroscopy. Both techniques aim to probe signal from a region of interest (ROI) while avoiding signal from outside of the region. Techniques that are based on the magnetic field gradients use slice selection applied consecutively in the three orthogonal directions with the application of a frequency selective RF pulse. Spatial localization provides better field homogeneity, as B_0 and B_1 variations are greatly reduced in small, localized volumes. Positioning the voxel allows for the specific characterisation of tissue, such as the difference between grey and white matter in the brain [46].

A voxel is a three-dimensional equivalent of a two-dimensional pixel.

4.3.1 *Single Voxel Spectroscopy*

Single voxel spectroscopy (SVS) allows for precise measurement of the chemical composition within the voxel, but does not provide information about the surrounding tissue. SVS has the advantages of having a well-defined volume with minimal contamination, good magnetic field homogeneity across the volume. The consecutive application selects a slice, then a column from the slice, and then a voxel. These techniques can be divided into two sub-categories: outer volume suppression (OVS) which leaves the magnetization in volume of interest (VOI) unperturbed, and techniques that rely on selective perturbation of the magnetic field such that only

the signal from the VOI remains.Since the inception of MR spectroscopy, various sequences have been developed. In this section, we will highlight some of the most significant ones.

Image selected in-vivo spectroscopy (ISIS) [47] involves the use of a selective inversion RF pulse with gradients followed by nonselective excitation pulse on the entire sample. The unwanted magnetization outside the VOI remains unaffected by the inversion pulse. This sequence requires multiple acquisitions, up to eight to perform three-dimensional localization. The result is obtained by adding or subtracting the acquisitions in such a way that the signal inside the VOI combines while the signal outside destructively interferes. The sequence can be combined with an out of volume and noise suppression to create the "Outer volume Suppressed Image Related In-vivo Spectroscopy" (OSIRIS) [48, 49].

Stimulated Echo Acquisition Mode (STEAM) [50] is a 3D localization technique that can be performed in a single shot. It uses three 90° pulses creating three FIDs, followed by four spin echos and one stimulated echo. Only the signal from the stimulated echo is of interest, while the signals from the other echoes are suppressed using additional gradients, known as crusher gradients. A disadvantage of this sequence is that it only captures half of the total signal compared to spin-echo.

Point Resolve Spectroscopy (PRESS) [51] is a double spin-echo method where slice-selective excitation is used in combination with two volume selective refocusing pulses. The first echo contains signal from the column at the intersection of the two volumes selected by the 90° and 180° pulses. The second echo only contains signal from the intersection of the three volumes resulting in the desired volume. Signal from outside the VOI is either not excited or not refocused, leading to a rapid dephasing of the signal with the application of the crusher gradients. PRESS is preferred at lower field strengths due to its higher SNR compared to STEAM.

Localization by Adiabatic Selective Refocusing (LASER) [52] uses adiabatic pulses that offer a larger bandwidth and produce a uniform flip angle despite variations in the B_1 field. LASER uses a non-slice-selective excitation pulse followed by three pairs of adiabatic full-passage (AFP) pulses for signal refocusing as well as the selection of three orthogonal planes in space. To minimize the echo time and the RF deposition, semi-LASER [53] is an identical sequence with the replacement of one of the AFP pair and the non-selective excitation with a slice-selective pulse.

4.3.2 *Chemical Shift Displacement*

In Section 3.4.6, the slice selection technique and the impact of applying a linear gradient during RF pulse excitation were introduced. As shown in Figure 15, the excitation of a bandwidth $\Delta\omega$ resulted in the selection of a slice thickness Δr according to the equation (3.45). When using localized spectroscopy, applying a linear gradient during excitation will result in the excitation of a localized voxel for on-resonance metabolite signals, but also in the excitation of off-resonance metabolite signals from a different voxel position. This effect is known as chemical shift displacement artifact (CSDA) or chemical shift displacement error (CSDE).

Figure 18 illustrates the chemical shift displacement artifact in a phosphorus spectrum. A frequency selective pulse is applied on the PCr resonance according to the black line, the excitation of a bandwidth centered at $\omega(r)$ results in a voxel at the position r. The same RF pulse also selects off-resonance, such as AMP and β-ATP in red and orange, respectively, resulting in signals from voxels at localization $r + \Delta r$ and $r + \Delta r'$.

The phosphorus spectrum and its resonances will be presented in the following section.

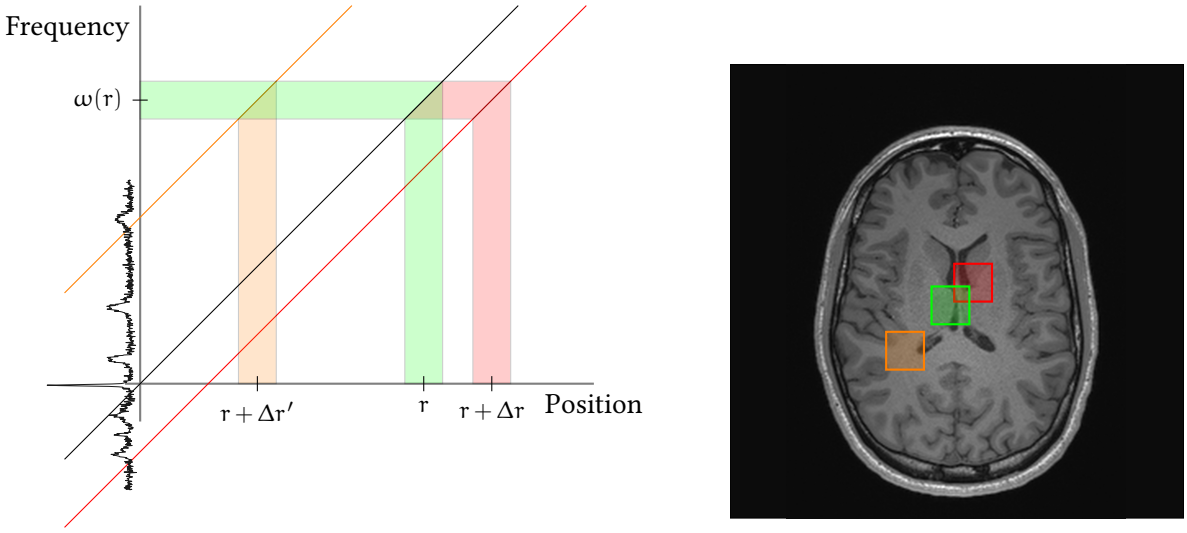

Figure 18: Adaptation of the Figure 15 for the localized spectroscopic application. The excitation of a bandwidth centered at $\omega(r)$ results in a voxel at the position r, but also selects off-resonance, such as AMP and β-ATP in red and orange, respectively, resulting in signals from voxels at localization $r + \Delta r$ and $r + \Delta r'$ [46]. Examples of voxel displacement is shown on the right-hand side (displacement not to scale).

The chemical shift displacement artifact error is given by the relationship between the slice thickness, the RF excitation bandwidth $\Delta\omega_{BW}$ and the chemical shift $\Delta\omega_{ij}$ between metabolite i and j.

$$\Delta r_{CSDA} = -\frac{\Delta\omega_{ij}}{\Delta\omega_{BW}}\Delta r \tag{4.35}$$

The chemical shift displacement artifact scales linearly with the static magnetic field strength. According to equation (4.35), the chemical shift displacement artifact can be minimized by increasing the pulse bandwidth $\Delta\omega_{BW}$. However, there are limitations to increasing the RF power, including hardware constraints and power deposition limitations in human tissue. Furthermore, when slice selection is applied in all three dimensions for MRSI, the overlap between voxels decreases further. Chemical shift displacement artifact can lead to misinterpretation of the results and contamination from others signals.

4.3.3 *Multi-Voxel Spectroscopy: MRSI*

In Section 4.3.1, the advantages of single voxel spectroscopy were presented. While single voxel spectroscopy provides valuable information about the chemical compounds in a tissue, its use is limited because it only focuses on a small volume in an organ and does not provide information about the spatial distribution of the signals. This can result in missing important information or areas of interest. Magnetic resonance spectroscopic imaging (MRSI), on the other hand, is a localized spectroscopic technique that acquires multidimensional arrays of localized voxels. MRSI allows for the investigation of an entire organ or body part, providing a comprehensive and unbiased characterization of the metabolic spatial distribution. However, the technique remains challenging due to significant magnetic field inhomogeneities across the volume being acquired, inter-voxel contamination, long acquisition times, and sometimes the need to process a large amount of data. The principles of magnetic resonance spectroscopic imaging (MRSI) are largely based on phase encoding principles, similar to those described in Section 3.4.5. Phase encoding is applied during the time between the excitation pulse and the sampling to encode

the k-space. The signal can be measured using a FID or a spin-echo. The nominal size of the voxel is obtained by dividing the field of view size by the number of encoding increments. One of the most basic MRSI techniques is chemical shift imaging (CSI) [54], which consists of an RF pulse followed by three phase encoding gradients and the acquisition of the free evolution signal. In practice, MRSI can be used with any of the previously described sequence in Section 4.3.1 by adding phase encoding steps. An example of 3D ^{31}P-MRSI acquisition using the 3D CSI acquisition sequence is illustrated in Figure 19. The grid is presented in the three orthogonal orientation, with a colour reference for each.

This technique can also be applied in 2D by using only two phase encoding gradient and a slice-selection gradient. But the use of slice selection will result in CSDA as previously described.

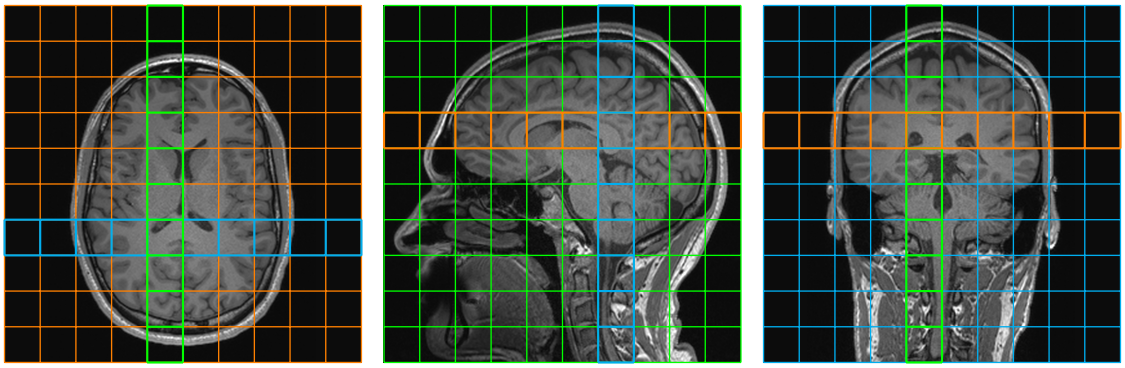

(a) Transverse (b) Sagittal (c) Coronal

Figure 19: Example of 3D ^{31}P-MRSI acquisition grid obtained using the sequence from Figure 20. The presented grid is a $10 \times 10 \times 10$ matrix, each voxel has a volume of $25\,mm^3$.

CSI has the advantage to have no slice or volume selection and thus no CSDA. This is the only sequence use for data acquisition throughout the thesis. Adapting the equation (3.38) to describe the CSI signal give the following equation.

$$s(\mathbf{k}, t) = \int_{-\infty}^{+\infty} \int_{\Omega \subset \mathbb{R}^3} \rho(\mathbf{r}, \sigma) \cdot e^{-2\pi i(\mathbf{k}\cdot\mathbf{r} - \sigma f_0 t)} d\mathbf{r} d\sigma \tag{4.36}$$

The modified equation includes the observation of the transverse magnetization evolution over time under the influence of chemical shifts, with the reference frequency f_0 chosen as a reference as described in Section 4.2.1. The relationship between $\mathbf{k}$ and the gradients is describe in Section 3.4.2 and in Section 7.2.2. The resulting signal obtained through MRSI is now a four-dimensional array comprising three spatial coordinates and a temporal axis. The data are then sampled at n points, separated by Δt, to encode the information along the temporal axis. Inverse Fourier is performed to obtain a spatial image with each voxel containing a spectrum. It is then possible to display images of a particular value of $sigma$. The acquisition time is now given by $T_{acq} = N_x N_y N_z T_R$, with TR on the order of 1 s leading to acquisition that can range from half an hour to an hour for a single CSI acquisition. The Figure 20 show an example of 3D CSI sequence.

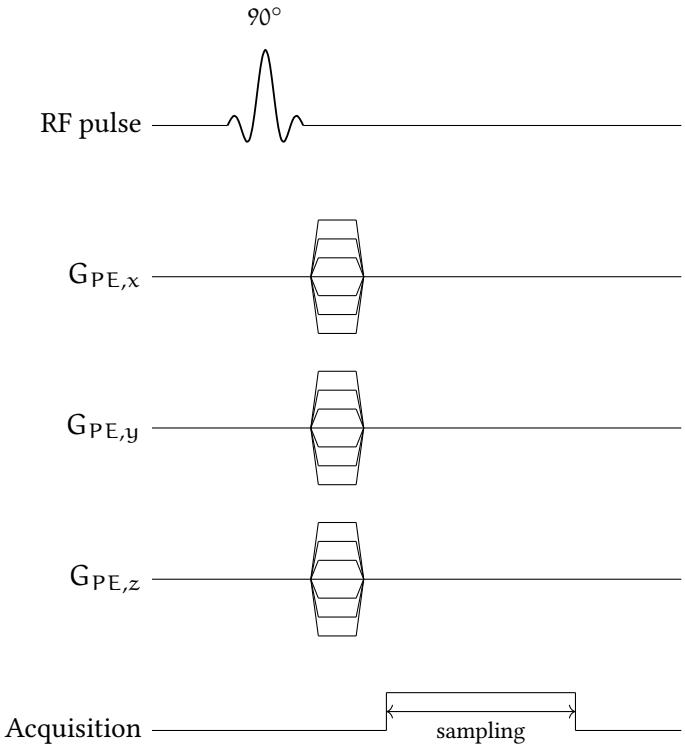

Figure 20: 3D CSI sequence with an 90 ° RF pulse followed by three phase encoding and the sampling of the signal [32].

4.4 PHOSPHORUS AND CELLULAR BIOLOGY

Phosphorus, a chemical element with symbol P, is an essential component of biological systems due to its crucial role in many cellular processes, such as energy metabolism, DNA synthesis, and the regulation of enzyme activity. The five valence electrons of the phosphorus atom allow for three or five covalent bonds, thus enabling it to bond easily with other atoms. The phosphate group, which contains a phosphorus atom, is among the seven most important chemical groups in biological processes. This group contributes a single negative charge when positioned inside a molecule and two negative charges when positioned at the end, endowing the molecule with the ability to react with water, releasing energy [55]. In addition, phosphorus plays a vital role in the synthesis of DNA and RNA, but this is outside the scope of this thesis.

4.4.1 *Phosphorus metabolites in ^{31}P MRS*

As mentioned above, there are many molecules that contain a phosphorus atom in their composition, but only a few of them can be observed using MRI. A list of the most commonly observed metabolites, along with their acronyms and chemical shifts, can be found in Table 3. For metabolites with multiple phosphorus atoms, the different resonances are also listed. Detailed descriptions of each metabolite can be found in the following sub-sections.

Compound	Acronym	Resonances	Chemical shift δ (ppm)
Adenosine monophosphate	AMP		6.3
Adenosine diphosphate	ADP	-α	−7.1
		-β	−3.1
Adenosine triphosphate	ATP	-α	−7.5
		-β	−16.3
		-γ	−2.5
Glycerol phosphorylcholine	GPC		2.8
Glycerol phosphorylethanolamine	GPE		3.2
Inorganic phosphate	Pi		5.0
Phosphocreatine	PCr		0.0
Phosphorylcholine	PCh		5.9
Phosphorylethanolamine	PE		6.8
Nicotinamide adenine dinucleotide, oxidized	NAD+		−8.2
Nicotinamide adenine dinucleotide, reduced	NADH		−8.1

Table 3: Chemical shift of the most prominent phosphorus compound [46].

4.4.2 *Phosphocreatine*

Phosphocreatine (PCr), also referred to as creatine phosphate, is a high-energy molecule that is found within cells, particularly muscle cells. It is produced through the reaction of creatine with adenosine triphosphate (ATP), which involves the transfer of a phosphate group from ATP to creatine. This reaction is reversible, and PCr can be broken down to regenerate ATP when cells require energy, such as during muscle activity [56]. The reaction occurs outside the mitochondrion. In phosphorus spectroscopy, PCr is often used as the chemical shift frequency reference. The chemical structure of PCr is depicted in Figure 21.

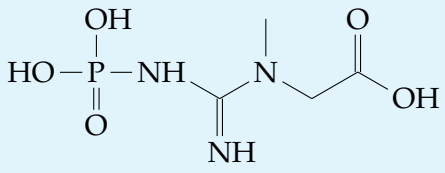

Phosphocreatine (PCr)

Figure 21: Chemical structure of the Phosphocreatine.

4.4.3 *Adenosine mono-, di-, and triphosphate*

Adenosine mono-, di-, or triphosphate (AMP, ADP, ATP) are molecules composed of a ribose sugar, which is made up of an adenine and a D-ribose, attached to one, two, or three phosphorus atoms. ATP has three distinct resonances for each of its phosphorus atoms, referred to as α—, β—, and γ— as shown in Figure 22. As shown in Table 3, the chemical shifts of phosphorus are sufficiently separated to be computed using the weak j-coupling approximation.

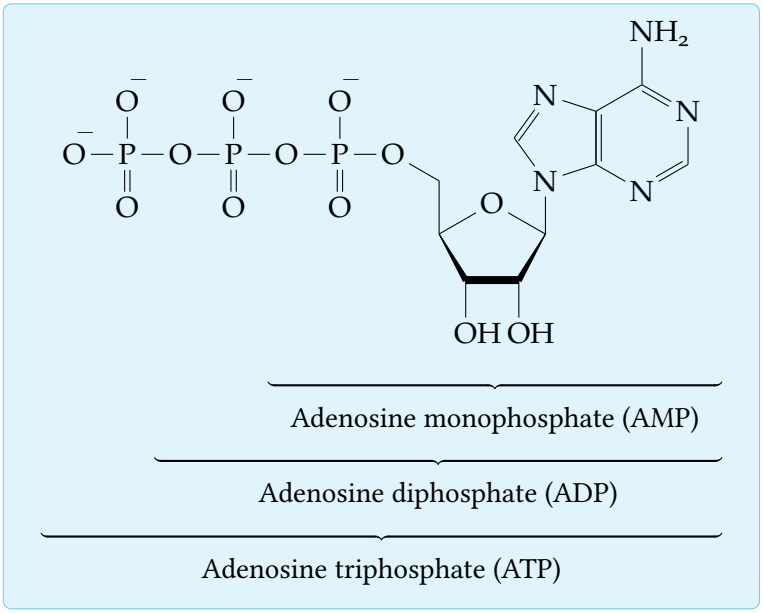

Figure 22: Chemical structure of the adenosine monophosphate (AMP), adenosine diphosphate (ADP) and adenosine triphosphate (ATP).

A working muscle cell is capable of regenerating its entire pool of ATP in less than a minute, representing 10 million molecules.

Adenosine diphosphate (ADP) only has two resonances, α— and β—, as it has only two phosphorus atoms. Together with PCr, ATP is a primary molecule involved in the transfer of energy in biological systems. While it is often said that ATP stores energy, it is more accurate to say that it stores the potential to react with water or other molecules, releasing energy in the process. The bonds between the phosphate groups can be broken through hydrolysis. When an ATP molecule reacts with a water H_2O molecule, the terminal phosphate bonds are broken, resulting in an ADP molecule and an inorganic phosphate (Pi) molecule. This reaction is exergonic and releases 7.3 kcal of energy per mole of ATP hydrolysed under standard conditions. However, the inside of a cell does not correspond to standard conditions, which would increase this value to 13 kcal, or almost 80% greater. The released energy is used by the cell to perform one of three types of work: cellular work, chemical work, or transport work. The released energy allows for endergonic reactions to occur. ATP is a renewable resource that can be regenerated through the addition of a Pi to an ADP. This process is endergonic and requires cellular respiration to provide the necessary energy [46, 55, 57].

4.4.4 *Phospholipids*

Phospholipids are a class of lipids that are an essential component of cell membranes. They are composed of a glycerol molecule bonded to two fatty acids and a phosphate group, which is usually bonded to a molecule of choline, ethanolamine, or serine. Phospholipids form the structural basis of cell membranes, such as the outer and inner mitochondrial membranes in Figure 28, by arranging themselves in a lipid bilayer. The phospholipids have a hydrophilic head facing

outward and a hydrophobic tail facing inward towards each other, resulting in a selectively permeable bilayer. There are multiple phospholipids, but the ones observed in the phosphorus spectrum are phosphorylethanolamine (PE) and phosphorylcholine (PCh), which can bond to glycerol compounds to form glycerophospholipids such as glycerol phosphorylethanolamine (GPE) and glycerol phosphorylcholine (GPC). PE and PCh are monoesters, while GPE and GPC are diesters due to the single or double alkoxy groups that substitute for hydroxyl groups. They are shown in Figure 23 and Figure 24.

Phosphatidylserine is an important phospholipid that plays a number of important roles in cellular processes, particularly in the process of apoptosis.

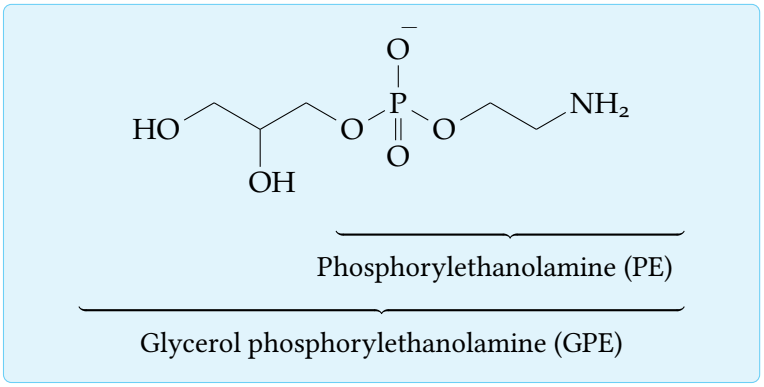

Figure 23: Chemical structure of the Phosphorylethanolamine and the Glycerol phosphorylethanolamine. For the Phosphorylethanolamine, an hydrogen atom is bounded to the oxygen instead of the glycerol.

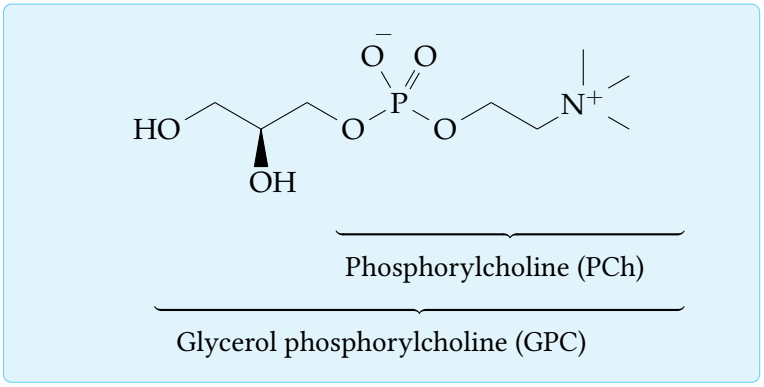

Figure 24: Chemical structure of the Phosphorylcholine and the Glycerol phosphorylcholine. For the Phosphorylcholine, an hydrogen atom is bounded to the oxygen instead of the glycerol.

4.4.5 *Inorganic phosphate*

Inorganic phosphate (Pi) is depicted in Figure 25. As previously mentioned, Pi is formed through the hydrolysis of ATP. Inorganic phosphate helps regulate pH in the body through its role in the buffering system. One way in which it acts as a buffer is by forming a complex with hydrogen ions (H^+). When hydrogen ions are added to a solution, the pH becomes more acidic. However, if inorganic phosphate is present, it can react with hydrogen ions to form a less acidic compound called mono-hydrogen or di-hydrogen phosphate. Inorganic phosphate exists in half as the mono-anion $H_2\,PO_4^-$ and in the other half as the di-anion HPO_4^{2-} [42, 58]. As the molecule changes its number of hydrogen atoms, it also changes its chemical shift. It is therefore possible to measure the physiological pH through the variation of the Pi's chemical shift with respect to PCr. The exchange between the two forms can be written as $HA \rightleftharpoons H^+ + A$, where the unprotonated molecule HPO_4^{2-} is written as A. The chemical shift (δ) of Pi is given by:

$$\delta = x_A \delta_A + (1 - x_a)\delta_{AH} \tag{4.37}$$

The value x_a represents the molar fraction of the unprotonated molecule. Using the relation $pH = pK + \log_{10}(x_A/(1 - x_A))$, intercellular pH can be obtained through the variation of the chemical shift [59, 60].

$$pH = pK + \log_{10}\left(\frac{\delta - \delta_{AH}}{\delta_A - \delta}\right) \tag{4.38}$$

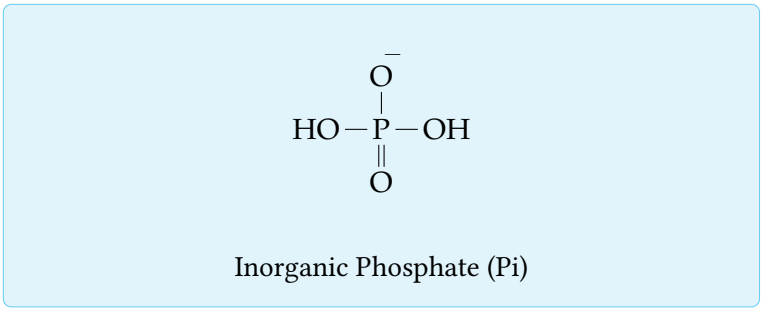

Figure 25: Chemical structure of the inorganic phosphate (Pi).

4.4.6 *Nicotinamide adenine dinucleotide*

Nicotinamide adenine dinucleotide exists in two related coenzymes: the reduced form (NADH) and the oxidized form (NAD+) that are presented in Figure 26.

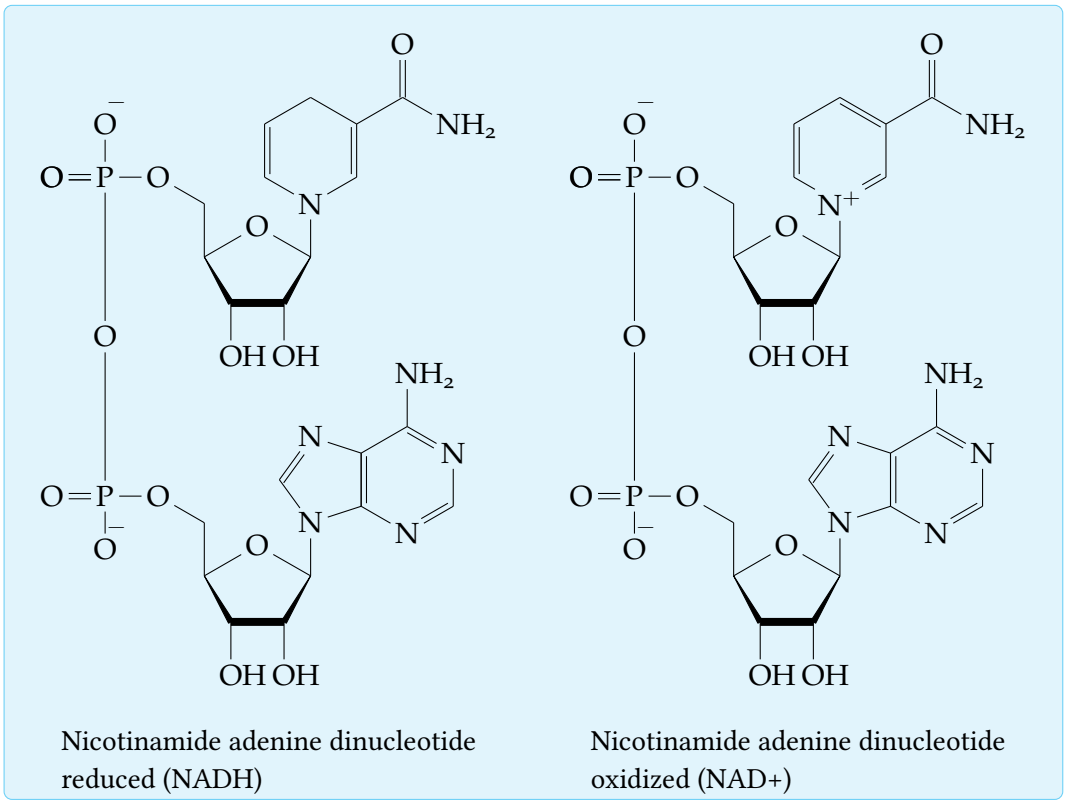

Figure 26: Chemical structure of the Nicotinamide adenine dinucleotide reduced (NADH) and oxidized (NAD+).

NAD+ is the most versatile electron acceptor in cellular respiration and plays a role in several redox steps of glucose breakdown.

These are electron carriers because they can cycle between the two forms in cellular reduction-oxidation (redox) reactions. An enzyme called dehydrogenase has the ability to remove a pair of hydrogen atoms (both protons and electrons) from a substrate (for example, glucose). The enzyme then delivers two electrons and a proton to NAD+, forming NADH and releasing the other proton as a hydrogen ion. The stored electrons do not lose potential energy as they move from NAD+ to NADH, representing stored energy that can be used to produce ATP. The electron transport chain will be discussed below. The combination of O_2 and H_2 yields a large amount of energy, and through the breakdown of water molecules into multiple steps, cells are able to produce multiple molecules of ATP, thereby controlling their energy storage.

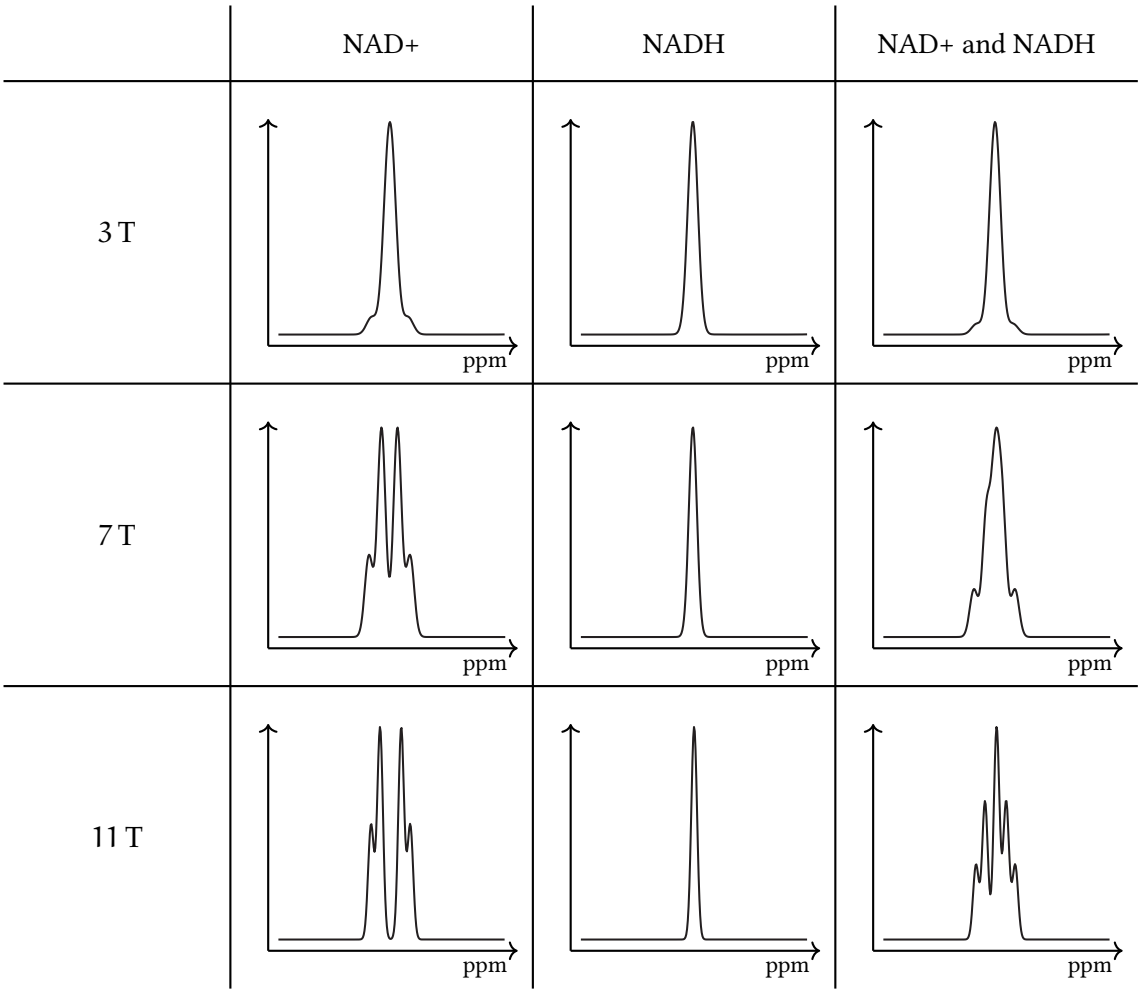

Figure 27: Example of NAD+ and NADH resonances for magnetic field of 3 T, 7 T, and 11 T with a linewidth of 15 Hz.

The ratio of NAD+ to NADH is known as the redox state of a cell and is a crucial indicator of the activity and health of cells. However, as shown in Table 3, both molecules have similar chemical shifts and NAD+ charge small asymmetry leads to different electron shielding, causing a strong coupling between the two phosphorus atoms. This results in a resonance that appears as a doublet of doublet. The overlapping of the two NADH and NAD+ resonances, along with the multiple peaks for NAD+, makes it challenging to evaluate the redox state at low field. The Figure 27 presents the NAD+ and NADH resonances individually and together at different field with a linewidth of 15 Hz.

4.4.7 *Mitochondria is the Powerhouse of the Cell*

Mitochondria are organelles found in most eukaryotic cells and are responsible for producing the majority of the cell's adenosine triphosphate (ATP), the primary source of energy for the cell. This has earned them the nickname of *powerhouses of the cell* [61]. A schematic view of a mitochondrion is shown in Figure 28. The inner and outer membranes are composed of a double layer of phospholipids, the green and red ovals represent embedded proteins that allow the passage of specific molecules. The membrane consists of various proteins, forming a mosaic of tiles. More than 50 different proteins can be found on the membrane, which can be divided into two categories: integral proteins and peripheral proteins. The former can penetrate through the membrane and some can even go through the other side, while the latter only remain loosely bound to the surface. The green and red proteins shown in Figure 28 are integral proteins as they are transport proteins that allow the passage of substances through the membrane. The green proteins allow hydrogen nuclei to travel to the intermembrane space and the red proteins allow them to return to the matrix of the membrane to be used for ATP production. Ion channels facilitate the diffusion of ions across the membrane.

The inside of the inner mitochondrial space is called the matrix.

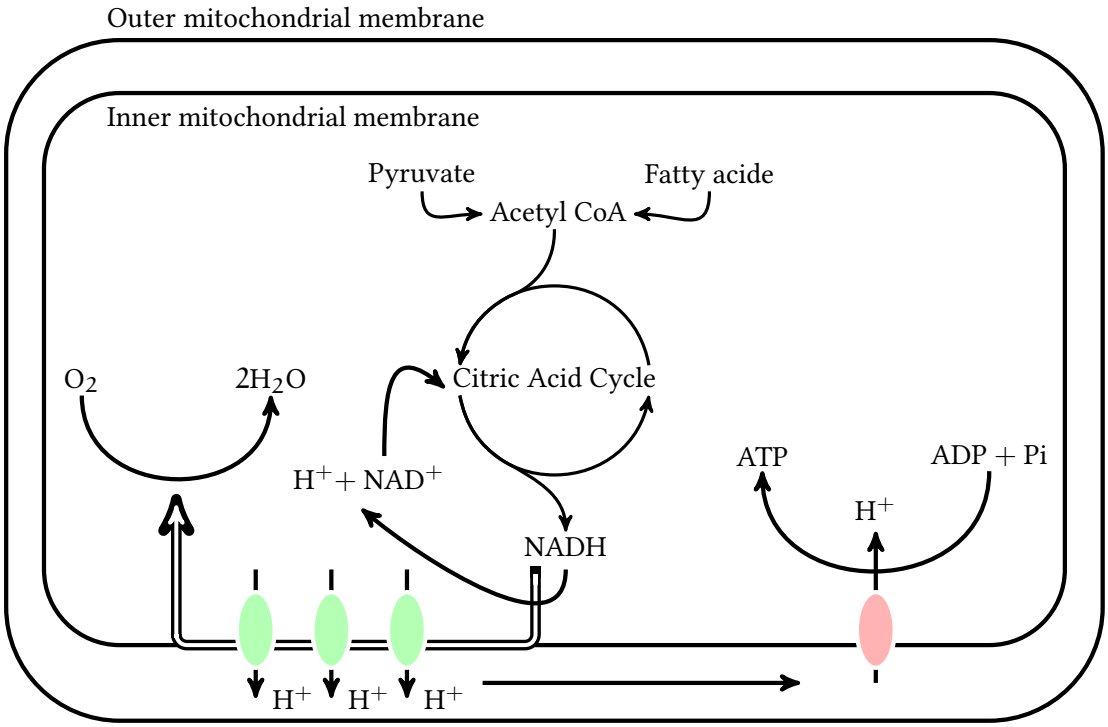

Figure 28: General schematic view of the mitochondrial citric acid cycle and the oxidative phosphorylation. It shows the coupling of the respiratory chain with the phosphorylation of ADP to ATP by ATP synthase. The oxidations that occur during the flow of electrons along the respiratory chain release energy, which is used by proteins to create a proton concentration gradient around the inner mitochondrial membrane. The resulting electrochemical gradient provides energy to drive a molecular reactions that allows ATP synthase to produce ATP [55, 58].

Phosphorus-based molecules, like ATP, are found in mitochondria and play a crucial role in energy metabolism. The citric acid cycle, also known as the Krebs cycle, is a series of chemical reactions that occur in mitochondria and are responsible for the production of ATP. The citric acid cycle involves the breakdown of glucose and other organic molecules to release energy. After glucose is broken down into pyruvate through multiple steps, it is transported into

the mitochondrion. Pyruvate is first converted to acetyl coenzyme A (Acetyl CoA), releasing CO_2 and transferring energy to NAD+ through the formation of NADH. Acetyl CoA then enters the citric acid cycle, which produces $2CO_2$, reduces FAD to $FADH_2$, generates ATP, and reduces three NAD+ to NADH. The resulting NADH participates in the oxidative phosphorylation process, which occurs through the electron transport chain in the inner membrane of the mitochondrion (shown in Figure 28 by the black and white arrow). The process starts with NADH as the highest energy in the chain and ends with the capture of electrons and hydrogen ions by O_2 molecules to form water. The release of energy at each step of the chain is stored in a way that the mitochondrion can use it to form ATP from ADP. The synthesis of ATP is called oxidative phosphorylation because it is powered by redox reactions. For every molecule of glucose converted to CO_2 or H_2O, the cell can produce up to 32 molecules of ATP. Hydrogen ions are transferred from the matrix to the intermembrane space and move to the ATP synthase protein (shown in the red oval in Figure 28), where they are transferred back to the matrix to produce ATP [46, 55].

Part II

ARTIFICIAL INTELLIGENCE ANALYSIS: DEEP LEARNING AND CONVOLUTIONAL NEURAL NETWORKS

5

DEEP LEARNING

"Thou shalt not make a machine to counterfeit a humain mind."

- Frank Herbert, *Dune*

Contents

5.1 INTRODUCTION

The concept of artificial intelligence (AI) has captured the imagination of humans for centuries, although its practical applications have only existed for less than a century. The notion of animating inanimate objects with the ability to think can be traced back to ancient Greek mythology, where the myth of Talos, a robot created by the god Hephaestus to guard the princess Europa, serves as an early example of AI [62]. Other well-known examples can be found in the story of Galatea, a statue brought to life by Pygmalion [63]. These tales illustrate humanity's fascination with creating AI and the prospect of bringing non-living entities to life.

The practical application of AI in our daily lives differs substantially from the fictional depictions of AI. The field of AI research originated in the 1950s with the advent of modern computers. Computers possess an inherent ability to excel at computation and can outperform humans in computation-intensive tasks. The primary objective of AI is to design systems that can outperform humans in specific tasks, such as data analysis and prediction, which can be abstract and mentally challenging for humans. Conversely, tasks that are intuitive for humans, such as object recognition, have only been achieved by computers in recent decades. The challenge in creating AI lies in imparting the computer with knowledge about the world to enable intelligent behavior. Early attempts at AI using a knowledge-based approach were not very successful, as researchers attempted to manually encode rules into the system. This approach was limited in its effectiveness as the rules could never fully encompass the complexity of the world [64]. Such algorithms were only functional in limited environments with simple rules. An exemplary instance of this is Deep Blue, a chess-playing expert system run on a dedicated supercomputer that defeated Garry Kasparov, the chess world champion in 1997. Deep Blue had almost a million grandmaster chess games stored in its memory and could compute millions of positions to determine the best moves [65].

The field of AI experienced a significant breakthrough with the advent of machine learning (ML), which enables machines to learn and derive their knowledge from data analysis. The efficacy of machine learning is contingent on the data representation provided to the machine. The challenge in this approach lies in the numerous factors that may influence the observed data and the requirement for the machine to extract high-level, abstract features from the data to perform accurately. Deep learning (DL) was developed to tackle this challenge by utilizing multiple layers to progressively encode raw input into higher-level features or simpler, more compact representations of information. [64, 66]. Presently, AI has widespread applications,

such as self-driving cars, facial recognition, and personalized movie and music recommendations. These advances demonstrate the ongoing progress in AI and its growing impact on our daily lives.

This chapter introduces the concepts of artificial intelligence essential to comprehend the content of Chapter 6. The first section presents the general concepts of machine learning. The second section elaborates on deep learning, and the third section focuses on convolutional neural networks, which is a special use case of deep learning.

5.2 MACHINE LEARNING

Deep Learning is a specialized field of Machine Learning, which in turn is a subfield of artificial intelligence. Machine learning algorithms can be employed to address a wide range of problems, including but not limited to image and speech recognition, natural language processing, regression, classification, and predictive modeling. Deep learning models cannot be regarded as stacking of simpler units since this would overlook the importance of the complex hierarchical arrangement that enables the models to achieve optimal performance. The multiple layers each performing a mathematical transformation that become slightly more abstract to model complex non-linear relationships. The architecture of deep learning networks is critical to their accuracy and efficiency. To fully comprehend the principles of deep learning, it is essential to first grasp the fundamentals of machine learning.

The term "deep" in the context of deep learning refers to the significant number of layers that are involved in transforming input data into output.

A machine is considered to have learned if *as a result of experience* E *with respect to a given task* T*, its performance* P *improves* [67]. The task may encompass any of the examples outlined in the introduction, and each task has a specific input and output. For instance, classification may accept an image as input and return a numerical code identifying the object within the image, while language translation may take a sequence of text as input and return its translation into another language. Performance is evaluated by determining the percentage of incorrect outputs. The models of machine learning are categorized based on their experiences, which can be either supervised or unsupervised. In supervised learning, the machine is trained using labeled data, meaning that the input-output pairs are already known. A well designed model would generalize the relationship between the input and output, allowing it to produce accurate predictions on new, unseen data within the training data distribution. In contrast, unsupervised learning involves training the model on unlabelled data, seeking to identify patterns and structures within the data itself. The machine is expected to extract features and relationships from the data without any prior knowledge of the input-output mapping. This chapter will focus on supervised learning, as unsupervised learning is outside of the scope of the thesis.

5.2.1 *General model: Linear regression*

One of the most basic machine learning algorithms is the linear regression model, which seeks to predict a scalar value y based on an input vector $\mathbf{x} \in \mathbb{R}^n$. In this model, the algorithm computes a linear combination of the elements in the input vector and maps it to an output value $\hat{y}$. Specifically, the model can be expressed mathematically as:

$$\hat{y} = \sum_{i=1}^{n} w_i \cdot x_i + b \tag{5.1}$$

$$= \mathbf{w}^T \mathbf{x} + b \tag{5.2}$$

The bias b can also be written as w_0.

The model consists of a weight vector $\mathbf{w} \in \mathbb{R}^n$ and a scalar bias term b. The weight vector represents the relative importance of each input feature in the prediction, while the bias term

accounts for the model's prediction in the absence of input. The model's task T is to perform the prediction $\hat{y}$ given $\mathbf{x}$. To train the model, a labeled dataset is employed where each input has a corresponding output label. The model's objective is to find the optimal values of the weight vector $\mathbf{w}$ and bias term b that minimize the discrepancy between the predicted output $\hat{y}$ and the actual output y. This difference can be computed by defining a loss function $\mathcal{L} : (\hat{y}, y) \in \mathbb{R} \times \mathbb{Y} \longrightarrow \mathcal{L}(\hat{y}, y) \in \mathbb{R}$, where $\mathbb{Y}$ denotes the set of possible output labels. The most commonly used loss functions are presented in the Table 4.

LEAST SQUARED ERROR	LOGISTIC LOSS	HINGE LOSS	CROSS-ENTROPY
$\frac{1}{2}(y-\hat{y})^2$	$\log(1+e^{y\hat{y}})$	$\max(0, 1-y\hat{y})$	$-[y\log(\hat{y})+(1-y)\log(1-\hat{y})]$

Table 4: Example of the most commonly used Loss functions.

Table 4 also presents the logistic loss, which is primarily utilized for logistic regression, while the hinge loss is typically favoured for support vector machines.

The choice of loss function is based on the machine learning model. For example, the least squared error will mostly be used for linear regression model whereas the cross-entropy loss will be mostly used for neural network. The loss function is used in by the cost function $\mathcal{J}$, where the error is computed for m training examples.

$$\mathcal{J}(\mathbf{w}) = \frac{1}{m}\sum_{k}^{m}\mathcal{L}(\hat{y}^{(k)}, y^{(k)}) \tag{5.3}$$

The loss function is calculated on both the training set and a previously unseen testing set to ensure that the model does not solely learn the training data instead of learning the underlying data representation.

5.2.2 *Gradient Descent*

In order to enhance the performance of the algorithm, it is necessary to minimize the cost function $\mathcal{J}(\mathbf{w})$ with respect to the weight vector $\mathbf{w}$. The algorithm can subsequently update the weights iteratively, until convergence is achieved. One common technique for minimizing the cost function is through the use of gradient descent algorithms. This approach involves calculating the derivative of the cost function with respect to the parameters, and then updating the weights accordingly. The gradient descent algorithm can be expressed as follows:

The bias b is updated in a similar way as the weights.

$$\mathbf{w} \leftarrow \mathbf{w} - \alpha\nabla_{\mathbf{w}}\mathcal{J} \tag{5.4}$$

Here, $\alpha \in \mathbb{R}$ is referred to as the learning rate. It is typically assigned a small constant value to prevent divergence. The iterative nature of the gradient descent algorithm is illustrated in Figure 29. It is worth mentioning that some application may be interested in the second derivative by computing the Hessian matrix $\mathbf{H}$, and applying the Newton algorithm bellow

$$\mathbf{w} \leftarrow \mathbf{w} - \mathbf{H}^{-1}\nabla_{\mathbf{w}}\mathcal{J} \tag{5.5}$$

$$\text{where} \quad H_{ij} = \partial_{w_i}\partial_{w_j}\mathcal{J} \tag{5.6}$$

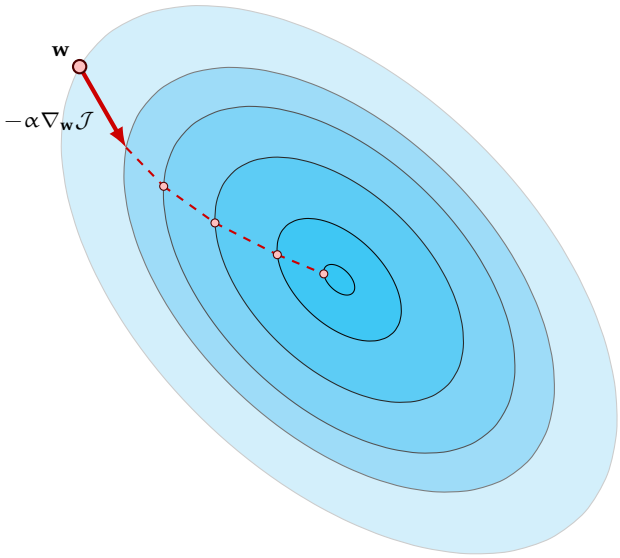

Figure 29: Schema of a two-dimensional top view representation of a multi-dimensional plane illustrating the gradient descent algorithm. The ellipses denote areas that share the same $\mathcal{J}$ value, with the blue color indicating the minimum value at the center in a darker blue shade, gradually increasing in value in a lighter blue shade. The figure showcases the trajectory of the updated weights in red, depicting each step of the process until the cost function is minimized at the center. Inspired by [68].

5.2.3 *Stochastic Gradient Descent*

Stochastic gradient descent (SGD) is a powerful alternative to gradient descent, which operates similarly by computing the gradient of the loss function. However, rather than calculating the gradient of the cost function, SGD calculates the gradient of the loss function and update the weights for each training example. This can be expressed as follows:

$$\nabla_{\mathbf{w}}\mathcal{J} = \frac{1}{m}\sum_{k}^{m}\nabla_{\mathbf{w}}\mathcal{L}(\hat{y}^{(k)}, y^{(k)}, \mathbf{w}) \tag{5.7}$$

One disadvantage of this method is the requirement to compute the derivation for all examples, therefore the computational time scale linearly with the number of training examples m. An alternative approach is to use mini-batch training, where the training set is randomly and uniformly divided into j subsets, each with a size of $m' < m$. SGD is then computed for each mini-batch $\nabla_{\mathbf{w}}\mathcal{J}^{(j)}$, as shown below:

$$\nabla_{\mathbf{w}}\mathcal{J}^{(j)} = \frac{1}{m'}\nabla_{\mathbf{w}}\sum_{k}^{m'}\mathcal{L}(\hat{y}^{(k)}, y^{(k)}, \mathbf{w}) \tag{5.8}$$

Updating the weights after each mini-batch results in faster cost function minimization than the original gradient descent. Additionally, the computational cost of SGD does not scale with the size of the training dataset, as the size of the mini-batches can be kept constant. Mini-batch gradient descent can offer significant improvements over true stochastic gradient descent. The algorithm is faster as it is no longer computing each training separately. This allows for a smoother convergence, since the gradient computed at each step is averaged over more training samples.

5.2.4 *Hyperparameters*

Hyperparameters refer to parameters that are predetermined by the user prior to the commencement of training a model, distinct from the model parameters that are acquired through training data. As presented previously, hyperparameters such as the learning rate and the size of the mini-batch can be adjusted prior to the training process. There exist other hyperparameters, including regularization, number of hidden layers, convolution kernel, and padding, which will be expounded upon in the following section. Notably, the list of hyperparameters is non-exhaustive and is dependent on the type of machine learning or deep learning method employed. The significance of hyperparameters lies in their ability to significantly impact model performance. The search for optimal hyperparameter values is often an empirical process.

5.2.5 *Motivation to deep learning*

The presentation of machine learning in this section is not exhaustive, as it omits numerous applications beyond linear models (classification model, decision trees, ...). While conventional machine learning methods may suffice for many tasks, certain domains necessitate the use of deep learning techniques. A significant challenge posed by traditional machine learning methods is their inability to extract and represent high-level features from raw data. In contrast, deep learning approaches are designed to learn these features effectively by utilizing multiple layers of nonlinear processing units. Moreover, deep learning algorithms typically outperform machine learning algorithms in a variety of tasks such as image and speech recognition, as well as natural language processing. Deep learning algorithms also tend to generalize better than conventional machine learning algorithms, making them more robust and reliable. However, the application of deep learning methods is not without challenges, as their capacity to handle large amounts of data is balanced by their need for substantial training data and computational resources for both training and deployment.

5.3 DEEP LEARNING

In contrast to conventional machine learning algorithm, deep learning algorithms utilize neural networks with multiple hidden layers. The depth of the model is defined by the number of hidden layers, which can be viewed as either the number of sequential instructions executed, such as summation and multiplication, or as a computational graph flowchart that describes the interconnection between concepts, such as a function that performs multiple operations. As both representations do not lead to the same depth value, there is no consensus on the minimum depth required for a model to be classified as "deep".

Learning in deep learning also follows a distinct philosophy from machine learning. In machine learning, the task T is considered to be improved if the performance P increases with training. The reduction of error E through the cost function $\mathcal{J}$ serves as a performance improvement proxy as it is hoped that reducing the error will lead to performance enhancement. In deep learning, the primary goal of learning is the minimization of the cost function. This approach was deemed problematic in the 1990s since machine learning models are designed to optimize a convex problem, enabling gradient descent to converge to a global minimum, whereas deep learning models are challenged by non-convex situations with multiple minima. However, in the 2010s, it was uncovered that for a network of sufficient size, the majority of local minima exhibit a cost value low enough to render the search for a global minimum unnecessary [69].

5.3.1 *Single layer: Perceptron*

The Perceptron constitutes a fundamental concept in the domain of artificial neural networks and deep learning. Its originates dates back to the late 1950s and early 1960s when it emerged as one of the initial models designed to simulate the cognitive processes of the human brain within the context of machine learning. The Perceptron, at its core, represents a simplistic binary classifier that leverages an activation function to make binary predictions based on input features. Although the initial Perceptron model was confined to performing separable binary classification tasks, the development of multilayer Perceptron (MLP) networks has significantly extended the capabilities of the Perceptron to address complex nonlinear classification and regression challenges. An MLP network is composed of numerous layers of interconnected Perceptrons, with each layer progressively transforming the input data into increasingly abstract representations. The Perceptron concept was the basis or the essential design of Artificial Neural Network (ANN) and has consequently started the evolution of numerous modern deep learning models, including Convolutional Neural Networks (CNNs) and Recurrent Neural Networks (RNNs).

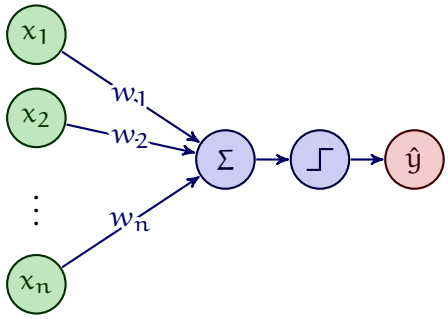

Figure 30: Example of the Perceptron architecture, inspired by [68]

As shown in Figure 30, the perceptron takes a vector $\mathbf{x} \in \mathbb{R}^n$ as input and outputs a prediction $\hat{y}$ based on a linear combination of the input vector and a set of learned weights, as described in the equation (5.2). Specifically, the perceptron computes the dot product of the input vector and weight vector, followed by an activation function $\Phi(\cdot)$, which maps the linear combination to a binary output. Traditionally, the perceptron used the sign function as its activation function, defined as:

The sign function can sometimes be defined as $sign(x) = 0$ *if* $x < 0$.

$$\text{sign}(x) = \begin{cases} -1, & \text{if } x < 0 \\ +1, & \text{if } x > 0 \end{cases} \tag{5.9}$$

The sign function is applied in order to convert the dot product between the input and the weights to a class label. However, other activation functions have been introduced to improve the performance of the perceptron, which will be discussed in Section 5.3.2. The perceptron's output can be written as:

$$\hat{y} = \Phi(\mathbf{w}^T\mathbf{x} + b) \tag{5.10}$$

where Φ is the activation function. With a binary prediction, the error is restricted to the set $\{-2, 0, 2\}$. The weights are updated using the SGC described in the Section 5.2.3, using the least squared error loss presented in Table 4. While the computation is performed in two steps, first the dot product and then the activation, it is actually considered to be a single computational layer network.

5.3.2 *Activation Functions*

As presented in the preceding section, the application of deep learning involves an activation function that is employed at each node following the computation of the dot product between the output of the previous layer and the weights. The fundamental objective of the activation function is to introduce non-linearity into the model's computation, thereby allowing non-linear evaluations. The non-linearity of the activation function is of critical importance, as a linear function applied to a linear function would result in an output that is linear with respect to the input. This would simplifies in a linear regression. The most noteworthy activation functions, denoted by $\Phi : \mathbb{R} \longrightarrow \mathbb{R}$, are presented in the following equations.

$$\Phi(x) = \frac{1}{1+e^{-x}} \quad \text{(sigmoid)} \tag{5.11}$$

$$\Phi(x) = \frac{e^{x}-e^{-x}}{e^{x}+e^{-x}} \quad \text{(tangent hyperbolid)} \tag{5.12}$$

$$\Phi(x) = \max\{0,x\} \quad \text{(Rectified Linear activation Unit (ReLU))} \tag{5.13}$$

$$\Phi(x) = \max\{0,x\} + \alpha \cdot \min\{0,x\} \quad \text{(Parametric ReLU (PReLU))} \tag{5.14}$$

The four equations are plotted in the Figure 31.

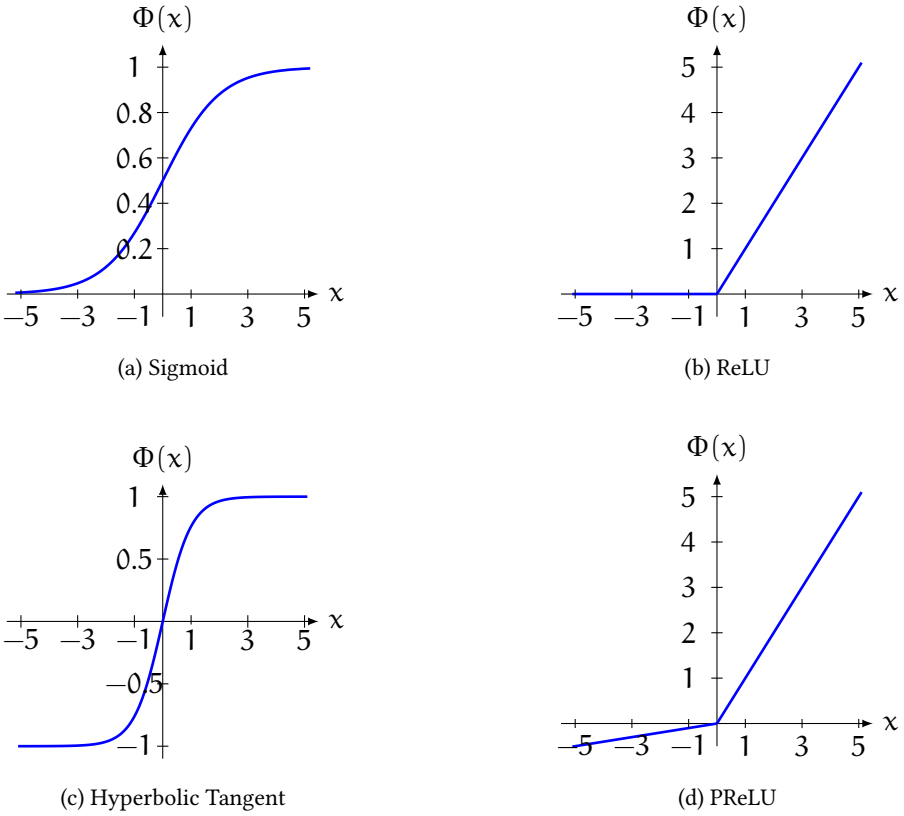

(a) Sigmoid

(b) ReLU

(c) Hyperbolic Tangent

(d) PReLU

Figure 31: Example of the most important activation functions.

The sigmoid function and the hyperbolic tangent function exhibit comparable characteristics in their output ranges, with the former yielding results within the interval [0,1], and the latter within [-1,1]. On the other hand, the Rectified Linear activation unit (ReLU) and the Parametric ReLU (PReLU) are variants of the linear function, that allow for easier optimization with gradient-based techniques. The sign function, while useful for binary classification tasks, lacks differentiability in contrast to the aforementioned fonctions that are monotone, continuous and differentiable.

5.3.3 *Multilayer perceptron*

The feed-forward network stands in contrast to a recurrent neural network (RNN), where the output of a node can be connected to its input, creating a feedback loop that channels the output back into the input before proceeding to the subsequent layer.

A multilayer network comprises two or more layers, as exemplified by the 2-hidden-layer network depicted in Figure 32. The blue layers, are called hidden layers because the output of the computations performed in the layers are not accessible by the users. The illustrated architecture is a feed-forward network, where each layer's output feeds into the next layer in the forward direction, progressing from the input to the output.

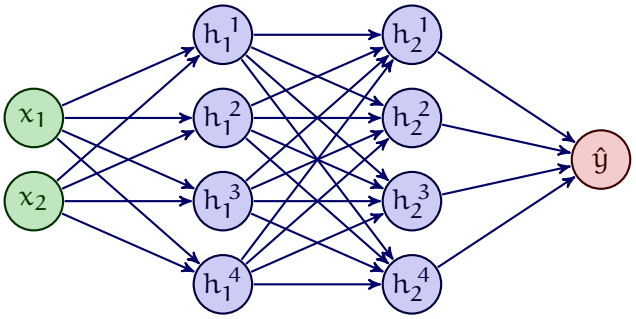

Figure 32: Example of a 2-hidden-layer feed-forward neural network. The input is presented in the green layer, the hidden layers in blue and the output layer in red. Inspired by [68]

One of the hyperparameters specified by the user when designing a neural network is the number of nodes in each layer. The number of nodes are referred to as the dimensionality of the layer. The computations at each layer can be succinctly described through the use of matrices.

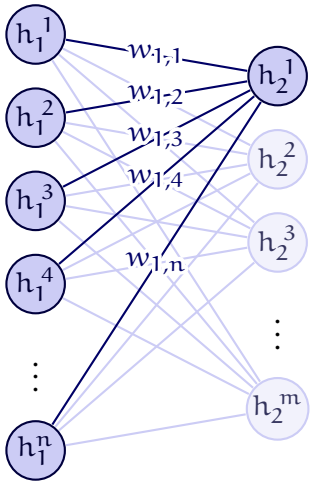

Figure 33: Computation between two hidden layers of different dimensionality. Inspired by [68]

As depicted in Figure 33, this matrix-based computation occurs between two hidden layers in a fully connected network the first with a dimensionality n and the second with a dimensionality m. The mathematical expression for the input received by the node h_2^1 can be represented using equation (5.16).

$$h_2^1 = \Phi\left(w_{1,1}h_1^1 + w_{1,2}h_1^2 + \ldots + w_{1,n}h_1^n + b_1^{(0)}\right) \tag{5.15}$$

$$= \Phi\left(\sum_{i=1}^{n} w_{1,i}h_1^i + b_1^1\right) \tag{5.16}$$

The computation can be generalized to all the nodes within the layer 2, and is outlined in the subsequent equations.

$$\begin{pmatrix} h_2^1 \\ h_2^2 \\ \vdots \\ h_2^m \end{pmatrix} = \Phi \left[\begin{pmatrix} w_{1,1} & w_{1,2} & \dots & w_{1,n} \\ w_{2,1} & w_{2,2} & \dots & w_{2,n} \\ \vdots & \vdots & \ddots & \vdots \\ w_{m,1} & w_{m,2} & \dots & w_{m,n} \end{pmatrix} \begin{pmatrix} h_1^1 \\ h_1^2 \\ \vdots \\ h_1^n \end{pmatrix} + \begin{pmatrix} b_1^1 \\ b_1^2 \\ \vdots \\ b_1^m \end{pmatrix} \right] \tag{5.17}$$

$$h_2 = \Phi \left(\mathbf{W}^{(0)} h_1 + \mathbf{b}_1 \right) \tag{5.18}$$

The activation function is applied element-wise to the vector, without explicit mention, and is assumed to be the same function throughout the network.

5.3.4 *Back propagation*

In Section 5.2.2, we presented an optimization technique for iteratively updating the weights. In deep neural networks, this process is known as backpropagation. Specifically, the gradient of the loss function with respect to the output of a given layer i can be computed by multiplying the gradient of the loss function with respect to the output of the following layer $i+1$ with the derivative of the activation function of the current layer i. This iterative process can be applied to each layer in the neural network, thereby allowing the gradient of the loss function with respect to the weights of the entire network to be determined. This procedure is executed using the chain rule. To illustrate, consider a single node and let $z_i = \mathbf{W}^\top h_i + \mathbf{b}_i$ the product between the weights and the hidden layer i, such that $h_{i+1} = \Phi(z_i)$. The chain rule for a specific weight yields

The term "backpropagation" derives from the propagation is computed from the output layers towards the input layers.

$$\frac{\partial \mathcal{J}}{\partial w_i} = \frac{\partial \mathcal{J}}{\partial h_{i+1}} \cdot \frac{\partial h_{i+1}}{\partial z_i} \cdot \frac{\partial z_i}{\partial w_i} \tag{5.19}$$

Equation (5.19) describes the first component as the derivative of the error with respect to the output of the node. The backpropagation will requiers to start from the output of the network $\partial \mathcal{J} / \partial \hat{y}$. The second component is the derivative of the activation function $\partial h_{i+1} / \partial z_i = \Phi'$, while the third component denotes the input of the associated weight with $\partial z_i / \partial w_i$. Expending this process, for a neural network with n hidden layer, the backpropagation between a two units h_{i-1} and h_i is

$$\frac{\partial \mathcal{J}}{\partial w_{(h_{i-1}, h_i)}} = \frac{\partial \mathcal{J}}{\partial \hat{y}} \cdot \left[\frac{\partial \hat{y}}{\partial h_n} \prod_{k=i}^{n-1} \frac{\partial h_{k+1}}{\partial h_k} \right] \cdot \frac{\partial h_i}{\partial w_{(h_{i-1}, h_i)}} \tag{5.20}$$

The above equation only considers a single path between unit h_{i-1} and the output. In order to generalize to any path, we must consider a set $\mathcal{P}$ of existing paths.

$$\frac{\partial \mathcal{J}}{\partial w_{(h_{i-1}, h_i)}} = \frac{\partial \mathcal{J}}{\partial \hat{y}} \cdot \left[\sum_{[h_i, h_{i+1}, \dots, h_n, \hat{y}] \in \mathcal{P}} \frac{\partial \hat{y}}{\partial h_n} \prod_{k=i}^{n-1} \frac{\partial h_{k+1}}{\partial h_k} \right] \cdot \frac{\partial h_i}{\partial w_{(h_{i-1}, h_i)}} \tag{5.21}$$

The equation presents a computational cost that can exponentially increase with the number of nodes. However, it is possible to compute backward layer by layer, allowing for the accumulation of gradients in the backward pass and processing of each node exactly once.

5.4 CONVOLUTIONAL NEURAL NETWORKS

Convolutional Neural Networks (CNNs) are a category of deep learning algorithms designed to perform convolutional operations on data, followed by non-linear transformations and pooling operations. Pooling layers are used to downsample the feature maps produced by the convolutional layers. The output of the final pooling layer, of the convolutional layers, is then fed into one or more fully connected neural network layers. An example of the general architecture of a CNN is presented in Figure 34. Compared to the multilayers perceptron, the novelty of these methods is the inclusion of convolutional layers between the input and the fully connected hidden layers. By the properties of the convolution, the network have the useful property of learning spatially invariant features, which make the technique robust to small translations or rotations in the input data.

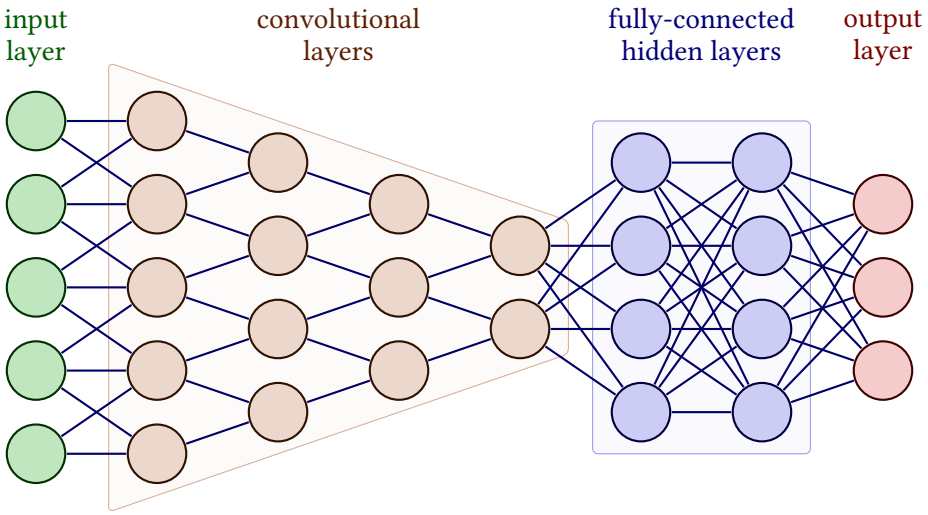

Figure 34: Example of a convolutional neural network architecture. Inspired by [68]

An important aspect that is not illustrated in Figure 34 is that the input to a CNN is typically multi-dimensional, and as the pooling layers downsample the original dimensions of the data, the network is designed to expand in one of the original dimensions, which becomes the filter dimension.

5.4.1 *Convolution*

The filter can also referred to as a kernel.

The convolutional operation constitutes a fundamental building block in CNNs. It involves the sliding of a filter over the input data, and computing the dot product between the filter and the corresponding input patch at each location. As a result, a feature map is generated that represents the presence of specific features or patterns in the input data. The weights of the filters are learned during the training process via backpropagation and gradient descent, enabling the network to learn filters that are optimized to specific features in the data. Mathematically, convolution is an operation between two functions that produces a third function, and it can be expressed in general form as follows:

$$h(t) = (f * g)(t) \tag{5.22}$$

$$= \int_{-\infty}^{+\infty} f(x)g(t-x)dx \tag{5.23}$$

Neural networks operate on finite and discrete inputs, thus the convolution operation should also be discrete. Consider the example of a two-dimensional image $\mathbf{I}$ as the input, which is convolved with a two-dimensional filter $\mathbf{K}$. The convolution operation is commutative, and thus one can use the relation $I * K = K * I$ to express the convolution as follows:

$$S(i,j) = (K * I)(i,j) \tag{5.24}$$
$$= \sum_m \sum_n K(m,n) \cdot I(i-m, j-n) \tag{5.25}$$

In certain programming libraries, a cross-correlation function is used instead of the convolution function. The cross-correlation function replaces the negative sign with a positive sign, resulting in a kernel that is not flipped as it is in the convolution function.

This expression is more intuitive as the sum goes through every element of the filter kernel, instead of the image element. The convolution can be simply presented with the diagram shown in Figure 35 below. The filter moves over all possible spatial positions of the image and convolves with it.

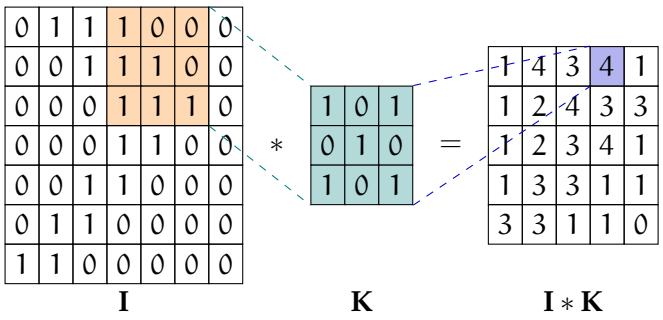

Figure 35: Example of convolution of a $7 \times 7 \times 1$ image with a $3 \times 3 \times 1$ filter [68]

The output of the convolution of the image with the filter is called the feature map. The more similar the filter is to a patch of the image, the highest the output of the convolution will be. As previously mentioned, CNNs are designed to expand in the filter dimension, and the number of filters to be applied on the input data is an important hyperparameter that can be defined by the user during network creation. The use of multiple filters results in the stacking of their respective outputs, thus increasing the filter dimension. An illustrative example of this process is shown in Figure 36.

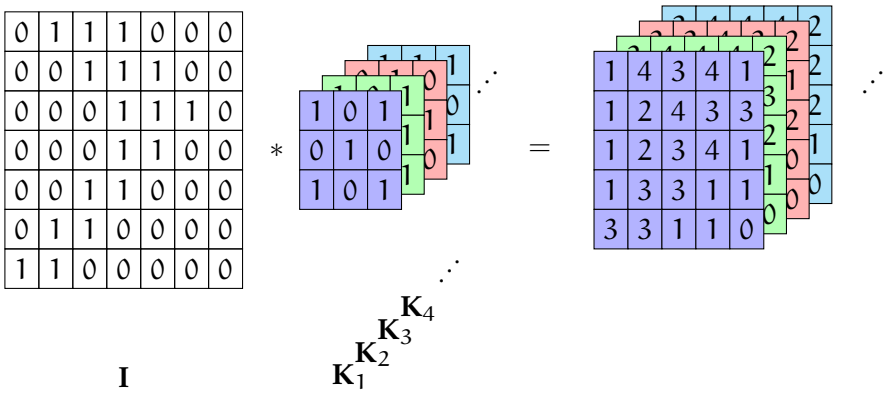

Figure 36: Example of convolution of an image with multiple filters. Inspired by [68]

The initial layers of the convolutional neural network (CNN) apply filters that extract low-level features, such as edges and basic shapes, from the input data. In contrast to the final hidden layer of the CNN where the extracted high-level features are abstract and are complex combinations of low-level features. This hierarchy of learned features enables the CNN to capture and represent the input data in an abstract and meaningful way.

5.4.2 *Padding*

An observation that can be made from both Figure 35 and Figure 36 is that the dimensionality of the output feature maps shrinks as the convolution operation is performed. Specifically, if the input image at a layer i has dimensions $l_i \times w_i$, applying a filter of dimensions $f_l \times f_w$ will result in an output feature map with dimensions

$$l_{i+1} = l_i - f_l + 1 \tag{5.26}$$
$$w_{i+1} = w_i - f_w + 1 \tag{5.27}$$

This can be represented as the movement of a filter across an image and can be quantified as the number of steps taken from one side of the image to the other, incremented by one to account for the initial position. The depth of the output is determined by the number of filters employed. Although reducing the dimension of the output is a key objective of CNNs, such reductions may result in complications, particularly at the image borders, where convolution is less applied compared to the center of the image, leading to a loss of information at the edges. Padding can be utilized to address this issue. This involves adding extra pixels around both the input image and feature maps before performing subsequent convolutions, without causing the output size to decrease. This technique can help to maintain the spatial information near the edges of the input image and improve the overall performance of the model. Two types of padding are commonly used: "valid" and "same". In valid padding, no extra pixels are added to the input image, resulting in a smaller output size compared to the input size, as illustrated in Figure 35. In same padding, the input image is padded with zeros such that the output size is the same as the input size, with $(f_l-1)/2$ and $(f_w-1)/2$ added on each side of the image. The prevalent technique for padding is zero-padding, where the additional values are set to zero. However, other padding methods also exist, including reflective padding, which mirrors the edges of the image, replicate padding, which duplicates the values at the edges, and circular padding, which wraps the values on the opposite side of the image.

Ultimately, the optimal padding strategy for a given dataset depends on the data representation used.

5.4.3 *Activation layer*

The activation layer is typically positioned following the convolutional layer and operates similarly to the method described in the preceding section. One-to-one computation is used for activation, which preserves the dimension of the feature maps. ReLU and PReLU are preferred activation functions for CNNs since they have demonstrated an ability to train deeper models and improve accuracy while being computationally light and have straightforward derivative, as supported by the literature [70]. They are also convenient because they are computationally light and theirs derivative are straightforward.

5.4.4 *Pooling*

Padding is used to prevent the loss of edge information, resulting in a convolution output that has the same dimensions as the input. To decrease the dimensions while preserving depth, a pooling operation is performed. This technique entails using a small grid of size $p_l \times p_w$, which is moved across the output, mostly the output of the convolution, and returns a single value per grid. The most common type of pooling is max pooling, which returns the maximum value. Other techniques, such as average pooling, calculate the average value of the grid. An instance of max pooling is illustrated in Figure 37.

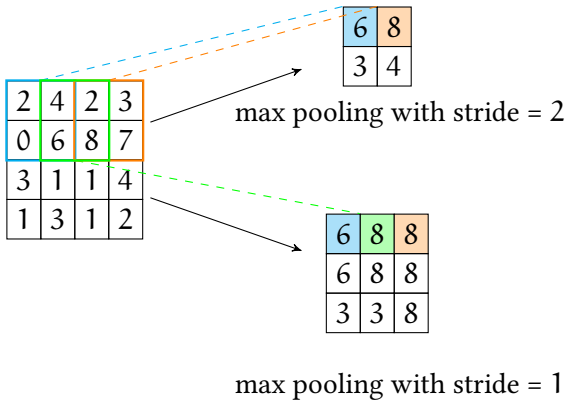

Figure 37: Example of max-pooling, with a stride of 1, and 2. Inspired by [68]

Figure 37 demonstrates the implementation of max-pooling with two distinct stride values. The stride value determines the pooling grid's motion increment. A stride of 1 moves the pooling grid by one step, while a value of 2 moves it by two steps. Given an output size of $l_i \times w_i$ from the convolution and a stride value of s, the size after pooling is determined by:

$$l_{i+1} = \frac{l_i - p_l}{s} + 1 \tag{5.28}$$

$$w_{i+1} = \frac{w_i - p_w}{s} + 1 \tag{5.29}$$

Using 2×2 pooling with a stride of 2 results in non-overlapping pooled regions, as illustrated in the top portion of Figure 37. Although Section 5.4.1 presented the use of filters with a stride value of 1, it is feasible to increase this value for convolution.

5.4.5 *Fully connected layers and overfitting*

After multiple successions of convolution, activation, and pooling, the final module comprises fully connected layers that act as a multilayer perceptron feed-forward network, as previously described. The fully connected layers contain a large number of connections, while the convolutional layers have a large number of activations but fewer connections. Most of the network parameters are present in the last layers. The model uses supervised learning to update the weights using backpropagation. An essential aspect of learning is to avoid both under-fitting and over-fitting. A model that is too simple, not suitable for the application, or that lacks sufficient training examples may under-perform. Conversely, a model that is overly complex for the task, with too many parameters in the model, and/or trained on too many iterations, may learn every training example, leading to over-performance on the training sets but under-

performance in its general application. A schematic example of under-fitting and over-fitting is illustrated in Figure 38.

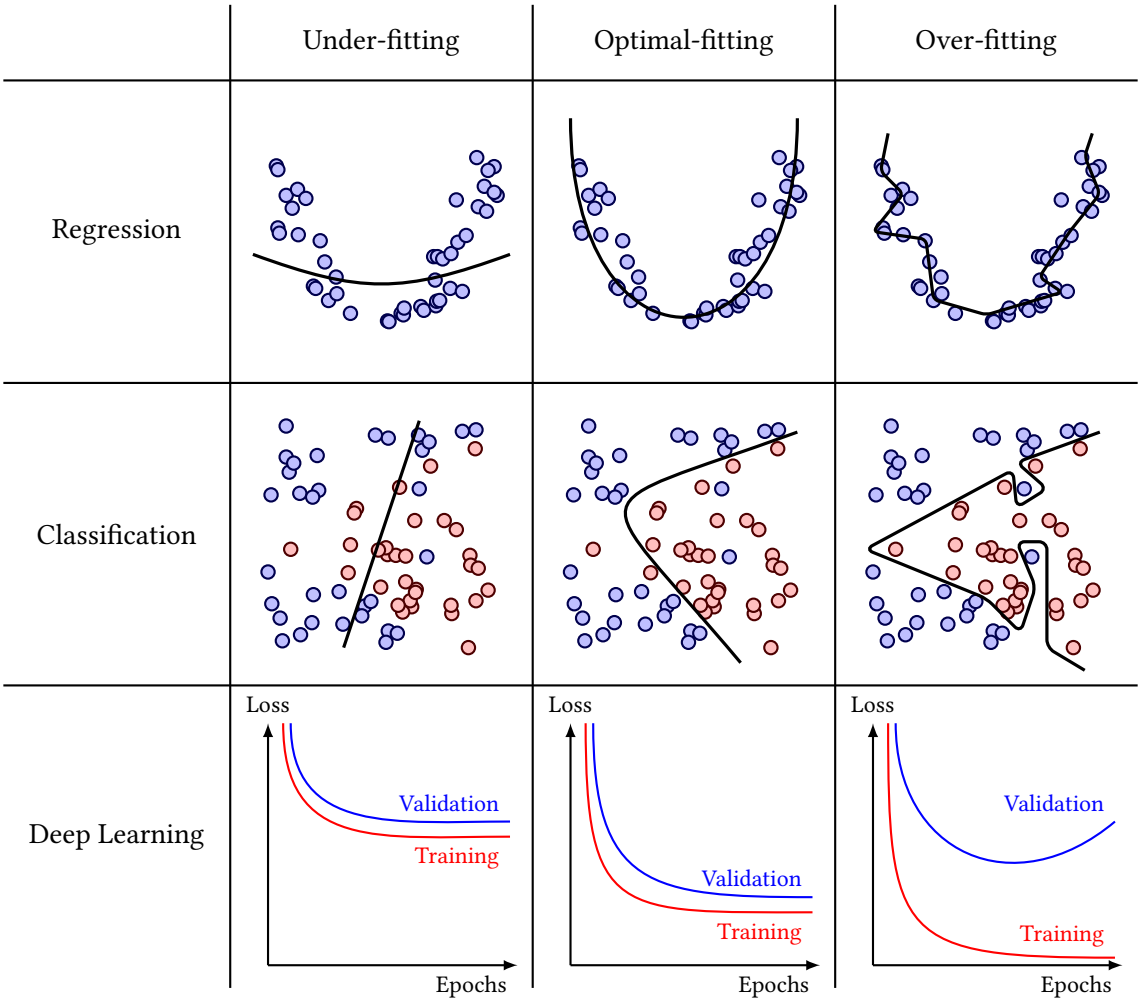

Figure 38: Schematic representation of under-fitting, over-fitting and optimal-fitting, for various application. Inspired by [68]

Achieving optimal model fitting involves ensuring that the model performs well on both the training and validation datasets. In the literature, optimal fitting is often likened to the Ockham's razor principle, where simpler models and features are favored over more complex ones, since they are more likely to be generalizable.

5.4.6 *Dropouts*

In order to mitigate over-fitting, regularization techniques can be employed. One of the most commonly used methods is known as dropout. As demonstrated by equation (5.21), there exist a vast number of possible pathways that connect the input and output nodes, with an exponential increase in complexity as the number of layers and nodes increase. Dropout relies on stochasticity during the training process, randomly setting certain nodes to zero and thus eliminating some of the connections during one training batch or mini-batch. This prevents the model from becoming too reliant on particular nodes or features, which can lead to over-fitting of the training data. The dropout technique is simple to implement, and enhances model robustness by using a more diverse range of nodes rather than relying heavily on a few key ones.

Additionally, it is computationally efficient, as it reduces the workload during the backpropagation phase. The user can specify the percentage of dropout in each training iteration as an hyperparameter. An example of dropout is illustrated in Figure 39.

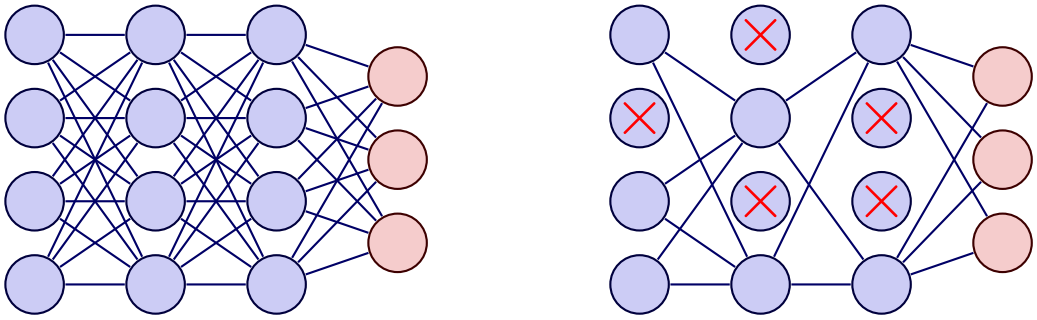

Figure 39: Schematic representation of the fully connected layers on the left hand-side, and a 40% dropout on the right hand-side. Inspired by [68]

5.4.7 *Dataset*

The act of making predictions appears to be a simple endeavor, as it involves a straightforward mapping of input to output. However, generating accurate predictions is a considerably more complex task. It is contingent upon the utilization of a precise training (and validation) dataset, which must be free of bias. Instances of biased datasets resulting in prediction failures are all too common.

The significance of data in the process of training machine learning and deep learning algorithms is often overlooked, despite its critical role. Training a neural network necessitates access to training data. Both supervised and unsupervised learning techniques require data, with supervised learning necessitating labeled data. Two approaches can be employed to obtain data: real-world measurements such as real images and spectra, which necessitate manual labelling by an expert for supervised learning, or data generated from simulations. The process of manually labelling measurements can prove to be time-consuming, particularly when attempting to achieve an adequate quantity of training examples. Collaboration with multiple experts or entities may prove to be an effective means of addressing such challenges. In contrast, the simulation of datasets necessitates the development of a physical or mathematical representation of the data. While this approach may not be applicable in every scenario, when feasible, it allows for the rapid generation of labeled datasets. When simulated, many learning algorithms benefit from standardisation of the data where the distribution is centered at zero and the standard deviation is fixed, such that they can be scaled while keeping their properties. It is important that datasets possess a uniform distribution, as the over-representation of a particular parameter or group of parameters may result in inaccurate predictions.

6

PHOSPHORUS SPECTROSCOPIC ANALYSIS WITH DEEP LEARNING

"A process cannot be understood by stopping it. Understanding must move with the flow of the process, must join it and flow with it."

- Frank Herbert, *Dune*

Contents

6.1 SUMMARY

Chapter 4 provided an introduction to phosphorus magnetic resonance spectroscopy, highlighting its potential for in-vivo probing of cellular metabolism as well as the challenges associated with a relatively lower sensitivity compared to the hydrogen atom at a given magnetic field. To compensate for the low sensitivity, larger voxels are used during acquisition, up to an order of magnitude higher, to achieve a satisfactory signal-to-noise ratio (SNR). The acquisition must also respect an acceptable scan time to avoid patient discomfort, which limits the number of measurable acquisition averages. Fitting algorithms, such as LCModel or AMARES, are traditionally used to analyze and quantify the measured spectra. Both algorithms rely on prior knowledge, in the form of a basis set of each resonance. AMARES utilizes prior knowledge based on high SNR spectra to fit low SNR spectra [71], while LCModel uses simulated spectra for its basis, utilizing known chemical shift and J-coupling [72]. Fitting methods iteratively fit all resonances along with the baseline until the difference between the fit and the data is minimized. The software tools perform non-linear optimization to fit the experimental data with a linear combination of reference basis spectra and to estimate various spectral parameters, including line shape, overlap, and chemical shift of the metabolites. However, fitting methods encounter challenges as they necessitate the individual analysis of all acquired spectra, which results in a significant computation time. The methods also suffers from reliable quantification at low SNR.

The utilization of artificial intelligence in the medical field has gained increasing attention, particularly in the field of magnetic resonance imaging [73]. The applications of deep learning have been proposed for the entire MRI workflow, from image acquisition [74–76], to image reconstruction [77–79], image restoration [80, 81], image registration [82, 83], and image segmentation [84, 85]. Among the deep learning methods, convolutional neural networks (CNNs) have been widely used due to their ability to learn useful representations for image-oriented tasks. The field of magnetic resonance spectroscopy has also seen the emergence of artificial intelligence techniques, such as machine learning decision trees [86] and CNNs for spectral quantification [87] where Hatami et al. utilized a simple physical model to develop a regression framework for evaluating spectral parameters using proton spectroscopy.

The present study addresses the challenges encountered in phosphorus spectroscopy by investigating the application of deep learning methods, specifically convolutional neural networks, for analyzing phosphorus spectroscopic data. This research is detailed in our article 6.2. Two different CNN architectures, namely LeNet5 [88] and U-Net [89], were employed in the study. To train the model, we simulated 10^6 spectra using the physical model of resonances [36]. The simulated spectra were assigned labelled spectral parameters, including 0^{th} and 1^{st} order phases, chemical shift, frequency shift, line width, baseline, and SNR, as well as metabolic concentration for each resonance. The former model was developed to evaluate the parameters and metabolic concentration, while the latter was used to evaluate the baseline. Furthermore, we proposed a reconstruction pipeline that utilized the physical model from the simulation, together with the evaluated parameters from the CNN, to reconstruct the spectra. The analysis was performed without measuring a reference signal, and as such, absolute quantification was not feasible. LCModel was used as a reference for comparison in the analysis. The proposed ^{31}P-Spectral Analysis With Neural Networks (31P-SPAWNN) demonstrated high accuracy and robustness, particularly at low SNR levels, enabling high-resolution reconstruction with an extremely rapid computation time.

Received: 20 April 2022 | Revised: 16 August 2022 | Accepted: 18 August 2022

DOI: 10.1002/mrm.29446

RESEARCH ARTICLE

Magnetic Resonance in Medicine

In vivo magnetic resonance ^{31}P-Spectral Analysis With Neural Networks: 31P-SPAWNN

Julien Songeon[1] | **Sébastien Courvoisier**[1,2] | **Lijing Xin**[2,3] | **Thomas Agius**[4] | **Oscar Dabrowski**[1] | **Alban Longchamp**[4] | **François Lazeyras**[1,2] | **Antoine Klauser**[1,2]

[1]Department of Radiology and Medical Informatics, University of Geneva, Geneva, Switzerland

[2]CIBM Center for Biomedical Imaging, Geneva, Switzerland

[3]Animal Imaging and Technology, Ecole Polytechnique Fédérale de Lausanne (EPFL), Lausanne, Switzerland

[4]Department of Vascular Surgery, Centre Hospitalier Universitaire Vaudois and University of Lausanne, Lausanne, Switzerland

Correspondence
Julien Songeon, Département De Radiologie Et Informatique Médicale, University Hospitals Geneva, Rue Gabrielle-Perret-Gentil 4, 1211 Geneva, Switzerland.
Email: julien.songeon@unige.ch

Funding information
Schweizerischer Nationalfonds zur Förderung der Wissenschaftlichen Forschung, Grant/Award Number: 320030_182658

Purpose: We have introduced an artificial intelligence framework, 31P-SPAWNN, in order to fully analyze phosphorus-31 (^{31}P) magnetic resonance spectra. The flexibility and speed of the technique rival traditional least-square fitting methods, with the performance of the two approaches, are compared in this work.

Theory and Methods: Convolutional neural network architectures have been proposed for the analysis and quantification of ^{31}P-spectroscopy. The generation of training and test data using a fully parameterized model is presented herein. In vivo unlocalized free induction decay and three-dimensional ^{31}P-magnetic resonance spectroscopy imaging data were acquired from healthy volunteers before being quantified using either 31P-SPAWNN or traditional least-square fitting techniques.

Results: The presented experiment has demonstrated both the reliability and accuracy of 31P-SPAWNN for estimating metabolite concentrations and spectral parameters. Simulated test data showed improved quantification using 31P-SPAWNN compared with LCModel. In vivo data analysis revealed higher accuracy at low signal-to-noise ratio using 31P-SPAWNN, yet with equivalent precision. Processing time using 31P-SPAWNN can be further shortened up to two orders of magnitude.

Conclusion: The accuracy, reliability, and computational speed of the method open new perspectives for integrating these applications in a clinical setting.

KEYWORDS

convolutional neural network, deep learning, in vivo, LCModel, phosphorus magnetic resonance spectroscopy

1 | INTRODUCTION

Phosphorus-31 magnetic resonance spectroscopy (^{31}P-MRS) is a noninvasive technique that is widely used to probe cellular metabolism in vivo.[1,2] ^{31}P-MRS notably allows to measure high-energy phosphate metabolites that are associated with the metabolic activity of the cell, and represents an alternative method for estimating the intracellular pH.[3-5] ^{31}P-MRS acquisition displays a lower relative sensitivity than hydrogen-1 (^{1}H) at a constant magnetic field.[6] Thus, acquisition is usually performed using larger voxel sizes to achieve a sufficient signal-to-noise ratio (SNR), while maintaining an acceptable scan time for the patient. When performed in combination with spatial phase encoding, ^{31}P-MRS imaging (MRSI) provides a multi-voxels acquisition that maps metabolites across the entire field-of-view (FOV).[7] As the current resolution is still a limitation for clinical applications, there has been increasing interest in achieving efficient quantification, while improving the spatial resolution.[8-10]

In recent decades, advances in computing power and parallelization capability have resulted in the rapid development of a wide variety of machine learning algorithms. These performance improvements along with the renewed interest in the field have broadened its scope of application.[11] One popular deep learning (DL) technique has so far been the convolutional neural network (CNN). CNNs are employed to detect and extract structural relationship features from data samples. This general characteristic is used for many applications, including visual and speech recognition, localization, segmentation, and general regression analysis, as well as classification.[12] The method requires a labeled training dataset that must be representative of the actual data to be analyzed. For some applications, the labeled dataset can be generated by simulation so as to create a training set of arbitrary size. Once trained, the CNN model is able to process large datasets within a short time without further adjustments.[13]

The widely used method of reference in this field, LCModel, is an a priori knowledge software for MRS fitting and quantification. The software performs a nonlinear optimization in order to fit the data with a linear combination of reference basis spectra, as well as to estimate spectral parameters, including line shape, phase, and chemical shift of the metabolites. However, the method requires non-negligible computing time and may thus be limited in quantifying low SNR spectra.[14] While the software has been originally developed to fit ^{1}H[15] spectra, researchers were able to extend its use further in order to analyze carbon-13 (^{13}C)[16] and ^{31}P[17] spectra.

CNNs are increasingly employed for medical image analysis such as MRI.[18-21] Preliminary application of machine learning[14,22] and CNN[23-26] in proton MRSI revealed high robustness to noise. In addition, CNNs can be applied in order to perform concentration quantification.[23] Application of CNN to ^{1}H-MRS has demonstrated this method to display equal or better level of performance, while having a faster computational time than current standard MRS metabolites quantification methods like LCModel.[24]

Whereas current methods for estimating metabolite concentration in MRS primarily rely on spectral fitting with residual least-square minimization, we have herein proposed an alternative approach using 31P-SPAWNN. Its objective function is based on residual minimization of the spectra parameters (i.e., metabolite concentrations). A spectrum can be reconstructed based on these estimates, which must, however, not be confused with a spectrum fitting.

Using our proposed 31P-SPAWNN method, we have demonstrated its feasibility and reliability in accurately quantifying ^{31}P-MRS related metabolite concentrations and spectral parameters, even at low SNR, obtained on both simulated and in vivo data. The current study describes SPAWNN's architecture, and the generation of simulated datasets for supervised learning, as well as the reconstruction based on the physical model for comparison with fitted spectra. A performance evaluation is provided based on a comparison of our model with LCModel using simulated datasets. Lastly, we present the results using our proposed technique on the ^{31}P-MRS in vivo and brain data acquired on a 3 tesla (T) clinical MRI.

2 | THEORY

2.1 | Generation of simulated spectra

The simulation of spectra must incorporate an extensive set of parameters in order to faithfully mimic the measured MRS spectra. The signal of a metabolite is the combination of multiple resonance modes, $M_m(t)$, based on the NMR parameters observed in vitro.[27] The complex magnetization of a molecule of metabolite m at time t after an excitation RF pulse can be calculated based on the expected value of the spin-raising operator for the corresponding coupled-spin system[28(p. 158-165)]

$$M_m(t) = \sum_{n}^{\text{modes}} A_{m,n} \cdot e^{i\phi_{m,n}} e^{2\pi i t \psi_{m,n}}, \tag{1}$$

where n is the transition index between energy states within the density matrix formalism, which we refer to as "mode". $A_{m,n}$ is the transition amplitude, $\phi_{m,n}$ the phase modulation (e.g., due to J-coupling), $\psi_{m,n}$ the transition frequency (chemical shift) of the n^{th} mode, and i is the

imaginary unit. A mode corresponds to a singlet resonance or one of the multiplet resonances observed in the frequency domain, such as the phosphocreatine (PCr) singlet, the α-adenosine triphosphate (ATP) doublet, or the β-ATP triplet. The spectroscopic signal (FID) $S_j(t)$ of a sample is a linear combination of all the metabolite time domain signals. A spectrum of index j versus time can be written as follows

$$S_j(t) = e^{i\Phi_j^0} \sum_{m}^{\text{metabolites}} C_{m,j} M_m(t + \Delta t_j) \cdot e^{2\pi i t \Psi_{m,j}} e^{-(tL_{m,j} + t^2 G_{m,j}^2)} + B_j(\Delta t_j) + \epsilon_j(t), \quad (2)$$

where Φ_j^0 is the zeroth-order phase and $C_{m,j}$ is the concentration of the m^{th} metabolite, which multiplies the corresponding $M_m(t)$ metabolite time series signal. $\Psi_{m,j}$ corresponds to the chemical shift variation specific to the m^{th} metabolite. In the context of an excite–acquire acquisition scheme (FID-MRS, FID-MRSI), Δt_j represents the acquisition delay time between the RF pulse and the beginning of the signal acquisition. This delay is associated with the first-order phase of the spectrum. $L_{m,j}$ and $G_{m,j}$ correspond to the Lorentzian and Gaussian parameters that combine into a Voigt linewidth $V_{m,j}$. $\epsilon_j(t)$ is the noise, while $B_j(t)$ is a baseline created by the sum of multiple Gaussian components, computed as follows

$$B_j(t) = \sum_{k}^{\text{no. of Gaussian components}} \xi_k \cdot e^{i\alpha_k} e^{2\pi i t \beta_k} e^{-t^2 \gamma_k^2}, \quad (3)$$

where ξ_k is the amplitude, α_k is the zero-order phase, β_k is the frequency shift, and γ_k is the width of one component. The time domain signal $S_j(t)$ is finally Fourier transformed in order to obtain the simulated spectrum used as input for either the SPAWNN or LCModel approaches that are described below.

2.2 | Convolutional neural networks architectures

For our proposed SPAWNN method, we have combined two different CNN models, one being a variant of a LeNet-5 model[29] and the other being based on a U-Net model.[30]

LeNet-5, which is one of the most common neural network models, is widely used for classification and regression.[31] LeNet-based CNNs have been applied in the spectroscopy field.[25,32,33] The model consists of consecutive convolution layers that encode the data into features, and it is terminated by fully connected layers. Each convolution layer convolves the output of the previous layer using different filters, while extracting at each step higher-level features and patterns.[34] Fully connected layers enable nonlinear relationships between features and extraction of targeted information. This SPAWNN-Quantification (SPAWNN-Q) model takes the Fourier transform of $S_j(t)$ from Equation (2) as input, and it returns a finite number of target values. Our proposed approach uses the SPAWNN-Q model in order to estimate the metabolite concentrations, as well as the values of spectral parameters like Φ_j^0 or Δt_j from Equation (2).

The U-Net combines both low-level detail information and high-level semantic information.[35] This type of model that is mainly used for segmentation purposes[30] finds applications in MRS.[36,37] The model has been successfully applied to medical image classification, segmentation, and detection tasks.[38] The U-Net type model's architecture is first composed of an encoding part, and then of a decoding part. The contracting part uses a series of convolutional and down-sampling layers to extract information in features, while the expanding part then performs a series of up-sampling in order to recover the initial input's dimension.[30] At each up-scaling step, the U-Net performs a concatenation between the upscaled layer and the corresponding layer of the contracting part, allowing for higher resolution and less encoded information to be mixed in the subsequent decoding. Our SPAWNN-Baseline (SPAWNN-Bl) U-Net model estimates the baseline, taking as input the Fourier transform of $S_j(t)$ from Equation (2) and returning the estimated baseline $B_j(t)$ from Equation (3).

3 | METHODS

3.1 | Spectra simulation and training dataset

The following metabolites have been included in the simulated spectra: phosphocreatine (PCr), inorganic phosphate (Pi), membrane phospholipids (MP), adenosine triphosphate (α-ATP, β-ATP, and γ-ATP), and nicotinamide adenine dinucleotide (NAD+ and NADH). In addition, the phosphomonoesters (PME), composed of phosphocholine (PC) and phosphoethanolamine (PE), and the phosphodiesters (PDE), composed of glycerophosphocholine (GPC) and glycerophosphoethanolamine (GPE), were also included. Spectra were simulated with this 12-metabolite set, as previously described in the theory section. The resulting dataset consisted of 10^6 simulated spectra for training, 10^4 simulated spectra for validation, and 10^4 simulated spectra for testing. Generating the training dataset took 1.5 h. The generated spectra were set to reproduce the experimental conditions at a 3T field strength, using spectra made from discrete time series of 2048 points with a dwell time of 0.25 ms, corresponding to a 4000 Hz

bandwidth ranging from −40 to 40 ppm centered at the PCr resonance.

The structural modes of each metabolite multiplet were calculated by means of a density matrix simulation using GAMMA software library, including ^{31}P-^{31}P J-coupling (J_{PP}) as appropriate, while yielding the mode amplitude, the resonance frequency and the phase according to Equation (1).[39] Homonuclear values of J_{PP} were found using the previously reported values of chemical shift and J-coupling.[17] Each metabolite time series was then multiplied by a concentration value C_m chosen following a normal distribution with a mean value of 1 and a standard deviation of 5, and taking account of its absolute value so as to impose positive concentration values.

Each Fourier transform $S_j(t)$ of the Equation (2) was generated from randomly chosen parameters. The following parameters were chosen using a uniform probability distribution: $\Phi^0 \in [0, 2\pi]$ rad, $\Delta t \in [0, 0.6]$ ms, and $\Psi \in [-20, 20]$ Hz. Each of the metabolites was chemically shifted within a range of ±16 Hz, in addition to the chemical shift Ψ of the spectrum. The Voigt linewidth was set between 1 and 80 Hz, before being decomposed into a Lorentzian L coefficient and a Gaussian G coefficient. Given that the B_0 inhomogeneity was the same for all metabolites, the linewidth was assumed to reflect a T2 effect, so PCh, PE, GPE, and GPC were grouped with the same linewidth coefficients values. ATPs were grouped together, as were NAD+ and NADH, while Pi, PCr, and MP all displayed their independent T2 values. The value of $\phi_{m,n}$ turned out to be negligible and was thus set to zero as our data were acquired with an excite–acquire sequence.

The baseline B was a sum of 30 Gaussian components. Each Gaussian function exhibited four random parameters, chosen with a uniform probability distribution. The amplitude ranged from 0 to the spectrum's maximum amplitude. The Gaussian displayed the zero-order phase between 0 rad and 2π rad, along with a frequency shift to cover the spectrum's 80 ppm range, and a linewidth with a minimum value of 300 Hz. The noise ϵ was simulated as a complex white noise, exhibiting a normal distribution centered around zero, and with a scaled deviation to the metabolite spectrum's energy so as to reach SNR values between 0.5 and 20. SNR was therefore defined as the ratio metabolite signals' mean value to the standard deviation of the noise. As all metabolites contributed to the SNR in our definition, we labeled SNR_{mean} for SPAWNN. This definition was useful upon developing the neural network for generating noise in the simulated dataset with the broad metabolite concentration variation.

The neural network was trained using a generated data set with specific parameter ranges, including spectrum frequency shift, metabolite chemical shifts, and linewidth. A trained network was then be able to accurately estimate these parameters within the simulation ranges. For example, given that the range of metabolite chemical shifts was between −16 and +16 Hz, the neural network's estimation in an in vivo spectrum is anticipated to be accurate, provided that the actual metabolite chemical shifts are within this range.

3.2 | Convolutional neural network

All the networks were trained on 10^6 simulated spectra. The regression loss function was calculated based on the mean squared error (MSE) function, and we used Adam as an optimized gradient descent algorithm.[40] Figure 1 illustrates the flowchart of our method with the input data preparation and the different neural networks. The CNNs were trained on spectra ranging from 10 to −25 ppm, corresponding to the in vivo metabolites chemical shifts range. With a resolution of 25.6 points/ppm, the frequency windowing of the spectrum corresponded to an array of 899 complex points. Prior to the input, each spectrum was normalized with respect to its energy, following which complex values were represented by two-channel arrays of 899 points.

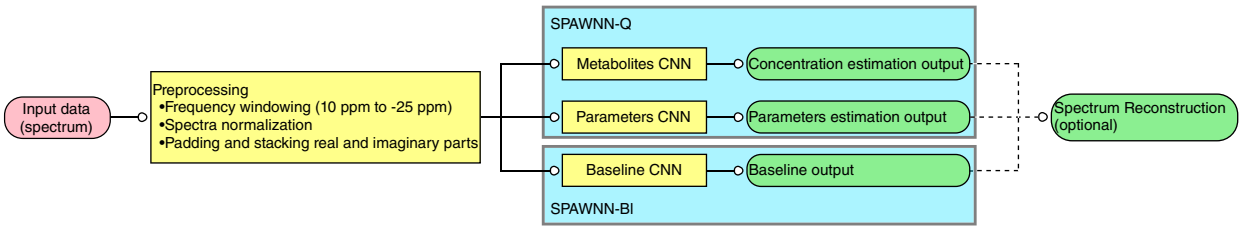

FIGURE 1 Data analysis flowchart illustrating the different steps of the Spectral Analysis With Neural Networks (SPAWNN) pipeline. The method uses three convolutional neural networks (CNN) to estimate the metabolite concentrations, spectrum parameters, and baseline. Data preparation consists of spectrum normalization, with windowing over the range of 10 to −25 ppm. Padding (mirror replication of the first and last 5 points of the array) and stacking of the real and imaginary parts (switch from a complex array of 1×899 points to a real array of 2×909 points by separating the real and complex part of each point) were then applied.

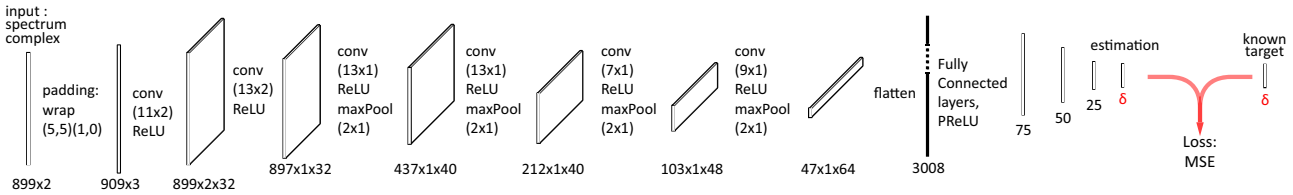

FIGURE 2 SPAWNN-Quantification (SPAWNN-Q) model architecture for metabolite concentration and parameter estimation. The convolutional neural network takes the spectrum as an input layer and performs six successive steps of convolution, ReLU activation, and pooling. Then, the five final steps are fully connected layers with PReLU activation. δ is equal to 20 for the parameters, and 14 for the metabolite concentration estimations.

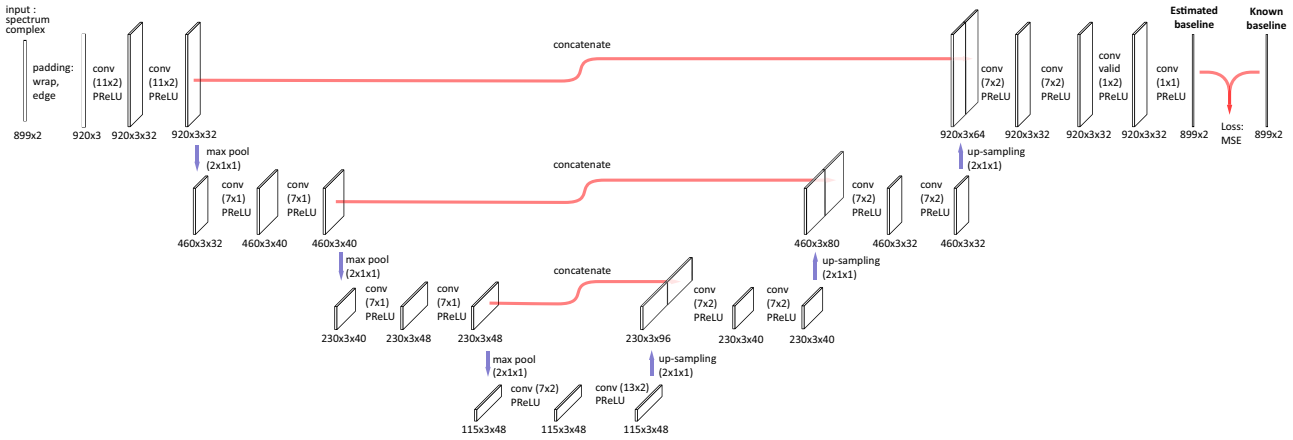

FIGURE 3 SPAWNN-Baseline (SPAWNN-Bl) model architecture for baseline estimation. The U-Net takes the spectrum as an input layer and performs three down-sampling steps with convolution and PReLU activation. Then, it performs three up-scaling steps with convolution and PReLU activation. At each up-scaling, the new layer is concatenated with the corresponding down-sampling layer. The output is the estimation of the baseline and has the same dimension as the input.

The first two CNNs, which were inspired by a LeNet-5 model, were designed to assess metabolite concentration quantification and parameter estimation, as shown in Figure 2, with a network's output represented by δ, as the number of targeted values returned by SPAWNN. For the metabolite concentration estimation, SPAWNN was trained to estimate the concentration of the 12 metabolites listed in section (III.A), along with adding the sum of PMEs and PDEs, whereby the metabolite concentration estimation returned 14 values. The second CNN was trained to estimate the values of 28 spectral parameters, including zero-order phase, time delay, spectrum frequency shift, metabolite chemical shifts, Voigt linewidths, Gaussian linewidths, and SNR_{mean}. The Lorentzian linewidths were then calculated with the Voigt and Gaussian values using the pseudo-Voigt approximation.[41] The CNNs were implemented in Python (3.6.9) using the libraries TensorFlow (2.2.2) and Keras (2.4.3). The networks were trained on 80 epochs with 800 spectra per mini-batch. There were about $3 \cdot 10^5$ parameters to train, with the training time taking less than 2 h on the GPU (NVIDIA Titan V).

The third network was a U-Net model, as shown in Figure 3. The network was able to estimate the input spectrum's baseline, returning an array of the same size (899 complex points). The U-Net was trained on 50 epochs with 500 spectra per mini-batch. There were about $4 \cdot 10^5$ parameters to train, with the training time taking around 6 h.

3.3 | LCModel

As reference for comparison, we have analyzed all ^{31}P-spectra using LCModel (Version 6.3-1L).[42] The basis spectra were simulated using the GAMMA software library[39] using the same physical model as for the simulated data for SPAWNN. The metabolites included in the basis were the 12 metabolites described above. Since phosphorus spectra were centered on the PCr peak at 0ppm,

the reference peak was set at 15 ppm (PPMK = −15) for generating the basis set. The basis was created using a fixed linewidth of 5 Hz, with the LCModel parameters: DEEXT2 = 15 and DESDT2 = 10. For LCModel fitting, Pi and γ-ATP were chosen as reference metabolites, resulting in the following parameters: CHUSE1 = 'Pi','gATP' and PPMREF(1,2) = 5. We set SDDEGP = 50 and SDDEGZ = 50 to enable LCModel to find the correct zero- and first-order phases. The other parameters used were the same as those reported by Deelchand et al.[17]

3.4 | Magnetic resonance spectroscopy protocol

In vivo measurements were performed on a clinical Prisma-fit 3T MRI scanner (Siemens Healthineers, Erlangen, Germany) equipped with multinuclear capabilities. Data were obtained from 10 healthy volunteers. Written informed consent was given by all the volunteers before participation and the study protocol was approved by the institutional ethics committee. No decoupling was applied during the phosphorus acquisition. Anatomical reference ^{1}H images were obtained with T1-weighted MP-RAGE acquisition. The volunteers were scanned using a dual-tuned ^{1}H and ^{31}P head coil (Clinical MR solutions, Brookfield, Wi.)

The unlocalized FID sequence consisted of a rectangular excitation pulse of 0.25 ms with a flip angle of 45°. The repetition time (TR) was set at 1500 ms, and the echo time (TE) was 0.35 ms with 32 averages. The bandwidth was 4000 Hz for 2048 sampling points. The acquisition took about 1 min. For three volunteers out of 10, another unlocalized FID was obtained using the same parameters, yet with 600 averages.

The 3D ^{31}P-MRSI was acquired on the whole brain with a $10 \times 10 \times 10$ matrix. The FOV dimension was 250 mm isotropic for a nominal spatial resolution of 25 mm isotropic. The sequence consisted of a rectangular excitation pulse of 0.25 ms with a flip angle of 45°. The repetition time (TR) was set at 1500 ms, and the echo time (TE) was 0.5 ms with 24 weighted averages.[43] The bandwidth was 4000 Hz for 2048 sampling points. The acquisition took 37 min.

3.5 | Spectrum processing

The in vivo FID data were extracted from the MRI raw data format. Averages and Fourier transforms were calculated using a Python script (Python Software Foundation, version 3.6.9), and the data were converted to Hierarchical Data Format (HDF5). No preprocessing was applied to the spectra prior to analysis.

3.6 | Data analysis and statistic

The results estimated on the simulated dataset were analyzed using the coefficient of determination R^2.[44] To compute the variability of the coefficient of determination, bootstrap statistics was performed on the data.[45] The bootstrapping was performed by selecting randomly spectrum subsets with replacement and repeated computation of R^2 on these subsets. This evaluation was repeated 2000 times in order to compute the probability distribution of R^2.

Concerning volunteer data, no reference measurement was available to correct for variation of B1 and signal intensity, allowing absolute concentration estimation. Both methods, LCModel and SPAWNN, returned normalized concentration values that were within a constant, yet unknown, factor of the actual concentration value. The results were presented and analyzed as metabolite concentration ratios, since the ratio of two metabolites is independent of the scaling factor.[46]

The computational analysis was performed using Python.

4 | RESULTS

Results of simulated data are shown in Figure 4. An example of a simulated spectrum with three decreasing SNR_{mean} (no noise added, 4, 2) is presented in panel (A). For illustration purposes, the simulated spectra shown in the figure do not contain baselines, phase or frequency shifts, and significant linewidth. Panel (B) illustrates the performance of SPAWNN and LCModel with the coefficient of determination R^2 and bootstrapping. The performance was assessed on another test set of 10^4 spectra that were independent of the training dataset and never evaluated by the model before. The bootstrap statistics was computed using random spectra subset selection with replacement and repetition of the analysis 2000 times. The results showed similar to slightly better performance of SPAWNN compared with LCModel for the quantifying Pi, ATPs, PCr, PE, PCh, and GPE, with similar or higher R^2 values and smaller variance. Since LCModel displayed strong pairwise correlations between NAD+ and NADH, the total NAD (tNAD) concentration was computed for both methods for comparison purposes. The performance of SPAWNN in quantifying tNAD ($R^2 = 0.813$ [±0.005]) was comparable to that of other metabolites, whereas the results of LCModel were less accurate ($R^2 = 0.771$ [±0.006]). GPC concentration was

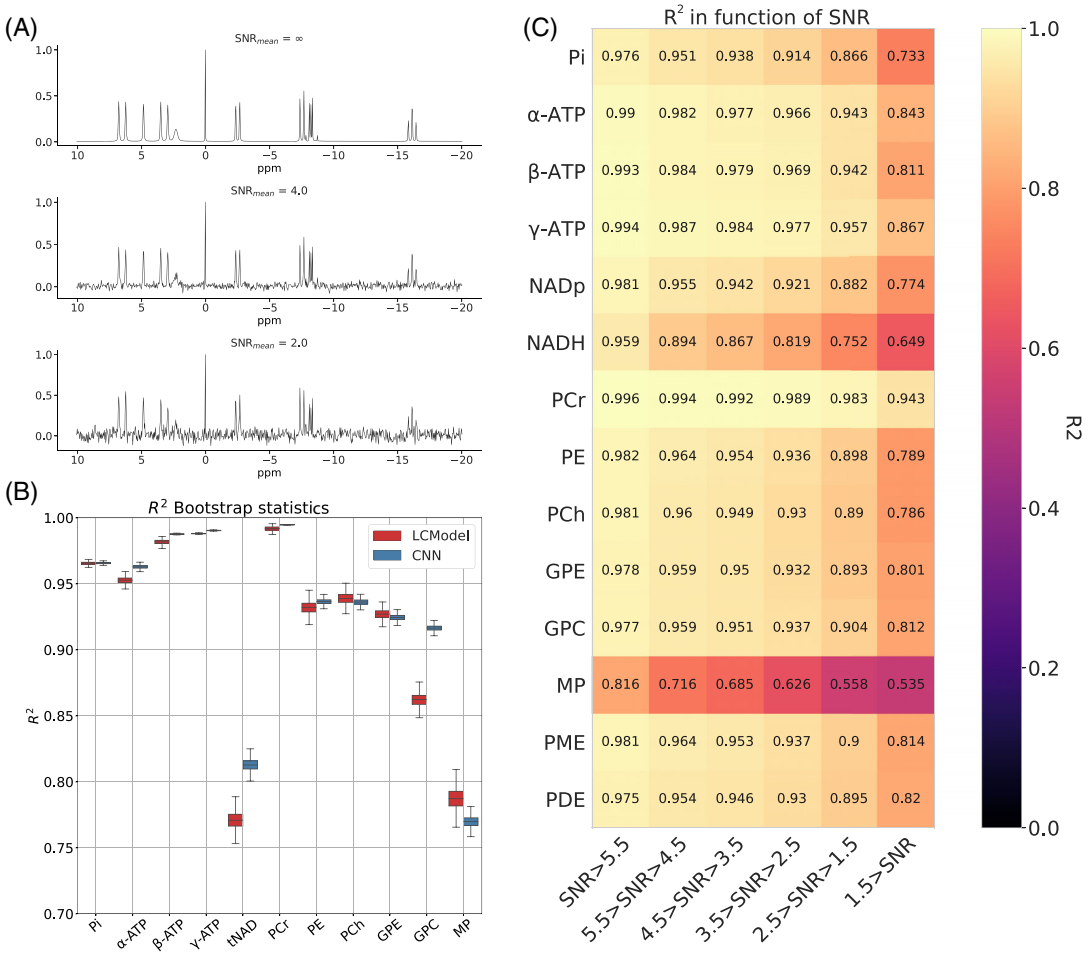

FIGURE 4 Results on simulated data. (A) Examples of SNR_{mean} for a simulated spectrum with no noise (top), SNR_{mean} of 4 (middle), and SNR_{mean} of 2 (bottom). (B) Comparison of the coefficient of determination R^2 with bootstrapping between SPAWNN and LCModel for each metabolite. A new dataset of 10^4 spectra was created to compare the two methods. (C) SPAWNN's coefficient of determination R^2 for each metabolite concentration estimation as a function of the SNR_{mean} range.

better estimated with SPAWNN ($R^2 = 0.916$ [± 0.002]) than LCModel ($R^2 = 0.862$ [± 0.005]). Regarding MP estimation, both SPWANN ($R^2 = 0.770$ [± 0.004]) and LCModel ($R^2 = 0.787$ [± 0.008]) exhibited a low performance compared with all other metabolites, regardless of SNR bins (Figure 4C). Figure 4C shows the SPAWNN's coefficient of determination R^2 for each metabolite concentration estimation as a function of SNR range. The evaluation was performed on the simulated test dataset of 10^4 spectra, separated in SNR bins with increment of 1. The coefficient of determination R^2 was computed on the entire test dataset between the model evaluation concentration and the ground truth. For all the metabolites, the value of the coefficient of determination decreased with SNR. Most metabolites had an R^2 value greater than 0.8 for all SNR bins. SPAWNN-Bl evaluation of the test set baseline yielded a coefficient of determination of $R^2 = 0.97$ calculated between the pairwise correlation of the true baseline and the estimated baseline.

Analyzed ^{31}P-MRSI in vivo data are shown in Figure 5 for SPAWNN (left) and LCModel (right). The data displayed are the sum of 8 voxels from the occipital cortex of one of the volunteers. The top plots are the spectra with either the reconstruction or the fit from each model. The middle plots are the residuals and the bottom plots show the signals for each metabolite separately. For SPAWNN, reconstruction of a spectrum was performed by using the estimated baseline, parameters, and concentration values, and by recreating the spectrum after Fourier transform of equation (2). The reconstructed spectrum is shown in red overlapping the in vivo data.

Comparative analysis of the metabolite concentration ratio between LCModel and SPAWNN is displayed in Figure 6. The results were derived from the sum of 8 MRSI voxels located in the occipital region for each of the 10 volunteers. The mean value of α-ATP, β-ATP, and γ-ATP was computed and reported as ATP. The concentration of PCr

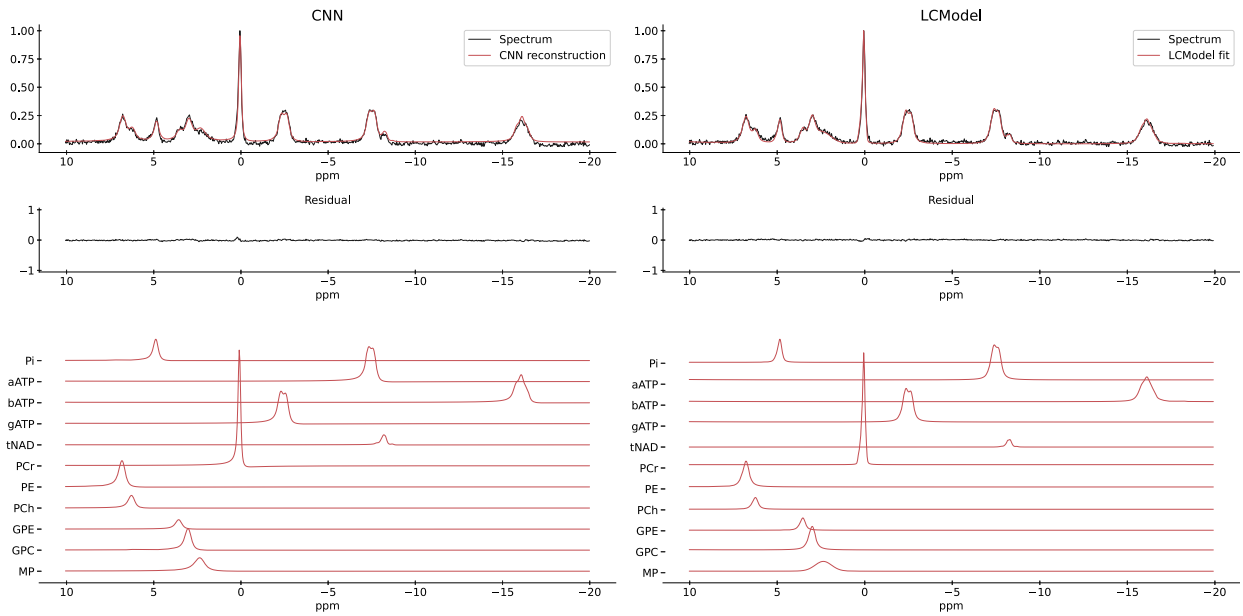

FIGURE 5 Comparison of in vivo ^{31}P-MRSI spectrum (TR = 1.5 s, TE = 0.5 ms, sum of 8 voxels with 24 weighted averages each) evaluated and reconstructed with SPAWNN (left) and fitted with LCModel (right). The figure displays SPAWNN reconstruction and the LCModel fit (top), the residuals (middle), and the contribution of each metabolite (bottom). No correction was applied before analysis.

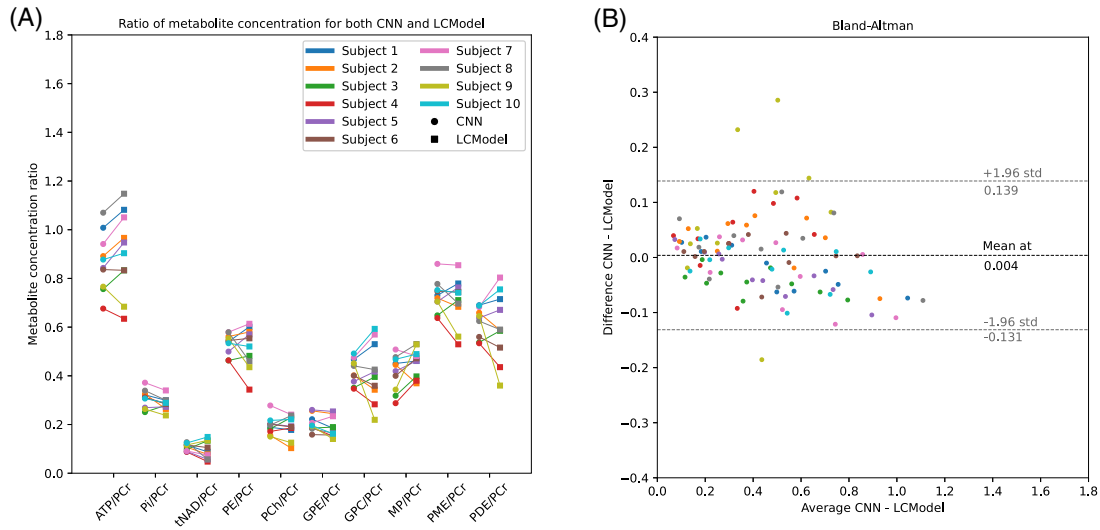

FIGURE 6 Results on ^{31}P-MRSI data, with the sum on 8 voxels. (A) Comparison of metabolite concentration ratios for the 10 volunteers with SPAWNN (circles) and LCModel (squares). ATP concentration is computed by averaging the concentration of the three resonances. (B) Bland–Altman plot of the difference between estimated values by SPAWNN and LCModel versus the average of the estimated values across all metabolite ratios and subjects.

was used as denominator for the ratios. Figure 6A shows a plot of the metabolite concentration ratio estimated by SPAWNN and LCModel, with a line connecting the data of the same subject. Figure 6B shows a Bland–Altman plot of the data from Figure 6C, with the difference between the SPAWNN and LCModel estimations versus the average of the two values. The mean difference between the two methods is $4.0 \cdot 10^{-3}$, and the limits of agreements ($\pm 1.96\sigma$) are +0.139 and −0.131. The Bland–Altman plot shows few outliers, but no systematic bias. Relative differences and relative standard deviations are presented in Table 1. A statistical *t*-test with Bonferroni correction was performed, and the *p*-values are reported in the table as well. The Bonferroni correction took into account the

TABLE 1 Statistics of the comparison of the metabolic concentration ratio for the 10 volunteers with SPAWNN and LCModel from Figure 6

Metabolite ratio	Relative difference (%)	Relative standard deviation (%)	*p*-value (uncorrected)
ATP/PCr	−4.69	6.93	0.073
Pi/PCr	7.37	7.68	0.018
tNAD/PCr	14.8	31.1	0.19
PE/PCr	3.0	13.6	0.53
PCh/PCr	2.16	15.5	0.68
GPE/PCr	8.36	11.4	0.055
GPC/PCr	1.63	11.3	0.83
MP/PCr	−10.4	15.5	0.075
PME/PCr	3.0	9.4	0.36
PDE/PCr	3.9	17.6	0.52

Note: Statistical *t*-test was performed with Bonferroni correction for multiple comparisons resulting in a lower threshold for rejecting the null hypothesis to $\alpha = 0.0056$. No difference in metabolite ratios was found to be significant.

repeated *t*-tests (10 metabolites) and reduced the threshold for rejecting the null hypothesis to $\alpha = 0.0056$. The metabolite ratios showed relative differences lower than 10% for most of the ratios, except for tNAD/PCr and MP/PCr. All metabolite ratios had a relative standard deviation higher than the relative differences, with none found to be significant.

Figure 7 illustrates the quantification performance of SPAWNN and LCModel with respect to noise. The data used were unlocalized FIDs with 600 averages acquired on three volunteers. The 600 spectra acquired were randomly selected retrospectively and averaged in groups ranging from 1 to 600 spectra. We considered the reference values to be the values estimated with 600 averages. The convergence was then defined as the difference between the mean value of the estimations and the reference value, with precision representing the standard deviation of the reference value. Figure 7 presents the results for the γ-ATP, PCr, PE, PCh, GPC, and GPE. The two spikes in Subject #3 originate from an LCModel fatal error where the model failed to converge.

Analysis of single voxels from in vivo ^{31}P-MRSI with the two methods is shown in Figure 8. The SPAWNN spectrum reconstruction from two distinct brain voxels is displayed. The T1 MP-RAGE ^{1}H image is presented on the left; the grid shows the voxel locations in the sagittal view (top) and the corresponding axial slice (bottom) centered on the blue box location. The analysis of voxel A and B with SPAWNN and LCModel is shown on the right. Each spectrum is presented with either the reconstruction or the fit, with the residual underneath. The estimated SNR_{mean} for the spectra were 1.56 and 1.63, and the LCModel SNRs were 16 and 20 for voxels A and B, respectively.

5 | DISCUSSION

This study demonstrated the ability of SPAWNN to evaluate, quantify, and reconstruct ^{31}P-MRS data. We focused on two network architectures specifically developed to fully identify spectral features of MRS data. SPAWNN-Q, displayed in Figure 2, was used to extract the metabolite concentrations and spectral parameters. We used two separate networks running in parallel for efficiency and flexibility, which also allowed for a better control of the training phase during model development. However, a single LeNet for both concentration and parameters estimation was tested and yielded similar results. SPAWNN-Q parameter network can be applied to MRSI data for phases and frequency shift correction in order to sum individual spectra before complete quantification. SPAWNN-Bl (Figure 3) was used for spectral baseline estimation.

Our synthetic dataset was simulated by summing independent metabolite signals. However, ATP was simulated as three independent resonances for γ-, α-, and β-ATP, thereby rendering the network more flexible in estimating concentration as well as chemical shift. The reason for this choice was that other metabolites, such as adenosine diphosphate (ADP), may overlap with γ- and α-ATP and influence the estimated concentration. In addition, three ATP resonances were shown to exhibit different chemical shifts with varying concentrations of Mg^{2+}.[47] However, our physical model assumed the same linewidth for the three ATP resonances because of their identical T2 relaxation times. SPAWNN results demonstrated a high performance on simulated datasets as well as on in vivo data (Figures 4 and 6). This indicates that our simulation model (equation (2)) is a good emulation of the physical NMR signal and faithfully represents the measured spectra using excite–acquire sequences. The SPAWNN evaluations presented in Figures 5 and 8 show the reconstruction of the spectra and illustrate the ability of SPAWNN to provide a good estimation of the spectral parameters, concentrations, and baseline, as the reconstructions matched the spectra. Artificial intelligence (AI) approaches, such as CNN, perform accurately if the measured parameters are in the range of the training set. For specific applications, it might be possible to train the network with a smaller range of concentrations to possibly achieve better performance. One could imagine having a specialized model for each organ, with the concentration distribution centered on the values reported in the literature. However, training

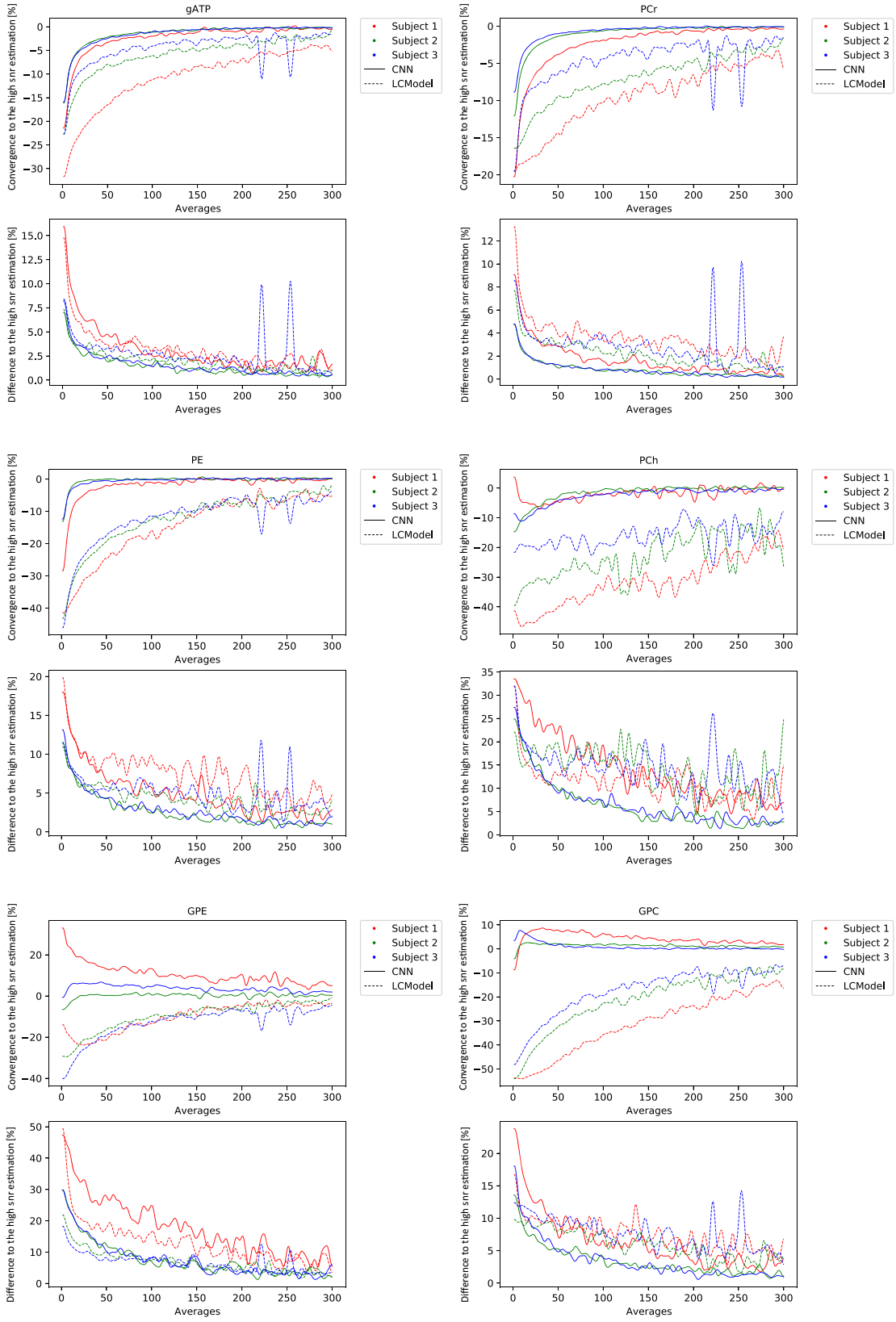

FIGURE 7 Results from unlocalized FID data of the occipital lobe. Comparison of metabolite concentration estimation by SPAWNN and LCModel. The reference value is the estimate obtained with the average of the full acquisition (600 spectra). The plots show the convergence and the difference in estimation of each model with respect to the highest SNR estimate.

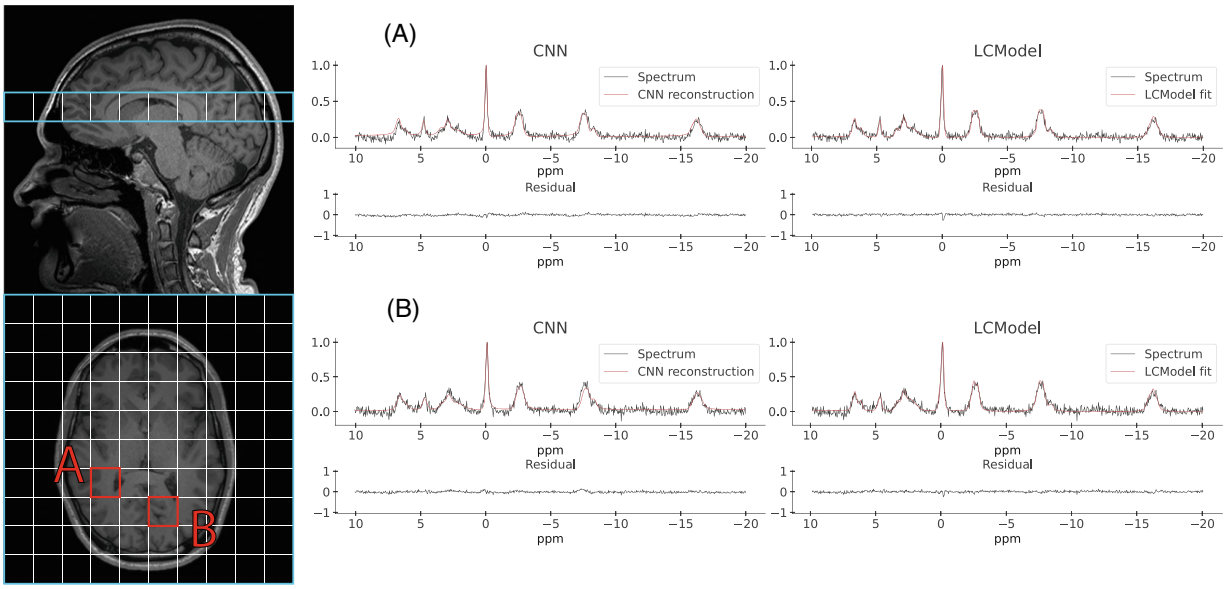

FIGURE 8 Examples of SPAWNN evaluation of a 3D ^{31}P-MRSI acquired on a human brain. The figure shows two spectra (TR = 1.5 s, TE = 0.5 ms, 24 weighted averages) arising from two brain regions. The T1 MP-RAGE ^{1}H MRI is displayed on the left, indicating the slice position and voxel locations. The voxel has a resolution of 25 mm isotropic. The spectra on the left represent the SPAWNN reconstruction with the measurement data, and the spectra on the right the LCModel fitting for voxels A and B.

with a narrower parameter distribution could induce a bias in the analysis of specific conditions or pathologies that strongly affects the metabolism. Moreover, in a situation where data are acquired with parameters outside the training range (e.g., strong artifact), the results of the analysis should be discarded. The spectral reconstruction based on estimates is an important tool to visually validate whether the neural network estimate matches the in vivo spectrum, in which case the results should be discarded. In this study, we chose to train the networks over a very wide range of parameter values to avoid this limitation. This wide range does not compromise the quantification accuracy while avoiding bias.

On the simulated data, SPAWNN compared favorably to LCModel in terms of precision. The coefficient of determination R^2 per metabolites, as a whole, was similar for both approaches (Figure 4B). Of the 11 metabolites, only three significantly differed between the two methods. SPAWNN performed better for tNAD and GPC, while LCModel showed better performance on MP. NAD+ and NADH can be accurately estimated with LCModel at 7T,[48] due to the higher signal and greater chemical shift dispersion. By contrast, at 3T without proton decoupling, the distinction between NAD+ and NADH is more difficult, as illustrated by the results where tNAD was estimated with the least accuracy. MPs were also estimated with low accuracy by both SPAWNN and LCModel. This is due to the larger peak width that makes the distinction between the baseline and noise difficult. Figure 4B shows that with bootstrap statistics, the standard deviation of the coefficient of determination of the LCModel was larger than that of SPAWNN for all metabolites. In addition, SPAWNN estimates remained accurate ($R^2 > 0.8$) for most metabolites at a very low SNR (Figure 4C), highlighting the robustness of the method.

In vivo data (Figures 5 and 8) showed that SPAWNN can estimate the spectral parameters with good accuracy, since the reconstruction of the spectra based on these estimates closely matched the measured data. An example of analysis with both methods for a volunteer is presented in Figure 5. The data were obtained by summing 8 neighbor voxels in the occipital region. By contrast, an analysis with both methods for singles voxels of the volunteer data is shown in Figure 8. The individual signals of each metabolite as estimated by SPAWNN and LCModel are displayed in Figures 5 and 8. The two methods showed consistent signal for each metabolite. The residuals are low with both approaches but nevertheless slightly higher with SPAWNN. This is explained by the fact that LCModel is a fitting algorithm while SPAWNN does not aim at minimizing the residuals. Figure 6 presents the concentration ratio values of the metabolites obtained on 8 averaged voxels from the occipital region of each subject. The results are in very good agreement with the values reported using PCr as internal reference.[46,49,50] The Bland–Altman plot shows that the mean difference of the two methods was much smaller than the standard deviation and demonstrates the absence of bias. The outlier points in Subject #9 could be explained by poor B0 homogeneity during the acquisition. By contrast, Subject #7 was the one with

the best B0 homogeneity and showed close estimation with both methods. Table 1 reveals that all relative standard deviations were greater than the relative differences, indicating that inter-subject variation was greater than between-method variation.

Figure 7 shows the convergence toward the estimated value at high SNR by SPAWNN and LCModel. The data originate from unlocalized FID with 600 averages acquired from three volunteers. Unlocalized FID was used instead of MRSI in order to get optimum SNR with reasonable acquisition duration considering 600 averages. The plots aim to present the convergence of both models toward the reference value estimated at the highest SNR, corresponding to the spectra obtained with 600 averages. For high-signal metabolites, such as PCr and ATPs, both models displayed similar speed of convergence. For lower-signal metabolites, such as PCh and GPC, the estimation with LCModel differed by more than 10% from the high SNR value even with high numbers of averages. SPAWNN showed faster asymptotic convergence toward the concentration reference. Both SPAWNN and LCModel demonstrated similar precisions, with more variation across subjects than across methods. Spectra from Subject #1 had more noise and half lower SNR compared with the other two subjects, which can be due to worst shimming. The discontinuities observed in Subject #2 are attributable to LCModel failure to converge ("fatal errors") and were considered as outliers. Over all the metabolites, SPAWNN displayed more consistency and stability, especially at low SNR. This result suggests that the SPAWNN approach is more robust at low SNR than LCModel, thus implying a fewer number of averages to match the results of traditional fitting methods. This could translate into shorter acquisition time in a clinical setting or higher reconstruction resolution for MRSI.

SPAWNN training time was 4 and 6 h for the two submodels. Nevertheless, once the weights were computed, spectral analysis with SPAWNN was almost instantaneous. Indeed, the evaluation of 10^5 spectra required approximately 5 min. This could be useful in the prospect of applying the method to 3D metabolite mapping, which requires the analysis of the full dataset. As illustrated in Figure 8, the 10^3 voxels of the dataset were analyzed in a few minutes, whereas the same analysis performed by LCModel lasted almost 1 h. Faster computing time is a clear advantage for clinical applications where a fast online processing is highly desired.

Our study results compared with those of previously published works that used neural network approaches to analyze MRS.[14,23,24] Das et al.[14] presented a method using random forest machine learning, while Hatami et al.[23] used a DL CNN model for quantification. Compared with both methods, the physical model proposed here for generating the simulated training set includes a larger number of parameters, which should result in a more complete variety of spectra, as well as artifacts and distortions, as observed in vivo. The approach proposed by Lee et al.[24] aimed to learn the reconstruction of the spectral real part, while ours aimed to learn the metabolite concentration and parameters directly, without optimized reconstruction. Other studies used a different approach to applying AI to NMR, such as the one conducted by Da-Wei et al.[51] who used a neural network approach to perform deconvolution on overlapping peaks.

The analysis was performed without measuring a reference signal, with therefore no possibility of absolute quantification, and LCModel was used as a fair reference for comparison of metabolite ratios. In a possible perspective, both models could be compared for absolute quantification with the measurement of an in vitro reference with a known concentration. The influence of the training parameter ranges over SPAWNN robustness and stability remains to be established. As mentioned above, narrow specific parameter ranges might improve accuracy but SPAWNN results would be unreliable for spectral parameters falling outside the training range. Possible improvements of SPAWNN can be explored: the physical model could notably be improved by taking into account more distortions, such as eddy current effects. Future developments also include implementing SPAWNN for metabolite mapping and determining a confidence interval for the estimated values.

In conclusion, we presented a DL method of evaluation, quantification, and baseline estimation for ^{31}P-MRS, combined with a reconstruction pipeline for spectral reconstruction. The proposed SPAWNN method had a high accuracy and robustness overall, especially at low SNR, thereby allowing higher resolution reconstruction in MRSI schemes. Our proposed approach had an extremely fast computation time that offers the ability to analyze large ^{31}P-MRSI datasets almost instantaneously, which is a significant advantage for possible applications in a clinical setting.

ACKNOWLEDGMENTS

This study was supported by the Swiss National Science Foundation (320030_182658). We gratefully acknowledge NVIDIA Corporation for the donation of the Titan V GPU used for this research. Open access funding provided by Universite de Geneve.

DATA AVAILABILITY STATEMENT

The source code for the proposed 31P-SPAWNN model can be downloaded from this link: https://gitlab.unige.ch/Julien.Songeon/31P-SPAWNN.

ORCID

Julien Songeon https://orcid.org/0000-0001-8760-6862
Lijing Xin https://orcid.org/0000-0002-5450-6109
Antoine Klauser https://orcid.org/0000-0003-3019-9914

REFERENCES

1. Reto B, Dieter M, Ernst M, Peter B. Assessment of absolute metabolite concentrations in human tissue by 31P MRS in vivo part II: muscle, liver, kidney. *Magn Reson Med*. 1994;32:453-458.
2. Chmelik M, Schmid A, Gruber S, et al. Three-dimensional high-resolution magnetic resonance spectroscopic imaging for absolute quantification of 31P metabolites in human liver. *Magn Reson Med*. 2008;60:796-802.
3. Webb Graham A, ed. Methods and applications of phosphorus NMR spectroscopy in vivo. *Annual Reports on NMR Spectroscopy*. Vol 75. Academic Press; 2012.
4. Jong-Hee H, Soo CC. Use of in vivo magnetic resonance spectroscopy for studying metabolic diseases. *Exp Mol Med*. 2015;47:e139.
5. Rudin M, ed. *In-Vivo Magnetic Resonance Spectroscopy III: In-Vivo MR Spectroscopy: Potential and Limitations*. Springer Berlin Heidelberg; 1992.
6. Boulangé CL. Nuclear magnetic resonance spectroscopy-applicable elements| Phosphorus-31. *Reference Module in Chemistry, Molecular Sciences and Chemical Engineering*. Elsevier; 2017.
7. Maudsley AA, Hilal SK, Perman WH, Simon HE. Spatially resolved high resolution spectroscopy by "four-dimensional" NMR. *J Magn Reson*. 1983;51:147-152.
8. Thulborn KR, Atkinson IC. Quantitative metabolic magnetic resonance imaging of sodium, oxygen, phosphorus and potassium in the human brain. *Magnetic Resonance Spectroscopy*. Elsevier; 2014:291-311.
9. Hongyan Q, Xiaoliang Z, Zhu X-H, Fei D, Wei C. In vivo 31P MRS of human brain at high/ultrahigh fields: a quantitative comparison of NMR detection sensitivity and spectral resolution between 4T and 7T. *Magn Reson Imaging*. 2006;24:1281-1286.
10. Ladislav V, Marek C, Martin M, et al. Dynamic31P-MRSI using spiral spectroscopic imaging can map mitochondrial capacity in muscles of the human calf during plantar flexion exercise at 7T. *NMR Biomed*. 2016;29:1825-1834.
11. Goldenberg S, Larry NG, Salcudean Septimiu E. A new era: artificial intelligence and machine learning in prostate cancer. *Nat Rev Urol*. 2019;16:391-403.
12. Scott K. Feature learning and deep learning architecture survey. *Computer Vision Metrics: Textbook Edition*. Springer International Publishing; 2016:375-514.
13. Jinchao L, Margarita O, Lorna A, Michael F, Solomon Christopher J, Gibson Stuart J. Deep convolutional neural networks for Raman spectrum recognition: a unified solution. *Analyst*. 2017;142:4067-4074.
14. Dhritiman D, Eduardo C, Schulte Rolf F, Menze Bjoern H. Quantification of metabolites in magnetic resonance spectroscopic imaging using machine learning. *Medical Image Computing and Computer Assisted Intervention - MICCAI 2017*. Springer International Publishing; 2017:462-470.
15. Provencher S. Automatic quantitation of localized in vivo 1H spectra with LCModel. *NMR Biomed*. 2001;14:260-264.
16. Pierre-Gilles H, Gülin Ö, Stephen P, Rolf G. Toward dynamic isotopomer analysis in the rat brain in vivo: automatic quantitation of 13C NMR spectra using LCModel. *NMR Biomed*. 2003;16:400-412.
17. Kumar DD, Tra-My N, Xiao-Hong Z, Fanny M, Pierre-Gilles H. Quantification of in vivo 31P NMR brain spectra using LCModel. *NMR Biomed*. 2015;28:633-641.
18. Selvikvåg LA, Arvid L. An overview of deep learning in medical imaging focusing on MRI. *Z Med Phys*. 2019;29:102-127.
19. Singh SP, Lipo W, Sukrit G, Haveesh G, Parasuraman P, Balázs G. 3D deep learning on medical images: a review arXiv e-prints, arXiv:2004.00218.
20. Marina C, Simone S, Francesco S. Trimboli Rubina Manuela. Artificial intelligence for breast MRI in 2008–2018: a systematic mapping review. *Am J Roentgenol*. 2019;212:280-292.
21. Aurélien B, Niccolo F, Botnar René M, Claudia P. From compressed-sensing to artificial intelligence-based cardiac MRI reconstruction. *Front Cardiovascular Med*. 2020;7:17.
22. Fan L, Yudu L, Guo R, Bryan C, Zhi-Pei L. Ultrafast magnetic resonance spectroscopic imaging using SPICE with learned subspaces. *Magn Reson Med*. 2019;83:377-390.
23. Nima H, Michaël S, Hélène R. Magnetic resonance spectroscopy quantification using deep learning. *Medical Image Computing and Computer Assisted Intervention – MICCAI 2018*. Springer International Publishing; 2018:467-475.
24. Hun LH, Hyeonjin K. Deep learning-based target metabolite isolation and big data-driven measurement uncertainty estimation in proton magnetic resonance spectroscopy of the brain. *Magn Reson Med*. 2020;84:1689-1706.
25. Fan L, Yahang L, Xi P. Constrained magnetic resonance spectroscopic imaging by learning nonlinear low-dimensional models. *IEEE Trans Med Imaging*. 2020;39:545-555.
26. Courvoisier S, Klauser A, Lazeyras F. High-resolution magnetic resonance spectroscopic imaging quantification by convolutional neural network. Proceedings of the 2019 Annual Meeting of the International Society for Magnetic Resonance in Medicine (ISMRM). 2019; 27: 0519.
27. Varanavasi G, Karl Y, Maudsley Andrew A. Proton NMR chemical shifts and coupling constants for brain metabolites. *NMR Biomed*. 2000;13:129-153.
28. Ernst RR, Bodenhausen G, Wokaun A. *Principles of Nuclear Magnetic Resonance in One and Two Dimensions*. Vol 7. Wiley; 1988:158-165.
29. Lecun Y, Bottou L, Bengio Y, Haffner P. Gradient-based learning applied to document recognition. *Proc IEEE*. 1998;86:2278-2324.
30. Olaf R, Philipp F, Thomas B. U-net: convolutional networks for biomedical image segmentation. *LNCS*. 2015;9351: 234-241.
31. Bhargab BM, Dinthisrang D, Khwairakpam A, Debdatta K. Handwritten character recognition from images using CNN-ECOC. *Procedia Comput Sci*. 2020;167:2403-2409.
32. Shengnan C, Heng Z, Yang X, et al. Raman spectroscopy reveals abnormal changes in the urine composition of prostate cancer: an application of an intelligent diagnostic model with a deep learning algorithm. *Adv Intel Syst*. 2021;3:2000090.
33. Dicheng C, Wang Z, Guo D, Vladislav O, Xiaobo Q. Review and prospect: deep learning in nuclear magnetic resonance spectroscopy. arXiv e-prints, arXiv:2001.04813.
34. Albawi S., Mohammed T.A. and Al-Zawi S. Understanding of a convolutional neural network. Proceedings of the

2017 International Conference on Engineering and Technology (ICET), 2017, pp. 1-6.
35. Zhang Z, Liu Q, Wang Y. Road extraction by deep residual U-net. *IEEE Geosci Remote Sens Lett*. 2018;15:749-753.
36. Zohaib I, Dan N, Albert TM, Steve J. Deep learning can accelerate and quantify simulated localized correlated spectroscopy. *Sci Rep*. 2021;11:8727.
37. Kyathanahally SP, Döring A, Kreis R. Deep learning approaches for detection and removal of ghosting artifacts in MR spectroscopy. *Magn Reson Med*. 2018;80:851-863.
38. Zahangir AM, Chris Y, Mahmudul H, Taha Tarek M, Asari Vijayan K. Recurrent residual U-net for medical image segmentation. *J Med Imag*. 2019;6:1.
39. Smith SA, Levante TO, Meier BH, Ernst RR. Computer simulations in magnetic resonance. An object-oriented programming approach. *J Magn Reson A*. 1994;106:75-105.
40. Kingma DP, Jimmy B. ADAM: a method for stochastic optimizationarXiv e-prints, arXiv:1412.6980. 2014.
41. Ida T, Ando M, Toraya H. Extended pseudo-Voigt function for approximating the Voigt profile. *J Appl Crystallogr*. 2000;33:1311-1316.
42. Provencher Stephen W. Estimation of metabolite concentrations from localized in-vivo proton NMR spectra. *Magn Reson Med*. 1993;30:672-679.
43. Rolf P, Markus K. Accurate phosphorus metabolite images of the human heart by 3D acquisition-weighted CSI. *Magn Reson Med*. 2001;45:817-826.
44. Davide C, Warrens Matthijs J, Giuseppe J. The coefficient of determination R-squared is more informative than SMAPE, MAE, MAPE, MSE and RMSE in regression analysis evaluation. *Pee rJ Comput Sci*. 2021;7:e623.
45. Efron B. Bootstrap methods: another look at the Jackknife. *Anna Stat*. 1979;7:1-26.
46. Andreas R, Ruth S, Stephanie M, et al. Energy metabolis measured by 31P magnetic resonance spectroscopy in the healthy human brain. *J Neuroradiol*. 2022.
47. Gout E, Rebeille F, Douce R, Bligny R. Interplay of mg^{2+}, ADP, and ATP in the cytosol and mitochondria: unravelling the role of mg^{2+} in cell respiration. *Proc Natl Acad Sci U S A*. 2014;111:E4560-E4567.
48. Xin L, Ipek Ö, Beaumont M, et al. Nutritional ketosis increases NAD+/NADH ratio in healthy human brain: an in vivo study by 31P-MRS. *Front Nutr*. 2018;5:62.
49. Jensen J, Eric DDJ, Menon Ravi S, Williamson Peter C. In vivo brain 31P-MRS: measuring the phospholipid resonances at 4 tesla from small voxels. *NMR Biomed*. 2002;15:338-347.
50. Jimin R, Dean SA. Malloy Craig R. 31P-MRS of healthy human brain: ATP synthesis, metabolite concentrations, pH, and T1 relaxation times. *NMR Biomed*. 2015;28:1455-1462.
51. Da-Wei L, Hansen Alexandar L, Chunhua Y, Lei B-L, Rafael B. DEEP picker is a DEEP neural network for accurate deconvolution of complex two-dimensional NMR spectra. *Nat Commun*. 2021;12:5229.

How to cite this article: Songeon J, Courvoisier S, Xin L, et al. In vivo magnetic resonance ^{31}P-Spectral Analysis With Neural Networks: 31P-SPAWNN. *Magn Reson Med*. 2022;1-14. doi: 10.1002/mrm.29446

Part III

ACCELERATED ACQUISITION AND RECONSTRUCTION TECHNIQUES: COMPRESS SENSING AND LOW RANK

7

IMAGING RECONSTRUCTION

"Physicists have come to realize that mathematics, when used with sufficient care, is a proven pathway to truth."

- Brian Greene, *The Fabric of the Cosmos*

Contents

7.1 INTRODUCTION

Chapter 3 presents the fundamental mathematical principles of MRI. The chapter explains how the signal is generated in a coil by an electromotive force induced by the magnetic field variation in the sample. In Section 3.4.2, the Fourier transform is introduced as a mathematical approach to transform the signal data $s(k)$ into the spin density distribution $\rho(x)$. The signal is presented as the Fourier transform of the spin density, and an inverse Fourier transform can recover the spin density distribution. The transformation is performed by integrating the signal over the three-dimensional volume of interest, and the results appear straightforward to obtain. However, as Brian Cox and Jeff Forshaw have emphasized in The Quantum Universe: *"Translating the mathematics of quantum mechanics into the real-world context of an experiment is not always straightforward"*. The analog signal generated by MRI is continuous, but it is sampled and stored as finite and digitized data. The measurement involves a finite amount of point collection in k-space. Therefore, it is critical for the data to be acquired in such a way that they can be transformed by Fourier analysis to recover the spin density distribution.

Fourier transform has largely contributed to the success of MRI; however, the uniform sampling of k-space and periodic spacing between points can restrict data acquisition. These constraints, coupled with other limitations, can result in lengthy acquisition times, which can be impractical for patients. Consequently, the total measurement time is limited. To address this issue, various methods have been proposed to accelerate data acquisition and reduce image reconstruction time. Notable examples include echo-planar spectroscopic imaging (EPSI) [90, 91], parallel imaging [92–94], and compressed sensing (CS) [95].

This chapter serves as an introduction to the materials necessary to understand the contents of Chapter 8. The first section provides an overview of Fourier transformations, while the second section delves into the acceleration and reconstruction techniques used, with a specific emphasis on compressed sensing acceleration and low-rank reconstruction methods.

7.2 FOURIER TRANSFORMS AND K-SPACE SAMPLING

7.2.1 *Fourier transforms and discretization of the sampling*

Fourier transform is a powerful mathematical tool, which underpins the success of MRI. The fourier transform hastily been presented in Section 3.4.2, specifically in the equation (3.40). For this chapter, we will reduce to a one dimensional situation. The generalization to the two and three dimensions is straightforward. The spin density lives in the x-space (the position space), while the signal lives in the k-space (the spatial-frequency space). The general form of the Fourier transform (FT) can be written as

$$s(k) = \mathcal{F}\{\rho\}(k) \tag{7.1}$$
$$= \int_{-\infty}^{\infty} \rho(x) \cdot e^{-2\pi i k \cdot x} dx \tag{7.2}$$

And its inverse function, the inverse Fourier transform (IFT) is

$$\rho(x) = \mathcal{F}^{-1}\{s\}(x) \tag{7.3}$$
$$= \int_{-\infty}^{\infty} s(k) \cdot e^{+2\pi i k \cdot x} dk \tag{7.4}$$

The application of the Fourier transform on its inverse is a self-identity operation. It results in the retrieval of the initial function due to the integral of the exponential leading to a Dirac delta function in either space. While the aforementioned representation of the Fourier transform is widely used, there are alternative forms of the transform that differ in the absence of the 2π factor in the exponential and the presence of a normalization factor in front of the integral.

The DC component in a Fourier transform represents the constant part of the signal, which can be seen as the average value of the signal. It is represented by the zero frequency term in the Fourier series.

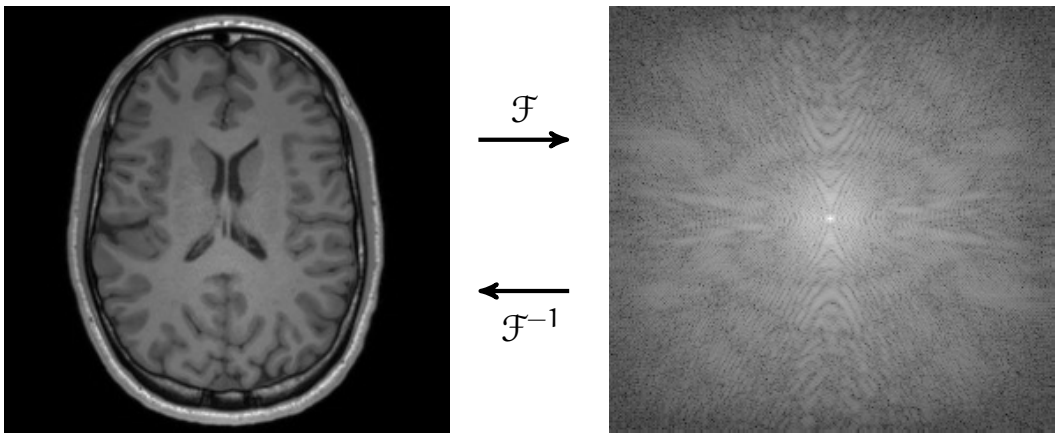

Figure 40: Illustration of the Fourier transform and its inverse applied to a brain slice in the transverse plane. The image on the left represents the original brain slice, while the image on the right shows its Fourier transform. The values in the Fourier transform image have been logarithmically scaled to visualize the non-DC components, as the DC component has a very high value that makes the non-DC components appear black.

As outlined in the opening section of this chapter, the signal emitted by the sample in the coil cannot be recorded as a continuous function, and is instead measured at a finite number of points. Due to the discrete nature of the sampling process, differences can arise between the physical spin density $\rho(x)$ and the reconstructed MR image $\hat{\rho}(x)$. These differences may be attributable to errors in data acquisition or signal processing, and are generally referred to as

artifacts. In some cases, differences may arise due to complex values being acquired when the expected image is purely real, resulting in a constant phase difference with the real density spin. Such artifacts may manifest as a linear phase when points are shifted in the k-space. To avoid dependence on phases, a common practice is to compute the magnitude of the reconstructed image. In order to describe the discrete sampling, the Dirac comb distribution can be utilized as a sampling function. This distribution, and its Fourier transform, are defined as follows.

$$\mathrm{III}_T(k) = T \sum_{p=-\infty}^{\infty} \delta(k - pT) \tag{7.5}$$

$$\mathcal{F}^{-1}\{\mathrm{III}_T\}(x) = \frac{1}{T} \cdot \mathrm{III}_{\frac{1}{T}}(x) \tag{7.6}$$

This distribution is defined in such a way that its product with a continuous function is zero everywhere except at the points where the function is sampled. The Fourier transform of the comb distribution is also a sampling function. It can be obtained using the two following relationship.

$$\sum_{n=-\infty}^{\infty} e^{+2\pi i n a} = \sum_{n=-\infty}^{\infty} \delta(a - n) \tag{7.7}$$

$$\delta(ax) = \frac{1}{|a|}\delta(x) \quad \Rightarrow \quad |a|\delta(x) = \delta\left(\frac{x}{|a|}\right) \tag{7.8}$$

The first relation, expressed in equation (7.7), defines a relationship of the delta form of the Dirac comb and its representation as a Fourier series. The second relation, given in equation (7.8), defines one of the identities of the delta distribution. Consequently, the sampled signal can be expressed as the product of the continuous function and the Dirac comb distribution.

$$s_{\mathrm{III}}(k) = s(k) \cdot \mathrm{III}_{\Delta k}(k) \tag{7.9}$$

$$= \Delta k \sum_{p=-\infty}^{\infty} s(p\Delta k) \cdot \delta(k - p\Delta k) \tag{7.10}$$

The reconstruction of the spin density from the sampled signal $s_{\mathrm{III}}(k)$ can be achieved by computing the inverse Fourier transform.

$$\hat{\rho}(x) = \mathcal{F}^{-1}\{s_{\mathrm{III}}\}(x) \tag{7.11}$$

$$= \int_{-\infty}^{\infty} \Delta k \sum_{p=-\infty}^{\infty} s(p\Delta k) \cdot \delta(k - p\Delta k) \cdot e^{+2\pi i k \cdot x} dx \tag{7.12}$$

$$= \Delta k \sum_{p=-\infty}^{\infty} s(p\Delta k) \cdot e^{+2\pi i p \Delta k \cdot x} \tag{7.13}$$

The spin density reconstructed from the sampled signal can be represented as an infinite Fourier series, which serves as an approximation of the continuous function in the form of a histogram. To express the reconstructed spin density in terms of the physical spin density, we can use the convolution theorem which states that the Fourier transform of a product is the convolution of the Fourier transforms of the individual functions, i.e., $\mathcal{F}\{g \cdot h\}(x) = G(k) * H(k)$. We can apply this theorem directly to equation (7.9) to obtain the following equation.

$$\hat{\rho}(x) = \left(\mathcal{F}^{-1}\{s\} * \mathcal{F}^{-1}\{\mathrm{III}_{\Delta k}\}\right)(x) \tag{7.14}$$

$$= \rho(x) * \frac{1}{\Delta k}\mathrm{III}_{\frac{1}{\Delta k}}(x) \tag{7.15}$$

$$= \sum_{q=-\infty}^{\infty} \rho\left(x - \frac{q}{\Delta k}\right) \tag{7.16}$$

The result presents a translation invariance with the transformation $x \to x + q/\Delta k$. The reconstructed function is expressed as an infinite repetition of spin distributions uniformly spaced at intervals of $1/\Delta k$. It is noteworthy that the interval value represents the field of view, such that $1/\Delta k = \mathrm{FOV}$.

7.2.2 *Nyquist-Shannon sampling criterion*

The field of view is an important aspect in imaging. If the field of view is chosen to be too small in comparison to the size of the imaged object, the reconstructions will overlap and result in an aliasing artifact in the reconstructed image. For ease of notation, we define the spatial length of the scanned image as $L = \mathrm{FOV}$ and the size of the object being analyzed as A. To avoid aliasing, the Nyquist-Shannon criterion dictates that the field of view must be larger than the size of the imaged object, that is, $L > A$ or equivalently $\Delta k < 1/A$. The criterion dictates the choice of sampling intervals. In equation (3.37), a relationship was established between the spatial frequency k and the applied gradients. During sampling in the read direction, data points are acquired at time intervals of Δt while a gradient G_R is applied, resulting in intervals of Δk_R given by:

$$\Delta k_R = \gamma \int_t^{t+\Delta t} G_R(t')dt' \tag{7.17}$$

When considering a rectangular gradient, the integral yields $\Delta k_R = \gamma G_R \Delta t$. To satisfy the Nyquist criterion, we must have $\gamma G_R \Delta t = 1/L_R$, where L_R denotes the length of the region of interest in the read direction. Consequently, the sampling frequency for a constant read gradient is $BW_{\mathrm{read}} = 1/\Delta t = \gamma G_R L_R$, subject to the condition that $\gamma G_R L_R > \gamma G_R A_R$. The criterion also applies for the phases encoding gradient, with τ_{PE} the duration of the phase encoding pulse.

$$\Delta k_{PE} = \gamma \int_t^{t+\tau_{PE}} \Delta G_{PE}(t')dt' \tag{7.18}$$

With the same rectangular gradient consideration, the intervals in the phase encoding direction are $\Delta k_{PE} = \gamma \Delta G_{PE} \tau_{PE}$.

7.2.3 *Discrete Fourier transform*

A special case of the continuous Fourier transform is the Discrete Fourier transform (DFT), which represents an exact Fourier transform of a set of uniformly spaced and finite points. Along with the DFT, the discrete inverse Fourier transform (DIFT) is also introduced, which is equivalent to the inverse Fourier transform. The DFT shares the same properties as the continuous FT described above. The MR acquisition of a finite number of points can be perceived as a truncation of the data or as a windowing operation. In a similar manner to the previous section, we can model the truncation using a function. The rectangular function, denoted as *rect*, is defined as follows:

The rectangular function is also known as the Heaviside Pi, or the boxcar function.

$$\text{rect}_p(k) = \begin{cases} 0, & \text{if } |k| > p/2 \\ 1/2, & \text{if } |k| = p/2 \\ 1, & \text{if } |k| < p/2 \end{cases} \tag{7.19}$$

The rectangular function possesses a Fourier transform which is $\mathcal{F}^{-1}\{\text{rect}_W\} = W \cdot \text{sinc}(Wx)$, with the normalized cardinal sine function $\text{sinc}(x) = {}^{\sin(\pi x)}/_{\pi x}$. By applying the rectangular function to the signal, the resulting expression of the signal can be obtained by multiplying equation (7.9) with the rectangular function:

The normalized sinc function has an integral value of 1 instead of π for the un-normalized function.

$$\begin{aligned} s_{III,W}(k) &= s(k) \cdot III_{\Delta k}(k) \cdot \text{rect}_W(k + {}^{\Delta k}/_2) && (7.20) \\ &= \Delta k \sum_{p=-N/2}^{N/2-1} s(p\Delta k) \cdot \delta(k - p\Delta k) && (7.21) \end{aligned}$$

The summation is no longer carried out to infinity; rather, it is now summed up to a total of N sampled points, which in turn defines the size of the window as $W = N\Delta k$. The rectangular function has an additional term, as shifting the points by ${}^{\Delta k}/_2$ leads to a symmetrical sampling in the k-space with respect to the origin. Similar to the previous section, the reconstructed spin density can be determined by performing the discrete inverse Fourier transform (DIFT) on the equation (7.20).

$$\begin{aligned} \hat{\rho}(x) &= \mathcal{F}^{-1}\{s_{III,W}\}(x) && (7.22) \\ &= \left(\mathcal{F}^{-1}\{s\} * \mathcal{F}^{-1}\{III_{\Delta k}\} * \mathcal{F}^{-1}\{\text{rect}_W(\cdot + {}^{\Delta k}/_2)\}\right)(x) && (7.23) \\ &= \rho(x) * \frac{1}{\Delta k} III_{\frac{1}{\Delta k}}(x) * \left(W \cdot \text{sinc}(Wx) \cdot e^{-\pi i x \Delta k}\right) && (7.24) \\ &= \sum_{p=-N/2}^{N/2-1} \rho\left(x - \frac{p}{\Delta k}\right) \cdot W \cdot \text{sinc}(Wx) \cdot e^{-\pi i x \Delta k} && (7.25) \\ &= \Delta k \sum_{p=-N/2}^{N/2-1} s(p\Delta k) \cdot e^{2\pi i p x \Delta k} && (7.26) \end{aligned}$$

The exponential term in equation (7.24) is a result of the half-point shift in the rectangular function. For ease of use, equation (7.25) has been simplified to equation (7.26), which will be beneficial in subsequent discussions. To establish a Fourier pair between the discrete signal and the spin density, the discrete spin density must be connected to its Fourier transform to establish a relationship with a signal using the DFT. The discretized spin density can be written as follow.

$$\begin{aligned} \rho_{III,L}(x) &= \hat{\rho}(x) \cdot III_{\Delta x}(x) \cdot \text{rect}_L(x + {}^{\Delta x}/_2) && (7.27) \\ &= \Delta x \sum_{q=-M/2}^{M/2-1} \hat{\rho}(q\Delta x) \cdot \delta(x - q\Delta x) && (7.28) \end{aligned}$$

There exists a relationship between the size of the field of view and the number of samples taken $L = M\Delta x$, which is analogous to the window of the signal. The Fourier transform of equation (7.28) is expressed as follows:

$$\hat{s}(k) = \mathcal{F}^{-1}\{\rho_{III,L}\}(k) \tag{7.29}$$

$$= \Delta x \sum_{q=-M/2}^{M/2-1} \hat{\rho}(q\Delta x) \cdot e^{-2\pi i q k \Delta x} \tag{7.30}$$

In order for the two sets s and $\hat{\rho}$ to form a discrete Fourier pair, they must have an equal number of points in both domains, i.e., $N = M$. By substituting equation (7.26) into equation (7.30) and vice versa, we obtain:

$$s(p\Delta k) = \Delta x \sum_{q=-N/2}^{N/2-1} \hat{\rho}(q\Delta x) \cdot e^{-\pi i q p/N} \tag{7.31}$$

$$\hat{\rho}(q\Delta x) = \Delta k \sum_{p=-N/2}^{N/2-1} s(p\Delta k) \cdot e^{+\pi i q p/N} \tag{7.32}$$

A final rewriting of these equations enables linking the Fourier pairs with the field of view L.

$$s(\frac{p}{L}) = \sum_{q=-N/2}^{N/2-1} \hat{\rho}(\frac{qL}{N}) \cdot e^{-2\pi i q p/N} \tag{7.33}$$

$$\hat{\rho}(\frac{qL}{N}) = \frac{1}{N} \sum_{p=-N/2}^{N/2-1} s(\frac{p}{L}) \cdot e^{+2\pi i q p/N} \tag{7.34}$$

The last equations represent the discrete Fourier pair describing the reconstructed spin density with the acquired signal. The normalization in the final equation arises from $1/N = \Delta k \Delta x$.

7.2.4 *Pointspread Function*

The Point Spread Function (PSF) describes the spatial resolution of the imaging system. The PSF is defined as the response of the system to a point source of signal, which would be the MR signal in this context, and describe the spread of the signal in space. The effect of the PSF reduces the sharpness and resolution of the image, making it more difficult to distinguish small details. In absence of filtering, the PSF is define as follow.

$$PSF = \left(\mathcal{F}^{-1}\{III_{\Delta k}\} * \mathcal{F}^{-1}\{rect_W\}\right)(x) \tag{7.35}$$

$$= \sum_{p=-N/2}^{N/2-1} e^{2\pi i p x \Delta k} \tag{7.36}$$

The impact of the PSF on the reconstructed spin density has been describe above. The PSF can be used to quantify the blur of the reconstructed image.

7.3 NON-FOURIER RECONSTRUCTION

The Fourier transform has been instrumental in the success of MRI. Since data are acquired in the k-space, the Fourier transform has been the reconstruction method of choice. This technique is unbiased of the acquisition scheme, but requires the complete sampling of the k-space and assumes that the data are band-limited to the acquired spatial frequencies. The technique also assumes that the Nyquist criterion is met in the sampling interval of the data; otherwise, it results in artefacts. Although the Fourier transform provide the best reconstruction when MRI satisfied its requirements, the constant improvement of methods has pushed these requirements to their limits. The acquisition speed is defined by the ability to traverse the k-space, limited by hardware capacity and the maximum amplitude that can be generated with the gradients, as well as the physiological limitation of peripheral nerve stimulation with rapid gradient switching. Furthermore, techniques such as MRSI require long scan times, necessitating multiple averages to achieve sufficient SNR. These limitations have led to a different approach, where fewer measurements are acquired and the full k-space is not sampled. The Fourier transform is inadequate for reconstruction since zero-filling the missing points will not change the sub-Nyquist nature of the data that will produce artefacts. Novel methods are required to face this challenge and reconstruct these data.

7.3.1 *Model-based*

The measurement of the MR signal involves acquiring noisy samples of the signal [96]. Mathematically, the MR signal s can be expressed as a linear mapping encoding $\mathcal{A}$ of the input function f. However, in practice, the measured signal $\tilde{s}$ is a combination of the signal s and noise η. Hence, the emitted signal and the measured signal can be mathematically formulated as follows.

$$\begin{aligned} s &= \mathcal{A}\{f\} && (7.37)\\ \tilde{s} &= s + \eta && (7.38)\\ &= \mathcal{A}\{f\} + \eta && (7.39) \end{aligned}$$

The noise η in MR signal measurements is an additive complex, zero-mean, temporally white Gaussian noise. The primary objective of reconstruction is to generate a function $\hat{f}$ from the measured signal $\tilde{s}$ that accurately represents the original function f. One commonly employed approach to achieve this objective is through the utilization of least square residual minimization, which involves minimizing the sum of the squared difference between the acquired signal and the acquisition model prediction. Mathematically, the least-squares method is defined as:

$$\hat{f} = \arg\min_{f} \|\tilde{s} - \mathcal{A}\{f\}\|_{L^2}^2 \quad (7.40)$$

The least-squares method is a statistical technique that seeks to obtain the optimal solution for a linear equation. This method employs the L^2 norm, which is appropriate for the optimization problem because it is quadratic in the error terms. This quadratic property results in a convex optimization problem. Considering the discretization of the sampling process, the optimization problem can be formulated in a vector form. Specifically, the input vector $\mathbf{x} \in \mathbb{C}^N$, the measured signal $\tilde{\mathbf{s}} \in \mathbb{C}^M$, and the mapping $\mathbf{A} \in \mathbb{C}^{M \times N}$ can be represented in this form. The optimization problem can now be formulated as follow.

$$\hat{\mathbf{x}} = \arg\min_{\mathbf{x}} \|\tilde{\mathbf{s}} - \mathbf{A}\mathbf{x}\|_{l_2}^2 \quad (7.41)$$

The norm has been replaced with the pseudo-norm in the equation (7.41) with the discretization.

The equation (7.41) admits as solution the equation (7.42).

$$\hat{\mathbf{x}} = (\mathbf{A}^{H}\mathbf{A})^{-1}\mathbf{A}^{H}\tilde{\mathbf{s}} \tag{7.42}$$

For simplification, it is possible to express $(\mathbf{A}^{H}\mathbf{A})^{-1}\mathbf{A}^{H} = \mathbf{A}^{+}$, where $\mathbf{A}^{+}$ represents the Moore-Penrose pseudo-inverse. For the application in MRSI, a set of $\mathcal{K} = \{\mathbf{k}_m\}^M$ spatial positions and $\mathcal{T} = \{t_i\}^T$ temporal measurements can be defined. Equation (4.36) can be reformulated as follows:

$$\tilde{s}\Big|_{\{\mathcal{K},\mathcal{T}\}} = \tilde{s}[\mathbf{k}_m, t_i] \tag{7.43}$$

$$= \int_{-\infty}^{+\infty}\int_{\Omega\subset\mathbb{R}^3} \rho(\mathbf{r},\sigma)\cdot e^{-2\pi i(\mathbf{k}_m\cdot\mathbf{r}-\sigma f_0 t_i)}\,d\mathbf{r}\,d\sigma + \eta[\mathbf{k}_m, t_i] \tag{7.44}$$

$$= \sum_n F_n[\mathbf{k}_m]c_n[t_i] + \eta[\mathbf{k}_m, t_i] \tag{7.45}$$

The integral in equation (7.44) is discretized using the sum in equation (7.45). In this representation, $F \in \mathbb{C}^{M\times N}$ is the Fourier matrix comprising the Fourier exponentials $e^{-2\pi i\mathbf{k}_m\mathbf{r}_n}$, with n indexing the spatial positions $\{\mathbf{r}_n\}^N$. In the latter equation, the amplitude coefficients for each time sample are represented by the vector $\mathbf{c}$. F is assumed to be square, resulting in its unitarity by construction. Therefore, equation (7.45) can be expressed in a vectorized form.

$$\tilde{\mathbf{s}}[t_i] = \mathbf{F}\mathbf{c}[t_i] + \mathbf{n}[t_i] \tag{7.46}$$

Using the least square equation, the equation (7.46) has for solution

$$\hat{\mathbf{c}}[t_i] = \mathbf{F}^{H}\tilde{\mathbf{s}}[t_i] \tag{7.47}$$

The equation indicates that the solution corresponds to the discrete inverse Fourier transform. It is noteworthy that the inverse Fourier transform is a viable solution; however, it represents a particular case of the optimization-based reconstruction.

7.3.2 *Regularization*

Reconstructions that rely on optimization techniques are often referred to as ill-posed problems due to the need for inverting an ill-conditioned linear system during the reconstruction process. In many cases, such as when dealing with undersampled k-space, the number of unknowns exceeds the number of measurements, resulting in an underdetermined problem. This generates a multitude of possible solutions that can fit the measured data, rendering it challenging to identify the correct solution uniquely. The kernel of the mapping $\mathcal{A} : V \to W$ is defined as follows.

$$\ker(\mathcal{A}) = \{v \in V \mid \mathcal{A}(v) = 0_W\} \tag{7.48}$$

The existence of multiple solutions arises from the fact that the kernel of the mapping is nontrivial, $\ker(\mathcal{A}) \neq \{0\}$. This indicates that the function is not injective, allowing for different values to be mapped to the same output. To overcome this issue, regularization techniques have been developed to impose additional constraints on the reconstruction, improving the

uniqueness and stability of the solution. These regularization techniques can be incorporated into the reconstruction algorithm with an additional term $\mathcal{R}$ that acts as a penalty term that promotes a smoother or sparser solution.

$$\hat{f} = \arg\min_{f} \|\tilde{s} - \mathcal{A}\{f\}\|_{l_2}^2 + \mathcal{R}\{f\} \tag{7.49}$$

7.3.3 *Compressed sensing*

Compressed sensing is a signal processing technique that allows for the efficient acquisition and reconstruction of signals that are in a specific representation. The techniques relies on several key components, including a sparse transformation that is known a priori in a specific domain, the incoherence of the undersampling artifacts, and a non-linear reconstruction algorithm. Sparsity refers to the property of having a small number of non-zero elements, which can be utilized to compress a signal. A sparse transformation of an image or an object refers to the idea of compression without any perceptible loss of information. To achieve this, various methods rely on a sparse transformation that maps the image into vectors of coefficients, and then encodes the sparse vector by approximating the most significant one and discarding the others. The concept of compressed sensing takes advantage on the sparsity or compressibility of signals by acquiring them in a compressed form, utilizing only a small number of random measurements. These measurements are then used to reconstruct the original signal through a non-linear optimization algorithm that enforces sparsity or compressibility in the signal domain [95, 97, 98].

In contrast, dense signals have most of their elements non-zero.

In many cases, techniques leverage the sparse nature of MR images to recover undersampled signals. To achieve this, the most commonly used regularization method can be formulated as follows:

$$\mathcal{R}(\mathbf{x}) = \lambda\|\mathbf{x}\|_{l_1} \tag{7.50}$$

The use of the l_0 pseudo-norm indeed encourages the sparsity of the reconstruction, but its non-convex nature makes it unsuitable for optimization problems. Therefore, it is replaced by the convex l_1 pseudo-norm which is widely used in compressed sensing. The parameter $\lambda \in \mathbb{R}$ is a regularization weight that controls the trade-off between the data fidelity term and the regularization penalty term. For compressed sensing, the regularization is performed on the sparse transformation Ψ of the image, such that $\mathbf{x}$ becomes Ψm in the context of MRI.

Compressed sensing has showed better performence using random undersampling with variable density sampling, as the majority of the energy distribution in an MR image is concentrated at the center and quickly decays towards the periphery of the k-space. The incoherence in random sampling can be assessed by means of the transform point spread function (TPSF), which extends the concept of the point spread function (PSF). The TPSF measures how a single transform coefficient of the underlying object affects other transform coefficients of the measured undersampled object. Let S be the sample subset of the k-space and $\mathcal{F}_S$ be the Fourier transform evaluated only at the frequencies of the subset. The point spread function of the pixel (i, j) is given by

$$\mathrm{PSF}(i, j) = (\mathcal{F}_S^* \mathcal{F}_S)(i, j) \tag{7.51}$$

The PSF equals the identity in the case of Cartesian sampling. A non-zero value at pixel (i, j) indicates that pixel i is affected by interference from pixel $j \neq i$. Thus, the PSF provides a

measure of the blurring and artefact caused by the leakage of energy from one pixel to another. Using Ψ to represent the sparsifying transform, the TPSF can be defined as

$$\mathrm{TPSF}(i,j) \quad = \quad (\Psi^* \mathcal{F}_S^* \mathcal{F}_S \Psi)(i,j) \tag{7.52}$$

The degree of coherence is determined by $\max_{i \neq j} |\mathrm{TPSF}(i,j)|$. Incoherence, therefore small values of coherence, is preferred. Using the equation (7.49) to reconstruct an image represented by a complex vector m, given the measured k-space y, the equation becomes:

$$\arg\min_m \|\mathcal{F}_S m - y\|_{l_2}^2 + \lambda \|\Psi m\|_{l_1} \tag{7.53}$$

The equation try fo find a solution that is compressible by the transformation Ψ. The parameter λ is a small constant that determines the tolerance level for the reconstruction error.

7.3.4 *TV regularization*

The concept of total variation (TV) arises in cases when finite-differences is used as the sparsifiying transform. TV quantifies the degree of variation or change in an image or signal. In the context of images, total variation represents the magnitude of changes in color or brightness between adjacent pixels. For a function $f \in L^1(\Omega)$ where $\Omega \subset \mathbb{R}$ denotes an open subset, the total variation of f is defined by the equation (7.54) [99].

$$\mathrm{TV}_\Omega(f) \quad = \quad \sup \left\{ \int_\Omega f(x) \cdot \nabla \phi(x) dx \;\middle|\; \phi \in C_c^1(\Omega, \mathbb{R}^n),\ \|\phi\|_{L^\infty(\Omega)} \leqslant 1 \right\} \tag{7.54}$$

A function f is said to possess bounded variation if its total variation is finite. Here, $C_c^1(\Omega, \mathbb{R}^n)$ represents the set of continuously differentiable vector functions of compact support in Ω. If $f \in C_c^1(\Omega, \mathbb{R})$ and the subset has $\partial\Omega$ of class C^1, then the definition is simplified as follows:

$$\begin{aligned} \int_\Omega f(x) \cdot \nabla \phi(x) dx \quad &= \quad -\int_\Omega \phi(x) \cdot \nabla f(x) dx && (7.55) \\ &\leqslant \quad \int_\Omega |\phi(x)| \cdot |\nabla f(x)| dx && (7.56) \\ &\leqslant \quad \int_\Omega |\nabla f(x)| dx && (7.57) \end{aligned}$$

The last step can be performed because the supremum of phi has been constructed to be 1 at max by def. We can then redefined the TV as

$$\mathrm{TV}(f) = \int_\Omega |\nabla f(x)| dx \tag{7.58}$$

The regularization with total variation encourages sparsity in the solution by penalizing large gradients, resulting in a smooth and piecewise-constant structure. This can be implemented as a regularization in equation (7.53), which can be rewritten as:

$$\arg\min_m \|\mathcal{F}_S m - y\|_{l_2}^2 + \lambda \|\Psi m\|_{l_1} + \alpha \mathrm{TV}(m) \tag{7.59}$$

α trades the Ψ sparsity with finite-differences sparsity. TV models are particularly advantageous in the context of removing random noise while preserving image edges. However, the underlying assumption of TV is that images comprise regions that are piecewise constant. In practice, this assumption may be violated due to the inhomogeneities of the exciting B_1 field in high-field systems, or simply because images are generally not piecewise constant. Furthermore, even in situations where this assumption of piecewise-constancy holds, the use of TV may result in staircasing artifacts, which is a known limitation of this regularization method [98, 100].

7.3.5 *TGV regularization*

Total generalized variation (TGV) is a regularization method that shares similar properties with total variation (TV) in terms of preserving edges and removing noise from images. However, unlike TV, TGV can be applied in imaging situations where the assumption of piecewise-constancy does not hold because TGV tend to sparsify higher order spatial derivative [100, 101].

$$\mathrm{TGV}^k_\alpha(f) = \sup \left\{ \int_\Omega f(\mathbf{x}) \cdot \nabla^k \phi(\mathbf{x}) d\mathbf{x} \;\middle|\; \phi \in C^k_c(\Omega, \mathrm{Sym}^k(\mathbb{R}^d)), \; \|\nabla^l \phi\|_{L^\infty(\Omega)} \leqslant \alpha_l, l = 0, \ldots, k-1 \right\} \tag{7.60}$$

The equation includes $\mathrm{Sym}^k(\mathbb{R}^d)$, which represents the space of symmetric tensors of order k with arguments $\mathbb{R}^d$. Additionally, the parameters α_l are fixed positive constant values.

$$\mathrm{Sym}^k(\mathbb{R}^d) \quad = \quad \{\xi : \underbrace{\mathbb{R}^d \times \ldots \times \mathbb{R}^d}_{k\text{times}} \to \mathbb{R} \;\mid\; \xi \text{ k-linear and symmetric}\} \tag{7.61}$$

The equation (7.60) recovers the total variation for $k = 1$ and $\alpha > 0$: $\mathrm{TGV}^1_\alpha(f) = \alpha \mathrm{TV}(f)$. In most applications, TGV is used at the second order with $k = 2$. At the second order, the equation (7.60) can be expressed as

$$\mathrm{TGV}^2_\alpha(f) = \inf_p \alpha_1 \int_\Omega |\nabla f(\mathbf{x}) - p(\mathbf{x})| d\mathbf{x} + \alpha_0 \int_\Omega |\varepsilon_p(\mathbf{x})| d\mathbf{x} \tag{7.62}$$

where $\varepsilon_p = \frac{1}{2}(\nabla p + \nabla p^\top)$ represents the symmetrized derivative of p in the distributional sense. The TGV optimization now considers both the first and second-order derivatives, which promotes piecewise linear solutions and helps to mitigate the staircase effect [33].

7.3.6 *Low-Rank*

The low-rank decomposition is a mathematical method utilized to approximate a high-dimensional matrix by factorizing it into a product of three lower-dimensional matrices. The partial-separability assumption allow us to express the Low rank decomposition with two matrices. The concept of representing an object as a finite linear combination of unspecified components motivates a feature-based interpretation of the data, as opposed to the conventional voxel-based analysis. This bilinear model decomposition approximation can be formulated as follows:

The bilinear model is often referred to as partially-separable model.

$$\rho(\mathbf{r}, f) \quad = \quad \sum_{\kappa=1}^{K} u_\kappa(\mathbf{r}) v_\kappa(f) \tag{7.63}$$

The objective of the decomposition is to disentangle the spatial and temporal signal characteristics while retaining the underlying spatio-temporal correlations through the previously outlined variational framework. Constraints such as non-negativity or sparsity may be applied independently to the temporal and spatial components. By exploiting the commutativity of the spatial and temporal Fourier transforms, the low rank decomposition can be applied to acquired measurements under ideal conditions.

$$\tilde{s}(\mathbf{k}, t) = \int_{-\infty}^{+\infty} \int_{\Omega \subset \mathbb{R}^3} \sum_{\kappa=1}^{K} u_\kappa(\mathbf{r}) v_\kappa(f) \cdot e^{-2\pi i (\mathbf{k}_m \cdot \mathbf{r} - f t_i)} d\mathbf{r} df \tag{7.64}$$

$$= \sum_{\kappa=1}^{K} \underbrace{\int_{\Omega \subset \mathbb{R}^3} u_\kappa(\mathbf{r}) \cdot e^{-2\pi i \mathbf{k}_m \cdot \mathbf{r}} d\mathbf{r}}_{\chi_\kappa(\mathbf{k})} \cdot \underbrace{\int_{-\infty}^{+\infty} v_\kappa(f) \cdot e^{2\pi i f t_i} df}_{\xi_\kappa(t)} \tag{7.65}$$

$$= \sum_{\kappa=1}^{K} \chi_\kappa(\mathbf{k}) \xi_\kappa(t) \tag{7.66}$$

The acquired measurements comprise a set of k-space points $\{\mathbf{k}_m\}_{m=1}^{M}$ and temporal samples $\{t_i\}_{i=1}^{T}$, resulting in a matrix $\tilde{\mathbf{s}} \in \mathbb{C}^{M \times T}$ that represents the measured signal. The validity of the decomposition in equation (7.66) hinges on the rank K of the number of components, which must satisfy $K \leqslant \min(M, T)$. In cases where the measurements are non-ideal, estimating the rank K becomes non-trivial. In MRSI, the use of a bilinear model is justified in in-vivo settings due to the limited number of detectable metabolites in a given spectrum. Thus, an upper and lower bound on K can be imposed in this context [102].

8

IMPROVED PHOSPHORUS MRSI THROUGH COMPRESSED SENSING AND LOW-RANK

"The ability to manipulate the environment thoughtfully provides the capacity to shift our vantage point, to hover above the timeline and contemplate what was and imagine what will be."

- Brian Greene, *Until the End of Time*

Contents

8.1 SUMMARY

Chapter 7 provides an overview of MR reconstruction techniques. In particular, it emphasizes the significance of non-Fourier-based reconstruction methods that enable flexible acquisition sampling. Although Fourier-based methods have been pivotal in MRI, they require complete sampling of k-space and assume that the Nyquist criterion is satisfied. This approach imposes constraints on acquisition that can be time-consuming and clinically impractical, such as when evaluating organs for transplantation or ensuring patient comfort. Additionally, multiple averages can be employed to compensate for low SNR in ^{31}P-MRSI, but this results in prolonged scan times.

Within the category of non-Fourier-based techniques, there exist certain reconstruction methodologies that approach the reconstruction process as an optimization problem. Compressed sensing (CS) is a prominent example of such methods, which has garnered considerable attention due to its capability to shorten scanning time while preserving superior image quality [97, 98, 103]. CS has been applied in various spectroscopy applications, including 2D and 3D ^{1}H-MRSI [104–106], resulting in fast high-resolution metabolic mapping of the brain [107–109]. Low-Rank (LR) reconstruction has been demonstrated to be particularly advantageous for applications requiring improved SNR, as it can achieved promising results in denoising and signal recovery [110, 111].

The present study aims to address a challenge encountered in phosphorus spectroscopy by investigating the potential of compressed sensing combined with low-rank and total generalized variation regularization approach to enhance the acquisition process using an acceleration reconstruction method. The framework of the CS-LR methods is presented in our article 8.2, detailing the novelty of utilizing distinct random undersampling patterns for each k-space average to prevent the suppression of identical points, thereby enabling greater k-space coverage without altering the acceleration factor. The effectiveness of the methods was evaluated using healthy volunteers' brain data from Chapter 6 and ex-vivo perfused kidney from Chapter 10. Results indicate that the methods significantly improved the SNR while preserving spectral and spatial quality, even when the acquisition is accelerated threefold. Furthermore, the metabolite peak linewidth remained constant at all acceleration factors, and anatomical information could be recovered from signal attenuation. This study achieved fast acquisition with reliable reconstruction to reduce the scan time.

Improved Phosphorus MRSI acquisition through Compressed Sensing Acceleration combined with Low-Rank Reconstruction

Julien Songeon,[1] Sébastien Courvoisier,[1,2] Thomas Agius,[3] Oscar Dabrowski,[1] Raphael Ruttimann,[4] Christian Toso,[4] Alban Longchamp,[3] François Lazeyras,[1,2] and Antoine Klauser[1,2]

[1]*Department of Radiology and Medical Informatics, University of Geneva, Switzerland*
[2]*CIBM Center for Biomedical Imaging, Switzerland*
[3]*Department of Vascular Surgery, Lausanne University Hospital and University of Lausanne, Switzerland*
[4]*Visceral and Transplant Surgery, Department of Surgery, Geneva University Hospitals and Medical School, Geneva, Switzerland*

(Submitted to Magnetic Resonance in Medicine on: April 14, 2023)

Purpose: Phosphorus-31 magnetic resonance spectroscopic imaging (^{31}P-MRSI) is a valuable non-invasive tool for assessing cellular high-energy metabolism in-vivo. However, its acquisition suffers from a lower sensitivity, which necessitates larger voxel sizes or multiple averages to achieve an acceptable signal-to-noise ratio (SNR), resulting in long scan times.
Theory and Methods: To overcome these limitations, we propose an acquisition and reconstruction scheme for FID-MRSI sequences. Specifically, we employed Compressed Sensing (CS) and Low-Rank (LR) with Total Generalized Variation (TGV) regularization in a CS-LR method. Additionally, we used a novel approach to k-space undersampling that utilizes distinct random patterns for each average. To evaluate the proposed method's performance, we tested it on healthy volunteers' brains and ex-vivo perfused kidneys.
Results: The presented method effectively improves the SNR while preserving the spectral and spatial quality even when the acquisition is accelerated threefold. We were able to recover signal attenuation of anatomical information, and the SNR improvement was obtained while maintaining the metabolites peaks linewidth.
Conclusion: We presented a novel combined CS-LR acceleration and reconstruction method for FID-MRSI sequences, utilizing a unique approach to k-space undersampling. Our proposed method has demonstrated promising results in enhancing the SNR making it applicable for reducing scan time.

Keywords: Acceleration, Compressed-Sensing, Low Rank, Regularization, Phosphorus Magnetic Resonance Spectroscopic Imaging (^{31}P-MRSI)

I. INTRODUCTION

Phosphorus-31 magnetic resonance spectroscopy (^{31}P-MRS) is a non-invasive technique that provides valuable information on cellular high-energy metabolism in-vivo [1–5]. When combined with spatial phase encoding, ^{31}P-MRS imaging (MRSI) allows for multi-voxel acquisition, enabling metabolite mapping across the entire field-of-view (FoV) [6]. In addition, ^{31}P-MRS can provide an estimation of intracellular pH (pHi) from the chemical shifts, which can be utilized for pH mapping [7–11]. The unique information obtained through phosphorus spectroscopy has generated increasing interest towards developing the map distribution of biochemicals in-vivo. These features find widespread applications in studying various medical conditions such as diabetes [12–14], Alzheimer's disease [15, 16], migraine [17, 18], oxidative stress [19], muscular dystrophies [20–22], and cancer [23–25].

Despite the advantages of ^{31}P-MRS, its acquisition displays a lower relative sensitivity than hydrogen-1 (^{1}H) at a constant magnetic field, necessitating larger voxel sizes to achieve a sufficient signal-to-noise ratio (SNR) while maintaining an acceptable scan time for the patient [26, 27]. Furthermore, to compensate for a low SNR, multiple averages can be employed, but this comes at the expense of prolonging the scan time. Thankfully, lengthy acquisition could be overcome by using acceleration techniques, such as Compressed Sensing (CS), which has been widely studied in ^{1}H-MRSI and is gaining popularity in other nuclei as well [28].

Compressed Sensing (CS) is an acquisition acceleration method involving random k-space undersampling [29, 30]. This technique has been demonstrated to significantly reduce scan time while maintaining high image quality, making it attractive in clinical settings [31]. The application of CS in ^{1}H imaging has been extensively investigated and has been shown to be effective for a variety of applications [32–35]. In parallel, CS has been applied in spectroscopy, specifically in 2D and 3D ^{1}H-MRSI [36–38], enabling fast high-resolution metabolic mapping of the brain [39–41]. The success of CS in ^{1}H imaging and spectroscopy has opened up opportunities to explore its application to other nuclei, such as ^{1}3C to accelerate hyperpolarized 3D-MRSI acquisition that requires short acquisition time [42–45].

The Low-Rank (LR) method has been employed to reconstruct accelerated CS data. This approaches is

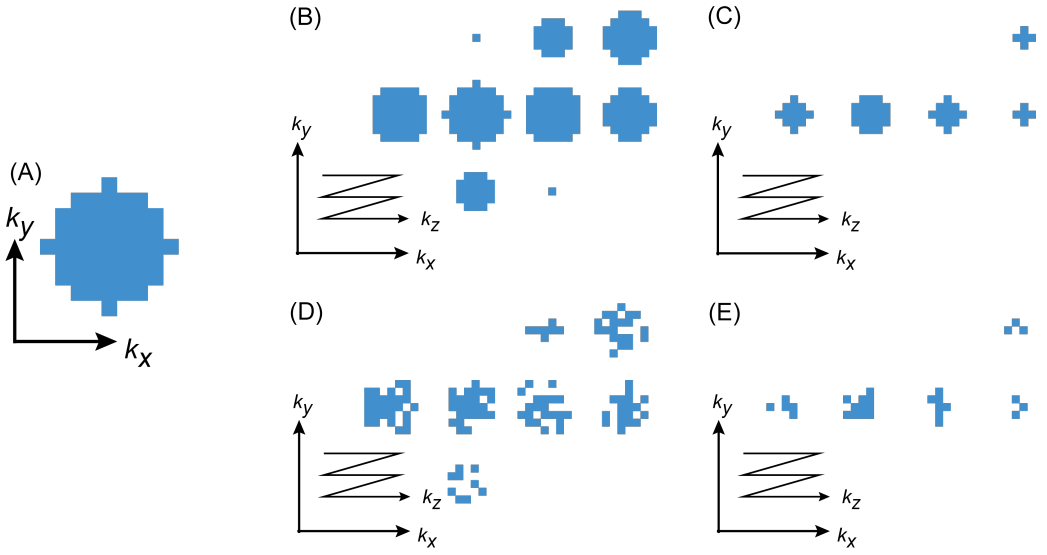

FIG. 1. Example of k-space filling of a $10 \times 10 \times 10$ voxel acquisition, illustrating the differences between fully sampled k-space and randomly undersampled k-space. Panel (A) shows the center slice of fully sampled k-space, while panels (B) and (C) depict the first and the 10th (out of 24) weighted average, respectively. The impact of undersampling can be seen in panels (D) and (E), which display unique randomly undersampled k-space for an acceleration factor of 2.

particularly advantageous for application requiring an improved SNR, as they can effectively denoise as well [46, 47]. A LR method described as union-of-subspaces was successfully applied to ^{1}H-MRSI [48]. Likewise, LR tensor model has allowed sparse ^{31}P-MRSI acquisition scheme to be used, resulting in faster acquisition with high resolution and improved SNR [49]. The combination of CS-LR has been increasingly applied to MRI [50–52] and MRS [39–41], benefiting scan time acceleration while improving image quality and quantitation accuracy. By combining the CS-LR method with total generalized variation (TGV) for data regularization, the acquisition time of MRSI data can be significantly reduced without compromising the quality of the reconstructed image [53, 54].

The current study aims to demonstrate the feasibility of a novel approach that combines compressed sensing and low-rank techniques with total generalized variation regularization (CS-LR), specifically for ^{31}P-MRSI data obtained via the FID-MRSI 3D sequence, in situations where the signal-to-noise ratio (SNR) is low. The proposed approach utilizes elliptical encoding and weighted averages, with each average subjected to a random undersampling scheme. The resulting information is then incorporated into the reconstruction. To demonstrate the versatility of this CS-LR approach, the methods were applied in two distinct conditions: in-vivo on the human brain and ex-vivo on perfused pig kidneys.

II. METHODS

A. Acceleration and reconstruction

1. *Undersampling with weighted averaging*

Data acquisition is time-consuming and can become prohibitive in regard to clinical constrains such as organ evaluation before transplantation or patient comfort. One approach to accelerating MRSI data acquisition is to use weighted averages [55]. Initially, MRSI data were acquired with a weighted average elliptical sampled k-space, as illustrated on Figure 1(A), (B) and (C). This fully sampled k-space was a posteriori undersampled. To achieve this, the Fourier domain was characterized by a radius q, which was expressed as $q = \sqrt{(k_x/k_x^{\max})^2 + (k_y/k_y^{\max})^2 + (k_z/k_z^{\max})^2}$. The random sampling was constructed such that the density distribution had a density of q^{-1}. To simulate the accelerated acquisition, we removed retrospectively $\mathbf{k}_i$ values of the 3D phase encoded measurements, while maintaining a fully sampled center of the k-space for $q \leq \frac{1}{5}$ [39]. The acceleration is quantified using the acceleration factor (AF), which represents the inverse of the undersampling factor. The random undersampling was performed for each weighted average individually. Figure 1 depicts the fully sampled k-space for two averages (centered (B) and 10^{th} (C) averages) along with potential undersam-

pling patterns (D) and (E) respectively. Employing different random undersampling patterns for each average prevents the suppression of identical points, thereby enabling greater k-space coverage without altering the acceleration factor.

2. CS-LR reconstruction

The CS-LR method presented in this article has been developed based on the work of Klauser et al. [39–41]. In MRSI, the signal measured by a coil element at a specific time t and Fourier-space position $\mathbf{k}$ can be expressed using the integral equation shown in Equation (1).

$$s(\mathbf{k},t) = \int_{\Omega\subset\mathbb{R}^3} \rho(\mathbf{r},t)C(\mathbf{r})e^{-2\pi i t\Delta B_0(\mathbf{r})}e^{-2\pi i\mathbf{k}\cdot\mathbf{r}}d\mathbf{r} \quad (1)$$

Here, the local transverse magnetization $\rho(\mathbf{r},t)$ is modulated by the coil sensitivity profile $C(\mathbf{r})$ and is affected by the map of field inhomogeneity in Hz $\Delta B_0(\mathbf{r})$ over the measured object Ω. By employing a single coil element, we can combine $\rho(\mathbf{r},t)$ and $C(\mathbf{r})$. Although the sensitivity profile of a volumetric coil is uniform, this cannot be assumed for a loop coil. This implies a weighting of the transverse magnetization with the coil sensitivity profile. For a weighted average a, the equation (1) can be discretized to give the relationship between the measured signal $\mathbf{s}_a$, the Fourier transform operator $\mathcal{F}_a$ which includes the Fourier transform as well as the unique undersampling pattern of each average, the frequency shift operator created by the inhomogeneity $\mathcal{B}$, and the local transverse magnetization $\boldsymbol{\rho}$.

$$\mathbf{s}_a = \mathcal{F}_a\mathcal{B}\boldsymbol{\rho} + \epsilon \quad (2)$$

ϵ accounts for the noise and is assumed to be Gaussian. The CS-LR reconstruction provides a solution to the inverse problem that is the reconstruction of the local transverse magnetization $\boldsymbol{\rho}$ knowing $\mathcal{F}_a\mathcal{B}$ with $\mathbf{s}$. The method assumes that the MRSI data can be represented by a low-rank matrix, which decomposes the spectral data into a small number of dominant components K [56]. The low rank reconstruction is presented in the following equations.

$$\rho_{l,j} = \sum_{n=1}^{K} U_{l,n}V_{n,j} \quad (3)$$

$$\boldsymbol{\rho} = \mathbf{UV} \quad (4)$$

$\rho_{l,j}$ can be represented as a linear combination of a small number of characteristic spectra that are spatially distributed across the measured volume. T represents the time series, with $j = 1,...,T$; and N^r the number of $\mathbf{r}$ vectors in the image space with $l = 1,...,N^r$. The matrix $\mathbf{V} \in \mathbb{C}^{K\times T}$ contains the finite set of characteristic time series, and $\mathbf{U} \in \mathbb{C}^{N^r\times K}$ represents their spatial distribution. The proposed method is well-suited for processing MRSI data due to the finite number of metabolite resonances that are assumed to be partially separable of their spatial distribution [46, 49]. Moreover, noise within the MRSI dataset is typically stochastic and lacks specific spatial distributions, which renders the fitting of a low-rank model to be an effective denoising tool. Regularization applied on spatial metabolite components permits the denoising in space while preserving edges and enforcing data consistency [57]. The inverse problem is written as

$$\arg\min_{\mathbf{U},\mathbf{V}} \sum_a ||\mathbf{s}_a - \mathcal{F}_a\mathcal{B}\mathbf{UV}||_2^2 + \lambda\sum_{n=1}^{K}\mathrm{TGV}^2\mathbf{U} \quad (5)$$

The spatial and temporal components are obtained by minimizing the inverse problem in conjunction with total generalized variation (TGV) spatial regularization method [53]. In our research, the values of $K = 5$ and $\lambda = 0.001$ were determined empirically yielding optimal outcome. The CS-LR reconstruction with and without acceleration will be compared to traditional FFT transformation. The reconstruction was performed in Matlab (The MathWorks, Natick, Massachusetts, US), and required 5hours computation time for the 3D MRSI using 8 cores of a 3.00 GHz Intel(R) Xeon(R)-E5 CPU, and 124 GB of RAM.

B. MRI measurements

In-vivo measurements were conducted on a clinical Prisma-fit 3T MRI scanner (Siemens Healthineers, Erlangen, Germany) that is equipped with multinuclear capabilities. Notably, no decoupling was applied.

1. Brain

The present results were obtained retrospectively from anonymous raw data, for which written informed consent was given by all the volunteers and the initial study was approved by the institutional ethics committee [58]. T1-weighted MP-RAGE acquisition was employed to obtain anatomical reference ^{1}H images. The dual-tuned ^{1}H and ^{31}P head coil (Clinical MR solutions, Brookfield) was used for scanning 10 healthy volunteers. A $10 \times 10 \times 10$ matrix was employed for the acquisition of 3D ^{31}P-MRSI of the whole brain, with an isotropic field of view (FoV) dimension of 250mm yielding a nominal spatial isotropic resolution of 25mm. The sequence consisted of a rectangular excitation pulse of 0.25ms with a flip angle of 45°, a repetition time (TR) of 1500ms, and an echo time (TE) of 0.5ms with 24 weighted averages [55]. The bandwidth was 4000Hz for 2048 sampling points, and the MRSI acquisition lasted 37 minutes.

2. Kidney

In the context of a study aimed at improving and evaluating the viability of marginal grafts, MRSI was performed on ex-vivo pig kidneys. To enable imaging, the organs were perfused using a homemade MR-compatible perfusion system [59, 60], with a single-loop coil fixed to the bottom of the perfusion tank. The coil was interfaced with a specially designed transceiver that allowed for both 1H imaging and 31P spectroscopy (Clinical MR Solutions, Brookfield, WI). The body coil was used to perform ^{1}H imaging with a T2-weighted sequence (turbo SE, TR 6530ms, TE 110ms, 2mm slices) for kidney localization and structural imaging. The 3D ^{31}P-MRSI was acquired with a field of view of 250mm × 250mm × 160mm and a matrix size of 16 × 16 × 8, yielding a nominal spatial resolution of 15.6mm × 15.6mm × 20mm. The TR was set to 1000ms, the flip-angle was 45°, the echo delay was 0.6 ms, and the bandwidth was 4000Hz for 2048 sampling points. The acquisition employed elliptical encoding with 18 weighted averages, and the acquisition time was 45 minutes. The chemical shift signal was referenced to the inorganic phosphate (Pi) resonance at 5.2ppm, which can be considered homogeneously distributed over the surface of the coil.

C. Spectral quantification and reconstruction

The ^{31}P-MRSI spectra were analysed and quantified using the openly available 31P-SPAWNN method (`gitlab.unige.ch/Julien.Songeon/31P-SPAWNN`) [58]. The method uses convolution neural network (CNN) to estimate spectral parameters (phase, linewidth, frequency, etc.) and metabolite concentrations that are used to reconstruct individual spectra. The quantified metabolites included phosphocreatine (PCr), inorganic phosphate (Pi), adenosine triphosphate (α-ATP, β-ATP, and γ-ATP). Additionally, the phosphomonoesters (PME) consisting of phosphocholine (PC) and phosphoethanolamine (PE), and the phosphodiesters (PDE) consisting of glycerophosphocholine (GPC) and glycerophosphoethanolamine (GPE), as well as nicotinamide adenine dinucleotide (NAD+ and NADH) and membrane phospholipids (Mp) were also included in the quantification. MRSI data did not have an internal reference for quantification, and therefore, the results will only be presented as a ratio of metabolite concentrations.

D. Evaluation of performance

1. Error quantification

The performance of compressed sensing with the CS-LR model was evaluated using the normalized root mean square error (NRMSE).

$$NRMSE = \sqrt{\frac{\sum_i |\rho_i^{\text{no acc.}} - \rho_i^{acc.}|^2}{\sum_i \rho_i^{\text{no acc.}}}} \tag{6}$$

NRMSE was computed by comparing the undersampled data to the fully sampled data, both reconstructed using the CS-LR method. The sum over the index i was taken for all the voxels in the brain or the kidney. For the brain, the ratio of metabolite concentration was calculated with respect to PCr across the whole brain for the 10 subjects. For the kidney, the ratio was computed with respect to Pi.

2. Spectral evaluation

The present study evaluates the spectral quality by calculating the SNR for the voxels of interest, both for the original data and for the CS-LR methods implemented with and without acceleration. Specifically, the SNR is computed for the brain data by utilizing the PCr peak intensity as the reference signal and divided by the noise standard deviation. Similarly, for the kidney data, the PME peak is employed for this purpose. Additionally, linewidth of all resonances were measured to determine whether the implemented methods cause peak broadening.

3. Spatial evaluation

The study assesses the spatial quality of the data using metabolic mapping. An intensity map was obtained with the FFT of the original data and the CS-LR methods implemented with and without acceleration. The sharpness of the image was evaluated by computing the image gradient. To determine the sharpness and complexity of the image, the Sobel method presented by Yu et al. [61] was employed. Spatial information was estimated by computing the image gradient in both the horizontal and vertical directions. Subsequently, the root-mean-square (RMS) and its standard deviation of the edge magnitudes were computed from the spatial information values for each metabolite and method.

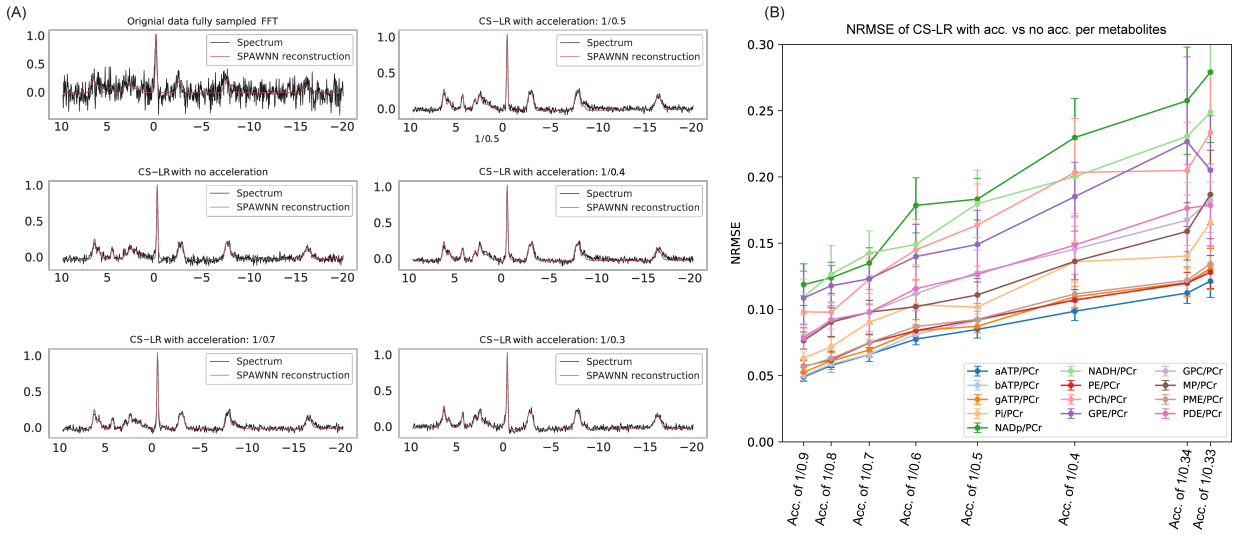

FIG. 2. Plots of a voxel from brain ^{31}P-MRSI data to demonstrate the effect of acceleration and reconstruction on the spectra. Panel (A) displays spectra of the FFT of the original data, the CS-LR methods without and with acceleration factors of 1.4, 1.9, 2.4, and 3. Panel (B) presents the plots of the normalized mean square error (NRMSE) for the concentration ratio of the estimated metabolites with acceleration compared to the non-accelerated method.

III. RESULTS

Figure 2 presents the brain results obtained on the 10 healthy volunteers. Figure 2(A) displays the spectra obtained from a voxel using different approaches, including the original data, the CS-LR method without acceleration, and with various acceleration factors (1.42, 1.93, 2.39, and 3.03) in combination with the LR approach. Spectra are displayed without any apodization. Normalized mean square error (NRMSE) in Figure 2(B) was calculated to assess the accuracy of the ratio estimation obtained with the CS-LR method with acceleration compared to the CS-LR method without acceleration. The computation was performed with the acceleration factor of 1.11, 1.24, 1.42, 1.64, 1.93, 2.39, 2.92 and 3.03; corresponding to 90%, 80%, 70%, 60%, 50%, 40%, and approximately 30% of the fully sampled k-space. The reduction in k-space sampling is associated with a linear decrease in scan time, the resulting scan times were 33, 29, 26, 22, 19, 15, and approximately 12 minutes, respectively. The NRMSE was computed on all the voxels, data points correspond to the mean and SD values across the 10 subjects. The application of the CS-LR approach led to a substantial enhancement in the SNR of the spectra, and is maintained for all acceleration factors. The NRMSE exhibited a monotonic trend, closely resembling a linear relationship with the acceleration factor. In the case of ATP metabolites, the error rate was approximately 5% at an acceleration of 1.11, increasing to 10% at an acceleration of 3.03. The concentration estimation of Pi, PME, and PDE presented an initial error rate between 7% and 10%, which escalated to a range of 13% to 17%.

Figure 3 displays the SNR measurements relative to the PCr of the original data, and the CS-LR method without acceleration, and with various acceleration factors combined. The figure also displays the width values of the PCr peak for all 10 volunteers. Similar results are presented for different metabolite resonances in Figure S1 for the width of Pi, ATP, and PME. The CS-LR methods resulted in a significant improvement of the SNR ranging from two to three times compared to the original data, without acceleration. This improvement was observed uniformly across all participants. Although the SNR exhibited some variation with a decreasing trend, the CS-LR method with an acceleration factor of 3.03 maintained an SNR value of at least twice that of the original data. No broadening of metabolite linewidth was observed, as indicated by a constant line in the linewidth values across all methods depicted in the figure.

Figure 4 displays the brain mapping of α-ATP for the original data, and the CS-LR method, without and with acceleration factors of 1.4, 1.9, and 3. The data are presented in a coronal plane as illustrated with anatomical reference images. Along with the mapping, the gradient of the image is presented. The gradient was calculated from left to right and shows the intensity variation between voxels. For the original data, and the CS-LR method without and with an acceleration factor of 3,

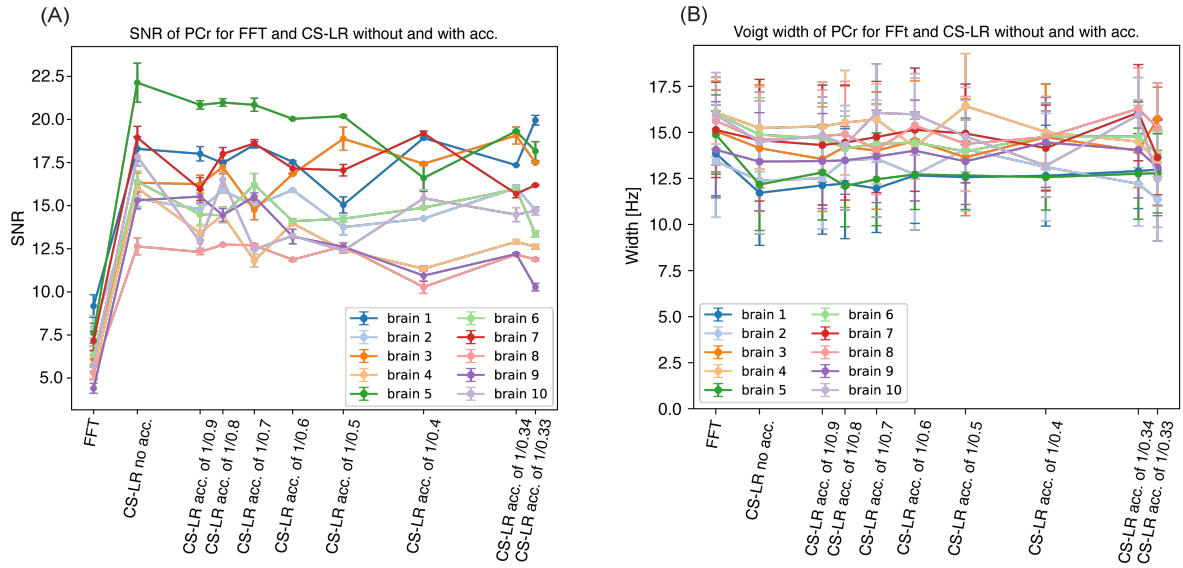

FIG. 3. A summary of the outcomes obtained from the group of 10 participants. Panel (A) signal-to-noise ratio (SNR) measurements relative to phosphocreatine (PCr) and Panel (B) the corresponding peak width of PCr for the FFT of the original data, the CS-LR method without, and with various acceleration factors.

the gradient maps are presented in 3D plots. The results present an improvement in metabolite signal through the use of CS-LR reconstruction, while maintaining spatial definition during acceleration. This observation is further supported by the gradient maps in Figure 4(C), which exhibit sharper edge measurements of the CS-LR reconstruction in comparison with fully sampled FFT.

Table I presents the quantitative results for the ability of the CS-LR method to enhance the complexity of acquired information. The table reports combined vertical and horizontal edge magnitudes using Sobel kernel. T-tests were performed to determine significant differences CS-LR method with each acceleration factor with respect to the FFT of the original data. To correct for multiple testing, the Bonferroni correction was applied to adjust the significance threshold by $\alpha' = \alpha/45$, since 45 independent t-tests were performed. The analysis of all major metabolites (ATPs, PCr, and Pi) revealed significant improvements in edge detection with the implementation of CS-LR as opposed to inverse FFT reconstruction, regardless of the acceleration factor used. Although the SNR of PCr was already relatively high, similar trends were observed but did not reach statistical significance ($p = 2.0 \cdot 10^{-3}$).

Figure 5 provides analogous findings as the previous figure, but applied to the kidney data. The Figure showcases maps of α-ATP intensity, its corresponding gradient, and an example of voxel spectra for the FFT of the original data, the CS-LR method without, and with acceleration factors of 2.4 and 3.2 in combination with the LR approach. The figure also presents NRMSE values for the metabolic quantification, with a reduced number of metabolites. Specifically, only ATPs, PME, and Pi are observed on the spectra, and the acceleration was extended to a maximum factor of 4. The analysis was also performed with the same 31P-SPAWNN model than the brain, highlighting its robustness to low SNR.

IV. DISCUSSION

The current study examines the efficacy of the Low Rank method in combination with Compressed Sensing (CS-LR) for acceleration and reconstruction of ^{31}P-MRSI. A unique feature of the presented acceleration is the use of different random patterns for each weighted average. The original data were compared to data reconstructed using the LR method alone, as well as with data reconstructed using the LR-CS method with varying acceleration factors. The utilization of acceleration has important practical implications, allowing for significant time savings and enhancing the feasibility of ^{31}P-MRSI in clinical settings. The results reported in this research are retrospective, obtained through a posteriori acceleration of ^{31}P-MRSI data acquired from both brain and kidney tissues. The acceleration was achieved by undersampling k-space while maintaining a hard radius at the center of k-space, which was fully sampled. The technique

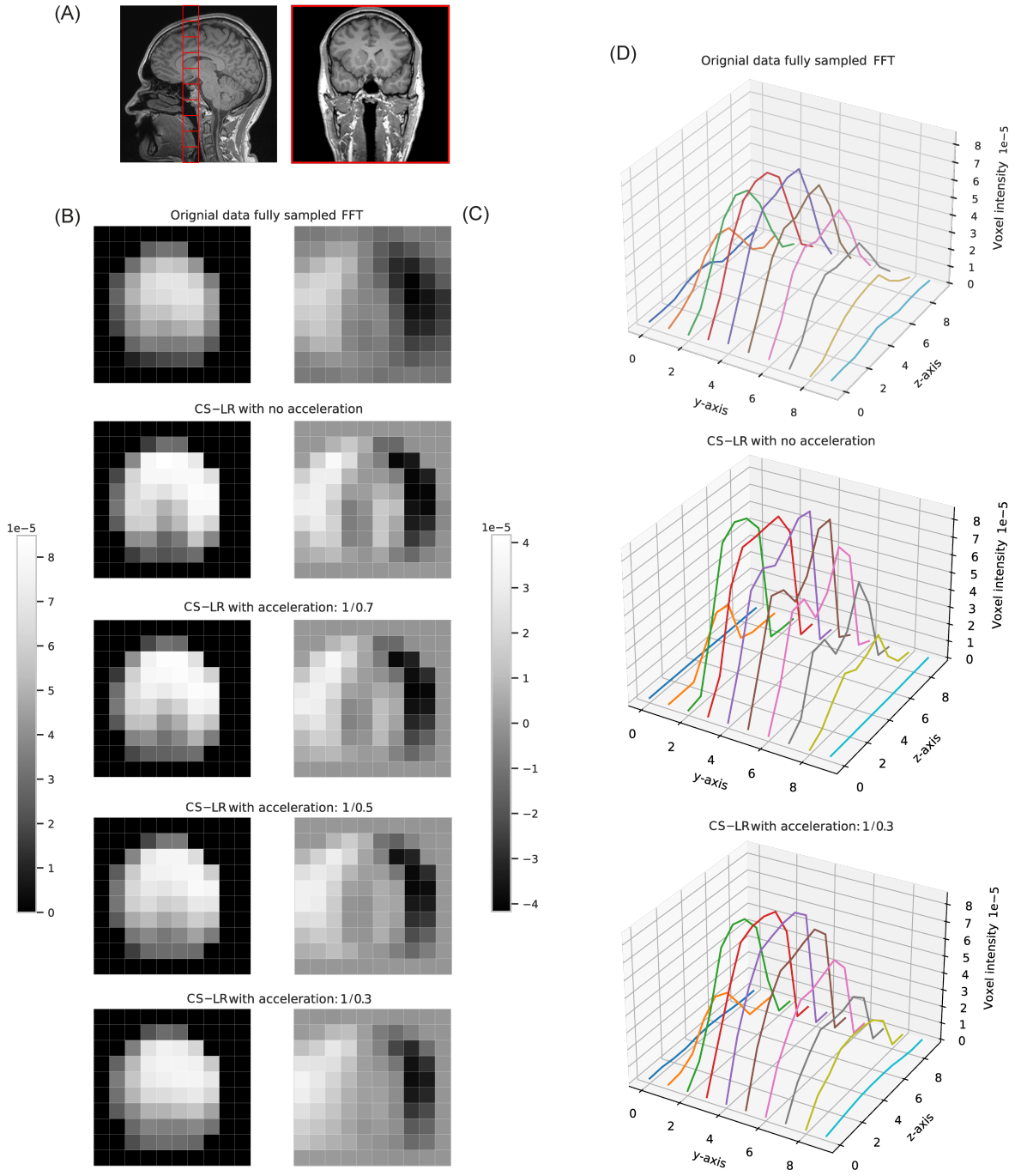

FIG. 4. Effects of CS-LR method on metabolic mapping. Panel (A) displays the reference anatomical images in the coronal axis. Panel (B) exhibits maps of the signal intensity of α-ATP with its corresponding left-to-right gradient on panel (C). The first row exhibits the FFT of the original data, while the succeeding rows display the reconstructed data using the CS-LR method. The second row illustrates the CS-LR method without acceleration, while the third, fourth, and fifth rows correspond to the CS-LR method with acceleration factors of 1.4, 2, and 3, respectively. Panel (D) depicts 3D plots of intensity profile corresponding to gradient maps of panel (C) with the FFT of the original data (top), the CS-LR reconstruction without acceleration (middle), and with acceleration of 3 (bottom).

	PCr	α-ATP	β-ATP	γ-ATP	Pi
IFFT	0.84 ± 0.04	0.90 ± 0.04	0.87 ± 0.04	0.92 ± 0.03	0.86 ± 0.06
LR no acc.	0.99 ± 0.10	$1.07 \pm 0.05^{\star\star}$	$1.07 \pm 0.05^{\star\star\star}$	$1.06 \pm 0.05^{\star\star}$	$1.04 \pm 0.05^{\star\star}$
LR acc. 1.11	$0.99 \pm 0.08^{\star}$	$1.07 \pm 0.05^{\star\star\star}$	$1.08 \pm 0.05^{\star\star\star}$	$1.06 \pm 0.04^{\star\star\star}$	$1.06 \pm 0.05^{\star\star}$
LR acc. 1.24	$1.00 \pm 0.08^{\star\star}$	$1.08 \pm 0.05^{\star\star\star}$	$1.07 \pm 0.06^{\star\star\star}$	$1.07 \pm 0.06^{\star\star}$	$1.06 \pm 0.07^{\star}$
LR acc. 1.42	$0.99 \pm 0.09^{\star}$	$1.05 \pm 0.06^{\star\star}$	$1.07 \pm 0.05^{\star\star\star}$	$1.05 \pm 0.06^{\star\star}$	$1.05 \pm 0.09^{\star}$
LR acc. 1.64	$0.98 \pm 0.10^{\star}$	$1.06 \pm 0.06^{\star\star\star}$	$1.06 \pm 0.05^{\star\star\star}$	$1.05 \pm 0.06^{\star\star}$	$1.05 \pm 0.08^{\star\star}$
LR acc. 1.93	$1.01 \pm 0.09^{\star\star}$	$1.06 \pm 0.08^{\star}$	$1.06 \pm 0.07^{\star\star\star}$	$1.06 \pm 0.07^{\star\star}$	$1.09 \pm 0.07^{\star\star\star}$
LR acc. 2.39	$1.00 \pm 0.08^{\star\star}$	$1.05 \pm 0.07^{\star}$	$1.04 \pm 0.05^{\star\star\star}$	1.05 ± 0.07	$1.06 \pm 0.12^{\star\star}$
LR acc. 2.92	$1.03 \pm 0.07^{\star\star\star}$	$1.08 \pm 0.09^{\star}$	$1.06 \pm 0.08^{\star\star}$	$1.07 \pm 0.08^{\star}$	$1.06 \pm 0.07^{\star\star}$
LR acc. 3.03	$0.99 \pm 0.09^{\star}$	$1.05 \pm 0.10^{\star}$	$1.04 \pm 0.10^{\star\star}$	1.07 ± 0.10	$1.07 \pm 0.12^{\star}$

TABLE I. Edges magnitudes RMS with their standard deviations computed from the Sobel kernel. T-tests were performed to determine significant differences CS-LR method with each acceleration factor with respect to the FFT of the original data. Bonferroni correction was applied to adjust the significance thresholds by $\alpha' = \alpha/45$, resulting in: * $p \leq 1.1 \cdot 10^{-3}$, ** $p \leq 2.2 \cdot 10^{-4}$, and *** $p \leq 2.2 \cdot 10^{-5}$.

leverages the elliptical weighted average to generate distinct random patterns for each average, consequently maintaining a higher k-space coverage. Overall, the results indicate that 31P-MRSI acquisition can be reduced to 12-15 minutes with an acceleration factor of 3 while keeping comparable data quality. SPAWNN was able to evaluate all spectra utilizing the same training model. The LR methods employed in the study demonstrated that a number of $K = 5$ components was optimal for the specific application. A lower number of components did not provide the model with sufficient information to extract the essential components required for reconstruction, while a higher number resulted in the absorption of noise into the final components, ultimately deteriorating the results. The regularization factor $\lambda = 1 \cdot 10^{-3}$ was determined empirically in the present study. Specifically, the value of λ was iteratively increased from a smaller value of $\lambda = 1 \cdot 10^{-5}$. For values of λ less than $1 \cdot 10^{-3}$, the reconstruction were observed to be noisy, and it was difficult to extract spectral components. On the other hand, when the values of λ exceeded this threshold, the reconstruction exhibited over-regularization, leading to solutions that were almost independent of λ.

The results of our study illustrate the efficacy of the CS-LR method in reducing noise in the acquired data, as demonstrated by the enhanced SNR values presented in Figures 2 and 3. Specifically, Figure 3(A) exhibited a 2-3 fold increase in SNR for brain spectra, computed with respect to the PCr peak, while Figure 5 indicates a gain factor of 1.5 SNR for kidney data, computed with respect to the PME peak. Although SNR values fluctuated as the acceleration factor varied, they remained markedly higher than those of the original data. The benefits of CS acceleration were thus maintained alongside the observed improvements in SNR.

Figure 3 illustrates a noteworthy finding that the enhancement in signal-to-noise ratio (SNR) is not accompanied by any increase in the linewidth of the phosphocreatine (PCr) peaks. This observation was consistent across different metabolite resonances, as demonstrated in Figure S1 for the Pi, ATP, and PME. Notably, the linewidth of the metabolite peaks remained stable across subjects, suggesting that the utilization of the CS-LR technique does not impact the linewidth of metabolites, in contrast to other approaches that enhance sensitivity, such as apodization and smoothing filters, which are associated with peak broadening. This conclusion is reinforced by the results presented in Figure S1, which provide additional evidence for the stability of the peak width. Thus, the use of LR technique offers the benefit of enhancing SNR while maintaining the linewidth of the metabolite resonance peaks, which allows more precise analysis.

The impact of the CS-LR methods on the accuracy of quantification is assessed with the NRMSE, as shown in Figures 2 and 5. The accuracy was evaluated by computing the NRMSE for the concentration ratios, which revealed a linear relationship between the quantification error and the acceleration factor, and subsequently the undersampling. The metabolites with high signal and low spectral overlap, including the three resonances of ATP and Pi, exhibited an error of less than 15% in the ratio estimation with the removal of 2/3 of the k-space.

For acceleration factors below 2, the brain's ATP, Pi, and PME over the PCr and kidney's ATP, Pi, and PME

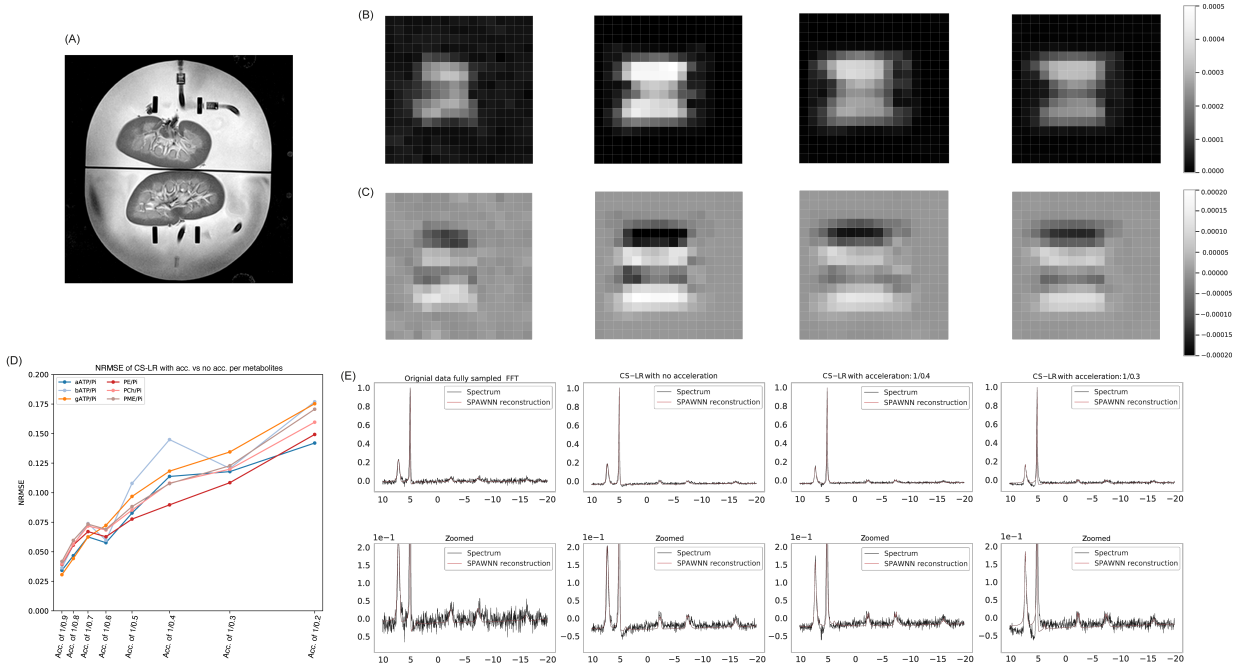

FIG. 5. Application of the CS-LR acceleration and reconstruction methods on the kidney data. Panel (A) displays the anatomical data in coronal axis. Panel (B) shows the signal intensity maps of the α-ATP with its corresponding gradient on panel (C), which is computed with a down-to-up gradient. Panel (E) presents the voxel spectra from the corresponding mapping. The first column corresponds to the FFT of the original data, the second column displays the CS-LR method without acceleration, the 3rd and 4th columns show the CS-LR method with an acceleration of 2.4 and 3.2 respectively. Panel (D) shows the NRMSE of the metabolic ratio estimation with respect to the Pi for the ATP and the PME.

over the Pi showed errors below 10%, indicating good agreement between the accelerated CS-LR data compared to the non accelerated CS-LR data. However, for an acceleration of 3 in the brain and between 3 and 4 for the kidneys, the error estimation reached 15%. Metabolites with lower signal levels and greater spectral overlap, such as PDE and NAD, displayed NRMSE values as high as 30%. It is worth noting that the acceleration also induced errors, as previously reported in the literature [36, 37, 40]. The loss of spatial information is due to the loss of frequency information in the k-space, and results in a smoothing effect as evidenced in Figures 4 and 5. The loss of spatial information is a consequence of the loss of frequency information in the k-space domain, which leads to a smoothing effect, as depicted in Figures 4 and 5. Since the reconstruction is non-linear, the loss of spatial information cannot be precisely quantified or recovered [39, 41]. Additionally, the effectiveness of the 31P-SPAWNN model in analyzing and reconstructing the MRSI data was demonstrated, as no adjustments were required to analyze the voxels throughout the entire dataset.

The results presented in Figure 4 illustrate the effectiveness of CS-LR reconstruction in improving the metabolite SNR while preserving the spectral quality during acceleration. These findings are consistent with the observed increase in SNR depicted in Figure 3 and the spectra SNR improvement shown in Figure 2. The CS-LR method succeeded in recovering signal attenuation illustrated by the presence of the anatomical oral cavity, which is discernible up to an acceleration factor of 2 as illustrated in Figure 4(B). Moreover, the 3D plots in Figure 4(D) emphasize the observation of signal attenuation at the center of the z-axis, with a clear reduction in signal intensity. As acceleration is applied, the structure becomes less evident, resulting in a smoothing effect and loss of spatial resolution. Notably, the signal and gradient maps of the original data and their counterparts with an acceleration factor of 3 display similar levels of information.Furthermore, the images of the kidneys presented in Figure 5 demonstrate the efficacy of the LR method in enhancing signal and edge sharpness.

Table I displays the quantitative evaluation of edge detection using the FFT of the original data and the CS-LR methods. The CS-LR methods without acceleration showed a significant improvement in edge sharpness for

all metabolites, except for PCr. The improvement in edge sharpness was observed for all acceleration factors, except for the γ-ATP that did not reach statistical significance for acceleration factor of 2.39 and 3.03 although showing the same trend. No statistical significance differences were found between the different acceleration factors and the CS-LR method without acceleration, indicating that the acceleration preserved edge sharpness. However, an increase in standard deviation was observed with increasing acceleration factor, indicating a decrease in measurement precision, consistent with the less precise measures seen in the NRMSE for the concentration in Figure 2.

The analysis of kidney data in Figure 5 yielded results similar to those observed in brain data analysis. Application of the CS-LR method resulted in improved SNR, particularly for the low signal of ATP. The α-ATP intensity map exhibited sharper signal resolution with clear contrast on the gradient map. For the kidney data, an acceleration factor of 3 resulted in higher signal resolution and a sharper gradient image than the original data. Similar to the brain data, the NRMSE exhibited a linear increase in error with acceleration, with an error of less than 20% for measured metabolites at an acceleration factor of 4 and less than 15% for an acceleration of 3.

The enhancement in SNR while keeping the linewidth constant for all metabolite resonance peaks provides distinct benefits for more accurate analysis. The technique confers significant advantages in terms of SNR gain, spectral quality and image quality and sharpness. With acceleration, the CS-LR method provides the potential to acquire data at a faster rate, albeit with an inherent tradeoff in spatial resolution and errors in metabolite quantification. Our results demonstrate that up to an acceleration of 2 for brain sequence acquisition and 3 for kidney sequence acquisition, the spatial loss and quantification errors remain within a 10% range. The ability to accelerate acquisition is highly desirable in clinical settings to ensure patient comfort and avoid lengthy acquisitions that could degrade data quality. This is particularly relevant in the context of the kidney scan, as the measurement of metabolite concentration in organs is crucial for ongoing research evaluating their viability for transplantation. Thus, a fast acquisition is a critical requirement in such applications.

A potential aspect of the CS-LR method that has yet to be explored in this study is the potential to utilize the acceleration to achieve an acquisition with the same acquisition time but at a higher resolution. In our ongoing research, we intend to modify the FID-MRSI sequence to include the acceleration into the acquisition protocol. One limitation of our experiment was the lack of multi-channel capability in the ^{31}P-MRSI coil. Incorporating multi-channel measurements from multiple spatial points, coupled with the coil sensitivity profile, would have provided more information for reconstruction and possibly improved results.

In a recent study by Santos-Díaz et al. [62], CS was combined with echo-planar spectroscopic imaging (EPSI) to accelerate the acquisition of dynamic ^{31}P-MRSI data. The researchers successfully applied CS to accelerate the acquisition of an 8×8 matrix by a factor of 2.7. In another study by Santos-Díaz et al. [63], the authors compared the performance of the CS model and the LR model, both in combination with a flyback EPSI sequence. The study demonstrated that the spectral quality was well preserved at accelerations of 2 and 3 using two CS reconstruction methods (one using L1 norm minimization and the other using low-rank Hankel matrix completion). The study demonstrated that the LR approach for reconstruction outperformed the CS methods at up to three-fold acceleration. This is in line with our results using combined CS-LR reconstruction.

In summary, we have presented a novel acquisition/reconstruction scheme, CS-LR, for the FID-MRSI sequence. A distinguishing aspect of this CS-LR method is the implementation of distinct random undersampling patterns for each weighted average. This approach of random k-space undersampling accelerates scan time and enables faster acquisition. Additionally, the reconstruction method has demonstrated remarkable efficiency in enhancing the SNR while preserving the spectral and spatial quality of the data at 3T.

ACKNOWLEDGMENTS

This study is supported by the Swiss National Science Foundation to F.L. (SNSF 320030_182658), and A.L. (SNSF PZ00P3_185927). We gratefully acknowledge the support of NVIDIA Corporation with the donation of the Titan V GPU used for this research. Open Access Funding provided by University of Geneva.

V. REFERENCES

[1] Buchli Reto, Meier Dieter, Martin Ernst, Boesiger Peter. Assessment of absolute metabolite concentrations in human tissue by 31P MRS in vivo. Part II: Muscle, liver, kidney *Magnetic Resonance in Medicine.* 1994;32:453-458.

[2] Chmelik M., Schmid A. I., Gruber S., et al. Three-dimensional high-resolution magnetic resonance spectroscopic imaging for absolute quantification of 31P metabolites in human liver *Magnetic Resonance in Medicine.* 2008;60:796-802.

[3] Webb Graham A.. , ed. *Chapter 3 - Methods and Applications of Phosphorus NMR Spectroscopy In Vivo*;75 of *Annual Reports on NMR Spectroscopy.* Academic Press 2012.

[4] Hwang Jong-Hee, Choi Cheol Soo. Use of in vivo magnetic resonance spectroscopy for studying metabolic diseases *Experimental & Molecular Medicine.* 2015;47:e139–e139.

[5] Rudin M.. , ed.*In-Vivo Magnetic Resonance Spectroscopy III: In-Vivo MR Spectroscopy: Potential and Limitations.* Springer Berlin Heidelberg 1992.

[6] Maudsley A.A, Hilal S.K, Perman W.H, Simon H.E. Spatially resolved high resolution spectroscopy by "four-dimensional" NMR *Journal of Magnetic Resonance (1969).* 1983;51:147–152.

[7] Klomp Dennis W. J., Bank Bart L., Raaijmakers Alexander, et al. 31P MRSI and 1H MRS at 7T: initial results in human breast cancer *NMR in Biomedicine.* 2011;24:1337–1342.

[8] Mandal Pravat K., Akolkar Himanshu, Tripathi Manjari. Mapping of Hippocampal pH and Neurochemicals from in vivo Multi-Voxel 31P Study in Healthy Normal Young Male/Female, Mild Cognitive Impairment, and Alzheimer's Disease *Journal of Alzheimer's Disease.* 2012;31:S75–S86.

[9] Parasoglou Prodromos, Xia Ding, Chang Gregory, Regatte Ravinder R.. 3D-mapping of phosphocreatine concentration in the human calf muscle at 7 T: Comparison to 3 T *Magnetic Resonance in Medicine.* 2013;70:1619–1625.

[10] Korzowski Andreas, Weinfurtner Nina, Mueller Sebastian, et al. Volumetric mapping of intra- and extracellular pH in the human brain using 31P MRSI at 7T *Magnetic Resonance in Medicine.* 2020;84:1707–1723.

[11] Franke Vanessa L., Breitling Johannes, Ladd Mark E., Bachert Peter, Korzowski Andreas. 31P MRSI at 7 T enables high-resolution volumetric mapping of the intracellular magnesium ion content in human lower leg muscles *Magnetic Resonance in Medicine.* 2022;88:511–523.

[12] Resnick L. M., Altura B. T., Gupta R. K., Laragh J. H., Alderman M. H., Altura B. M.. Intracellular and extracellular magnesium depletion in Type 2 (non-insulin-dependent) diabetes mellitus *Diabetologia.* 1993;36:767–770.

[13] Phielix Esther, Mensink Marco. Type 2 Diabetes Mellitus and Skeletal Muscle Metabolic Function *Physiology & Behavior.* 2008;94:252–258.

[14] Liu Yuchi, Mei Xunbai, Li Jielei, Lai Nicola, Yu Xin. Mitochondrial function assessed by 31P MRS and BOLD MRI in non-obese type 2 diabetic rats *Physiological Reports.* 2016;4:e12890.

[15] Barbagallo Mario, Belvedere Mario, Bella Giovanna Di, Dominguez Ligia J.. Altered ionized magnesium levels in mild-to-moderate Alzheimer's disease *Magnesium Research.* 2011;24:115–121.

[16] Das Namrata, Ren Jimin, Spence Jeffrey S., Rackley Audette, Chapman Sandra B.. Relationship of Parieto-Occipital Brain Energy Phosphate Metabolism and Cognition Using 31P MRS at 7-Tesla in Amnestic Mild Cognitive Impairment *Frontiers in Aging Neuroscience.* 2020;12.

[17] Lodi Raffaele, Iotti Stefano, Cortelli Pietro, et al. Deficient energy metabolism is associated with low free magnesium in the brains of patients with migraine and cluster headache *Brain Research Bulletin.* 2001;54:437–441.

[18] Reyngoudt Harmen, Paemeleire Koen, Descamps Benedicte, Deene Yves De, Achten Eric. 31P-MRS demonstrates a reduction in high-energy phosphates in the occipital lobe of migraine without aura patients *Cephalalgia.* 2011;31:1243–1253.

[19] Xin Lijing, Ipek , Beaumont Maurice, et al. Nutritional Ketosis Increases NAD^+/NADH Ratio in Healthy Human Brain: An in Vivo Study by 31P-MRS *Frontiers in Nutrition.* 2018;5.

[20] Reyngoudt Harmen, Kolkovsky Alfredo L. Lopez, Carlier Pierre G.. Free intramuscular Mg2+ concentration calculated using both 31P and 1H NMRS-based pH in the skeletal muscle of Duchenne muscular dystrophy patients *NMR in Biomedicine.* 2019:e4115.

[21] Torriani Martin, Townsend Elise, Thomas Bijoy J., Bredella Miriam A., Ghomi Reza H., Tseng Brian S.. Lower leg muscle involvement in Duchenne muscular dystrophy: an MR imaging and spectroscopy study *Skeletal Radiology.* 2011;41:437–445.

[22] Lodi Raffaele, Kemp Graham J., Muntoni Francesco, et al. Reduced cytosolic acidification during exercise suggests defective glycolytic activity in skeletal muscle of patients with Becker muscular dystrophy *Brain.* 1999;122:121–130.

[23] Taylor J S, Vigneron D B, Murphy-Boesch J, et al. Free magnesium levels in normal human brain and brain tumors: 31P chemical-shift imaging measurements at 1.5 T. *Proceedings of the National Academy of Sciences.* 1991;88:6810–6814.

[24] Stubbs Marion, Rodrigues Loreta, Howe Franklyn A., et al. Metabolic Consequences of a Reversed pH Gradient in Rat Tumors1 *Cancer Research.* 1994;54:4011-4016.

[25] Seelen Leonard W. F., Wildenberg Lieke, Kemp Wybe J. M., et al. Prospective of 31P MR Spectroscopy in Hepatopancreatobiliary Cancer: A Systematic Review of the Literature *Journal of Magnetic Resonance Imaging.* 2022.

[26] Boulangé Claire L.. Nuclear Magnetic Resonance Spectroscopy-Applicable Elements| Phosphorus-31 in *Reference Module in Chemistry, Molecular Sciences and Chemical Engineering*Elsevier 2017.

[27] Qiao Hongyan, Zhang Xiaoliang, Zhu Xiao-Hong, Du Fei, Chen Wei. In vivo 31P MRS of human brain at high/ultrahigh fields: a quantitative comparison of NMR detection sensitivity and spectral resolution between 4T and 7T *Magnetic Resonance Imaging.* 2006;24:1281–1286.

[28] Bogner Wolfgang, Otazo Ricardo, Henning Anke. Accelerated MR spectroscopic imaging—a review of current and emerging techniques *NMR in Biomedicine.* 2020;34.

[29] Block Kai Tobias, Uecker Martin, Frahm Jens. Undersampled radial MRI with multiple coils. Iterative image reconstruction using a total variation constraint *Magnetic Resonance in Medicine.* 2007;57:1086–1098.

[30] Lustig Michael, Donoho David, Pauly John M.. Sparse MRI: The application of compressed sensing for rapid MR imaging *Magnetic Resonance in Medicine.* 2007;58:1182–1195.

[31] Donoho D.L.. Compressed sensing *IEEE Transactions on*

Information Theory. 2006;52:1289-1306.

[32] Vranic J.E., Cross N.M., Wang Y., Hippe D.S., Weerdt E., Mossa-Basha M.. Compressed Sensing-Sensitivity Encoding (CS-SENSE) Accelerated Brain Imaging: Reduced Scan Time without Reduced Image Quality *American Journal of Neuroradiology.* 2018;40:92–98.

[33] Suh Chong Hyun, Jung Seung Chai, Lee Ho Beom, Cho Se Jin. High-Resolution Magnetic Resonance Imaging Using Compressed Sensing for Intracranial and Extracranial Arteries: Comparison with Conventional Parallel Imaging *Korean Journal of Radiology.* 2019;20:487.

[34] Kayvanrad Mohammad, Lin Amy, Joshi Rohit, Chiu Jack, Peters Terry. Diagnostic quality assessment of compressed sensing accelerated magnetic resonance neuroimaging *Journal of Magnetic Resonance Imaging.* 2016;44:433–444.

[35] Delattre Bénédicte Marie Anne, Boudabbous Sana, Hansen Catrina, Neroladaki Angeliki, Hachulla Anne-Lise, Vargas Maria Isabel. Compressed sensing MRI of different organs: ready for clinical daily practice? *European Radiology.* 2019;30:308–319.

[36] Geethanath Sairam, Baek Hyeon-Man, Ganji Sandeep K., et al. Compressive Sensing Could Accelerate ^{1}H MR Metabolic Imaging in the Clinic *Radiology.* 2012;262:985–994.

[37] Chatnuntawech Itthi, Gagoski Borjan, Bilgic Berkin, Cauley Stephen F., Setsompop Kawin, Adalsteinsson Elfar. Accelerated ^{1}H MRSI using randomly undersampled spiral-based k-space trajectories *Magnetic Resonance in Medicine.* 2014;74:13–24.

[38] Wilson Neil E., Iqbal Zohaib, Burns Brian L., Keller Margaret, Thomas M. Albert. Accelerated five-dimensional echo planar J-resolved spectroscopic imaging: Implementation and pilot validation in human brain *Magnetic Resonance in Medicine.* 2015;75:42–51.

[39] Klauser Antoine, Courvoisier Sebastien, Kasten Jeffrey, et al. Fast high-resolution brain metabolite mapping on a clinical 3T MRI by accelerated 1H-FID-MRSI and low-rank constrained reconstruction *Magnetic Resonance in Medicine.* 2018;81:2841–2857.

[40] Klauser Antoine, Klauser Paul, Grouiller Frédéric, Courvoisier Sébastien, Lazeyras François. Whole-brain high-resolution metabolite mapping with 3D compressed-sensing SENSE low-rank H FID-MRSI *NMR in Biomedicine.* 2021;35.

[41] Klauser Antoine, Strasser Bernhard, Thapa Bijaya, Lazeyras Francois, Andronesi Ovidiu. Achieving high-resolution 1H-MRSI of the human brain with compressed-sensing and low-rank reconstruction at 7 Tesla *Journal of Magnetic Resonance.* 2021;331:107048.

[42] Hu Simon, Lustig Michael, Chen Albert P., et al. Compressed sensing for resolution enhancement of hyperpolarized 13C flyback 3D-MRSI *Journal of Magnetic Resonance.* 2008;192:258–264.

[43] Hu Simon, Lustig Michael, Balakrishnan Asha, et al. 3D compressed sensing for highly accelerated hyperpolarized 13C MRSI with in vivo applications to transgenic mouse models of cancer *Magnetic Resonance in Medicine.* 2009;63:312–321.

[44] Larson Peder E. Z., Hu Simon, Lustig Michael, et al. Fast dynamic 3D MR spectroscopic imaging with compressed sensing and multiband excitation pulses for hyperpolarized 13C studies *Magnetic Resonance in Medicine.* 2010;65:610–619.

[45] Cao Peng, Shin Peter J., Park Ilwoo, et al. Accelerated high-bandwidth MR spectroscopic imaging using compressed sensing *Magnetic Resonance in Medicine.* 2016;76:369–379.

[46] Nguyen Hien M., Peng Xi, Do Minh N., Liang Zhi-Pei. Denoising MR Spectroscopic Imaging Data With Low-Rank Approximations *IEEE Transactions on Biomedical Engineering.* 2013;60:78–89.

[47] Liu Yan, Ma Chao, Clifford Bryan, Lam Fan, Johnson Curtis, Liang Zhi-Pei. Improved Low-Rank Filtering of Magnetic Resonance Spectroscopic Imaging Data Corrupted by Noise and B_0Field Inhomogeneity *IEEE Transactions on Biomedical Engineering.* 2015:1–1.

[48] Ma Chao, Lam Fan, Johnson Curtis L., Liang Zhi-Pei. Removal of nuisance signals from limited and sparse ^{1}H MRSI data using a union-of-subspaces model *Magnetic Resonance in Medicine.* 2015;75:488–497.

[49] Ma Chao, Clifford Bryan, Liu Yuchi, et al. High-resolution dynamic ^{31}P-MRSI using a low-rank tensor model *Magnetic Resonance in Medicine.* 2017;78:419–428.

[50] Zibetti Marcelo V.W., Sharafi Azadeh, Otazo Ricardo, Regatte Ravinder R.. Accelerating 3D-T_1mapping of cartilage using compressed sensing with different sparse and low rank models *Magnetic Resonance in Medicine.* 2018;80:1475–1491.

[51] Zhang Li, Athavale Prashant, Pop Mihaela, Wright Graham A.. Multicontrast reconstruction using compressed sensing with low rank and spatially varying edge-preserving constraints for high-resolution MR characterization of myocardial infarction *Magnetic Resonance in Medicine.* 2016;78:598–610.

[52] Zhao Bo, Haldar Justin P., Brinegar Cornelius, Liang Zhi-Pei. Low rank matrix recovery for real-time cardiac MRI in *2010 IEEE International Symposium on Biomedical Imaging: From Nano to Macro*IEEE 2010.

[53] Bredies Kristian, Kunisch Karl, Pock Thomas. Total Generalized Variation *SIAM Journal on Imaging Sciences.* 2010;3:492–526.

[54] Knoll Florian, Bredies Kristian, Pock Thomas, Stollberger Rudolf. Second order total generalized variation (TGV) for MRI *Magnetic Resonance in Medicine.* 2011;65:480-491.

[55] Pohmann Rolf, Kienlin Markus. Accurate phosphorus metabolite images of the human heart by 3D acquisition-weighted CSI 2001;45:817–826.

[56] Kasten Jeffrey, Lazeyras Franois, Van De Ville Dimitri. Data-Driven MRSI Spectral Localization Via Low-Rank Component Analysis *IEEE Transactions on Medical Imaging.* 2013;32:1853-1863.

[57] Lustig M., Donoho D.L., Santos J.M., Pauly J.M.. Compressed Sensing MRI *IEEE Signal Processing Magazine.* 2008;25:72–82.

[58] Songeon Julien, Courvoisier Sébastien, Xin Lijing, et al. In vivo magnetic resonance 31P-Spectral Analysis With Neural Networks: 31P-SPAWNN *Magnetic Resonance in*

Medicine. 2022;89:40–53.

[59] Longchamp Alban, Klauser Antoine, Songeon Julien, et al. Ex Vivo Analysis of Kidney Graft Viability Using 31P Magnetic Resonance Imaging Spectroscopy *Transplantation.* 2020;104:1825–1831.

[60] Agius Thomas, Songeon Julien, Klauser Antoine, et al. Subnormothermic Ex Vivo Porcine Kidney Perfusion Improves Energy Metabolism: Analysis Using 31P Magnetic Resonance Spectroscopic Imaging *Transplantation Direct.* 2022;8:e1354.

[61] Yu Honghai, Winkler Stefan. Image complexity and spatial information in *2013 Fifth International Workshop on Quality of Multimedia Experience (QoMEX)*:12-17 2013.

[62] Santos-Díaz Alejandro, Harasym Diana, Noseworthy Michael D.. Dynamic 31P spectroscopic imaging of skeletal muscles combining flyback echo-planar spectroscopic imaging and compressed sensing *Magnetic Resonance in Medicine.* 2019;81:3453–3461.

[63] Santos-Díaz Alejandro, Noseworthy Michael D.. Comparison of compressed sensing reconstruction algorithms for 31P magnetic resonance spectroscopic imaging *Magnetic Resonance Imaging.* 2019;59:88–96.

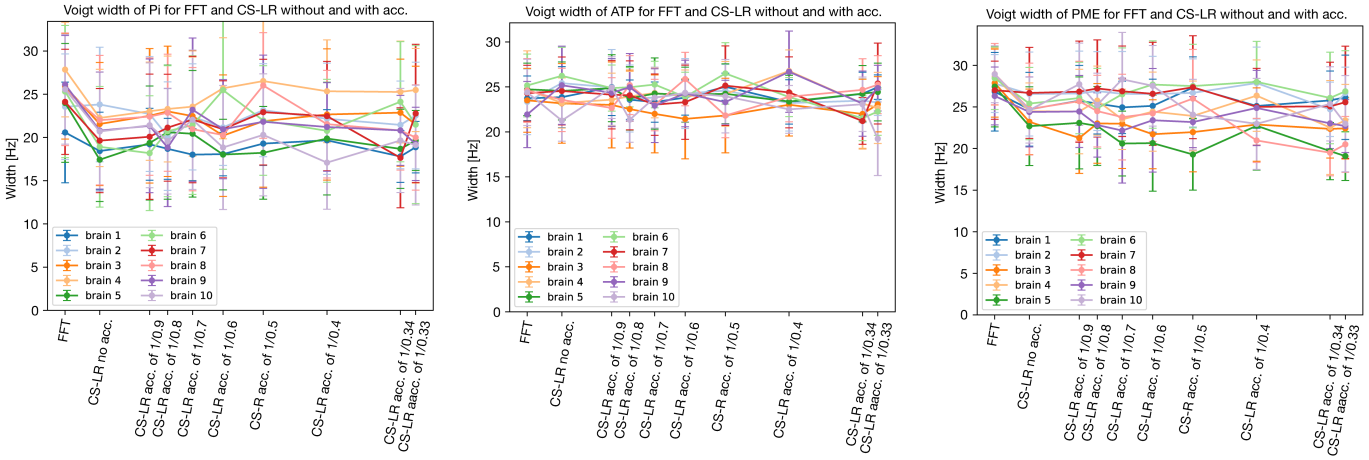

FIG. S1. This supplementary figure presents the peak width measurements of Pi, ATP, and PME. These peak width measurements were obtained using the same experimental setup as Figure 3, with the FFT of the original data and the CS-LR reconstruction without and with acceleration. The data were acquired from the same 10 volunteers and the peak widths were computed using the same fitting procedure. These measurements provide additional insights into the impact of the reconstruction methods on the spectral peaks.

Part IV

TRANSPLANTATION APPLICATIONS: PHOSPHORUS SPECTROSCOPIC IMAGING FOR PRE-TRANSPLANTATION KIDNEY PRESERVATION AND VIABILITY ASSESSMENT

9

TRANSPLANTATION ASSESSMENT BY MRI

"I learned that myth doesn't mean a lie; it means a traditional story that tells you something about people and their worldview and what they hold sacred."

- John Green *Looking for Alaska*

Contents

9.1 INTRODUCTION

The field of organ transplantation has seen significant growth since its inception in the 20^{th} century. The growing demand for transplantation has been met with improved clinical outcomes and higher survival rates, leading to a more reliable procedure[112]. The objective of transplant programs is to maximize the utilization of available organs. The success of transplantation is dependent on the quality of the donor graft, and chronic rejection or graft failure can often occur after an acute rejection episode [113, 114]. In order to prevent wastage and the use of organs that may lead to primary graft dysfunction, it is crucial to have a dependable evaluation of stored organ viability [115].

Magnetic Resonance Spectroscopy (MRS) can provide both a pre-transplant evaluation and a follow-up procedure [116]. MRI and MRS are non-invasive techniques that offer anatomical and metabolic information about the patient. These techniques are important as biopsy carries risks for the subject and is prone to sampling errors [117]. MRI has excellent soft tissue contrast and can detect organ function and morphology with high resolution, without being limited by the depth of tissue penetration [118]. MRI-based methodologies can not only identify the infiltration of immune cells at rejection sites but also evaluate organ dysfunction resulting from acute rejection.

Transplantation has become a preferred treatment option for patients suffering from end-stage organ dysfunction due to its expanding pool of transplantable solid organs, including the liver, kidney, heart, pancreas, stomach, and lungs [119]. Despite its success, the field of transplantation faces two major challenges. The first challenge is the high demand for transplants, which exceeds the current supply of available organs. The second challenge is the persistent issue of chronic allograft rejection, which remains a leading cause of mortality among transplant patients. Efforts have been made to expand the donor pool by considering organs from marginal donors or donors after circulatory death (DCD). This includes those from donors over 60 years of age without any pre-existing conditions and those between 50 and 60 years of age with specific conditions such as arterial hypertension or a history of cerebrovascular disease with no additional risk factors [120]. However, the use of marginal organs can result in pre-existing graft damage and increases the risk of ischemia-reperfusion injury, leading to delayed graft function, acute rejection, and poor long-term survival [121, 122]. In order to address these challenges, two areas of research stand out: early diagnosis of acute rejection and continued monitoring of transplanted organs. Early diagnosis would provide tools to expand the donor

pool by evaluating marginal organs, and improve the success of transplantation by reducing the risk of acute rejection. Additionally, given the limited success of retransplantation, there is also a need for improvement in the diagnosis and management of chronic allograft rejection [123].

This chapter will begin with a comprehensive literature review on the application of phosphorus magnetic resonance spectroscopy to the field of organ transplantation, conducted as part of an assessment for a doctoral course on *Advanced biomedical imaging methods and instrumentation*. The subsequent section will focus on the viability assessment and preservation of kidneys before transplantation using MRI. This discussion will provide an introduction to the succeeding chapters, namely Chapter 10, Chapter 11, and Chapter 12.

9.2 REVIEW OF TRANSPLANT ORGANS ASSESSMENT WITH ^{31}P-MRS

9.2.1 *Transplant Rejection: Diagnosis and Outcomes*

9.2.1.1 *Acute rejection*

The process of acute allograft rejection occurs when the transplant recipient's immune system identifies the newly transplanted organ as a foreign entity and launches an attack against it. This reaction is rapid and can occur within the first two weeks following transplantation, and it occurs in the absence of immunosuppression [124]. Macrophages and leukocytes, among other immune cells, infiltrate the graft and cause cell necrosis, vessel thrombosis, and a loss of organ function. T-lymphocytes and NK cells also directly damage myocytes, endothelial cells, and connective tissue [125]. The use of immunosuppressant medications can help to prevent acute rejection by reducing the activity of the immune system. Despite the use of such treatments, however, the graft can still undergo chronic rejection. Research has shown that an episode of acute rejection increases the likelihood of chronic rejection later on [126]. Despite advances in reducing early acute rejection and improving the efficacy of immunosuppressive treatments, the incidence of chronic rejection and late graft loss has not been significantly altered [127].

9.2.1.2 *Chronic rejection*

Chronic rejection is a significant issue in organ transplantation as it is the leading cause of late graft loss, leading to a gradual decline in graft function and a reduction in long-term survival rates [128]. The factors affecting the organ and resulting in rejection are numerous, including ischemia which negatively impacts the mitochondrial antioxidant system by reducing the activity of antioxidant enzymes, such as manganese superoxide dismutase, and depleting essential substrates such as glutathione, making cells more susceptible to oxidative stress during reperfusion [129–132]. Reperfusion, the reintroduction of oxygen after a period of ischemia, results in an increase in reactive oxygen species production, a decrease in ATP production, and cell death. The formation of these species is exacerbated by glutathione depletion, leading to further oxidative damage to thiols and hydroxyl radical formation. Additionally, reactive oxygen species produced during reperfusion may cause damage to proteins, lipids, and DNA, leading to further mitochondrial disruption, sterile immune inflammation, and cell death through necrosis and apoptosis [133, 134]. In heart transplantation, ischemia and reperfusion injury are inevitable due to the hypothermic preservation, warm ischemia, and reperfusion of the graft. These events may contribute to early graft failure and reduce the longevity of the donor heart. Preservation fluids are designed to limit oxidative stress and calcium overload, with cold ischemic storage being the cornerstone of myocardial preservation. However, hypothermia on its own is associated with cellular swelling and intracellular acidosis [135].

9.2.1.3 *Rejection diagnosis*

The evaluation of acute and chronic rejections in organ transplantation requires several tools. The clinical gold standard for diagnosing rejection is biopsy, where a small tissue sample from the graft is analyzed through hematologic analysis to determine immune cell infiltration and pathological changes [136]. Currently, biopsy is the only technique capable of differentiating between antibody-mediated rejection and acute cellular rejection. Despite its proven low risk, such as in endomyocardial biopsy, there is still a finite risk of morbidity and mortality [137, 138]. Furthermore, the procedure is invasive and susceptible to sampling errors due to limited tissue size and location [118]. Biopsy also has limitations. For instance, the presence of T cell-mediated rejection or antibody-mediated rejection in a kidney transplant biopsy sample is only inferred from the identification of nonspecific lesions in histology. These assessments are probabilistic and the true disease state is often uncertain as there is no external method to assess the accuracy of the diagnosis [139].

Acute and chronic rejection pose a significant risk to allograft survival. Thus, implementing reliable methods for organ viability assessment, prior to transplantation, are crucial in improving the viability of an allograft after transplantation. The next sections will explore the possibilities of assessing the viability of an organ before transplantation and its recovery after transplantation.

9.2.2 *Assessing organ viability before transplantation with ^{31}P-MRS*

9.2.2.1 *Evaluation of organ viability*

Organ transplantation outcome can be improved through effective evaluation of the quality of the organ to be transplanted. Currently, the selection of an organ is based on subjective criteria, such as the age and medical history of the donor. An ideal donor is considered to be under the age of 40, have died from trauma, be in hemodynamic stability at the time of procurement, have no underlying chronic liver lesions or steatosis, and not have any transmissible diseases [140, 141]. Such criteria have been associated with better transplant outcomes and reduced risk of initial organ dysfunction [142]. However, it is important to note that an ideal donor does not guarantee an ideal graft, as post-harvest factors, such as ischemia, can also affect the quality of the graft [143]. Donors who do not meet these criteria are typically discarded, but can still be considered as extended criteria donors. The use of extended criteria donors increases the risk of poor graft function, graft failure, or transmission of disease [144]. The possibility of a more thorough evaluation of grafts from extended criteria donors could help to expand the pool of available organs while reducing the risk of complications associated with their use.

9.2.2.2 *Kidney viability*

The study of the kidney using ^{31}P magnetic resonance spectroscopy (MRS) has a long and storied history, beginning in the late 1970s with the landmark study performed by Sher et al. [145, 146]. This pioneering work demonstrated the depletion of high energy phosphates in the kidney during cold ischemia and its subsequent recovery after reperfusion, and suggested that MRS could be used to assess the kidney during cold storage.

In the decades that followed, advances in MRS technology allowed for more detailed and nuanced assessments of kidney viability. One such study was performed by Bretan et al. [147] in the early 1990s. This study used ^{31}P-MRS analysis to investigate the impact of cold static storage (CSS) on 40 kidneys prior to transplantation, using a 1.5 Tesla magnetic field. The authors were able to observe the MRS parameters impact on the kidney and found no correlation with the CSS ($p=0.74$). However, the results showed that specific observed metabolites, α-ATP

and NAD+, were only present in 11 of the 40 kidneys studied, but their presence was associated with the best renal function on the post-operative day (POD). In addition, the authors observed that only 36% of patients with detectable α-ATP or NAD+ required dialysis, while 71% of patients without detectable metabolites required dialysis. The authors postulated that while the observation of α-ATP and NAD+ is useful for qualitative purposes, it is not quantitative. Kidneys that exhibit higher PME/Pi ratio, which is linked to better renal function, are characterized by observable levels of α-ATP or NAD+. The authors observed that a lower PME/Pi ratio is associated with prolonged non-function caused by acute tubular necrosis (ATN) ($p<0.001$). Furthermore, the PME/Pi ratio has a correlation ($p<0.002$) with renal function and the need for dialysis post-operative day (POD). This ratio can be used as a quantitative indicator of viability, with a ratio less than 0.5 indicating the need for dialysis, and a ratio greater than 0.5 indicating the lack of need for dialysis. The PME/Pi ratio has been found to be a sensitive and specific parameter for assessing renal function.

A study by Hené et al. [148] investigated deeper into the PME/Pi ratio using a ^{31}P-MRS study on kidneys preserved with non-phosphate fluid. The study included 42 kidneys, with 5 coming from living related donors (LRD), 28 from 22 heart beating donors (HBD), and 9 from 6 non-heart donors (non-HBD). The results showed that all recipients of kidneys from LRD had immediate postoperative function, while delayed function was observed in 21% of the HBD group and 56% in the non-HBD group. NMR assessment revealed that the kidneys from LRD had a higher mean PME/Pi ratio compared to the kidneys from the HBD and non-HBD groups ($p<0.01$). Both the HBD and non-HBD groups whose kidneys were from patients with ATN had a lower PME/Pi ratio compared to the LRD group ($p<0.05$). The authors also conducted a measurement of the time evolution of the PME/Pi ratio and found that kidneys from the HBD group and two non-implanted kidneys had an inverse correlation with time, showing a linear decrease in the ratio. This observation concurs with the findings of Bretan et al. [147] regarding the gradual decay of high-energy phosphate over time. The primary conclusion of this study highlights the relationship between high-energy phosphate and graft dysfunction caused by ATN. The authors suggest that transplanting an organ with a low PME/Pi ratio in patients with other risk factors could potentially lead to complications, and it may be wise to avoid such a transplant.

9.2.2.3 *Liver viability*

In addition to the ongoing research on the viability of kidneys, the liver viability was also being evaluated using ^{31}P-MRS. While the kidney had artificial support available, the liver lacked this support until recent times, requiring immediate graft function to treat end-stage liver diseases. The development of the first artificial support, known as the Molecular Adsorbent Recirculating System (MARS), began in the 1990s and became widely available for clinical use in 1998 [149]. The system is based on the principle of albumin dialysis [150]. Before this support was available, researchers sought to evaluate liver viability before transplantation by testing the integrity of adenine nucleotide composition, which determines the organ's intrinsic capacity to regain its original function. This was done through high-performance liquid chromatography but the technique was time-consuming and carried the risk of damaging the organ through biopsy.

In 1997, Wolf et al. publish a paper in which they assess donors liver before transplantation using ^{31}P-MRS as an alternative to the biopsy [151]. Their analysis revealed a positive correlation between the PME to NAD+/NADH ratio and fibrinogen concentrations in the three days following transplantation ($P<0.001$, $P<0.01$, and $P<0.01$, respectively). The authors observed that the presence of β-ATP in the spectrum was significantly correlated with several indicators of hepatocellular graft damage and liver metabolic function, such as postoperative bilirubin levels and prothrombin time. Based on their observations, they concluded that although a cor-

relation between PME and postoperative fibrinogen was found, PME in human livers is not a reliable prognostic indicator of postoperative organ function. They also noted that the presence of ATP was of prognostic significance for prothrombin time, bilirubin, and fibrinogen after transplantation.

9.2.3 *Assessing organ recovery after transplantation with ^{31}P-MRS*

9.2.3.1 *Post-transplantation evaluation*

The advancements in post-operative medical treatments have resulted in significant improvement in transplantation outcomes [152]. In order to monitor the progress of the graft, various techniques have been developed, including biopsy, immunological monitoring, computerized tomography, ultrasound, and MRI and MRS [117]. These techniques play a crucial role in ensuring the successful integration of the graft with the recipient's body. MRI is a commonly used method for monitoring transplanted organs. The method is based on the measurement of changes in T_1 and T_2 values, which are indicative of the state of the transplant. An increase in these values and an enlargement of the organ volume have been reported in cases of allograft rejection, including kidney transplantation [118]. By providing insight into the progress of the transplant, MRI plays an important role in ensuring the success of the transplantation process.

9.2.3.2 *Kidney evaluation*

In 1987, Shapiro et al. published a study on the use of ^{31}P-MRS to evaluate acute renal dysfunction in rat kidney transplantation [153]. The study aimed to investigate the causes of renal allograft rejection, including ischemia, cyclosporine toxicity, and ureteral obstruction. The results showed that rejected kidneys exhibited an increase in the inorganic phosphate signal (19.8 a.u. vs 6.6 a.u., $p<0.01$) and a decrease in β-ATP (8.6 a.u. vs 17.9 a.u., $p<0.01$), which was confirmed through histological analysis. The intercellular pH did not show any significant differences from the control group in cases of rejection. In the group subjected to ischemia, an increase in inorganic phosphate (21.7 a.u vs 6.6 a.u, $p<0.01$) and a decrease in β-ATP (7.6 a.u vs 17.9 a.u, $p<0.01$) were observed, along with a decrease in intercellular pH ($p<0.01$). The kidney from the ureteral obstructed group showed an enormous increase in phosphodiesters and urine phosphate (44.5 a.u vs 13.6 a.u, $p<0.01$), which the authors suggest could be linked to the increase in net urine phosphate caused by the obstruction. Interestingly, no distinguishable changes were observed in the spectroscopy of the kidney subjected to toxic doses of cyclosporine. This highlights the importance of using ^{31}P-MRS as a tool to better understand the mechanisms of renal dysfunction in transplantation and to develop more effective treatments for rejection.

The study by Boska et al. [154] evaluated the feasibility of obtaining high-quality spatially localized ^{31}P spectra in humans. The research was conducted on 14 volunteers with healthy kidneys and 6 patients with functioning kidney transplants for more than a year. The results revealed no statistically significant differences in the concentration of major peaks, such as the ATP resonances, PMD, PDE, and Pi, between the two groups. Grist et al. [155] conducted a similar study by performing ^{31}P-MRS on patients with functioning kidney transplants and those undergoing biopsy for suspected allograft dysfunction. Out of the 21 spectroscopy results obtained, 14 showed evidence of rejection, while 7 showed no evidence of rejection. In the case of patients with signs of rejection, biopsy results indicated that 5 had mild rejection, 5 had moderate rejection, and 4 had severe rejection. The results showed a statistically significant difference in the mean ratio of PDE/PME (1.43 for the rejecting group vs 0.55 for the control group, $p=0.024$) and Pi/ATP (1.1 for the rejecting group vs 0.35 for the control group, $p=0.017$). The study also revealed that the three patients with no evidence of rejection had cyclosporine

toxicity and a higher ratio of PDE/PME, but it was not statistically significant (0.79 vs 0.55, p=0.085). The authors reported that the elevation of the Pi/ATP ratio was consistent with animal models and was a sensitive indicator of tissue ischemia. However, they also noted that the low pH in urine was responsible for the chemical shift of Pi, resulting in overlap between Pi and PDE. This caused an increase in the PDE peak in urine Pi, but the authors found no signs of obstruction in the patients, contradicting the assumption in Shapiro's paper.

9.2.3.3 *Liver evaluation*

In early study on liver assessment after transplantation, Sumimoto et al. paper [156] investigated rat liver immediately after orthotopic transplantation. They studies rats livers after transplantation, and compared the ATP levels with bile flow. Four hours after the translation, livers exposed to warm ischemia (0-min, 15-min and 30-min) had a lower ATP resynthesis with a concentration of 2.27 —mol/g for the livers with no warm ischemia, and 1.79 —mol/g and 0.19 µmol/g for the livers with warm ischemia. The authors also observed a decrease of bile flow rate with 2.84 ml/g/hr for liver with no warm ischemia, and 1.98 ml/g/hr and 0.46 ml/g/hr for the others group respectively. The authors wrote that the results were an indicator that the bile rate flow recovery and ATP resynthesis, and that they are correlated with the survival rate of the animals.

^{31}P-MRSI was used to study the liver regeneration and energetic changes in rats following a hepatic radiating therapy and hepatocyte transplantation [157]. In their paper, Landis et al. investigate the metabolic changes on rodents that occur in the treatment of radiation-induced liver disease (RILD). The treatments studied were partial hepatectomy (PH), PH with hepatic irradiation (PHRT), and PHRT with hepatocyte transplantation (HT). Radiation therapy is used as treatment of solid tumours, but has limited usage on metastatic liver cancers as it has the potential of inducing complication with radiation-induced liver disease. The hepatocyte transplantation is proposed as treatment of RILD. The authors highlights the lack of early diagnostic for RILD, as symptoms appear in late stage, and emphasise that the need to monitor the success and efficacy of HT. They observed that ATP/Pi ratio was reduced within 24 h of PH and relate the significance of ATP/Pi ratio as a reliable index of the hepatic cytosolic energy status. HT has a gradual normalization of ATP over time, meaning that it restored the bioenergetic reserve and the liver function. The reduced ATP/Pi combined with the normalization of ATP levels in the PHRT-HT group suggested that the transplanted hepatocytes is able to restore the metabolic function and proliferate in time. The authors conclude that the results suggested the possibility of using ^{31}P-MRSI to monitor RILD and its improvement after transplantation.

9.2.4 *Review conclusion*

^{31}P-MRS and ^{31}P-MRSI represent powerful tools for investigating in vivo energy metabolism. Their development over the years has demonstrated their potential for application in the field of transplantation. While biopsy remains the gold standard for assessing graft status, its use is limited and invasive. On the other hand, phosphorus magnetic resonance spectroscopy provides a non-invasive approach for monitoring the status of transplanted organs and evaluating the health status of donor organs. ^{31}P-MRS has shown promising results throughout the transplantation procedure, and has the potential to become a future gold standard in this field.

9.3 KIDNEY PRESERVATION AND AND PRE-TRANSPLANT ASSESSMENT BY MRI

9.3.1 *Organ shortage and marginal grafts transplant*

As outlined in the introduction, organ transplantation is the preferred mode of treatment for end-stage disease; however, it is afflicted by a critical shortage of available organs. Figure 41 provides statistical information on the number of individuals on the organ transplant waiting list in Switzerland, the number of fatalities that occurred while awaiting transplantation, and the total number of successful transplantations that were carried out in the country in 2022. These figures comprise both deceased and living donor donations.

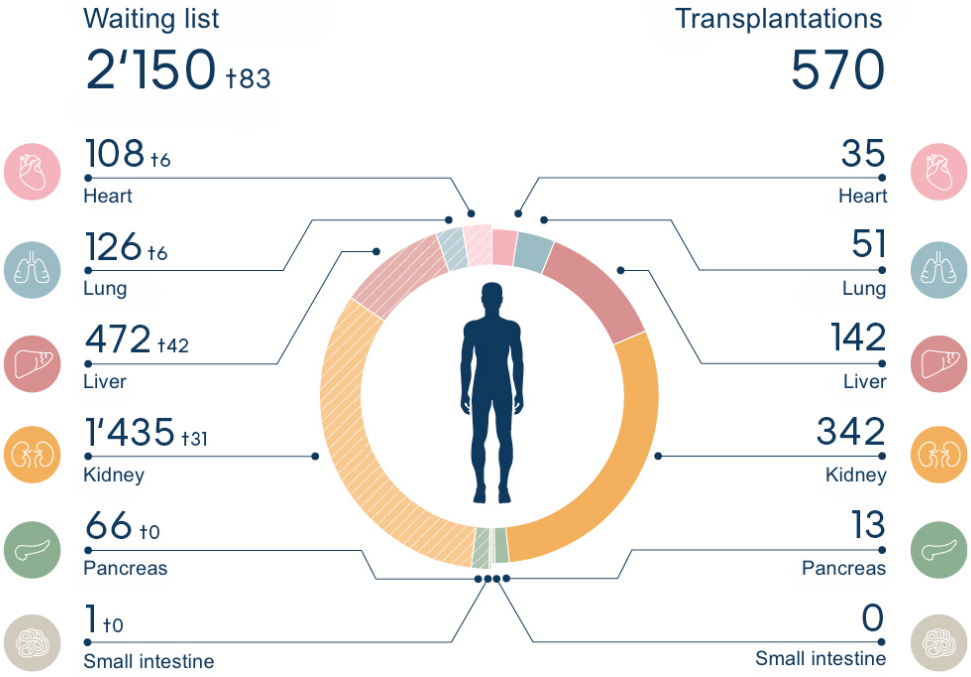

Figure 41: Number of persons on the waiting list (at least one day), number of deaths on the waiting list, and number of transplants in Switzerland in 2022 by organ (including living donor donations). Individuals who were on the waiting list for more than one organ are included in the corresponding waiting list for each organ but are only counted once for the overall total. Likewise, a combined transplantation involving multiple organs is counted for each relevant organ but only counted once for the overall total [22].

This information is crucial in enhancing comprehension of the present state of organ transplantation in Switzerland and the demand for organs. Of particular concern is the situation with respect to end-stage renal disease (ESRD), as the number of patients on the kidney waiting list is four times greater than that of any other organ. ESRD is a condition estimated to affect a minimum of two million individuals worldwide [158]. The limited availability of organs for transplantation forces many ESRD patients to rely on dialysis or face poor survival rates, with a 5-year survival rate of only 40%-50% and costs up to 10 times higher than transplantation [159]. To address the shortage of available organs, marginal donors are being considered. This donor pool has been expanded beyond standard-criteria donors to include extended-criteria donors (ECD) and donation after circulatory death (DCD) donors, also known as marginal donors [160, 161]. Marginal donors are defined as individuals over 60 years of age or over 50 years of age with a history of high blood pressure, creatinine levels greater than or equal to 1.5 mg/dL, or death due to a stroke [162]. However, the usage of marginal donors is limited by the lack of a reliable non-invasive means of determining kidney viability. Although the organs from

The reference range for normal creatinine levels is typically reported as 0.7 *to* 1.3 mg/dL *for men and* 0.6 *to* 1.1 mg/dL *for women.*

marginal donors have a better survival rate than dialysis [163], their usage is complicated by a higher rate of delayed graft function (DGF) [164] and acute rejection [159]. During the transplantation procedure, the organs are subjected to several stresses, including those associated with ischemia-reperfusion injury (IRI) because of the organ's reperfusion after a delay of cold or warm ischemia. Unfortunately, marginal organs are highly vulnerable to IRI and are at risk of transplant failure and subsequent poor long-term survival [159, 164].

9.3.2 *Ischemia-Reperfusion Injury*

The procurement of organs is inherently linked to ischemia-reperfusion injury (IRI), which occurs when the blood supply to a tissue is obstructed for several minutes to hours and then restored. IRI is associated with an increased likelihood of delayed graft function, acute graft rejection, and graft loss [121, 122]. Currently, the methods employed to reduce IRI during renal transplantation involve the use of optimized preservation solutions and cold storage of kidneys during the peritransplantation and transportation period [165]. However, these techniques have reached their maximum potential, and prolonged periods of cold ischemia (> 24 h) are still associated with acute tubular necrosis (ATN), delayed graft function, and poor graft survival [166–168].

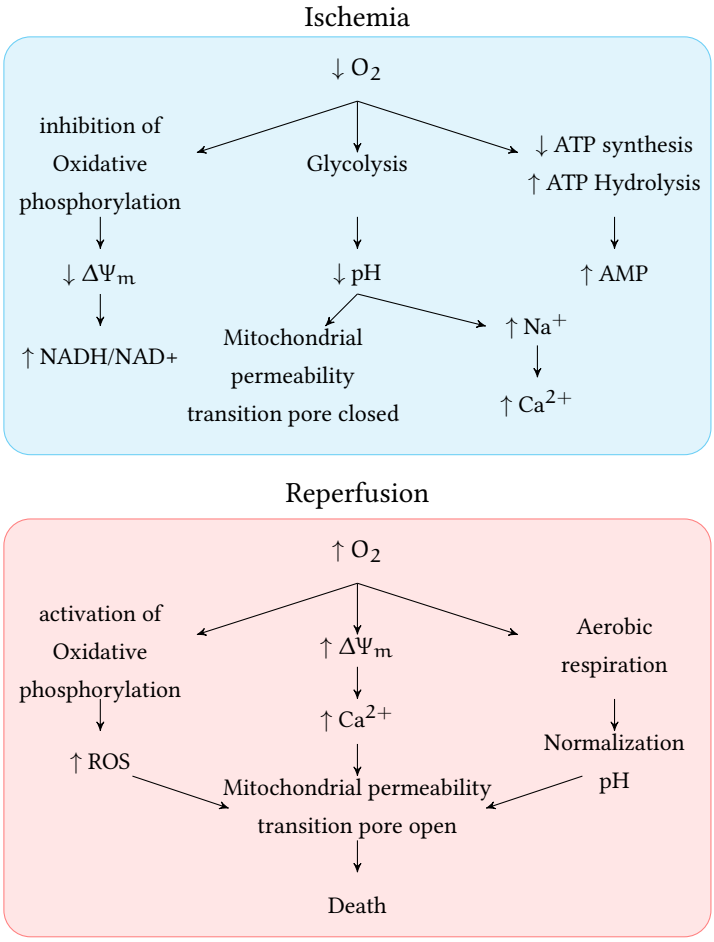

Figure 42: Schematic illustrating the principal components involved in ischemia-reperfusion injury (IRI), with the ischemic phase in blue and the reperfusion phase in red [169]

According to current consensus, human kidney tissue that experiences ischemia lasting more than 30 minutes is predisposed to further injury upon reperfusion. Although the majority of

the damage occurs during reperfusion, ischemic cells will die if blood flow is not restored. Figure 42 presents a schematic diagram that depicts the primary constituents implicated in the phenomenon of ischemia-reperfusion injury.

During the ischemic phase, the depletion of ATP inhibits mitochondrial Na^+/K^+ ion channels, which results in a decrease in mitochondrial membrane potential ($\Delta\Psi_m$), an increase in mitochondrial inner membrane permeability, an influx of calcium ions, and subsequent swelling of mitochondria. Inner membrane permeability also alters the redox state by oxidizing pyridines and thiols and modifying the reduced/oxidized of NADH/NAD+ ratio [169–171]. Ischemia also affects the mitochondrial antioxidant system by reducing the activity of antioxidant enzymes rendering cells more susceptible to oxidative stress during reperfusion [129, 130, 132, 172]. The deprivation of oxygen promotes a shift to anaerobic respiration, which generates lactate and causes a decrease in intracellular pH. The low pH also inhibits the opening of the mitochondrial permeability transition pore (mPTP) [173]. Upon reperfusion, the electron transport chain is restored, resulting in the normalization of intracellular pH and $\Delta\Psi_m$ and a significant influx of Ca^{2+} into the mitochondrion. The reperfusion is characterized by an increase in reactive oxygen species (ROS) formation, a decrease in ATP production, and cell death. Reintroduction of O_2 at reperfusion may lead to significant ROS production, worsening the oxidation of thiols and hydroxyl radical (OH) formation. ROS produced during reperfusion may also damage proteins, lipids, and DNA, resulting in further mitochondrial disruption, sterile immune activation [134, 174], and necrotic interaction of a dysfunctional respiratory chain with oxygen during reperfusion [175].

9.3.3 *Measuring IRI with ^{31}P-MRSI*

Section 9.2.2 described how ^{31}P-MRS can be utilized to provide valuable insights into the energetic metabolism of kidneys. As detailed in Chapter 4, phosphorus spectroscopy allows for the detection of signal contributions from various metabolites, including ATP, Pi, NAD+, NADH, PME (which contains cell membrane precursors, PCh and PE), and AMP. During cold ischemic conditions, oxidative phosphorylation ceases, and ATP levels rapidly decrease, while NAD+, NADH, and PME signals remain stable. The PME/Pi intensity ratio measured during cold storage before transplantation serves as a critical biomarker for graft viability[24]. In particular, viable cells should be able to rephosphorylate AMP to ATP, especially when the PME reserve is abundant. Furthermore, a reduction in PME and an increase in phosphodiesther levels reflect the degradation of cell membrane phospholipids [25]. Therefore, monitoring PME levels can provide valuable information about both cell membrane integrity and AMP storage.

NAD+/NADH plays a significant role in the mitochondrial mechanism against reactive oxygen species (ROS) [176]. During prolonged ischemia, the efficacy of the antioxidant system progressively declines, which can be detrimental to the cell during reperfusion that induces a burst of ROS [177]. Notably, the production of ROS and the deregulation of mitochondrial membrane permeability, both reflected by the NAD+/NADH ratio, are major factors for cell death and apoptosis after reperfusion [178]. In human kidney transplantation, a measurable level of NADH during cold storage has been linked to better post-transplantation function [147]. The measurement of the NAD+/NADH ratio is feasible in the human brain and may also be achievable in the kidney [179].

MRI is widely accepted as a diagnostic tool for identifying renal abnormalities, including tumors and cystic lesions [180]. Renal perfusion can be evaluated using dynamic MRI with the first passage of a bolus of gadolinium (Gd) [181]. Abnormal uptake of Gd may indicate arterial stenosis, glomerular filtration dysfunction , and ischemic kidney [182, 183]. The assessment of renal filtration function is not possible in isolated perfused kidney due to the low systolic pressure, which is insufficient for glomerular filtration. However, microcirculation anomalies

of the cortex and medulla caused by ischemic shunting effect [184] can be detected, providing a valuable indicator of ischemia [185].

9.3.4 *Organ preservation with ex-vivo machine perfusion*

The significance of energy metabolism, which is responsible for providing energy to living cells to maintain their viability, has been recognized in organ transplantation [186]. As a result, present-day preservation techniques focus on maintaining the energy-producing machinery of the organ and limiting the rate of energy depletion [187, 188]. When the energy reserves fall below a critical threshold, the ensuing damage becomes irreversible [189]. Static cold storage remains the most widely used approach for allograft preservation, with novel preservation methods involving machine perfusion that has emerged in recent years. Hypothermic machine perfusion without oxygen has been demonstrated to delay graft function and enhance 1- and 3-year graft survival compared with static cold storage in kidney transplantation [190]. Hypothermic oxygenated perfusion has also been shown to improve the quality of organ from donation after cardiac death and donation after brain death donors by preventing the development of post-transplantation complications [191]. Chapter 10 will present our study of oxygenated hypothermic storage with the assessment of cellular metabolic energy using ^{31}P-MRSI.

Recent studies have shown that preserving organs at more physiologically relevant temperatures (37 °C) can reduce injuries related to preservation and improve the outcomes of marginal grafts [192]. Normothermic perfusion of kidneys allows for high metabolic activity by providing a continuous flow of warmed, oxygenated perfusate with nutritional substrates, which enables reconditioning and repair protocols [193]. The use of a red blood cell-based plasma-free solution to perfuse marginal kidneys at 37 °C reduced the need for dialysis within the first 7 days compared to static cold storage [194]. However, the availability and cost of a blood perfusion system, the complexity of the heating system, tight pH and glucose control, red blood cell hemolysis, and the risk of infection limit the use of organ perfusion at 37 °C [195]. Perfusion of kidneys at sub-normothermic temperatures (22 °C) has been proposed as a more practical alternative to perfusion at 37 °C. Furthermore, in a DCD porcine model, perfusion at 22 °C using a human plasma mimetic reduced acute tubular necrosis compared to perfusion at 15 °C and 37 °C. Thus, 22 °C may be the optimal temperature to protect against kidney IRI and a more feasible approach. Prior to transplantation, perfusion at 22 °C promoted mitochondrial respiration and ATP stores in liver grafts, but viability assessment is yet to be well-defined [196]. Chapter 11 will describe our study on subnormothermic kidney perfusion at a temperature of 22 °C with a corresponding assessment of metabolism using ^{31}P-MRSI.

Hydrogen sulfide (H_2S) is a colorless gas that exerts toxicity to humans and most animals by inhibiting cellular respiration. However, endogenously produced H_2S has emerged as a vital signaling molecule that provides protection against renal ischemia-reperfusion injury [197], lowers blood pressure [198], and prevents neurodegeneration [199]. H_2S also exhibits anti-inflammatory and antioxidant properties, which limit inflammation, reduce reactive oxygen species (ROS) formation, and prevent apoptosis. These properties have been shown to be cytoprotective in cardiovascular diseases [200]. In vitro studies have demonstrated that H_2S reversibly reduces mitochondrial O_2 consumption and mitochondrial membrane potential [201]. Furthermore, ex vivo experiments revealed that H_2S reduces O_2 consumption and total ATP content in isolated perfused kidneys [202]. In the context of transplantation, pharmacologically reducing the demand for oxygen via oxidative phosphorylation is a promising strategy for minimizing unavoidable hypoxia-induced injuries, such as ischemia/reperfusion, and improving organ preservation. In Chapter 12, we present our study on the utilization of H_2S for organ preservation.

10

ANALYSIS OF EX-VIVO KIDNEY GRAFT VIABILITY

"If it takes a little myth and ritual to get through a night that seems endless, who among us cannot sympathize and understand ?"

- Carl Sagan, *Cosmos*

Contents

10.1 SUMMARY

Chapter 9 discussed the organ shortage crisis and the potential to expand the donor pool by considering marginal donors who do not meet the standard criteria for transplantation. However, the use of marginal donors is hindered by their poor outcomes. As highlighted in the earlier section of the chapter, conventional histological evaluation of procurement biopsies lacks predictive power for post-transplant outcomes and may deter the use of kidneys that are otherwise viable for transplantation. Therefore, phosphorus spectroscopy was introduced as a valuable method for evaluating high energy metabolism and assessing the viability of organs. Our research on the analysis of perfused organ with ^{31}P-MRSI is presented in the article Section 10.2.

In this article, we presented the experimental setup used to evaluate kidney viability. Our group employed a machine capable of perfusing kidneys, which is compatible with MRI technology. The perfusion machine is constructed of non-magnetic materials and is a pneumatically driven and controlled system. During MRI acquisition, the machine is dismantled, leaving only the perfusion module connected to the drive module, which is kept outside the Faraday cage of the MRI scanner to avoid any potential interferences. The perfusion is pulsatile, and the pH and pCO_2 levels are maintained constantly by gazometry. This hypothermic pulsatile perfusion system (HPP) was developed fully at the Geneva University Hospital (HUG) and is currently the only system in the world that is MR-compatible, includes MRI and ^{31}P-MRS acquisition capabilities, and is compatible with organ recovery procedures. In this study, porcine kidneys underwent either no warm ischemia, 30 minutes of warm ischemia, or 60 minutes of warm ischemia before being placed in the HPP system to simulate donation after circulatory death (DCD). Kidney function was assessed through measurements of high energy metabolites using ^{31}P-MRSI, Gadolinium elimination, and histopathological scoring.

The present study was successful in detecting ischemia-reperfusion damage through histological analysis of biopsy samples. Furthermore, a correlation between the descending slope of gadolinium perfusion elimination and histological damage scores was established. Nonetheless, a major constraint was encountered with a lengthy acquisition time (nearly 1 hour) which could potentially hinder the application of this diagnostic technique in a clinical environment. Additionally, under hypothermic perfusion conditions, we were able to calculate the time constant of ATP and PME levels, and our results suggest that ATP remains stable as long as adequate precursor (evaluated by PME level) is present.

Original Basic Science—General

Ex Vivo Analysis of Kidney Graft Viability Using 31P Magnetic Resonance Imaging Spectroscopy

Alban Longchamp, MD, PhD,[1] Antoine Klauser, PhD,[2,3] Julien Songeon, MS,[2] Thomas Agius, MS,[1] Antonio Nastasi, BS,[4] Raphael Ruttiman, BS,[4] Solange Moll, MD,[5] Raphael P. H. Meier, MD, PhD,[4,6] Leo Buhler, MD,[7] Jean-Marc Corpataux, MD,[1] and Francois Lazeyras, PhD[2,3]

Background. The lack of organs for kidney transplantation is a growing concern. Expansion in organ supply has been proposed through the use of organs after circulatory death (donation after circulatory death [DCD]). However, many DCD grafts are discarded because of long warm ischemia times, and the absence of reliable measure of kidney viability. ^{31}P magnetic resonance imaging (pMRI) spectroscopy is a noninvasive method to detect high-energy phosphate metabolites, such as ATP. Thus, pMRI could predict kidney energy state, and its viability before transplantation. **Methods.** To mimic DCD, pig kidneys underwent 0, 30, or 60 min of warm ischemia, before hypothermic machine perfusion. During the ex vivo perfusion, we assessed energy metabolites using pMRI. In addition, we performed Gadolinium perfusion sequences. Each sample underwent histopathological analyzing and scoring. Energy status and kidney perfusion were correlated with kidney injury. **Results.** Using pMRI, we found that in pig kidney, ATP was rapidly generated in presence of oxygen (100 kPa), which remained stable up to 22 h. Warm ischemia (30 and 60 min) induced significant histological damages, delayed cortical and medullary Gadolinium elimination (perfusion), and reduced ATP levels, but not its precursors (AMP). Finally, ATP levels and kidney perfusion both inversely correlated with the severity of kidney histological injury. **Conclusions.** ATP levels, and kidney perfusion measurements using pMRI, are biomarkers of kidney injury after warm ischemia. Future work will define the role of pMRI in predicting kidney graft and patient's survival.

(*Transplantation* 2020;104: 1825–1831).

INTRODUCTION

The lack of available kidneys for transplantation is a major concern, responsible for excess in morbimortality, and cost to healthcare systems.[1] Thus, to expand the organ supply, a variety of efforts have been made, such as accepting organs from donors after circulatory death (DCD), or with comorbidities (extended criteria donors [ECDs]). However, their usage is limited, due mainly to the fact that there is no reliable, noninvasive means to assess graft viability ex vivo. Shockingly, in the United States, 18% of all donated kidneys and 45% of ECD kidneys were not allocated for transplantation, despite that such kidneys could have been transplanted with good outcomes.[1,2] In addition, the introduction of policies that penalize centers with poor outcomes resulted in an increase in the number discarded marginal kidneys,[3] a practice called "risk-averse transplant behavior."[4]

A number of tools are used to predict the suitability of kidneys before transplantation. These include stratification of donors according to clinical parameters, risk scores, histological donor biopsy scores, machine perfusion characteristics, biomarkers, and so on.[5] Besides the dichotomous ECD classification,[6] none of the scoring tools are clinically used.[7] Consequently, transplant outcome remains difficult to predict based on current

Received 12 February 2020. Revision received 9 March 2020.

Accepted 24 March 2020.

[1] *Department of Vascular Surgery, Centre Hospitalier Universitaire Vaudois and University of Lausanne, Lausanne, Switzerland.*

[2] *Department of Radiology and Medical Informatics, University of Geneva, Geneva, Switzerland.*

[3] *Center for Biomedical Imaging (CIBM), Geneva, Switzerland.*

[4] *Visceral and Transplant Surgery, Department of Surgery, Geneva University Hospitals and Medical School, Geneva, Switzerland.*

[5] *Division of Clinical Pathology, Department of Pathology and Immunology, Geneva University Hospital and Medical School, Geneva, Switzerland.*

[6] *Department of Surgery, University of Maryland School of Medicine, Baltimore, MD, USA.*

[7] *Faculty of Science and Medicine, Section of Medicine, University of Fribourg, Switzerland.*

This work was supported by the Swiss National Science Foundation to J.-M.C., F.L. (SNSF 320030-182658), and A.L. (SNSF PZ00P3-185927) as well as the Mendez National Institute of Transplantation, and the Leenards Foundation to A.L.

The authors declare no conflicts of interest.

A.L., A.K., J.S., T.A., L.B., J.-M.C., and F.L. participated in research design. A.L., A.K., R.M., and F.L. participated in the writing of the article. A.L., A.K., J.S., T.A., A.N., R.R., S.M., R.M., J.-M.C., and F.L. participated in the performance of the research. A.N., R.R., S.M., and F.L. contributed new reagents or analytic tools. A.L., A.K., J.S., T.A., S.M., R.M., L.B., J.-M.C., and F.L. participated in data analysis.

Correspondence: François Lazeyras, PhD, Hôpitaux Universitaires de Genève, Service de Radiologie, CIBM Rue Gabrielle-Perret-Gentil 4, CH, 1211 Genève 14, Switzerland. (francois.lazeyras@unige.ch).

ISSN: 0041-1337/20/1049-1825

DOI: 10.1097/TP.0000000000003323

methods, and useful predictors of outcome that incorporate tissue viability are urgently needed.

The importance of energy metabolism, by which living cells acquire, and use the energy needed to stay alive, during organ transplantation has been duly acknowledged.[8] Consequently, current methods of organ preservation aim to preserve the energy machinery[9] and reduce the rate energy depletion.[10] The consensus is that a period of warm ischemia (>30 min in human kidney[11]), primes the tissue for subsequent damage upon reperfusion. During ischemia, ATP depletion disrupts mitochondrial Na^+/K^+ ion channels, which reduce mitochondrial membrane potential and increase mitochondrial inner membrane permeability, influx of calcium ions, and subsequent swelling of mitochondria.[12] Once energy levels have fallen beyond a critical point, the resulting injury is irreversible.[13] Respiratory defects were identified as early events of injury during preservation[13] and after ischemia-reperfusion.[14] In livers, ATP content correlated with transplant outcome.[15,16] Unfortunately, clinical applicability of ATP measurement has been limited by time-consuming, invasive, and costly methods of ATP analysis.[9]

Magnetic resonance imaging (MRI) is well established as a clinical diagnostic modality. Kidney perfusion can be assessed by dynamic MRI using the first passage of Gadolinium (Gd)-chelate bolus.[17] Abnormal Gd uptake may also reflect arterial stenosis, glomerular filtration dysfunction,[18] and ischemia.[19] In addition to imaging the hydrogen nucleus, MRI enables detection of high-energy phosphate metabolites (^{31}P MRI [pMRI] spectroscopy), such as ATP, phosphomonoesters (PMEs, that contain the ATP precursor AMP), phosphodiesters, and phosphocreatine. Therefore, this method could be particularly suitable for monitoring tissue function and graft viability during transplantation.

Here, we demonstrate that using pMRI, ATP can be quantified ex vivo in kidney graft. Importantly, kidney ATP levels significantly correlated with graft Gd perfusion, and tissue injuries after warm ischemia. Thus, pMRI could facilitate rapid, and accurate assessment of kidney viability, with the hope to predict survival of kidney recipients.

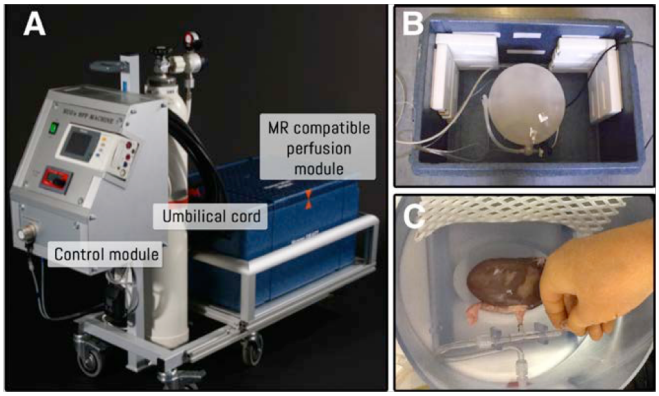

FIGURE 1. The homemade MR-compatible kidney ex vivo perfusion system. (A) The system is made of a control module to drive the pulsating pump and regulate the oxygenator, a perfusion tank containing the kidney graft, and linked through the umbilical cord. Compatible perfusion module fits in the MRI bore with a maximum size of 40 cm. (B, C) Inside view of the perfusion tank (B) with the kidney artery connected to a cannula (C). MRI, magnetic resonance imaging.

MATERIALS AND METHODS

Ex Vivo Hypothermic Oxygenated Pulsatile Perfusion

Kidneys were perfused by a homemade MRI-compatible machine with Belzer MPS UW Machine Perfusion Solution, and kept at 4°C for up to 22 h. All of the experiments were performed in presence of oxygen (100 kPa), as we previously demonstrated that the ability of the kidney to generate ATP relies on sufficient oxygenation.[20] The perfusion module, and its cooling box were MRI compatible. During the MRI acquisition, the control module was kept outside of the Faraday cage and was connected through the wall with an "umbilical cord," that ensured adequate kidney oxygenation (Figure 1) and pulsatile perfusion. Systolic and diastolic pressure were set at 50 and 15 mm Hg, respectively. Measurements were performed on a multinuclear Prisma-fit 3T whole-body MRI scanner (Siemens, Erlangen, Germany). Kidney localization was performed with a T2-weighted sequence (turbo spin echo, repetition time (TR) 5000 ms, echo time (TE) 108 ms, 3-mm slices).

Gadolinium Perfusion

Gd perfusion enables the observation of the internal distribution of the flow between the cortex and the medulla. Low molecular weight Gd has a predominant renal elimination by glomerular filtration without any tubular secretion or reabsorption. Having a similar pharmacokinetics as tracer, they allow glomerular filtration rate assessment with MRI. The perfusion-descending cortical slope (DS) is evaluated with the elimination of the Gd using the angle between the maximum signal value in the cortex and the lowest intensity point at the end of the flushing (around 200 s).[21] In this study, 5 mL (0.025 mmol/mL) Gd-diethylenetriaminepentaacetic acid bolus injection was used for the renal perfusion (at 4°C), followed by a 20-mL flush of MP Belzer. The perfusion is a fast sequence, as data were collected using a dynamic 2D saturation-prepared turbo flash sequence with the scanner body coil. This sequence has an inversion time of 240 ms, a flip angle of 12°, 1.0 mm × 1.3 mm resolution, 5 slices of 5 mm (1-mm gap), TR 460 ms, and a TE of 1.3 ms.

^{31}P Magnetic Resonance Imaging Spectroscopy

pMRI was performed with a single-loop coil tuned at 49.5 MHz, which was part of the perfusion machine, as it was fixed at the bottom of the perfusion tank. The coil was interfaced with a specially designed transceiver that allows both 1H imaging and ^{31}P spectroscopy (Clinical MR Solutions, Brookfield, WI). The field homogeneity was optimized with automatic shimming over the kidneys. pMRI consisted of 3D spatial encoding, with a field of view 250 mm × 250 mm × 160 mm, matrix size 16 × 16 × 8, nominal spatial resolution 15.6 mm × 15.6 mm × 20 mm, TR 1.0 s, flip-angle 45°, echo delay 0.6 ms, bandwidth 4000 Hz, 2k sampling points. Elliptical encoding with 32 weighted averages, resulted in an acquisition time of 45 min. Chemical shift signal was referenced to the inorganic phosphate (Pi) resonance at 5.2 ppm, which can be considered homogeneously distributed over the surface of the coil. A frequency offset of −500 Hz was used to center excitation pulse bandwidth over ATP frequency range. Afterward, the spectrum was processed with a 20-Hz exponential time filter, and order 0 and 1 phase corrections. The metabolites (ATP,

PME, Pi, phosphocreatine) were fitted with Gaussian peaks using the syngo software (SIEMENS, Erlangen, Germany) and were estimated over all the kidneys by averaging pMRI voxels containing kidney tissue (combined voxels resulting in a single spectrum). α, β, and γ ATP correspond to the resonances of the 3 ^{31}P nuclei contained in ATP. All 3 peak amplitudes are proportional to the ATP concentration but were quantified separately to prevent methodological bias. Indeed the excitation pulse profile might vary over the large frequency range spanned by the 3 peaks, and their quantification might be influenced by overlaps with other metabolite like nicotinamide adenine dinucleotide (NAD) (discussed further in the text). The metabolite concentrations were obtained as previously described.[20] Briefly, $[^{31}P_m]$, expressed as mmol/L (mM), was calculated using the following formula: $[^{31}P_m] = (S_m/S_{bPi}) \times [^{31}P_{buffer}] \times C_{sens}$, where S_m and S_{bPi} are the mean metabolite and buffer Pi signals (area), respectively. $[^{31}P_{buffer}]$ is the buffer phosphate concentration (25 mmol/L). C_{sens} is the sensitivity correction factor.

Animals

The study was approved by the University of Geneva animal ethics committee (protocol number: GE/53/14/22826). Five-month-old female pigs were obtained from the animal facility of Arare, Switzerland. All pigs were maintained under standard conditions. Water and food were provided ad libitum. Animals were first premedicated using azaperone (2.2 mg/kg IM), midazolam (1.6 mg/kg IM), and atropine (0.02 mg/kg IM) and anesthetized with ketamine (2–6 mg/kg/h), fentanyl (4–6 µg/kg/h), midazolam (0.2–0.4 mg/kg/h), and atracurium (1 mg/kg/h). Animals were then intubated and ventilated before a nasogastric tube was placed. The arterial line was placed in the internal carotid artery. Monitoring included heart rate, systemic blood pressure, pulse oximetry, and end-tidal CO_2. Following a midline incision, the peritoneal cavity was opened, and the bowels were reclined. First, the aorta, vena cava, and renal vessels were prepared. The pigs received 300 UI/kg heparin intravenous injections. Renal arteries and veins were clamped, and the kidneys were either immediately explanted or explanted after 30 and 60 min of warm ischemia (to mimic circulatory arrest during DCD procurement). Kidneys were then instantly flushed with 4°C Institut Georges Lopez-1 preservation solution on ice. Surgical kidney biopsies, including the cortex and the medulla, were formalin fixed and embedded in paraffin. The renal artery was cannulated, and the kidneys were cold perfused using our MR-compatible machine (Figure 1) before imaging. Pigs were sacrificed using 100 mEq of potassium chloride intravenous injections.

Histopathological Analysis of Biopsies

Sections of 3-µm thickness were prepared from formalin-fixed kidney biopsies and stained with silver Jones and Periodic Acid-Schiff. Histopathological analysis score was performed based on those described by Goujon et al[22,23] using Osirix software (www.osirix-viewer.com) and modified as previously described.[22,24] Four different representative fields were assessed and blinded to group assignment. Lesion severity was graded 0–5 according to the following criteria: no abnormality (0), mild lesions affecting, respectively, 1%–10% (1), 10%–25% (2), 25%–50% (3), 50%–75% (4), and >75% (5) of the sample surface. The final score for each biopsy ranges from 0 to 30. A higher score corresponding to the more severe ischemic damage.

Statistical Analysis

The statistical tests used are defined for each figure in the appropriate legend. A P value <0.05 was considered statistically significant. Computations were performed using Prism 7 (GraphPad Softwares, San Diego, CA).

RESULTS

Kidney ATP Is Rapidly Generated During Ex Vivo Perfusion

Kidneys were perfused using a homemade MRI-compatible, hypothermic-oxygenated pulsatile perfusion machine (Figure 1). During the ex vivo perfusion, kidneys metabolites were estimated by averaging pMRI voxels, resulting in a single spectrum (Figure 2A and B). In healthy kidneys (0 min of warm ischemia), pMRI allowed the detection of α-, β-, and γ-ATP, PME and inorganic phosphate (Pi, Figure 2B). ADP was below the detection threshold. ATP and PME concentration (mM) were extrapolated from their spectra peak area and the buffer phosphate concentration (Pi, 25 mmol/L). In absence of warm ischemia, kidney α-, β-, and γ-ATP, remained stable up to 22 h of perfusions (Figure 2C). On the other hand, PME concentration was 4 times higher than ATP at the initiation of the perfusion but gradually declined over time (Figure 2C). This is consistent with the hypothesis that the PME containing AMP signal is utilized over time to generate ATP.

Warm Ischemia Reduces Kidney ATP Levels

To determine the effect of warm ischemia and to ensure sufficient sensibility of ATP measurement using pMRI in injured grafts, kidneys underwent 0 (control), 30 or 60 min of warm ischemia before retrieval. There was a significant reduction in the amount of β-ATP after 30 min (–48.4%; P=0.04) and 60 min (–66.4%; P=0.007) of warm ischemia (compared with no warm ischemia, Figure 3A). Similarly, γ-ATP was significantly decreased after 60 min of ischemia (–45.5%; P=0.05; Figure 3A). α-ATP did not significantly decrease, which could be explained by the presence of NAD overlapping at –8.3 ppm (Figure 3A). Since the peak of α-ATP appears to be "contaminated" by NAD signal, ATP concentration was estimated by averaging β- and γ-ATP only. Compared with control, 60 min of warm ischemia induced a 58.5% fold reduction in total ATP (Student t test; P=0.03). On the other hand, PME concentrations were not altered by warm ischemia (Figure 3B).

ATP Levels and Kidney Perfusion Correlate With Histological Damage

To establish the relevance of ATP quantification using pMRI, we next examined the correlation with histological damage, as assessed by the Goujon score, which is thought to reflect kidney function.[22] As expected, 30 and 60 min of warm ischemia induced significant histological injuries (Figure 4A). Histological damages were quantified based on the number of tubules lumina with cellular debris, the loss of brush border, tubular dilatation, the percentage of floculus in Bowman's capsule, vacuolization, and

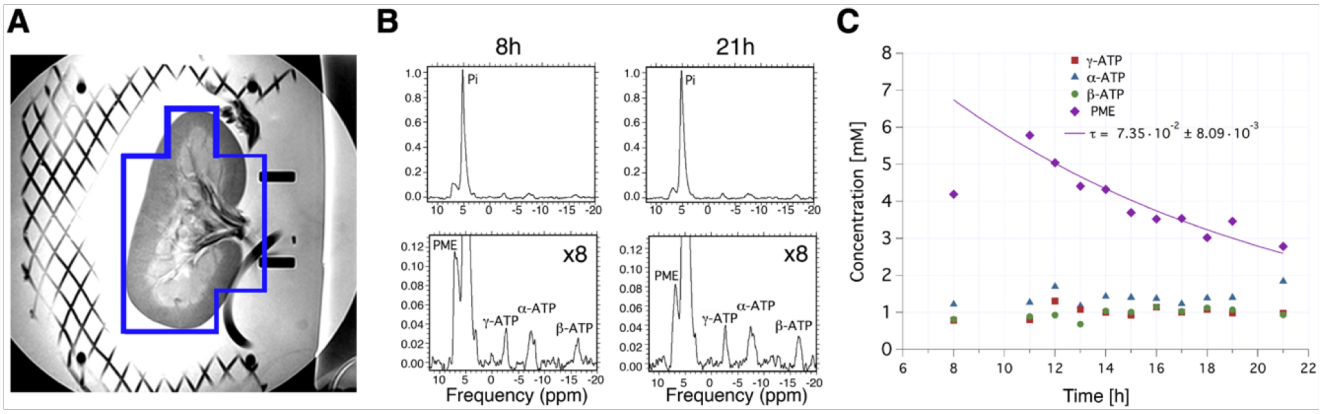

FIGURE 2. Representative pMRI spectra, and kidney ATP levels over time. (A) T2 image of a kidney, with the blue border representing the area of combined voxels that are analyzed for metabolite concentration. (B) Representative spectrum of kidney after 8 h (left) and 21 h (right) of hypothermic pulsatile perfusion. (C) Concentration (mM) of the indicated metabolites over time, in pig kidney, after 0 min of warm ischemia, during hypothermic pulsatile perfusion with a fixed pO_2 of 110 kPa. pMRI, ^{31}P magnetic resonance imaging; PME, phosphomonoester.

interstitial edema (Figure 4B), which were all increased by warm ischemia (except for vacuolization, Figure 4B). Of importance, the ability to produce ATP (Figure 4C and D) was tightly correlated with the degree of kidney injury (Figure 4D, Pearson's $R^2 = 0.52$; $P < 0.001$). Histological injury did not correlate with PME levels (data not shown).

Gd perfusion enables the observation of flow between the cortex and the medulla, which was suggested to be altered during injury.[21] Consistent with our previous findings, kidney Gd cortex, and medulla perfusion were altered after 60 min of warm ischemia. This was reflected by a decrease in the DS (Figure 5A). Interestingly, kidney injury assessed using the cortex DS was significantly correlated with kidney ATP and with histological damage (Figure 5B and C; Pearson's $R^2 = 0.64$ and 0.43, respectively; $P < 0.001$). Thus, combining both ATP and DS measurements might allow the accurate prediction of kidney damage before transplantation.

DISCUSSION

This study provides a noninvasive method to asses viability of kidneys ex vivo during hypothermic machine perfusion. In particular, the objective assessment of graft damage (eg, resulting from prolonged circulatory arrest, DCD) could translate into greater utilization of kidney allograft.

Besides being used to reduce the risk of delayed graft function and improved graft survival after kidney transplantation,[25] machine perfusion enables viability testing by offering a dynamic environment. Various parameters have been proposed as predictive biomarkers, ranging from intrarenal resistance, markers of acid-base homeostasis, or lactate production.[26] Interestingly, we observed an exponential decrease of PME during the ex vivo perfusion, suggesting that AMP reserve contained in the PME metabolites is consumed to produce ATP. This is consistent with the idea that the kidneys are functionally and metabolically active in presence of oxygen.[20,21] In addition, there is emerging evidence that oxygenation is an important advantage during hypothermic machine perfusion.[27,28] Oxygen supplementation during organ preservation may drive ATP production through oxidative phosphorylation. Thus, cells can use ATP to sustain metabolic processes that protect from ischemic damage.[29] These further suggest the importance of functional mitochondria and the dependence on oxidative metabolism in healthy kidney. In addition, this suggests that kidney viability depends on the ability to generate ATP and not only the remaining

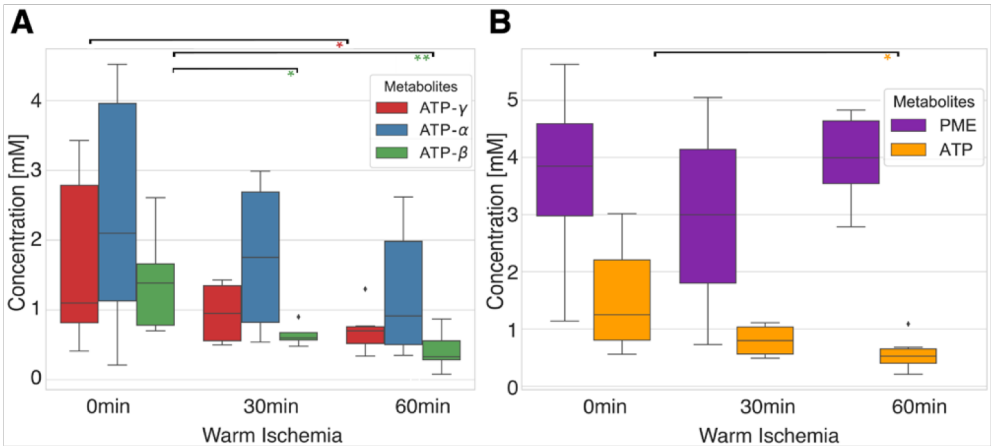

FIGURE 3. Kidney metabolite levels after 0, 30, and 60 min of warm ischemia. (A, B) α-, β-, and γ-ATP expressed individually (A), and β- and γ-ATP combined and PME (B) following 0, 30, or 60 min of warm ischemia. n = 4–9 per group. Metabolites levels represent an average throughout perfusion. Error bars indicate SD *$P < 0.05$, **$P < 0.01$, by 2-way ANOVA. PME, phosphomonoesters.

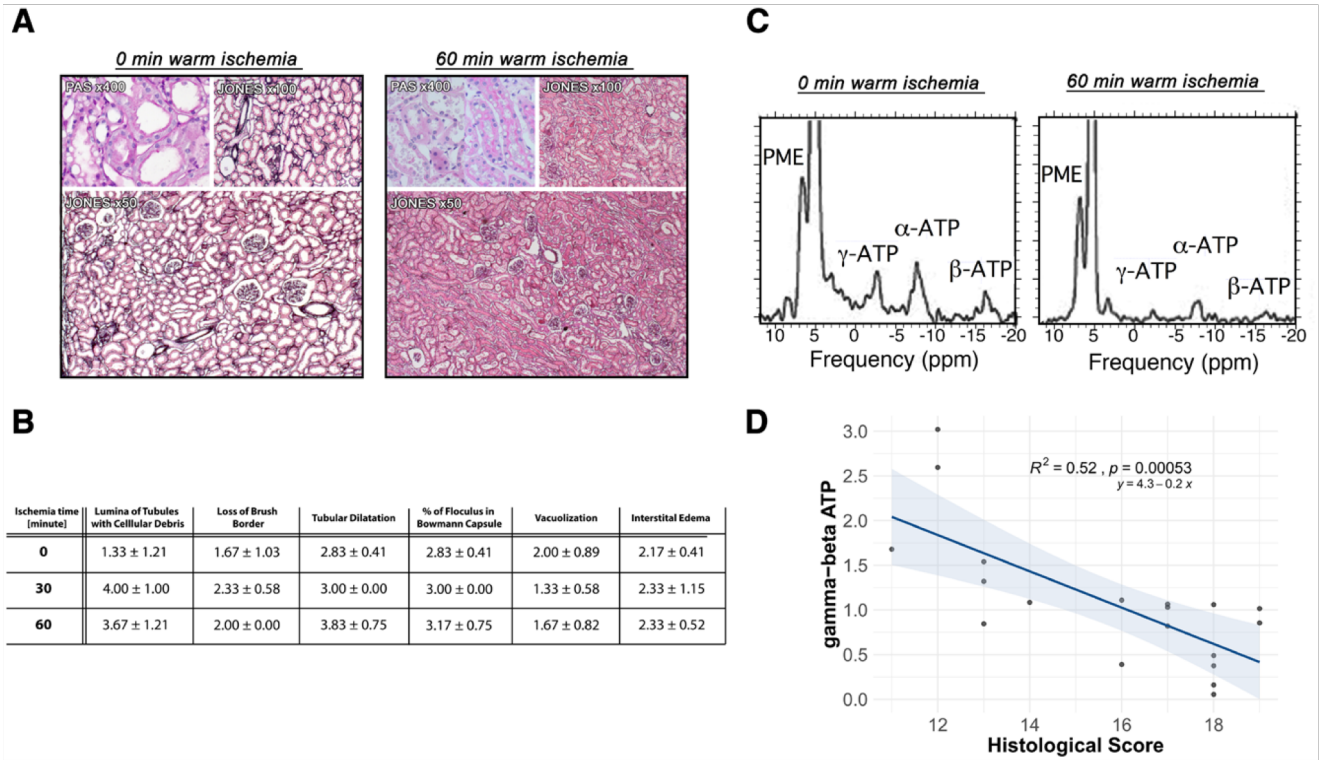

B

Ischemia time [minute]	Lumina of Tubules with Cellular Debris	Loss of Brush Border	Tubular Dilatation	% of Floculus in Bowmann Capsule	Vacuolization	Interstital Edema
0	1.33 ± 1.21	1.67 ± 1.03	2.83 ± 0.41	2.83 ± 0.41	2.00 ± 0.89	2.17 ± 0.41
30	4.00 ± 1.00	2.33 ± 0.58	3.00 ± 0.00	3.00 ± 0.00	1.33 ± 0.58	2.33 ± 1.15
60	3.67 ± 1.21	2.00 ± 0.00	3.83 ± 0.75	3.17 ± 0.75	1.67 ± 0.82	2.33 ± 0.52

FIGURE 4. ATP levels correlate with histological damage. (A) Representative kidney sections stained with PAS or Jones after no (left) or 60 min (right) of warm ischemia. (B) Details of histological scoring after various warm ischemia time as indicated. Data are expressed as mean ± SD. (C) Representative MRI fitting spectra after no (left) or 60 min (right) of warm ischemia. (D) Nonparametric Spearman's correlation between kidney γ- and β-ATP and histological score after 0–60 min of warm ischemia with the coefficient of determination R^2 and *P* value. Metabolites levels represent an average throughout perfusion. n = 27. MRI, magnetic resonance imaging; PAS, Periodic Acid-Schiff; PME, phosphomonoester.

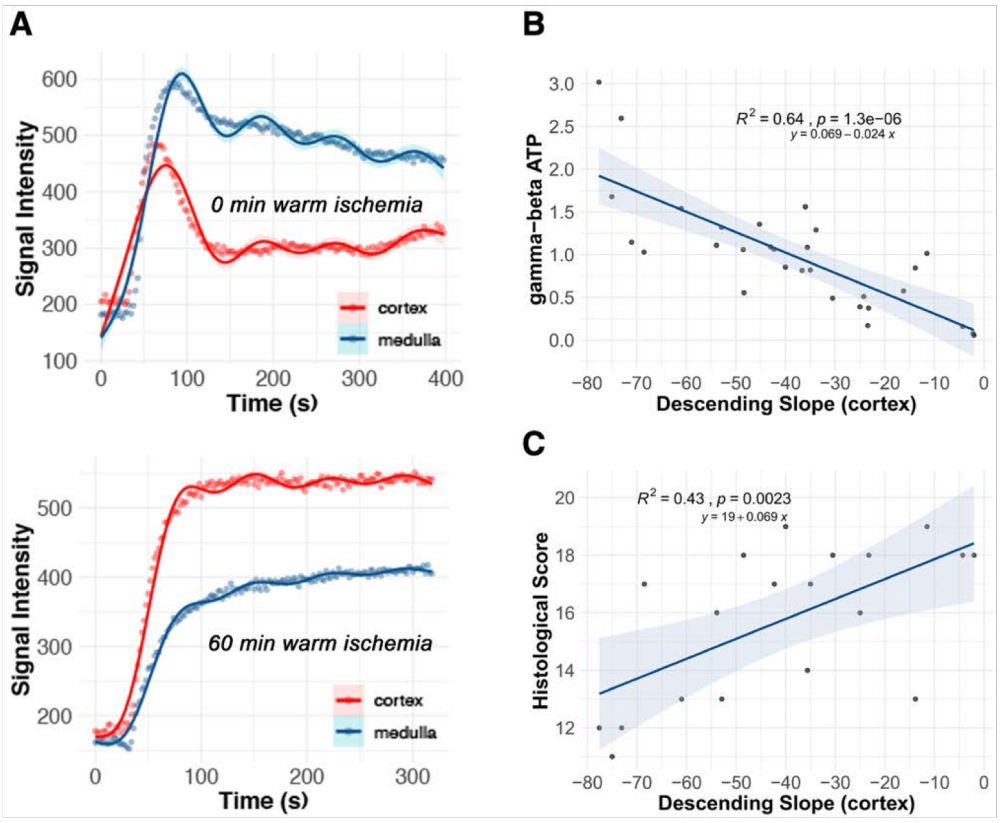

FIGURE 5. The perfusion-descending slope (DS) correlates with kidney ATP levels and histological damage. (A) Representative kidney Gd cortex (red line) and medulla (blue line) perfusion after no (top) or 60 min (bottom) of warm ischemia. (B, C) Unparametric Spearman's correlation between kidney cortex perfusion-descending slope, and γ/β–ATP (B) and with histological score (C) with their coefficient of determination R^2 and *P* value, n = 27.

ATP store. Several studies demonstrated that ATP levels correlate with ischemic injury of the kidney[30] and liver.[29] Moreover, ATP is often used as a marker of viability during ischemia.[31,32] In humans, ATP level in liver tissue is an independent predictor of initial graft function.[33] Interestingly, ATP levels measured after transplantation were inversely related to warm ischemia time.[16] Similarly, low ATP levels were significantly associated with primary graft nonfunction.[34] Of importance, the inadequate recovery might be different in various marginal organs. For instance, ATP levels were lower in the DCD and steatotic livers.[9] Despite good correlation with outcome, energy status is difficult to measure, and yet to be used routinely for clinical testing. ATP measurements would be a precious addition to the pretransplant assessment of suboptimal organs, particularly in the setting of uncontrolled DCD procurement, where in the exact maximal donor warm ischemia duration is unknown, which is responsible for a large variation of acceptance criteria between centers.[35]

Our study has several limitations that need to be acknowledged. First, the broader utility of this methodology in determining graft viability should be tested in all form of marginal donor, including kidney from old donor, after acute kidney injury, and after prolonged cold preservation. In addition, we did not correlate ATP levels with kidney function in vivo, or after transplantation, mostly because of local regulation, that did not allow survival surgery. All of the above will hopefully be tested in a future human clinical trial. Although the histological score was not validated in a prospective human cohort, it was previously correlated with the degree of kidney injury.[22-24] The clinical use of pMRI might be limited by the time of acquisition (45 min). However, the acquisition was performed during the hypothermic ex vivo perfusion,[27] and the imaging time could be reduced either by reducing spatial encoding resolution or by using advanced method for fast spatial encoding.[36] In addition, the fitting of α-ATP with a broad Gaussian probably includes the NAD+ and NADH signal at −8.3 ppm. Thus, the quantification of the pMRI spectra could be improved for overlapping metabolites, using a model that comprises each metabolite spectrum with multiplet structures. This could for instance allow for the specific detection of NAD+/H signal that is weak and overlaps with alpha-ATP peak.[37] Altogether, it is likely that the pMRI process can be integrated within the "normal" cold ischemia period.

In conclusion, pMRI performed on a kidney graft held in an ex vivo perfusion system produced excellent quality spectra. ATP levels and kidney perfusion measurements could accurately predict kidney damage caused by warm ischemia. In an era when up to 45% of ECD kidneys are discarded, this study provides a timely and innovative noninvasive tool to assess kidney viability before transplantation.

ACKNOWLEDGMENTS

We thank Jean-Pierre Gilberto for his excellent technical assistance.

REFERENCES

1. Hart A, Smith JM, Skeans MA, et al. OPTN/SRTR 2017 annual data report: kidney. *Am J Transplant*. 2019;19(Suppl 2):19–123. doi:10.1111/ajt.15274
2. Aubert O, Reese PP, Audry B, et al. Disparities in acceptance of deceased donor kidneys between the United States and France and estimated effects of increased US acceptance. *JAMA Intern Med*. 2019;179:1365–1374. doi:10.1001/jamainternmed.2019.2322.
3. Rege A, Leraas H, Vikraman D, et al. Could the use of an enhanced recovery protocol in laparoscopic donor nephrectomy be an incentive for live kidney donation? *Cureus.* 2016;8:e889. doi:10.7759/cureus.889
4. Heilman RL, Green EP, Reddy KS, et al. Potential impact of risk and loss aversion on the process of accepting kidneys for transplantation. *Transplantation.* 2017;101:1514–1517. doi:10.1097/TP.0000000000001715
5. Sung RS, Christensen LL, Leichtman AB, et al. Determinants of discard of expanded criteria donor kidneys: impact of biopsy and machine perfusion. *Am J Transplant.* 2008;8:783–792. doi:10.1111/j.1600-6143.2008.02157.x
6. Port FK, Bragg-Gresham JL, Metzger RA, et al. Donor characteristics associated with reduced graft survival: an approach to expanding the pool of kidney donors. *Transplantation.* 2002;74:1281–1286. doi:10.1097/00007890-200211150-00014
7. Dare AJ, Pettigrew GJ, Saeb-Parsy K. Preoperative assessment of the deceased-donor kidney: from macroscopic appearance to molecular biomarkers. *Transplantation.* 2014;97:797–807. doi:10.1097/01.TP.0000441361.34103.53
8. Vajdová K, Graf R, Clavien P-A. ATP-supplies in the cold-preserved liver: a long-neglected factor of organ viability. *Hepatology.* 2002;36:1543–1552. doi:10.1053/jhep.2002.37189
9. Bruinsma BG, Sridharan GV, Weeder PD, et al. Metabolic profiling during ex vivo machine perfusion of the human liver. *Sci Rep.* 2016;6:22415. doi:10.1038/srep22415
10. Miyagi S, Iwane T, Akamatsu Y, et al. The significance of preserving the energy status and microcirculation in liver grafts from non-heart-beating donor. *Cell Transplant.* 2008;17:173–178. doi:10.3727/000000008783906874
11. Tennankore KK, Kim SJ, Alwayn IP, et al. Prolonged warm ischemia time is associated with graft failure and mortality after kidney transplantation. *Kidney Int.* 2016;89:648–658. doi:10.1016/j.kint.2015.09.002
12. Chouchani ET, Pell VR, James AM, et al. A unifying mechanism for mitochondrial superoxide production during ischemia-reperfusion injury. *Cell Metab.* 2016;23:254–263. doi:10.1016/j.cmet.2015.12.009
13. van Golen RF, van Gulik TM, Heger M. Mechanistic overview of reactive species-induced degradation of the endothelial glycocalyx during hepatic ischemia/reperfusion injury. *Free Radic Biol Med.* 2012;52:1382–1402. doi:10.1016/j.freeradbiomed.2012.01.013
14. Nohl H, Koltover V, Stolze K. Ischemia/reperfusion impairs mitochondrial energy conservation and triggers O2.– release as a byproduct of respiration. *Free Radic Res Commun.* 1993;18:127–137. doi:10.3109/10715769309147486
15. Lanir A, Jenkins RL, Caldwell C, et al. Hepatic transplantation survival: correlation with adenine nucleotide level in donor liver. *Hepatology.* 1988;8:471–475. doi:10.1002/hep.1840080306
16. Kamiike W, Burdelski M, Steinhoff G, et al. Adenine nucleotide metabolism and its relation to organ viability in human liver transplantation. *Transplantation.* 1988;45:138–143. doi:10.1097/00007890-198801000-00030
17. Grenier N, Pedersen M, Hauger O. Contrast agents for functional and cellular MRI of the kidney. *Eur J Radiol.* 2006;60:341–352. doi:10.1016/j.ejrad.2006.06.024
18. Rusinek H, Kaur M, Lee VS. Renal magnetic resonance imaging. *Curr Opin Nephrol Hypertens.* 2004;13:667–673. doi:10.1097/00041552-200411000-00014
19. Laissy JP, Faraggi M, Lebtahi R, et al. Functional evaluation of normal and ischemic kidney by means of gadolinium-DOTA enhanced TurboFLASH MR imaging: a preliminary comparison with 99Tc-MAG3 dynamic scintigraphy. *Magn Reson Imaging.* 1994;12:413–419. doi:10.1016/0730-725x(94)92534-8
20. Lazeyras F, Buhler L, Vallee J-P, et al. Detection of ATP by "in line" 31P magnetic resonance spectroscopy during oxygenated hypothermic pulsatile perfusion of pigs' kidneys. *MAGMA.* 2012;25:391–399. doi:10.1007/s10334-012-0319-6
21. Buchs JB, Lazeyras F, Bühler L, et al. The viability of kidneys tested by gadolinium-perfusion MRI during ex vivo perfusion. *Prog Urol.* 2009;19:307–312. doi:10.1016/j.purol.2009.01.004
22. Meier RPH, Piller V, Hagen ME, et al. Intra-abdominal cooling system limits ischemia-reperfusion injury during robot-assisted renal transplantation. *Am J Transplant.* 2018;18:53–62. doi:10.1111/ajt.14399

23. Goujon JM, Hauet T, Menet E, et al. Histological evaluation of proximal tubule cell injury in isolated perfused pig kidneys exposed to cold ischemia. *J Surg Res.* 1999;82:228–233. doi:10.1006/jsre.1998.5526
24. Longchamp A, Meier RPH, Colucci N, et al. Impact of an intra-abdominal cooling device during open kidney transplantation in pigs. *Swiss Med Wkly.* 2019;149:w20143. doi:10.4414/smw.2019.20143
25. Moers C, Smits JM, Maathuis MH, et al. Machine perfusion or cold storage in deceased-donor kidney transplantation. *N Engl J Med.* 2009;360:7–19.
26. Kaths JM, Echeverri J, Chun YM, et al. Continuous normothermic ex vivo kidney perfusion improves graft function in donation after circulatory death pig kidney transplantation. *Transplantation.* 2017;101:754–763.
27. Kron P, Schlegel A, de Rougemont O, et al. Short, cool, and well oxygenated—HOPE for kidney transplantation in a rodent model. *Ann Surg.* 2016;264:815–822.
28. Venema LH, Brat A, Nijkamp DM, et al. Factors that complicated the implementation of a program of donation after unexpected circulatory death of lungs and kidneys. lessons learned from a regional trial in the Netherlands. *Transplantation.* 2019;103:e256–e262.
29. Berendsen TA, Izamis ML, Xu H, et al. Hepatocyte viability and adenosine triphosphate content decrease linearly over time during conventional cold storage of rat liver grafts. *Transplant Proc.* 2011;43:1484–1488.
30. Malek M, Nematbakhsh M. Renal ischemia/reperfusion injury; from pathophysiology to treatment. *J Renal Inj Prev.* 2015;4:20–27.
31. de Rougemont O, Breitenstein S, Leskosek B, et al. One hour hypothermic oxygenated perfusion (HOPE) protects nonviable liver allografts donated after cardiac death. *Ann Surg.* 2009;250:674–683.
32. Longchamp A, Mirabella T, Arduini A, et al. Amino acid restriction triggers angiogenesis via GCN2/ATF4 regulation of VEGF and H2S production. *Cell.* 2018;173:117–129.e14.
33. González FX, Rimola A, Grande L, et al. Predictive factors of early postoperative graft function in human liver transplantation. *Hepatology.* 1994;20:565–573.
34. Hamamoto I, Takaya S, Todo S, et al. Can adenine nucleotides predict primary nonfunction of the human liver homograft? *Transpl Int.* 1994;7:89–95.
35. Suntharalingam C, Sharples L, Dudley C, et al. Time to cardiac death after withdrawal of life-sustaining treatment in potential organ donors. *Am J Transplant.* 2009;9:2157–2165.
36. Vidya Shankar R, Kodibagkar VD. A faster PISTOL for 1 H MR-based quantitative tissue oximetry. *NMR Biomed.* 2019;32:e4076.
37. Graveron-Demilly D. Quantification in magnetic resonance spectroscopy based on semi-parametric approaches. *MAGMA.* 2014;27:113–130.

11

SUB-NORMOTHERMIC EX-VIVO KIDNEY PRESERVATION

"There is a strange comfort in knowing that no matter what happens today, the Sun will rise again tomorrow."

- Aaron Lauritsen, *100 Days Drive*

Contents

11.1 SUMMARY

Chapter 9 highlighted the significance of improving preservation procedures for marginal kidney grafts to increase the number of viable kidneys and improve patient outcomes. Enhanced preservation techniques for marginal kidney grafts have the potential to increase the availability of viable kidneys for transplantation. Warm ex-vivo perfusion at temperatures of 22 °C and 37 °C has been suggested as a means to reduce preservation injury, but the underlying mechanism is currently unknown. In this study, we investigated kidney quality, including adenosine triphosphate (ATP) production, during sub-normothermic (22 °C) versus hypothermic (4 °C) ex-vivo kidney machine perfusion in a porcine autotransplantation model using phosphorus magnetic resonance spectroscopic imaging (^{31}P-MRSI) coupled with a fitting method using LCModel. Our research on sub-normothermic preservation is presented in the article Section 11.2.

This article introduces a novel clinical approach that employs non-invasive ^{31}P-magnetic resonance spectroscopic imaging (MRSI) to evaluate energy metabolism in donation after circulatory death (DCD) grafts during two clinically relevant hypothermic ex-vivo perfusions and sub-normothermic ex-vivo perfusion in a porcine model of autotransplantation. We utilized ^{31}P-MRSI to measure ATP production and assess the perfusion quality of the perfused kidneys. Specifically, the study compared sub-normothermic preservation at 22 °C with active oxygenation to hypothermic preservation at 4 °C with active and passive oxygenation. To evaluate cellular ischemia-reperfusion injury (IRI), a histological score was performed on biopsy samples at four time points (baseline, after warm ischemia, after 4 hours of perfusion, and after transplantation). Notably, the histological score was only conducted on post-transplanted kidneys, whereas the ^{31}P-MRSI was performed on both pre- and post-transplanted kidneys.

Our study demonstrates that perfusion of kidney grafts at 22 °C results in increased ATP production and minimized ischemia-reperfusion injury (IRI) during transplantation compared to both passive and active oxygenated 4 °C perfusions. The observed differences in the sub-normothermic preservation versus hypothermic preservation are strongly correlated with the histological score, which measures cellular damage. Thus, perfusing kidney grafts at 22 °C may increase the utilization of kidney allografts, and warrants further investigation through clinical trials.

Organ Donation and Procurement

OPEN

Subnormothermic Ex Vivo Porcine Kidney Perfusion Improves Energy Metabolism: Analysis Using ^{31}P Magnetic Resonance Spectroscopic Imaging

Thomas Agius, MS,[1] Julien Songeon, MS,[2] Antoine Klauser, PhD,[2,3] Florent Allagnat, PhD,[1] Grégoire Longchamp, MD,[4] Raphael Ruttimann, BS,[4] Arnaud Lyon, MD,[1] Julijana Ivaniesevic, PhD,[5] Raphael Meier, MD, PhD,[6] Sébastien Déglise, MD,[1] James F. Markmann, MD, PhD,[7] Korkut Uygun, PhD,[8] Leo Buhler, MD,[9] Christian Toso, MD, PhD,[4] Jean-Marc Corpataux, MD,[1] Francois Lazeyras, PhD,[2,3] and Alban Longchamp, MD, PhD[1]

Background. The ideal preservation temperature for donation after circulatory death kidney grafts is unknown. We investigated whether subnormothermic (22 °C) ex vivo kidney machine perfusion could improve kidney metabolism and reduce ischemia-reperfusion injury. **Methods.** To mimic donation after circulatory death procurement, kidneys from 45-kg pigs underwent 60 min of warm ischemia. Kidneys were then perfused ex vivo for 4 h with Belzer machine perfusion solution UW at 22 °C or at 4 °C before transplantation. Magnetic resonance spectroscopic imaging coupled with LCModel fitting was used to assess energy metabolites. Kidney perfusion was evaluated with dynamic-contrast enhanced MRI. Renal biopsies were collected at various time points for histopathologic analysis. **Results.** Total adenosine triphosphate content was 4 times higher during ex vivo perfusion at 22 °C than at 4 °C perfusion. At 22 °C, adenosine triphosphate levels increased during the first hours of perfusion but declined afterward. Similarly, phosphomonoesters, containing adenosine monophosphate, were increased at 22 °C and then slowly consumed over time. Compared with 4 °C, ex vivo perfusion at 22 °C improved cortical and medullary perfusion. Finally, kidney perfusion at 22 °C reduced histological lesions after transplantation (injury score: 22 °C: 10.5 ± 3.5; 4 °C: 18 ± 2.25 over 30). **Conclusions.** Ex vivo kidney perfusion at 22°C improved graft metabolism and protected from ischemia-reperfusion injuries upon transplantation. Future clinical studies will need to define the benefits of subnormothermic perfusion in improving kidney graft function and patient's survival.

(*Transplantation Direct* 2022;8: e1354; doi: 10.1097/TXD.0000000000001354).

INTRODUCTION

Transplantation is the preferred treatment for end-stage kidney disease, but it suffers from a severe shortage of available organs. Approximately 100 000 patients are currently waiting for a donor kidney, with only 18 000 kidney transplants performed in the United States each year.[1] This

Received 23 May 2022.

Accepted 24 May 2022.

[1]Department of Vascular Surgery, Centre Hospitalier Universitaire VauDois and University of Lausanne, Lausanne, Switzerland.

[2]Department of Radiology and Medical Informatics, University of Geneva, Geneva, Switzerland.

[3]Center for Biomedical Imaging (CIBM), Geneva, Switzerland.

[4]Visceral and Transplant Surgery, Department of Surgery, Geneva University Hospitals and Medical School, Geneva, Switzerland.

[5]Metabolomics Platform, Faculty of Biology and Medicine, University of Lausanne, Switzerland.

[6]Department of Surgery, University of Maryland School of Medicine, Baltimore, MD, USA.

[7]Department of Surgery, Transplant Center, Massachusetts General Hospital, Harvard Medical School, Boston, USA.

[8]Department of Surgery, Center for Engineering in Medicine, Massachusetts General Hospital, Harvard Medical School, Boston, USA.

[9] Faculty of Science and Medicine, Section of Medicine, University of Fribourg, Fribourg, Switzerland.

T.A., J.S., F.L., and A.L. have contributed equally to this work.

The authors declare no conflicts of interest.

This work was supported by the Swiss National Science Foundation to J.-M.C., F.L. (SNSF 320030_182658), and A.L. (SNSF PZ00P3-185927), as well as the Mendez National Institute of Transplantation and the Leenards Foundation to AL.

A.L., A.K., J.S., T.A., L.B., J.-M.C., and F.L. participated in research design. A.L., A.K., R.M., K.U., J.F.M., and F.L. participated in the writing of the article. A.L., A.K., J.S., T.A., A.N., R.R., Ar.L., J.I., S.M., R.M., S.D., J.-M.C., and F.L. participated in the performance of the research. A.N., R.R., S.M., and F.L. contributed new reagents or analytic tools. A.L., A.K., J.S., T.A., S.M., R.M., L.B., J.-M.C., and F.L. participated in data analysis.

Supplemental digital content (SDC) is available for this article. Direct URL citations appear in the printed text, and links to the digital files are provided in the HTML text of this article on the journal's Web site (www.transplantationdirect.com).

Correspondence: Alban Longchamp, MD, PhD, Department of Vascular Surgery, Centre Hospitalier Universitaire VauDois and University of Lausanne, Rue du Bugnon 46, 1011 Lausanne, Switzerland. (alban.longchamp@chuv.ch).

ISSN: 2373-8731

DOI: 10.1097/TXD.0000000000001354

scarcity led to the expansion of the donor pool beyond standard-criteria kidney donors, including extended criteria donors and donation after circulatory death (DCD).[1,2] Although organs from these donors allow a higher survival rate than dialysis, their use is complicated by an increased rate of delayed graft function (DGF)[3] and acute rejection.[4]

DCD grafts are particularly vulnerable to ischemia-reperfusion (IR) injury, an issue that is not addressed at all by current standard storage strategies, including static cold storage and nonoxygenated hypothermic machine perfusion (eg, LifePort).[5,6] With this approach, prolonged periods (>24 h) of cold ischemia are associated with tubular necrosis, DGF, and poor graft survival.[4,7,8] Although static cold storage is the most prevalent method for renal allograft preservation, hypothermic machine perfusion without oxygen was shown to reduce DGF and to improve 1- and 3-y graft survival.[9] Hypothermic storage slows but does not entirely suspend cellular metabolism, resulting in a slow but inexorable consumption of cellular energy stores.[10] In a prior preclinical study, we found that, at 4 °C, oxygen supplementation was required to maintain adenosine triphosphate (ATP) levels.[10] In the COMPARE study, oxygen supplementation reduced biopsy-proven acute rejection but did not improve kidney graft survival or glomerular filtration rate at 12 mo.[11]

Although cold anoxic storage aims to arrest cell metabolism, ex vivo perfusion at physiologic normothermic temperature (37 °C) provides a continuous flow of warmed, oxygenated perfusate containing nutritional substrates, thereby maintaining the metabolic activity of the tissue.[12] Normothermic red cell–based-perfusion of porcine kidneys at 37 °C improved early postoperative creatinine and urea clearance in DCD grafts.[13] In addition, normothermic ex vivo perfusion allows graft assessment, reconditioning, and repair.[14,15] Using a red cell–based plasma-free solution, perfusion of marginal kidneys at 37 °C reduced DGF compared with static cold storage.[16] However, perfusion of organ at 37 °C is limited by the availability and cost of a blood perfusion system, complex heating system, tight pH and glucose control, red blood cell hemolysis, and risk of infection and immunization.[17,18] In addition, failure of the perfusion machine would rapidly lead to graft loss.

Subnormothermic (22 °C) ex vivo kidney perfusion was proposed as an alternative to perfusion at 37 °C.[19] Importantly, a previous study demonstrated that, compared with perfusion at 37 °C, kidney perfusion with blood:PlasmaLyte at 22 °C reduced acute tubular necrosis and improved kidney function in a DCD porcine model.[20] In liver grafts, perfusion of a cell-free, oxygenated perfusate at 22 °C promoted mitochondrial respiration and ATP stores before transplantation.[21] Overall, these studies suggest that 22 °C might be the optimal temperature to protect against kidney (IR) injuries, whereas avoiding complex normothermic perfusion machines.

Several tools are used to predict the suitability of kidney grafts. Although MRI is a well-established clinical diagnostic tool for assessing kidney graft function,[22] ^{31}P magnetic resonance spectroscopic imaging (pMRSI) enables the detection of high-energy phosphate metabolites such as ATP.[22] In fact, we previously reported that, in porcine kidneys, warm ischemia reduced energy stores, which correlated with kidney viability.[10]

MATERIAL AND METHODS

Ex Vivo Kidney Perfusion

Kidneys were assigned to the following ex vivo perfusion groups: (i) 4 °C with passive oxygenation of the perfusate (4 °C), (ii) 4 °C with active oxygenation (PO_2 >100kPa) of the perfusate (4 °C + O_2), (iii) 22 °C ex vivo kidney perfusion with active oxygenation (PO_2 >100kPa) of the perfusate (22 °C + O_2, Figure 1A). Passive oxygenation corresponded to ambient air oxygen diffusion.

Immediately after retrieval, kidneys were flushed with Belzer machine perfusion solution (MPS) UW Machine Perfusion Solution and immediately perfused for 4 h (before autotransplantation) or 42 h (time course experiment) using a homemade MRI-compatible pulsatile perfusion machine as published.[10] Belzer MPS UW solution can be stored between 2 °C and 25 °C and has a pH of 7.4 at 22 °C. Active oxygenation was achieved using a 0.15 m^2 membrane oxygenator (Biochrom Ltd, Cambridge, United Kingdom), maintaining the PO_2 levels at 100 kPa for the whole preservation time. The PO_2 levels during passive oxygenation were set at 20 kPa. The perfusion module was kept in an isolating box that passively kept the kidney at the desired temperature. Systolic and diastolic pressure were set at 40 and 20 mmHg, respectively.

MRI Imaging

Measurements were performed on a 3 Tesla multinuclear Prisma-fit 3T whole-body MRI scanner (Siemens Healthineers, Erlangen, Germany). ^{1}H imaging was performed with the body coil using a T2-weighted sequence (turbo SE, TR 6 530 ms, TE 110 ms, 2 mm slices) for kidney localization and structural imaging. Dynamic-contrast enhanced MRI with gadolinium (Gd-MRI) was used to determine the perfusion distribution between the cortex and the medulla and as an estimate of glomerular filtration rate as previously described.[7,10] Data were collected using a dynamic 2D saturation-prepared turbo flash sequence with the scanner body coil. This sequence has an inversion time of 255 ms, a flip angle of 12°, 1.3 mm × 1.3 mm resolution, and 6 slices of 4 mm (1 mm gap), TR 500 ms, and a TE of 1.4 ms. The perfusion-descending cortical slope was determined using the angle of the linear regression between the maximum signal value and the lowest intensity point after the initial peak.[21]

^{31}P Magnetic Resonance Imaging Spectroscopy

pMRSI was performed as described previously.[7] Briefly, a single loop ^{31}P-tuned coil fixed at the bottom of the perfusion tank allows the measurement of the signal. Scanner embedded body coil was used for ^{1}H imaging and for shimming to ensure field homogeneity. pMRSI consisted of 3D spatial encoding, with a field of view 250 × 250 × 160 mm^3, matrix size 16 × 16 × 8, nominal spatial resolution 15.6 × 15.6 × 20 mm^3, TR 1.0 s, flip angle of 35°, echo delay 0.6 ms, bandwidth 4000 Hz, and 2k sampling points. Elliptical encoding with 18 weighted averages resulted in an acquisition time of 45 min. The resonance of the inorganic phosphate (Pi, 5.2 ppm), which is uniformly present in the container and the kidney, was used as a reference for quantification of the pMRSI signal. Excitation pulse bandwidth has been adjusted to the ATP frequency range (Pi resonance—500 Hz). An exponential time filter with 20 Hz frequency width and zeroth and first order phase corrections were used to process the spectra. The metabolites (ATP, phosphomonoesters [PME], Pi, phosphocreatine/PCr) were fitted

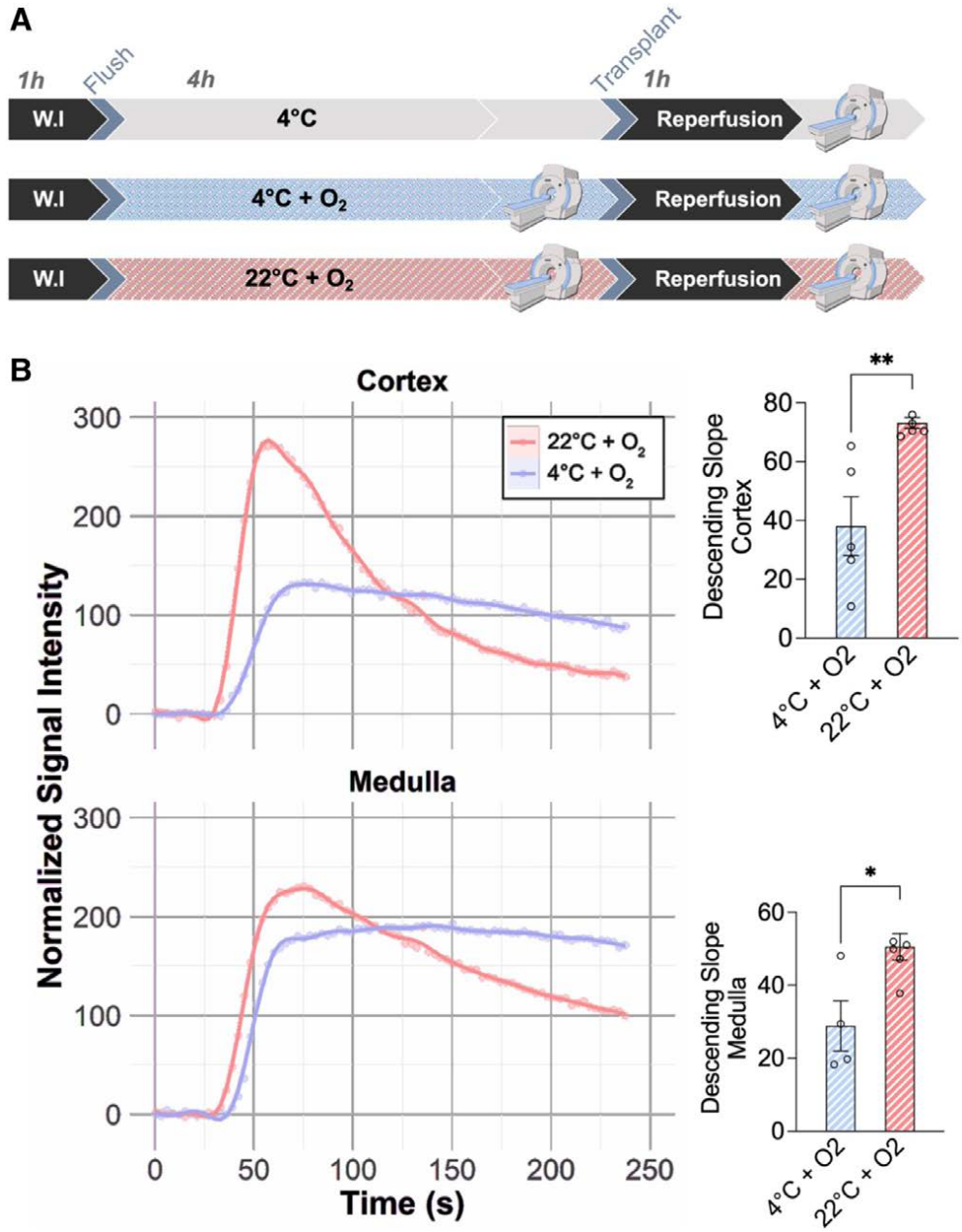

FIGURE 1. Ex vivo subnormothermic perfusion improves kidney perfusion. A, Experimental groups and design. Kidneys were retrieved after 60 min warm ischemia and placed into a hypothermic + passive oxygenation (4 °C), hypothermic + active oxygenation (4 °C + O_2), or subnormothermic + active oxygenation (22 °C + O_2) perfusion machine with or without oxygen for 4 h. Kidney were autografted into the same pig. Dynamic-contrast enhanced MRI analysis was performed prior (4 °C + O_2, 22 °C + O_2) and after transplantation (4 °C, 4 °C + O_2, 22 °C + O_2). B, Pretransplant representative Gd uptake in cortex (top) and medulla (bottom) of kidneys during hypothermic (blue line) or subnormothermic (red) perfusion and Gd perfusion-DS quantification (right, n = 5/group). Bars indicate mean ± SEM, and asterisks indicate the significance of the difference between perfusions methods by Student's *t* test or 1-way ANOVA and Tukey test. **P* < 0.05, ***P* < 0.01. n = 4 to 6 per group. DS, descending slope.

with Gaussian peaks using the syngo.via software (SIEMENS, Erlangen, Germany) and were estimated over the whole kidneys by averaging pMRSI voxels containing graft tissue, resulting in a single spectrum. Quantification results provided by 3D ^{31}P-MRSI at 3 T were analyzed with LCModel for magnetic resonance spectroscopy fitting as previously described.[23] The 3 ATP peaks were quantified separately to prevent methodological bias because of excitation profile imperfection. In each condition, pMRSI allowed the detection of α-, β-, and γ-ATP and PME composed by phosphocholine, phosphoethanolamine (PE), and adenosine monophosphate (AMP). ATP and PME concentration (mM) were quantified from the fitting and using the concentration of the inorganic-phosphate buffer (Pi, 25 mmol/L) as reference.[7] As single ATP concentration was calculated by average of the α-, β-, and γ-ATP values, ATP maps were generated using the spectroscopy software (Syngo MR Spectroscopy Evaluation, Siemens Healthineers, Erlangen, Germany). The colors represent the metabolite concentration normalized to the Pi for each voxel.

Animals and Surgery

The study was approved by the University of Geneva's animal ethics committee (protocol number: GE83/33556). Female pigs of 5 mo old were obtained from the animal facility

of Arare, Switzerland (n = 16). All pigs were maintained under standard conditions. Water and food were provided ad libitum. Animals were premedicated and anesthetized as previously described.[24] Animals were kept intubated and ventilated during the procedure. An arterial line was inserted in the internal carotid artery. Monitoring included heart rate, systemic blood pressure, pulse oximetry, and end-tidal CO_2.

Kidneys were explanted and transplanted back into the same animal (autotransplantation).[24] To mimic circulatory arrest during DCD procurement, renal arteries were crossed clamped for 60 min before collection. Kidneys were then immediately flushed and perfused as described earlier in the ex vivo kidney perfusion section above. At the end of the perfusion, both kidneys were transplanted sequentially onto the vena cava and aorta using a 6-0 running suture. After 2 h of reperfusion, pigs were sacrificed using 100 mEq of potassium chloride intravenously.

Histopathologic Analysis of Biopsies

Cortical kidney biopsies were obtained at baseline, after 60min of warm ischemia, after 4 h of ex vivo perfusion, and at 2 h after autotransplantation. Biopsies were immediately flash frozen or formalin fixed and embedded in paraffin. Fixed kidney biopsies were cut into sections of 3 µm thickness and stained with silver Jones and Periodic Acid-Schiff. Slides were scanned using a Axio Scan z1 slide scanner (Zeiss). Histopathologic analysis score was performed based on those described by Goujon et al[25,26] using Zen software (Zeiss). Whole biopsies were assessed and blinded to group assignment. The following categories were assessed: glomerular integrity, tubular dilatation, brush border integrity, cellular debris in lumina of tubules, interstitial edema, and tubular cell vacuolization. Briefly, to assess glomerulus integrity, >10 glomeruli were randomly selected from the section and assigned a score of 0 to 3. The same procedure was followed in the remaining categories. After that, the score for each category was converted to a percentage. The final score was converted to a final scale from 0 to 5 according to the percentage of damage: 0% to 15% (0), 15% to 30% (1), 30% to 45% (2), 45% to 60% (3), 60% to 75% (4), and >75% (5) using the following formula: ($Category_{Final\ Score}$/3) *100. The final score for each biopsy ranged from 0 to 30, with 30 the highest score corresponding to more severe damage. Scoring was performed blindly by 2 independent researchers.

RT-qPCR Analysis

Kidney biopsy powder was homogenized in Tripure Isolation Reagent (Roche, Switzerland). Total RNA was extracted as previously described.[27] cDNA was synthesized by random hexamer priming with the Verso cDNA kit (Prime Script RT reagent, Takara). RT-qPCR was performed with Power SYBR Green Master Mix (Ref: 4367659, Applied Biosystems, Thermo Fisher Scientific AG, Switzerland) in a ViiA 7 Real-Time PCR System (Applied Biosystems, Thermo Fisher Scientific AG, Switzerland). Amplification data were analyzed using the QuantStudio 1.3 software (Thermo Fisher Scientific AG, Switzerland). Fold changes were calculated using relative standard curves methods, using ribosomal protein RPL27 genes as standards. Inflammatory gene expression was quantified 2 h after reperfusion and compared with their respective baseline. Primers' sequences are indicated in Table S1 (SDC, http://links.lww.com/TXD/A437).

Metabolite Analysis

Tissue samples were preextracted and homogenized by the addition of 150 µL of MeOH:H2O (4:1) in the Cryolys Precellys 24 sample homogenizer (2 × 20 s at 10 000 rpm, Bertin Technologies, Rockville, MD, United States) with ceramic beads. The bead beater was air-cooled down at a flow rate of 110 L/min at 6 bar. Homogenized extracts were centrifuged for 15 min at 4000 *g* at 4 °C (Hermle, Gosheim, Germany). The resulting supernatant was collected and analyzed by hydrophilic interaction liquid chromatography coupled to tandem mass spectrometry (HILIC-MS/MS). Proteins were extracted using 20 mmol/L Tris-HCl (pH 7.5), 4M guanidine hydrochloride, 150 mmol/L NaCl, 1 mmol/L Na2EDTA, 1 mmol/L EGTA, 1% Triton, 2.5 mmol/L sodium pyrophosphate, 1 mmol/L betaglycerophosphate, 1 mmol/L Na3VO4, and 1 µg/mL leupeptin using the Cryolys Precellys 24 sample Homogenizer (2 × 20 s at 10 000 rpm, Bertin Technologies, Rockville, MD, United States) with ceramic beads. BCA Protein Assay Kit (Thermo Scientific, Massachusetts, United States) was used to measure (A562 nm) total protein concentration (Hidex, Turku, Finland), and samples were normalized based on the tissue weight before the LC-MS/MS analysis by extracting with different volumes of MeOH:H2O (4:1, v/v). Extracted samples were analyzed by HILIC-MS/MS in both positive and negative ionization modes using a 6495 triple quadrupole system (QqQ) interfaced with a 1290 UHPLC system (Agilent Technologies). Raw LC-MS/MS data were processed using the Agilent Quantitative analysis software (version B.07.00, MassHunter Agilent technologies). Relative quantification of metabolites was based on extracted ion chromatogram areas for the monitored MRM transitions. Peak areas of detected metabolites were analyzed in "R" software, and signal intensity drift correction and noise filtering (if necessary, using CV [QC features] >30%) was done within the MRM PROBS software.

Statistical Analysis

Data are presented as mean ± SEM, and differences are considered significant when $P < 0.05$. Comparisons between groups were analyzed using ANOVA and post hoc Tukey tests or Sidak's test when indicated. Tukey's and Sidak's test were used to test for differences between 22 °C + O_2 and 4 °C perfusions. Two-group comparisons were performed using Student *t* tests (Prism 9.2, GraphPad Softwares, San Diego, CA, United States). Fitting curves of the metabolites concentration over time were computed using R (version 4.1, https://cran.r-project.org).

RESULTS

Ex Vivo Kidney Perfusion Improves Kidney Perfusion and ATP Generation

To mimic DCD, kidneys underwent 60 min of warm ischemia before procurement. Kidney grafts were then perfused in a homemade MRI-compatible pulsatile perfusion machine at 22 °C with active oxygenation (22 °C + O_2), at 4 °C with active oxygenation (4 °C + O_2), or 4 °C without additional oxygen (4 °C, Figure 1A). After 4 h at 22 °C + O_2, cortical and medullary flows were improved compared with 4 °C + O_2. This was reflected by an increase in the perfusion-descending slope (+35% cortex +26% medulla, Figure 1B).

Next, mean ATP levels were measured by averaging pMRSI voxels containing graft tissue resulting in a single spectrum (Figure 2A). In fact, we previously demonstrated that mean ATP levels (average AUC of the β- and γ-ATP peaks) are reduced by warm ischemia and correlate with (IR) injuries.[10] Using pMRSI, α-, β-, and γ-ATP and PME containing AMP were only detected during ex vivo perfusion with active oxygenation at 4 °C and 22 °C (Figure 2A). In kidneys perfused at 22 °C + O_2, ATP and PME levels were 3 times higher than at 4 °C + O_2 perfusion (5.5 mmol/L versus 2.1 mmol/L and 0.79 mmol/L versus 0.26 mmol/L, Figure 2B). This increase of AMP and ATP levels at 22 °C + O_2 was confirmed by liquid chromatography-mass spectrometry (LC-MS, +59%, +36% and +45%, respectively; Figure 2C). Surprisingly, PME and ATP concentrations tended to be higher in the medulla independently of the perfusion conditions, as demonstrated by voxel mapping of the metabolites (Figure S1, SDC, http://links.lww.com/TXD/A437).

Kidney ATP Levels Increased up to 10 h During Ex Vivo Subnormothermic Kidney Perfusion

In healthy kidneys perfused at 4 °C + O_2, α-, β-, and γ-ATP remained stable for up to 22 h of perfusions.[10] To determine the effect of 22 °C perfusion on ATP production over time in DCD grafts, PME and α-, β-, and γ-ATP concentrations were monitored for 42 h (time course experiment). Kidney α-, β-, and γ-ATP concentrations were 2 times higher after 10 h of perfusion compared with baseline (0.5 mmol/L to 1 mmol/L for β-ATP, 0.75 mmol/L to 1.5 mmol/L for γ-ATP; Figure 3A) and 4 °C + O_2.[10] The PME concentration was 4 times higher than ATP at the beginning of the perfusion (4 mmol/L of PME versus 1 mmol/L of α-, β-, and γ-ATP), and rapidly decreased to reach a plateau at 2 mmol/L. This is consistent with the hypothesis that the PME containing the AMP is consumed over time to generate ATP. Finally, after 10 h of perfusion at 22 °C + O_2, ATP levels gradually decline to ultimately reach 0 mmol/L after 42 h of perfusion (Figure 3B). PME concentration remains stable for up to 42 h (Figure 3B).

Ex Vivo Kidney Perfusion at 22 °C Reduces Kidney Ischemia and Reperfusion Injuries

To evaluate the benefit of 22 °C ex vivo perfusion before transplantation, we examined the histological damage using a modified Goujon score (described in the methods section), shown to reflect kidney function.[10,25] Kidney biopsies were analyzed at baseline, after 60 min of warm ischemia, at the end of the ex vivo perfusion, and at 1 h after transplantation. Surprisingly, no significant damage was observed after warm ischemia (Figure 4A,B). Consistent with previous findings, histological damages were significantly increased at the end of the

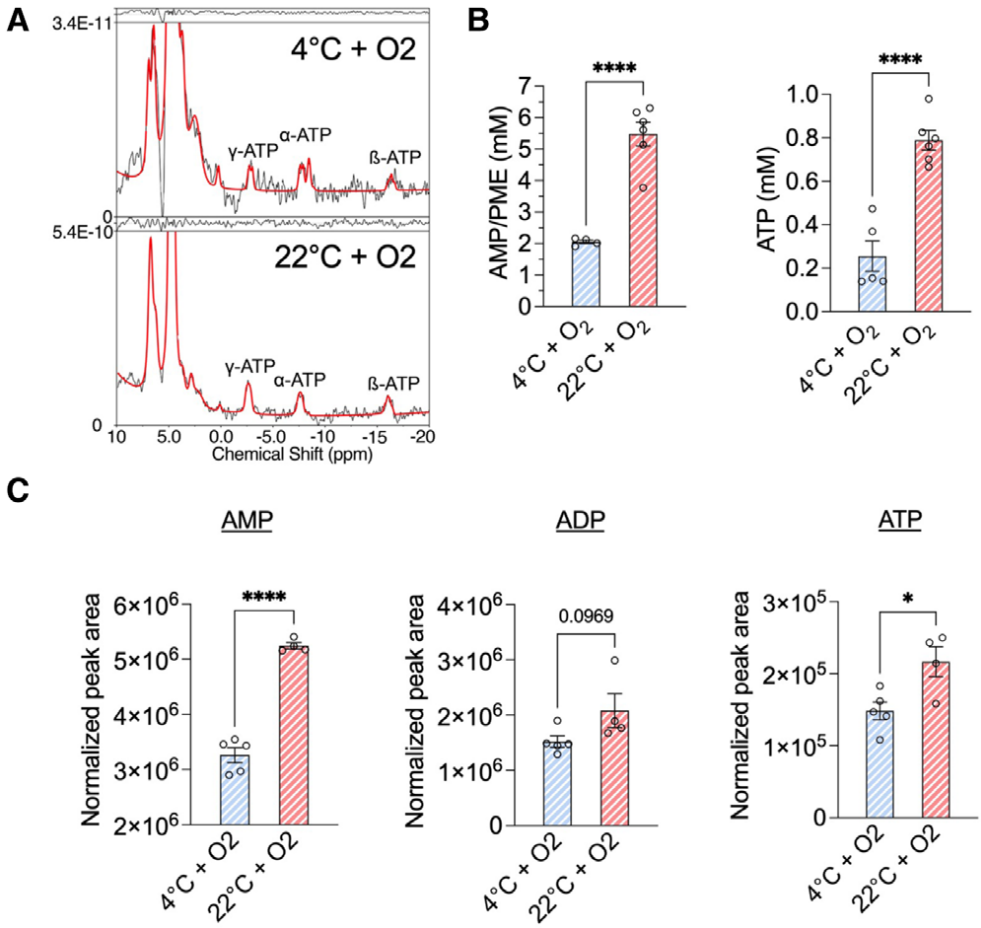

FIGURE 2. Energy metabolism is improved during subnormothermic perfusion. A and B, Representative of pMRSI spectra fitted with LCModel (A) and kidney PME and β, γ-mean ATP levels (B) during 4 °C + O_2 and 22 °C + O_2 perfusion before transplantation. C, Kidney AMP, ADP, and ATP levels measured by LC-MS. Bars indicate mean ± SEM, and asterisks indicate the significance of the difference between perfusions methods by Student's *t* test or 1-way ANOVA and Tukey test. ****$P < 0.0001$. n = 4 to 5 per group. ADP, adenosine diphosphate; AMP, adenosine monophosphate; ATP, adenosine triphosphate; LC-MS, liquid chromatography-mass spectrometry; PME, phosphomonoesters; pMRSI, ^{31}P magnetic resonance spectroscopic imaging.

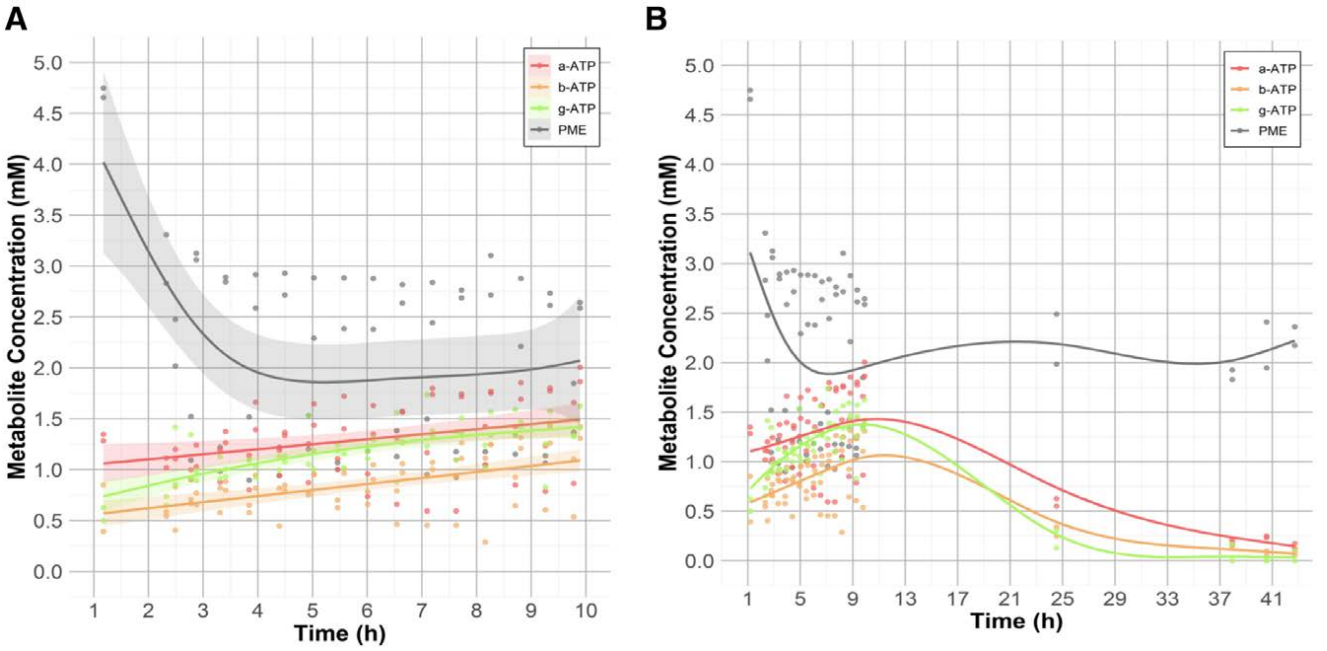

FIGURE 3. Kidney ATP levels increased up to 10 h during ex vivo subnormothermic kidney perfusion. A, Monitoring of ATP levels during 22 °C + O_2 perfusion (A) up to 10 h and (B) up to 42 h. Concentration (mM) of the indicated metabolites over time, in kidney, during 22 °C + O_2 perfusion. n = 4 per group. Fitting curves are generalized additive model (formula: y ~ s(x)) with a basis size of k = 15, n = 3. ATP, adenosine triphosphate; PME, phosphomonoesters.

ex vivo perfusion and after reperfusion in vivo (Figure 4A,B; Table S2, SDC, http://links.lww.com/TXD/A437). Importantly, 22 °C perfusion led to the greatest protection from IR injury (score of 22 °C + O_2, 4 °C + O_2, and 4 °C: 10.5 ± 2.3, 19.25 ± 3.9, and 18.3 ± 2.5, ± SD, Figure 4A,B). Perfusion of 22 °C significantly reduced tubular dilatation and luminal cell debris and protected the brush border (Figure 4A; Figure S2, SDC, http://links.lww.com/TXD/A437). In the 22 °C ex vivo perfusion group, interleukin (IL)-6 and IL-10 gene expressions were upregulated after transplantation (log2 fold-change of 22 °C + O_2, 4 °C + O_2, and 4 °C: 6.5 ± 0.8, 2.4 ± 0.9, and 3.9 ± 0.4 and 3.9 ± 0.4, 1.4 ± 0.9, 2.6 ± 0.7, respectively), whereas the expression of TNFalpha and Arg1 remained unaffected (Figure 4C). In addition, 2 h after kidney implantation, flow in the cortex and medulla improved at 22 °C + O_2 (+18% and +4% cortex, +17% and +11% medulla compared with 4 °C and 4 °C + O_2 respectively; Figure S2, SDC, http://links.lww.com/TXD/A437). Finally, ATP and, to a lesser extent, PME levels were significantly higher after transplantation in organs that were previously perfused 22 °C + O_2 (Figure 4D). Altogether, ex vivo perfusion at 22°C improved kidney metabolism and reduced (IR) injuries during transplantation.

DISCUSSION

Here, we found that kidney graft perfusion at 22 °C with an oxygenated MP-Belzer solution, without oxygen carrier, increased ATP production and minimized IR injuries during transplantation compared with perfusion at 4 °C. Of interest, active oxygenation did not increase ATP production at 4 °C. In addition, the simplicity of subnormothermic perfusion machine, without the need for a heating unit or oxygen carrier, could be easily used in a clinical setting and lower the costs. Altogether, perfusion of kidney graft at 22 °C could translate into greater utilization of kidney allograft.

Previously, the benefits of normothermic perfusion (37 °C) were linked to an increase in fatty acid metabolism and oxidative phosphorylation.[12] Similarly, kidney perfusion at 22°C improved mitochondrial ATP production, consistent with our hypothesis that, at 22 °C, kidneys are metabolically active.[22,28] Interestingly, in cold-stored organs, it has also been shown that gradual rewarming from hypothermia to normothermia before transplantation improves kidney function,[29,30] highlighting the importance of restoring metabolism before implantation. At 22 °C, we observed an increase in PME and ATP levels during the first 10 h of perfusion. After 10 h of perfusion at 22 °C, ATP level gradually declined to reach 0 mmol/L at 42 h of perfusion. We previously reported that, at 4 °C, in the absence of warm ischemia, ATP levels remained stable up to 22 h of perfusion but at significantly lower levels (0.26 mmol/L).[10] Similarly, ATP levels decrease during cold storage in the kidney[28] and liver[31] and correlate with the degree of injury. In humans, ATP predicted immediate graft function,[10,31] and ATP is often used as a marker of viability during ischemia.[27,32] Although long-term perfusion at 22 °C using MP-Belzer solution might not by viable, it is a promising strategy to recondition organs and improve initial graft function. Future studies should investigate the advantages of short-term (<10 h) reconditioning at 22 °C of previously cold-stored organs.

In this study, LC-MS/MS was used to validate the accurate quantification of nucleotides by pMRSI.[27] Indeed, the fitting of α-ATP with a broad Gaussian might include the NAD+ and NADH signal.[10,33] Recent improvements using deep learning algorithms were used to reduce concentration estimation bias of metabolites with overlapping spectra.[34] pRMSI also suffers from a relative low sensitivity compared with liquid chromatography or 1H imaging at a constant magnetic field.[10] Thus, the acquisition is generally performed with higher voxel size to achieve enough signal to noise ratio while keeping an

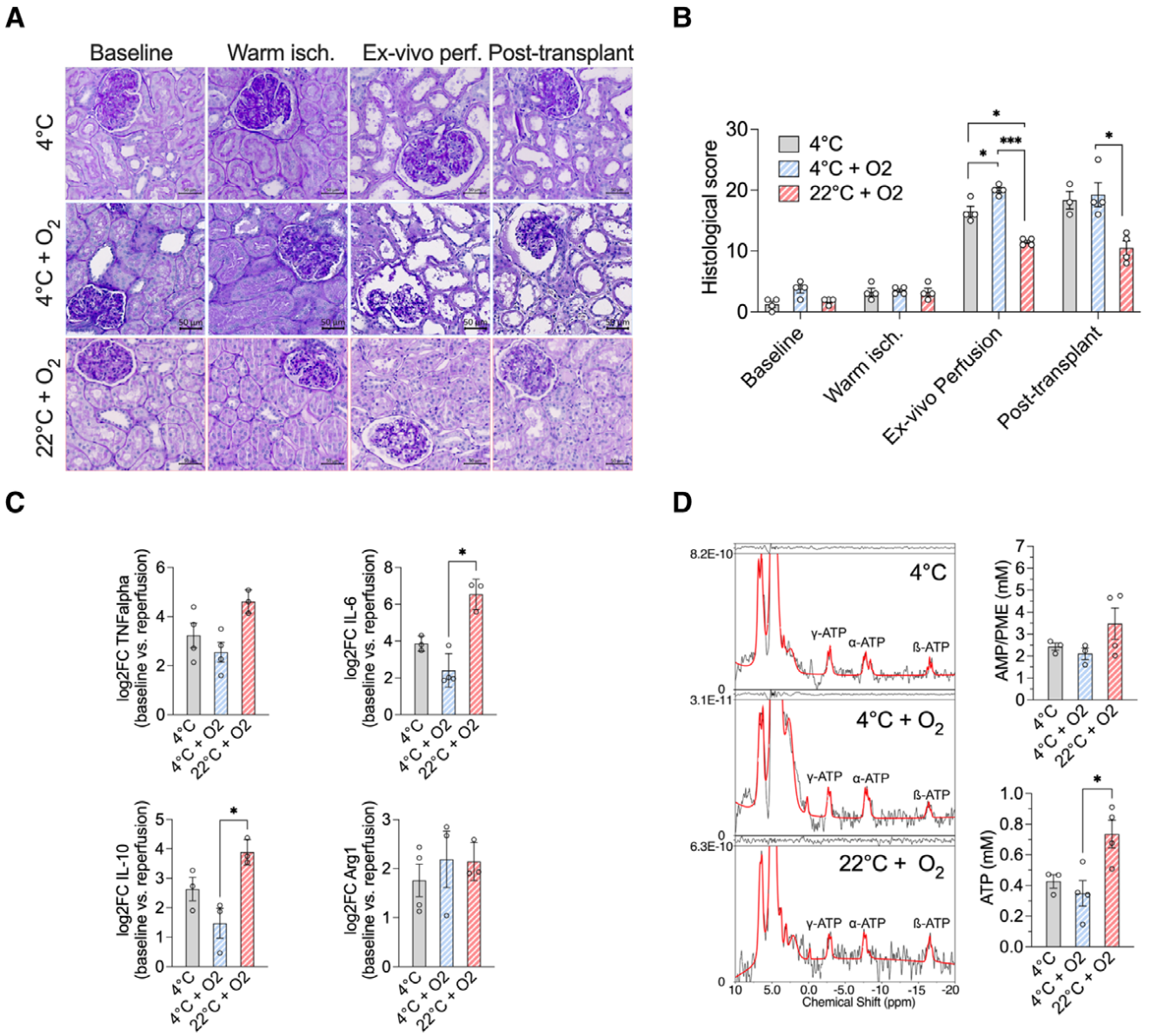

FIGURE 4. Subnormothermic perfusion reduces kidney damages. A and B, Representative cortical kidney sections (A) stained with PAS, and histological score (B) at the indicated time and conditions (4 °C, 4 °C + O_2, 22 °C + O_2). C, Expression of the indicated gene in kidney, analyzed by RT-PCR at baseline and after transplantation after 4 h of 4 °C, 4 °C + O_2, or 22 °C + O_2 perfusion. D, Representative of pMRSI spectra (left), and quantification (right) of kidney AMP and ATP levels during 4 °C, 4 °C + O_2, or 22 °C + O_2 perfusion after transplantation. The spectra are fitted using LCModel. Bars indicate mean ± SEM and median ± IQR. Asterisks indicate the significance of the difference between perfusions methods by 2-way ANOVA and Sidak post hoc test. *P < 0.05, ***P < 0.001, n = 4 per group. AMP, adenosine monophosphate; ATP, adenosine triphosphate; IQR, interquartile range; PAS, periodic acid-Schiff; PME, phosphomonoesters; pMRSI, ^{31}P magnetic resonance spectroscopic imaging.

acceptable scan time. As an example, this lack of sensitivity limitation hinders the measurement of ATP at 4 °C without oxygen. The application of machine learning[35] and neural network can further improve pMRSI sensitivity, spatial resolution, and computing time.[36] Indeed, ongoing improvement in pMRSI spatial resolution, in combination with spatial phase encoding, can provide multivoxels acquisition of the kidney graft that enables metabolite mapping over the full field of view (Figure S1, SDC, http://links.lww.com/TXD/A437[37]). Overall pMRSI remains a powerful, noninvasive tool to quantify ATP.[10]

During ex vivo perfusion at 22 °C, we did not compare passive versus active oxygenation of Belzer MPS UW, perfusion with Hb-based oxygen carrier, or packed red blood cells. Importantly, oxygenated machine perfusion at 22 °C lowers metabolic demand compared with organs perfused at 37 °C.[38] Thus, although still metabolically active, grafts maintained at 22 °C could be safely perfused with MP-Belzer without oxygen carriers. At 22 °C, Hb-based oxygen carrier achieved short-term kidney function equivalent to blood.[39] Similarly in human kidneys, compared with hemoglobin oxygen carrier, perfusion with packed red blood cells at 37 °C resulted in similar vascular flow, oxygen consumption, or ATP levels.[40] It is likely, that, although perfusion at 22 °C allows considerable recovery of energy metabolism compared with 4 °C, metabolism is significantly reduced (compared to 37 °C) so that passive oxygenation is sufficient for adequate oxygen delivery. Altogether, we hypothesize that adequate tissue oxygenation can be achieved at 22 °C without the use of packed red blood cells and complex blood perfusion machine.

Interestingly, we did not observe a benefit of active oxygenation at 4 °C, except for slightly improved graft perfusion. Consistently, the addition of oxygen to hypothermic machine perfusion did not significantly improved DCD porcine kidney function.[41] Similarly, a recent clinical trial failed to show 12-mo difference in eGFR between kidneys perfused at 4 °C with oxygen compared with hypothermic perfusion alone.[11] Previous studies comparing oxygenated perfusion used various flow rates (50–100 mL/min) and PO_2 levels (500–650 mmHg), complicating data interpretation.[11,42-44]

A potential disadvantage of normothermic preservation appears to be the generation of a proinflammatory milieu, with the accumulation of inflammatory mediators including cytokines and damage-associated molecular patterns.[45,46] Consistently, here both pro- and anti-inflammatory cytokines (IL-6 and IL-10, respectively) were increased after ex vivo perfusion at 22 °C. On the other hand, compared with 37 °C, ex vivo lung perfusion at 25 °C reduced the production of inflammatory mediators and was associated with reduced histologic graft injury after transplantation.[47] Altogether, cytokines profile and its relevance over time in kidney graft undergoing perfusion at 22 °C needs to be evaluated further.

Our study has several limitations that need to be acknowledged. First, the impact of perfusion at 22 °C and ATP levels on kidney function (serum creatinine, urea, and estimated glomerular filtration rate) or urine production after transplantation were not assessed. Consistent with previous reports, no urine output was recorded during the first hour following transplantation.[48] Interestingly, in human, urine production during normothermic ex vivo perfusion was not correlated with posttransplant kidney function.[49] Moreover, proper assessment of kidney function could not be performed because of local regulation, which did not allow survival surgery. Thus, the histological score, previously correlated with the degree of kidney injury,[10,24-26] was used as a surrogate endpoint of kidney function. Future clinical trials should help determine the benefits of perfusion at 22 °C on postoperative graft function. In addition, the benefits of subnormothermic perfusion should be tested in all forms of marginal donors, including kidneys from old donors, after acute kidney injury, and after prolonged cold preservation.

In conclusion, subnormothermic perfusion of porcine DCD kidneys improved ATP production and reduced IRI. Perfusion of DCD grafts at 22 °C should be tested in clinical trials to determine if it can improve posttransplant graft function and patient survival.

ACKNOWLEDGMENTS

We thank Jean-Pierre Giliberto from the department of surgery, University Hospitals of Geneva, as well as Hector Gallart Ayala from the Metabolomics Platform, Faculty of Biology and Medecine, University of Lausanne, Switzerland, for the excellent technical assistance.

REFERENCES

1. Assis-Borba L, Cristelli MP, Paula MI, et al. Expanding the use of expanded criteria donors in kidney transplantation. *Int Urol Nephrol*. 2014;46:1663–1671.
2. Summers DM, Watson CJ, Pettigrew GJ, et al. Kidney donation after circulatory death (DCD): state of the art. *Kidney Int*. 2015;88:241–249.
3. Tennankore KK, Kim SJ, Alwayn IP, et al. Prolonged warm ischemia time is associated with graft failure and mortality after kidney transplantation. *Kidney Int*. 2016;89:648–658.
4. Dragun D, Hoff U, Park JK, et al. Prolonged cold preservation augments vascular injury independent of renal transplant immunogenicity and function. *Kidney Int*. 2001;60:1173–1181.
5. Zhao H, Alam A, Soo AP, et al. Ischemia-reperfusion injury reduces long term renal graft survival: mechanism and beyond. *Ebiomedicine*. 2018;28:31–42.
6. Ponticelli C. Ischaemia-reperfusion injury: a major protagonist in kidney transplantation. *Nephrol Dial Transplant*. 2014;29:1134–1140.
7. Lee CM, Carter JT, Randall HB, et al. The effect of age and prolonged cold ischemia times on the national allocation of cadaveric renal allografts. *J Surg Res*. 2000;91:83–88.
8. Kayler LK, Magliocca J, Zendejas I, et al. Impact of cold ischemia time on graft survival among ECD transplant recipients: a paired kidney analysis. *Am J Transplant*. 2011;11:2647–2656.
9. Moers C, Smits JM, Maathuis MH, et al. Machine perfusion or cold storage in deceased-donor kidney transplantation. *N Engl J Med*. 2009;360:7–19.
10. Longchamp A, Klauser A, Songeon J, et al. Ex vivo analysis of kidney graft viability using 31p magnetic resonance imaging spectroscopy. *Transplantation*. 2020;104:1825–1831.
11. Jochmans I, Brat A, Davies L, et al; COMPARE Trial Collaboration and Consortium for Organ Preservation in Europe (COPE). Oxygenated versus standard cold perfusion preservation in kidney transplantation (COMPARE): a randomised, double-blind, paired, phase 3 trial. *Lancet*. 2020;396:1653–1662.
12. Urbanellis P, McEvoy CM, Škrtić M, et al. Transcriptome analysis of kidney grafts subjected to normothermic ex vivo perfusion demonstrates an enrichment of mitochondrial metabolism genes. *Transplant Direct*. 2021;7:e719.
13. Urbanellis P, Hamar M, Kaths JM, et al. Normothermic ex vivo kidney perfusion improves early DCD graft function compared with hypothermic machine perfusion and static cold storage. *Transplantation*. 2020;104:947–955.
14. Hosgood SA, Barlow AD, Hunter JP, et al. Ex vivo normothermic perfusion for quality assessment of marginal donor kidney transplants. *Br J Surg*. 2015;102:1433–1440.
15. Kaths JM, Hamar M, Echeverri J, et al. Normothermic ex vivo kidney perfusion for graft quality assessment prior to transplantation. *Am J Transplant*. 2018;18:580–589.
16. Nicholson ML, Hosgood SA. Renal transplantation after ex vivo normothermic perfusion: the first clinical study. *Am J Transplant*. 2013;13:1246–1252.
17. Parente A, Osei-Bordom DC, Ronca V, et al. Organ restoration with normothermic machine perfusion and immune reaction. *Front Immunol*. 2020;11:565616.
18. Eshmuminov D, Becker D, Bautista Borrego L, et al. An integrated perfusion machine preserves injured human livers for 1 week. *Nat Biotechnol*. 2020;38:189–198.
19. Kaths JM, Paul A, Robinson LA, et al. Ex vivo machine perfusion for renal graft preservation. *Transplant Rev (Orlando)*. 2018;32:1–9.
20. Bhattacharjee RN, Ruthirakanthan A, Sun Q, et al. Subnormothermic oxygenated perfusion optimally preserves donor kidneys ex vivo. *Kidney Int Rep*. 2019;4:1323–1333.
21. Bruinsma BG, Sridharan GV, Weeder PD, et al. Metabolic profiling during ex vivo machine perfusion of the human liver. *Sci Rep*. 2016;6:22415.
22. Lazeyras F, Buhler L, Vallee JP, et al. Detection of ATP by "in line" 31P magnetic resonance spectroscopy during oxygenated hypothermic pulsatile perfusion of pigs' kidneys. *MAGMA*. 2012;25:391–399.
23. Provencher SW. Automatic quantitation of localized in vivo 1H spectra with LCModel. *NMR Biomed*. 2001;14:260–264.
24. Longchamp A, Meier RPH, Colucci N, et al. Impact of an intra-abdominal cooling device during open kidney transplantation in pigs. *Swiss Med Wkly*. 2019;149:w20143.
25. Meier RPH, Piller V, Hagen ME, et al. Intra-abdominal cooling system limits ischemia-reperfusion injury during robot-assisted renal transplantation. *Am J Transplant*. 2018;18:53–62.
26. Goujon JM, Hauet T, Menet E, et al. Histological evaluation of proximal tubule cell injury in isolated perfused pig kidneys exposed to cold ischemia. *J Surg Res*. 1999;82:228–233.
27. Longchamp A, Mirabella T, Arduini A, et al. Amino acid restriction triggers angiogenesis via GCN2/ATF4 regulation of VEGF and H2S production. *Cell*. 2018;173:117–129.e14.

28. Buchs JB, Lazeyras F, Bühler L, et al. [The viability of kidneys tested by gadolinium-perfusion MRI during ex vivo perfusion]. *Prog Urol*. 2009;19:307–312.
29. Bruinsma BG, Yeh H, Ozer S, et al. Subnormothermic machine perfusion for ex vivo preservation and recovery of the human liver for transplantation. *Am J Transplant*. 2014;14:1400–1409.
30. Mahboub P, Ottens P, Seelen M, et al. Gradual rewarming with gradual increase in pressure during machine perfusion after cold static preservation reduces kidney ischemia reperfusion injury. *PLoS One*. 2015;10:e0143859.
31. González FX, Rimola A, Grande L, et al. Predictive factors of early postoperative graft function in human liver transplantation. *Hepatology*. 1994;20:565–573.
32. de Rougemont O, Breitenstein S, Leskosek B, et al. One hour hypothermic oxygenated perfusion (HOPE) protects nonviable liver allografts donated after cardiac death. *Ann Surg*. 2009;250:674–683.
33. Graveron-Demilly D. Quantification in magnetic resonance spectroscopy based on semi-parametric approaches. *MAGMA*. 2014;27:113–130.
34. Iqbal Z, Nguyen D, Thomas MA, et al. Deep learning can accelerate and quantify simulated localized correlated spectroscopy. *Sci Rep*. 2021;11:8727.
35. Lam F, Li Y, Guo R, et al. Ultrafast magnetic resonance spectroscopic imaging using SPICE with learned subspaces. *Magn Reson Med*. 2020;83:377–390.
36. Lee HH, Kim H. Deep learning-based target metabolite isolation and big data-driven measurement uncertainty estimation in proton magnetic resonance spectroscopy of the brain. *Magn Reson Med*. 2020;84:1689–1706.
37. Klauser A, Klauser P, Grouiller F, et al. Whole-brain high-resolution metabolite mapping with 3D compressed-sensing SENSE low-rank. *NMR Biomed*. 2022;35:e4615.
38. Raigani S, Carroll C, Griffith S, et al. Improvement of steatotic rat liver function with a defatting cocktail during ex situ normothermic machine perfusion is not directly related to liver fat content. *PLoS One*. 2020;15:e0232886.
39. Bhattacharjee RN, Patel SVB, Sun Q, et al. Renal protection against ischemia reperfusion injury: hemoglobin-based oxygen carrier-201 versus blood as an oxygen carrier in ex vivo subnormothermic machine perfusion. *Transplantation*. 2020;104:482–489.
40. Aburawi MM, Fontan FM, Karimian N, et al. Synthetic hemoglobin-based oxygen carriers are an acceptable alternative for packed red blood cells in normothermic kidney perfusion. *Am J Transplant*. 2019;19:2814–2824.
41. Venema LH, Brat A, Moers C, et al. Effects of oxygen during long-term hypothermic machine perfusion in a porcine model of kidney donation after circulatory death. *Transplantation*. 2019;103:2057–2064.
42. De Beule J, Jochmans I. Kidney perfusion as an organ quality assessment tool-are we counting our chickens before they have hatched? *J Clin Med*. 2020;9:E879.
43. Jochmans I, Akhtar MZ, Nasralla D, et al. Past, present, and future of dynamic kidney and liver preservation and resuscitation. *Am J Transplant*. 2016;16:2545–2555.
44. Hoyer DP, Gallinat A, Swoboda S, et al. Subnormothermic machine perfusion for preservation of porcine kidneys in a donation after circulatory death model. *Transpl Int*. 2014;27:1097–1106.
45. Scheuermann U, Zhu M, Song M, et al. Damage-associated molecular patterns induce inflammatory injury during machine preservation of the liver: potential targets to enhance a promising technology. *Liver Transpl*. 2019;25:610–626.
46. Sadaria MR, Smith PD, Fullerton DA, et al. Cytokine expression profile in human lungs undergoing normothermic ex-vivo lung perfusion. *Ann Thorac Surg*. 2011;92:478–484.
47. Gloria JN, Yerxa J, Kesseli SJ, et al. Subnormothermic ex vivo lung perfusion attenuates graft inflammation in a rat transplant model. *J Thorac Cardiovasc Surg*. 2021;164:e59–e70.
48. Juriasingani S, Ruthirakanthan A, Richard-Mohamed M, et al. Subnormothermic perfusion with H. *Biomolecules*. 2021;11:446.
49. Mazilescu LI, Urbanellis P, Kim SJ, et al. Normothermic ex vivo kidney perfusion for human kidney transplantation: first north American results [published online ahead of print, 2022 Mar 1]. *Transplantation*. 2022; doi:10.1097/TP.0000000000004098

12

BENEFITS OF SODIUM HYDROSULFIDE (H_2S) FOR KIDNEY PROTECTION

"It takes a fearless, unflinching love and deep humility to accept the univers at it is. The most effective way he knew to accomplish that, the most powerful tool at his disposal, was the scientific method, which over time winnows out deception. It can't give you absolute truth because science is a permanent revolution, always subject to revision."

- Ann Druyan, *Cosmos*

Contents

12.1 SUMMARY

In Chapter 9, ischemia-reperfusion injury (IRI) has been shown to be associated with decreased oxygen availability within the organ during ischemic events, as well as with the reintroduction of oxygen upon reperfusion. A potential strategy to minimize IRI-induced damages involves reducing the oxygen demand of the organ. Hydrogen sulfide (H_2S) has been shown to reduce oxygen and ATP consumption in isolated perfused kidneys, as well as inflammation and improve renal function following IRI in rodents. Investigating the effects of H_2S during warm ischemia, specifically as an extension of cold storage time, could lead to larger geographic organ-sharing regions, reduced procedural logistics, and optimized recipient preparation. These advancements could contribute to worldwide donor sharing with improved outcomes, thereby mitigating the donor shortage. Our research on the benefits and applicability of H_2S in clinical settings is presented in the article Section 12.2.

In this study, porcine kidneys underwent either no warm ischemia or 60 minutes of warm ischemia before undergoing oxygenated hypothermic machine perfusion (HMP) to simulate donation after circulatory death (DCD). An intra-arterial bolus of 100 µM of NaHS, an H_2S donor, was injected before the warm ischemia. Following 2 hours of HMP, the kidneys were transplanted and reperfused for 1 hour before being harvested. Kidney function was assessed through measurements of high energy metabolites using ^{31}P-MRSI, Gadolinium elimination, and histopathological scoring before, during, and after ex vivo perfusion. Warm ischemia (60 minutes) caused significant histological damage, delayed cortical and medullary Gadolinium elimination (perfusion), and reduced ATP levels, but not its precursors (AMP). As expected, ATP levels and kidney perfusion both inversely correlated with the severity of kidney histological injury.

The results indicate that administration of H_2S did not result in significant reductions in ischemia-reperfusion injuries or improvements in kidney metabolism. When NaHS was administered via the renal artery before ischemia, both donation after brain death (DBD) and DCD pig kidneys showed similar renal perfusion and ATP levels as the control group after 4 hours of ex-vivo perfusion. Additionally, no significant difference was observed in renal artery injection of NaHS or auto-transplantation in histological lesions or cortical/medullary kidney perfusion. Therefore, this study suggests that the use of NaHS to deliver H_2S treatment does not significantly improve renal graft function in porcine kidneys. Further studies are required to determine the potential benefits of H_2S in humans and explore the use of other molecules.

Sodium Hydrosulfide (NaHS) Treatment During Porcine Kidney Ex-Vivo Perfusion and Transplantation.

Thomas Agius,[1,2,3] Julien Songeon,[4,5] Arnaud Lyon,[1] Justine Longchamp,[1] Raphael Ruttimann,[6] Florent Allagnat,[1] Sébastien Déglise,[1] Jean-Marc Corpataux,[1] Déla Golshayan,[7] Leo Buhler,[8] Raphael Meier,[9] Heidi Yeh,[2,3] James F Markmann,[2,3] Korkut Uygun,[3] Christian Toso,[6] Antoine Klauser,[4,5] François Lazeyras,[4,5] and Alban Longchamp[1,2,3]

[1] *Department of Vascular Surgery, Lausanne University Hospital and University of Lausanne, Switzerland*
[2] *Transplant Center, Dept. of Surgery, Massachusetts General Hospital, Harvard Medical School*
[3] *Center for Engineering in Medicine, Dept. of Surgery, Massachusetts General Hospital, Harvard Medical School**
[4] *Department of Radiology and Medical Informatics, University of Geneva, Switzerland*
[5] *Center for Biomedical Imaging (CIBM), Geneva, Switzerland*
[6] *Visceral and Transplant Surgery, Department of Surgery, Geneva University Hospitals and Medical School, Geneva, Switzerland*
[7] *Department of Medicine, Transplantation Centre , Lausanne University Hospital, 1011 Lausanne, Switzerland*
[8] *Faculty of Science and Medicine, Section of Medicine, University of Fribourg, Switzerland*
[9] *Department of Surgery, University of Maryland School of Medicine, Baltimore, MD, USA*

(Accepted for publication in Transplantation Direct on: May, 2023)

In rodents, Hydrogen Sulfide (H_2S) reduces ischemia reperfusion injuries and improves renal graft function after transplantation. However, the benefits of H_2S in larger mammals, or in grafts donated after circulatory death (DCD) is unknown. To test the benefits of H_2S in a relevant pre- clinical model, both DBD and DCD adult porcine kidneys were exposed to 100uM NaHS *i.* during the hypothermic ex-vivo perfusion only *ii.* During warm ischemia only, and *iii.* During both warm ischemia and ex-vivo perfusion. Kidney perfusion was evaluated with dynamic contrast enhanced magnetic resonance imaging (MRI). MRI spectroscopy was further employed to assess energy metabolites including ATP. Renal biopsies were collected at various time points for histopathological analysis. Both DBD and DCD pig kidneys perfused with Belzer MPS® UW + NaHS showed similar renal perfusion and ATP levels than the control kidney after 4hrs of ex-vivo-perfusion. Similarly, no difference was observed when NaHS was administered in the renal artery prior to ischemia. After auto-transplantation no improvement in histological lesions or cortical / medullary kidney perfusion was observed upon H_2S administration. In addition, AMP and ATP levels were identical in both groups. In conclusion, treatment of porcine kidney grafts using NaHS did not result in a significant reduction or ischemia-reperfusion injuries or improvement of kidney metabolism. Future studies will need to define the benefits of H_2S in human and using other molecules.

I. INTRODUCTION

One of the challenges in organ transplant is improving the organ preservation method especially in the grafts with inferior quality. The current clinical standard for kidney preservation is hypothermic storage at 4 °C for a typical storage duration of ≈20 hours, which results in unwanted side-effects that severely compromise graft quality. Hypothermic machine perfusion (HMP) has been developed as an alternative preservation method to static cold storage (SCS) with promising short-term result [1]. In a landmark study including 672 kidney recipients, HMP reduced ischemia reperfusion injuries, clinically manifest as delayed graft function (DGF) [2]. These results were confirmed by later meta-analyses, demonstrating that HMP reduces the incidence of DGF in all types of donors (standard and extended criteria donor, DBD, DCD) [1].

Hydrogen sulfide (H_2S) is a small, endogenously produced gaseous molecules produced by cystathionine gamma-lyase (CGL or CTH) or cystathionine beta-synthase (CBS) [3, 4] . H_2S is an important signaling molecule that was shown to have vasorelaxant and angiogenic properties, and reduced blood pressure [5]. H_2S has anti-inflammatory and antioxidant properties, and can reversibly inhibit the mitochondrial electron transport chain, thus reducing ROS formation during reperfusion [6]. During ischemia, H_2S could further promote glucose uptake and glycolytic ATP production3. Compared with wild-type mice, CGL deficiency was associated with increased damage and mortality after re-

* Authorship: AL, AK, JS, FA, TA, LB, JMC and FL participated in research design. AL, AK, RM, KU, DG, CT, HY, JFM, and FL participated in the writing of the paper. AL, AK, JS, TA, AN, RR, Ar, SM, RM, RR, SD, JMC, and FL participated in the performance of the research. AL, AK, JS, TA, SD, RM, LB, JMC, and FL participated in data analysis.

nal ischemia/reperfusion injury, which could be rescued by exogenous H_2S (NaHS) [7]. Similarly, we demonstrated that administration of NaHS reduced hepatic and renal ischemia/reperfusion injuires [8]. SCS of rat kidney in H_2S-suplemented Belzer MPS® UW solution (150 μM150 NaHS) treatment reduced necrosis, apoptosis and improved early allograft function after transplantation, compared to Belzer MPS® UW preservation solution alone [9]. In porcine kidneys subjected to 2 hours of warm ischemia, administration of H_2S systemically or into the renal artery prior reperfusion improved creatine clearance, reduced apoptosis and tubular injury [10]. In addition, the addition of AP39 (a mitochondrial targeted H_2S donor) during porcine kidneys subnormothermic perfusion (21 °C) for 4 hours with an O_2 carrier (Hemopure) improved urine output and graft oxygenation [11].

During ischemia, ATP depletion causes inhibition of mitochondrial Na+/K+ ion channels, resulting in increased mitochondrial inner membrane permeability and cell death. In prior studies, we used magnetic resonance imaging (MRI), and ^{31}P magnetic resonance spectroscopic imaging (pMRSI) [12] to image the hydrogen nucleus and for detection of high-energy phosphate metabolites such as ATP during kidney transplantation. Our group further demonstrated that ATP levels and kidney Gd perfusion could predict graft function after transplantation [13, 14]. In fact, recovery from (IR) injury is an ATP-dependent process [15], and ATP level was shown to determine kidney graft function following transplantation [13].

Here, using MRI and pMRSI, we examined the effect of exogenous H_2S (NaHS) in a relevant porcine ex-vivo HMP model and auto-transplantation. The effect of H_2S was evaluated in both DBD and DCD model. To increase the translational value of our study, NaHS was given in relevant clinical situations, including ex-vivo perfusion only, or concomitant to heparin administration prior to warm ischemia.

II. MATERIAL AND METHODS

A. Animals and Surgery

The study was approved by the University of Geneva's animal ethics committee (protocol number: GE83/33556). 5-months-old female pigs were obtained from the animal facility of Arare, Switzerland. All pigs were maintained under standard conditions. Water and food were provided ad libitum. Animals were premedicated, anesthetized then kept intubated and ventilated during the procedure [16]. An arterial line was inserted in the internal carotid artery. Monitoring included heart rate, systemic blood pressure, pulse oximetry, and end-tidal CO_2. Following a midline incision, the peritoneal cavity was opened, and the bowels were reclined. First, the aorta, vena cava, and renal vessels were prepared. The pigs received 300 UI/kg heparin intravenous injections. In some groups, 1 mL of 100 μM NaHS was administered into the renal artery 10 min before clamping. The kidneys were either immediately explanted (DBD) or explanted after 60 min of warm ischemia (to mimic circulatory arrest during DCD procurement). Kidneys were then instantly flushed flushed with 1 L of Belzer MPS® UW Machine Perfusion Solution on ice with or without 100 μM NaHS. The renal artery was cannulated, and the kidneys were perfused for 3 hours (see below), as previously described [13, 17] using our MR-compatible machine. At the end of the perfusion, both kidneys were transplanted sequentially onto the vena cava and aorta using a 6-0 running suture. After 2 hours of reperfusion, pigs were sacrificed using 100 mEq of potassium chloride intravenously.

B. Ex-vivo kidney perfusion

Flushed kidney were perfused for 3 hours (before auto-transplantation) with Belzer MPS® UW Machine Perfusion Solution, in presence or absence of 100 μM NaHS (as indicated in the figures and legends) Active oxygenation was achieved using a 0.15 m^2 membrane oxygenator (Biochrom Ltd, Cambridge, UK), maintaining the pO_2 levels at 100 kPa for the whole preservation time. The perfusion module was kept in an isolating box containing ice that kept the kidney at 4 °C. Systolic and diastolic pressure were set at 40 and 20 mmHg, respectively.

C. MRI imaging

MRI and pMRSI (see below) were performed during the ex-vivo perfusion prior (pre-Tx), and after transplantation (post-Tx), as indicated in the figures and legends. Measurements were performed on a multi-nuclear Prisma-fit 3 T whole-body MRI scanner (Siemens Healthineers, Erlangen, Germany). ^{1}H imaging was performed with the body coil using a T2-weighted sequence (turbo SE, TR 6530 ms, TE 110 ms, 2 mm slices) for kidney localisation and structural imaging. Dynamics-contrast enhanced MRI with gadolinium (Gd-MRI) was used to determine the perfusion distribution between the cortex and the medulla, a surrogate of glomerular filtration rate (GFR) as previously described [7, 13, 17]. Data were collected using a dynamic 2D saturation-prepared turbo flash sequence with the scanner body coil. This sequence has an inversion time of 255 ms, a flip angle of 12 °, 1.3 mm x 1.3 mm resolution, and six slices of 4 mm (1 mm gap), TR 500 ms, and a TE of 1.4 ms. The perfusion-descending cortical slope (DS) was determined using the

angle of the linear regression between the maximum signal value and the lowest intensity point after the initial peak [17].

D. ^{31}P Magnetic resonance imaging spectroscopy

pMRSI was performed as described previously [7, 17, 18]. Briefly, a single loop ^{31}P-tuned coil fixed at the bottom of the perfusion tank allows the measurement of the signal. Scanner embedded body coil was used for ^{1}H imaging and for shimming to ensure field homogeneity. pMRSI consisted of 3D spatial encoding, with a field-of view (FOV) $250 \times 250 \times 160\,\mathrm{mm}^3$, matrix size 16x16x8, nominal spatial resolution $15.6 \times 15.6 \times 20\,\mathrm{mm}^3$, TR 1.0 s, flip-angle 35 °, echo delay 6.0 ms, bandwidth 4000 Hz, 2k sampling points. Elliptical encoding with 18 weighted averages resulted in an acquisition time of 45min. The resonance of the inorganic phosphate (Pi, 5.2 ppm), which is uniformly present in the container and the kidney, was used as a reference for quantification of the pMRSI signal. Excitation pulse bandwidth has been adjusted to the ATP frequency range (Pi resonance - 500 Hz). An exponential time filter with 20 Hz frequency width, 0^{th} and 1^{st} order phase corrections were used to process the spectra. The metabolites (ATP, phosphomonoesters/PME, Pi, Phosphocreatine/PCr) were fitted with Gaussian peaks using the syngo.via software (SIEMENS, Erlangen, Germany) and were estimated over the whole kidneys by averaging pMRSI voxels containing graft tissue, resulting in a single spectrum. Quantification results provided by 3D ^{31}P-MRSI at 3 T were analyzed with LCModel for MRS fitting as previously described [19]. The three ATP peaks were quantified separately to prevent methodological bias due to excitation profile imperfection. In each condition, pMRSI allowed the detection of α-, β-, and γ-ATP and phosphomonoesters (PME) composed by phosphocholine (PCh), phosphoethanolamine (PE) and adenosine monophosphate (AMP). ATP and PME concentration (mM) were quantified from the fitting and using the concentration of the inorganic-phosphate buffer (Pi, 25 mM) as reference7. As single ATP concentration was calculated by average of the α-, β-, and γ-ATP values.

E. Histopathological analysis of biopsies

Surgical kidney cortical biopsies were collected at baseline (before clamping), after warm ischemia (Post W.I.), at the end of the ex-vivo perfusion (Pre-Tx), and after 2 hours of reperfusion/transplantation (Post Tx) and were formalin fixed then embedded in paraffin. Fixed kidney biopsies were cut into sections of $3\,\mu$m thickness and stained with silver Jones and Periodic Acid-Schiff (PAS). Slides were scanned using a Axio Scan z1 slide scanner (Zeiss®). Histopathological analysis score was performed based on those described by Goujon et al. [17, 20, 21] using Zen software (Zeiss®), and previously demonstrated to reflect the degree of injury post-transplantation [13, 17]. Whole biopsies were assessed and blinded to group assignment. The following categories were assessed: glomerular integrity, tubular dilatation, brush border integrity, cellular debris in lumina of tubules, interstitial edema, and tubular cell vacuolization. Briefly, to assess glomerulus integrity, more than ten glomeruli were randomly selected from the section and assigned a score of 0 to 3. The same procedure was followed in the remaining categories. After that, the score for each category was converted to a percentage. The final score was converted to a final scale from 0 to 5 according to the percentage of damage: 0-15% (0), 15-30% (1), 30-45% (2), 45-60% (3), 60-75% (4) and >75% (5) using the following formula: $(\mathrm{Category}_{\mathrm{Final\ Score}}/3) \times 100$. The final score for each biopsy ranged from 0 to 30 with 30 the highest score corresponding to more severe damage. Scoring was performed blindly by two independent researchers.

F. Statistical analysis

Data are presented as mean ±SEM, and differences are considered significant when $p < 0.05$. Comparisons between groups were analyzed using ANOVA and post hoc Tukey's tests. Two-group comparisons were performed using Student's t tests (Prism 9.2, GraphPad Softwares, San Diego, CA, USA). Fitting curves of the metabolites concentration over time were computed using R (4.1, `https://cran.r-project.org`).

III. RESULTS

A. H_2S treatment during hypothermic machine perfusion in DBD

We first examined the effect of H_2S administration during ex-vivo perfusion in a DBD model (Figure 1A). Immediately after harvest, kidneys were flushed and perfused during 2hrs with 4 °C Belzer MPS® UW solution with or without (Ctrl) $100\,\mu$M NaHS before auto-transplantation. After 2 hours of cold perfusion, cortical and medullary flow were similar in both the Ctrl and the NaHS treated kidneys (Figure 1B). This was reflected by the absence of significant differences in the perfusion-descending slope (DS, -78 ± 1.32 and $p = 0.53$ cortex, -67 ± 14.8 $p = 0.10$ medulla for Ctrl and NaHS respectively, Figure 1B). Next, mean ATP levels were measured by averaging pMRSI voxels containing graft tissue [13, 17]. Alpha (α), beta (β), and gamma (γ) adenosine triphosphate (ATP), and PME containing AMP, were

similar in both groups (Figure 1C). Similarly, post auto-transplantation, cortical and medullary flow (Figure 1D) as well as ATP levels (Figure 1E) were similar in both Ctrl and NaHS treated kidneys. Finally, we examined the histological damage using a modified Goujon score (described in the methods section), shown to reflect kidney function [13, 17, 20]. Kidney biopsies were analyzed at baseline, at the end of the ex-vivo perfusion (Pre-Tx), and 2 hours after transplantation (post-Tx). Consistent with previous findings, histological damages, were significantly increased after transplantation / reperfusion (Figure 1F). Importantly, treatment with NaHS during ex-vivo perfusion did not reduce histological injuries, such as tubular dilatation, luminal cell debris and brush border lesions before and after transplantation (Figure 1F).

B. H_2S treatment during hypothermic machine perfusion in DCD grafts

Since we did not observe any benefits of H_2S treatment in "healthy" DBD organs, we next investigated the effect of NaHS in kidneys obtained via donation after circulatory death (DCD). After 60min of warm ischemia, kidneys were after harvested, flushed and perfused during 2 hours with 4 °C Belzer MPS® UW solution with 100 μM NaHS or vehicle (Ctrl) before auto-transplantation (Figure 2A). In DCD kidneys, at the end of 4 °C ex-vivo perfusion, cortical and medullary flow were similar in both the Ctrl and the NaHS treated kidneys (Figure 2B). Similarly, at the end of ex-vivo perfusion, ATP levels were unaffected by NaHS administration (Figure 2C). In addition, after transplantation, kidney perfusion (Figure 2D), ATP levels (Figure 2E) and histological injuries (Figure 2F) were not reduced in by administration of NaHS during the ex-vivo perfusion.

C. H_2S treatment prior to ischemia in DCD

The absence of significant differences observed between the Ctrl and H_2S treated DCD kidneys might be related to the timing of NaHS administration. Thus, we next investigated the effect of a single injection of 100 μM NaHS, directly into the renal artery and prior to the interruption of blood flow (warm ischemia, Figure 3A). In these conditions, kidney perfusion and descending slopes were similar in both the Ctrl and NaHS treated kidney (Figure 3B) during ex-vivo perfusion. Similarly, intra-arterial NaHS administration prior to ischemia did not impact ATP production in perfused kidneys (Figure 3C). After transplantation, cortical and medullary perfusion were similar in both groups (Figure 3D). Similarly, we did not observe differences in ATP concentration (Figure 3E) or histological injuries (Figure 3F).

We reasoned that single injection of NaHS prior to warm ischemia might be insufficient due to uncontrolled rapid delivery of H_2S observed with NaHS. Therefore 100 μM NaHS was administered i.a. prior to warm ischemia as well as in the perfusate, during the entire ex-vivo perfusion period (Figure 4A). Under this condition, cortical and medullary perfusion after transplantation were similar in the vehicle and NaHS treated kidney (Figure 4B). Alpha (α), beta (β), and gamma (γ) adenosine triphosphate (ATP), and PME containing AMP, were similar in both groups (Figure 4C). Finally, using the Goujon score, we did not detect significant differences in histological damages in both groups (Figure 4D).

IV. DISCUSSION

In this study we found that 100uM NaHS administration during ex-vivo kidney perfusion in DBD and DCD kidney porcine graft, or prior to warm ischemia in a DCD model, did not improve energy metabolism, kidney perfusion of histological injury. In addition, early post-transplantation outcomes were similar in both vehicle or NaHS-treated kidneys.

Our group and others previously demonstrated that NaHS protected against renal ischemia/reperfusion in injury in several models of warm tissue ischaemia [3, 8, 10], as well as during cold preservation prior to transplantation in rodents [22]. However, we could not recapitulate these findings here in an adult pig model (approx. animal weight 35 kg) during cold storage followed by in-vivo reperfusion/transplantation. Of interest, in mice, exposure to 20-80 ppm gaseous H_2S dose-dependently decreased energy expenditure within a few minutes, as assessed by whole-body O_2 uptake and CO_2 production. This fall in metabolic activity was associated with bradypnea and consecutive hypothermia, with core temperature falling to levels close to ambient values [23]. Subsequent work has thus described and studied H_2S induced suspended animation - a hibernation like state. Various other rodent models confirmed these observations: Inhaling gaseous H_2S [24] and infusing the soluble sulfide salts (NaHS or Na2S) Na_2S also induced a reversible reduction in energy expenditure with a subsequent fall in core temperature [25]. Of utmost importance, the metabolic depressant property of H_2S appears to depend on the animal size. In rats H_2S-induced decrease in O_2 uptake was several-fold lower than in mice [26]. In larger species (swine, sheep), various authors failed to confirm any H_2S-related reduction in metabolic activity at all, regardless of whether inhalation of gaseous H_2S or injection of sulfide salts were studied [27]. Similarly, in sheep, gaseous H_2S administration whole body O_2 uptake, CO_2 production, and cardiac output remained unaffected [28]. Altogether, these data are consis-

tent with our latest findings, and suggest that achieving metabolic suppression (suspended animation-like status), and subsequent protection from warm and cold in larger animals, or humans will be more difficult and require much more time because of the small surface area/mass ratio [29].

NaHS dissociates to Na^+ and HS^-, and then binds partially to H^+ to form undissociated H_2S. While H_2S levels were not measured in this study, NaHS rapidly released H_2S, the effect occurring within seconds [3]. Thus, NaHS rapid and uncontrolled delivery of H_2S might contribute to the results of our study. Alternatively, it was shown that NaHS can affect protein structure [30], and H_2S promotes the sulfhydration of enzymes in energy metabolism and stimulates glycolytic flux [31]. DATS (Diallyl trisulfide) and DADS (Diallyl disulfide) are other H_2S-releasing molecules that protect from ischemia/reperfusion [32] but are also unstable and short lived. Morpholin-4-ium-4-methoxyphenyl phosphinodithioate (GYY4137) might be a more attractive alternative, as is it releases h_2S at a slow and steady rate at physiological pH and temperature [33]. GYY4137 was shown to mitigate renal acute kidney injury following ischemia/reperfusion in mice [34], but remained to be tested during cold preservation and in larger animals. Invitro, the mitochondrial targeted H_2S prodrug AP39 was shown be significantly more potent than GYY413722. Similarly, AP39 improved renal allograft survival following 24 hours SCS and allogeneic renal transplantation [22]. In DCD porcine kidneys, ex vivo subnormothermic perfusion (SNMP, 21 °C) with autologous blood and AP39 improved urine output and reduced apoptosis compared to SCS or SNMP alone for 4 hours [11]. Of note, reperfusion was assessed ex-vivo with autologous blood at 37 °C, and the kidneys were not transplanted [11].

We did not compare the effect of NaHS at higher perfusion temperature (SNMP 21 °C or NMP at 37 °C). Indeed, the rationale was to uses H_2S specific inhibition of the mitochondrial electron transport chain3 during cold preservation and reduce ROS generation during reperfusion, rather than only relying on passive temperature effects to depress metabolism. On the other hand, (S)NMP provides a continuous flow of warmed, oxygenated perfusate containing nutritional substrates, instead aiming to maintain the metabolic activity of the kidney [35].

Here, ATP measurement relied exclusively on pRMSI. However, we previously, demonstrated that nucleotide quantification with pRMSI was accuarate [17]. pRMSI also suffers from a relative low sensitivity compared to liquid chromatography or ^1H imaging at a constant magneticfield [13]. Thus, the acquisition is generally performed with higher voxels size to achieve enough signal to noise ratio while keeping an acceptable scan time. Of importance this lack of sensitivity limitation hinders the measurement of ATP at 4 °C without oxygen. The application of machine learning [36] and neural network can further improve pMRSI sensitivity, spatial resolution and computing time [37]. Overall pMRSI remains a powerful, non-invasive tool to quantify ATP [13].

Our study has several limitations that need to be acknowledged. Kidney function (serum creatinine, urea, and estimated glomerular filtration rate) or urine production after transplantation was not assessed. Kidney function could not be performed due to local regulation, which did not allow survival surgery. Thus, the histological score, previously correlated with the degree of kidney injury [10, 24–26] was used as a surrogate endpoint of kidney function. Similarly, the sample size was small, thus increasing the risk of type II errors. As discussed above, other H_2S-releasing molecules and/or gaseous H_2S should be evaluated in (pre)-clinical model of kidney transplantation. In addition, our study only included health adult pig kidney. Similar studies should be performed using marginal (e.g. old) kidney grafts.

In conclusion, perfusion of porcine DBD and DCD kidneys with NaHS did not improve preservation nor reduced ischemia / reperfusion. Perfusion of organ with alternative H_2S-donors, and/or at different temperatures should be tested to determine if H_2S can improve post-transplant graft function, and patient survival.

ACKNOWLEDGMENTS

This work was supported by the Swiss National Science Foundation to JMC, FL (SNSF 320030_182658), and AL (SNSF PZ00P3_185927) as well as the Mendez National Institute of Transplantation, and the Mercier Foundation to AL. We thank Jean-Pierre Giliberto from the department of surgery, University Hospitals of Geneva for the excellent technical assistance.

V. REFERENCES

[1] Tingle Samuel J, Figueiredo Rodrigo S, Moir John AG, Goodfellow Michael, Talbot David, Wilson Colin H. Machine perfusion preservation versus static cold storage for deceased donor kidney transplantation *Cochrane Database of Systematic Reviews.* 2019.

[2] Moers Cyril, Smits Jacqueline M., Maathuis Mark-Hugo J., et al. Machine Perfusion or Cold Storage in Deceased-Donor Kidney Transplantation *New England Journal of Medicine.* 2009;360:7–19.

[3] Longchamp Alban, Mirabella Teodelinda, Arduini Alessandro, et al. Amino Acid Restriction Triggers Angiogenesis via GCN2/ATF4 Regulation of VEGF and H2S Production *Cell.* 2018;173:117–129.e14.

[4] Hine Christopher, Kim Hyo-Jeong, Zhu Yan, et al. Hypothalamic-Pituitary Axis Regulates Hydrogen Sulfide Production *Cell Metabolism.* 2017;25:1320–1333.e5.

[5] Yang Guangdong, Wu Lingyun, Jiang Bo, et al. H_2S as a Physiologic Vasorelaxant: Hypertension in Mice with Deletion of Cystathionine γ-Lyase *Science.* 2008;322:587–590.

[6] Chouchani Edward T., Pell Victoria R., James Andrew M., et al. A Unifying Mechanism for Mitochondrial Superoxide Production during Ischemia-Reperfusion Injury *Cell Metabolism.* 2016;23:254–263.

[7] Bos Eelke M., Wang Rui, Snijder Pauline M., et al. Cystathionine γ-Lyase Protects against Renal Ischemia/Reperfusion by Modulating Oxidative Stress *Journal of the American Society of Nephrology.* 2013;24:759–770.

[8] Hine Christopher, Harputlugil Eylul, Zhang Yue, et al. Endogenous Hydrogen Sulfide Production Is Essential for Dietary Restriction Benefits *Cell.* 2015;160:132–144.

[9] Zhang Max Y., Dugbartey George J., Juriasingani Smriti, et al. Sodium thiosulfate-supplemented UW solution protects renal grafts against prolonged cold ischemia-reperfusion injury in a murine model of syngeneic kidney transplantation *Biomedicine & Pharmacotherapy.* 2022;145:112435.

[10] Sekijima Mitsuhiro, Sahara Hisashi, Miki Katsuyuki, et al. Hydrogen sulfide prevents renal ischemia-reperfusion injury in CLAWN miniature swine *Journal of Surgical Research.* 2017;219:165–172.

[11] Juriasingani Smriti, Jackson Ashley, Zhang Max Yulin, et al. Evaluating the Effects of Subnormothermic Perfusion with AP39 in a Novel Blood-Free Model of Ex Vivo Kidney Preservation and Reperfusion *International Journal of Molecular Sciences.* 2021;22:7180.

[12] Lazeyras Francois, Buhler Leo, Vallee Jean-Paul, et al. Detection of ATP by in line 31P magnetic resonance spectroscopy during oxygenated hypothermic pulsatile perfusion of pigs' kidneys *Magnetic Resonance Materials in Physics, Biology and Medicine.* 2012;25:391–399.

[13] Longchamp Alban, Klauser Antoine, Songeon Julien, et al. Ex Vivo Analysis of Kidney Graft Viability Using 31P Magnetic Resonance Imaging Spectroscopy *Transplantation.* 2020;104:1825–1831.

[14] Berendsen T.A., Izamis M.L., Xu H., et al. Hepatocyte Viability and Adenosine Triphosphate Content Decrease Linearly Over Time During Conventional Cold Storage of Rat Liver Grafts *Transplantation Proceedings.* 2011;43:1484–1488.

[15] Szeto Hazel H., Liu Shaoyi, Soong Yi, et al. Mitochondria-Targeted Peptide Accelerates ATP Recovery and Reduces Ischemic Kidney Injury *Journal of the American Society of Nephrology.* 2011;22:1041–1052.

[16] Longchamp Alban, Meier Raphael P. H., Colucci Nicola, et al. Impact of an intra-abdominal cooling device during open kidney transplantation in pigs *Swiss Medical Weekly.* 2019.

[17] Agius Thomas, Songeon Julien, Klauser Antoine, et al. Subnormothermic Ex Vivo Porcine Kidney Perfusion Improves Energy Metabolism: Analysis Using 31P Magnetic Resonance Spectroscopic Imaging *Transplantation Direct.* 2022;8:e1354.

[18] Songeon Julien, Courvoisier Sébastien, Xin Lijing, et al. In vivo magnetic resonance 31P-Spectral Analysis With Neural Networks: 31P-SPAWNN *Magnetic Resonance in Medicine.* 2022;89:40–53.

[19] Provencher Stephen W.. Automatic quantitation of localized in vivo 1H spectra with LCModel *NMR in Biomedicine.* 2001;14:260–264.

[20] Meier R.P.H., Piller V., Hagen M.E., et al. Intra-Abdominal Cooling System Limits Ischemia/Reperfusion Injury During Robot-Assisted Renal Transplantation *American Journal of Transplantation.* 2018;18:53–62.

[21] Goujon J.M, Hauet T, Menet E, Levillain P, Babin Ph, Carretier M. Histological Evaluation of Proximal Tubule Cell Injury in Isolated Perfused Pig Kidneys Exposed to Cold Ischemia *Journal of Surgical Research.* 1999;82:228–233.

[22] Lobb Ian, Davison Michael, Carter David, et al. Hydrogen Sulfide Treatment Mitigates Renal Allograft Ischemia-Reperfusion Injury during Cold Storage and Improves Early Transplant Kidney Function and Survival Following Allogeneic Renal Transplantation *Journal of Urology.* 2015;194:1806–1815.

[23] Blackstone Eric, Morrison Mike, Roth Mark B.. H_2S Induces a Suspended Animation-Like State in Mice *Science.* 2005;308:518–518.

[24] Blackstone Eric, Roth Mark B.. Suspended animation-like state protects mice from lethal hypoxia *Shock.* 2007;27:370–372.

[25] Morrison Michael L., Blackwood Jennifer E., Lockett Summer L., Iwata Akiko, Winn Robert K., Roth Mark B.. Surviving Blood Loss Using Hydrogen Sulfide *Journal of Trauma: Injury, Infection & Critical Care.* 2008;65:183–188.

[26] Haouzi Philippe, Bell Harold J., Notet Veronique, Bihain Bernard. Comparison of the metabolic and ventilatory response to hypoxia and H2S in unsedated mice and rats *Respiratory Physiology & Neurobiology.* 2009;167:316–322.

[27] Drabek Tomas, Kochanek Patrick M., Stezoski Jason, et al. Intravenous Hydrogen Sulfide Does Not Induce Hypothermia or Improve Survival from Hemorrhagic Shock in Pigs *Shock.* 2011;35:67–73.

[28] Derwall Matthias, Francis Roland CE, Kida Kotaro, et al. Administration of hydrogen sulfide via extracorporeal membrane lung ventilation in sheep with partial cardiopulmonary bypass perfusion: a proof of concept study on metabolic and vasomotor effects *Critical Care.* 2011;15:R51.

[29] Asfar Pierre, Calzia Enrico, Radermacher Peter. Is pharmacological, H2S-induced 'suspended animation' feasible in the ICU? *Critical Care.* 2014;18:215.

[30] Mustafa Asif K., Gadalla Moataz M., Sen Nilkantha, et al. H_2S Signals Through Protein S-Sulfhydration *Science Signaling.* 2009;2.

[31] Gao Xing-Huang, Krokowski Dawid, Guan Bo-Jhih, et al. Quantitative H2S-mediated protein sulfhydration reveals metabolic reprogramming during the integrated stress response *eLife.* 2015;4.

[32] Yu Liming, Di Wencheng, Dong Xue, et al. Diallyl trisulfide exerts cardioprotection against myocardial ischemia-reperfusion injury in diabetic state, role of AMPK-mediated AKT/GSK-3β/HIF-1α activation *Oncotarget.*

2017;8:74791–74805.

[33] Li Ling, Whiteman Matthew, Guan Yan Yi, et al. Characterization of a Novel, Water-Soluble Hydrogen Sulfide/Releasing Molecule (GYY4137) *Circulation.* 2008;117:2351–2360.

[34] Zhao Hongmei, Qiu Yun, Wu Yichen, Sun Hong, Gao Sumin. Protective Effects of GYY4137 on Renal Ischaemia/Reperfusion Injury through Nrf2-Mediated Antioxidant Defence *Kidney and Blood Pressure Research.* 2021;46:257–265.

[35] Urbanellis Peter, McEvoy Caitriona M., Škrtić Marko, et al. Transcriptome Analysis of Kidney Grafts Subjected to Normothermic Ex Vivo Perfusion Demonstrates an Enrichment of Mitochondrial Metabolism Genes *Transplantation Direct.* 2021;7:e719.

[36] Lam Fan, Li Yudu, Guo Rong, Clifford Bryan, Liang Zhi-Pei. Ultrafast magnetic resonance spectroscopic imaging using SPICE with learned subspaces *Magnetic Resonance in Medicine.* 2019;83:377–390.

[37] Lee Hyeong Hun, Kim Hyeonjin. Deep learning-based target metabolite isolation and big data-driven measurement uncertainty estimation in proton magnetic resonance spectroscopy of the brain *Magnetic Resonance in Medicine.* 2020;84:1689-1706.

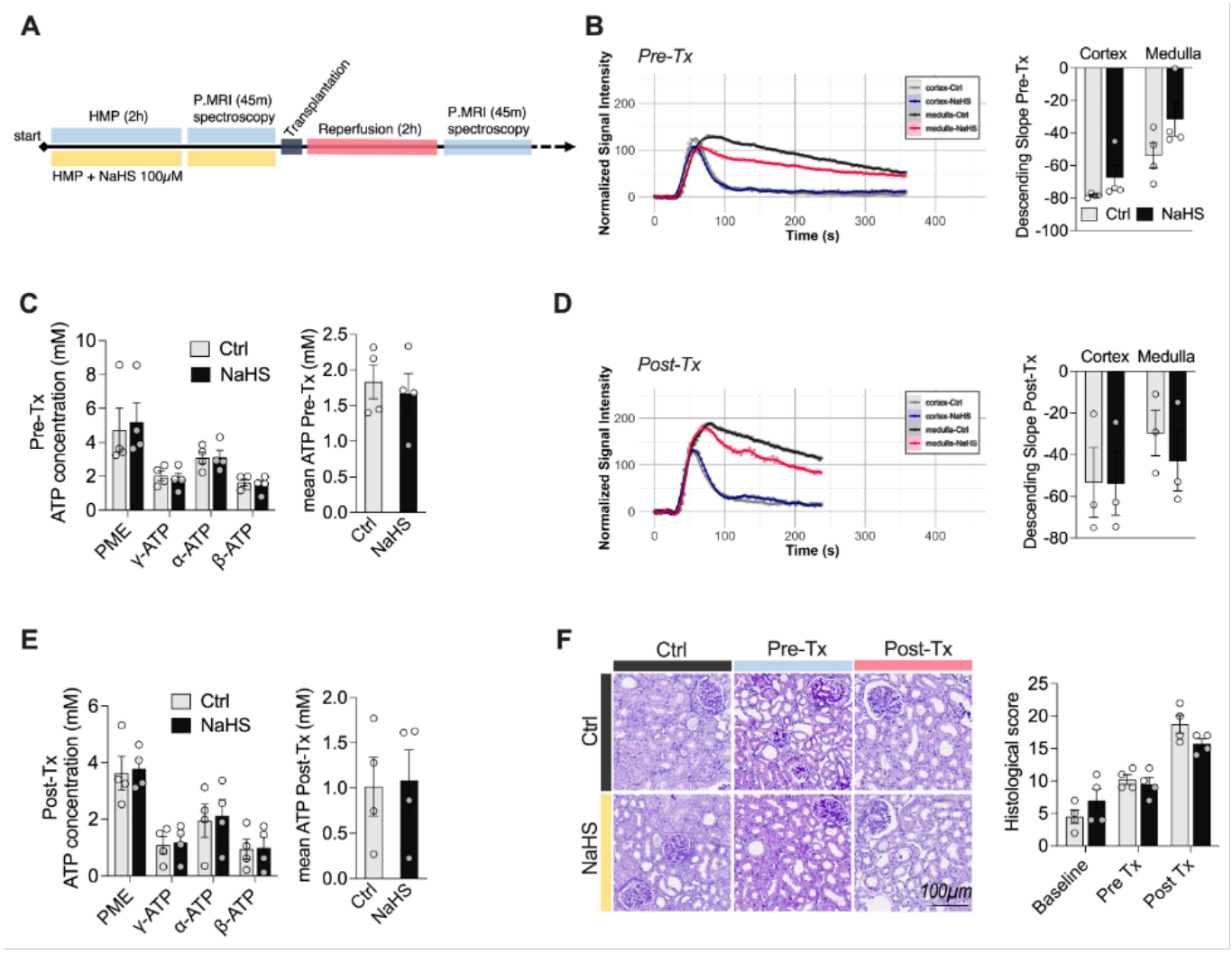

FIG. 1. Effects of Hydrogen Sulfide Supplementation during Hypothermic Machine Perfusion in a DBD model. (A) Experimental design. Pig kidneys were perfused at 4 °C with O_2 (HMP) with Belzer MPS® UW with or without 100 μM NaHS for 2hrs, during ^{31}P MRSI and prior to auto-transplantation (reperfusion) and post-transplant ^{31}P MRSI during ^{31}P MRSI and prior to auto-transplantation (reperfusion) and post-transplant ^{31}P MRSI (B) Pre-transplant cortical and medullar Gd normalized signal intensity over time (right) and quantification (descending slopes, left) in the indicated groups. (C) Pre-transplant PME, α, β, and γ ATP levels (left) and mean ATP (right) in Ctrl and NaHS treated kidney. (D) Post-transplant cortical and medullar Gd normalized signal intensity over time (right) and quantification (descending slopes, left) in the indicated groups. (E) Post-transplant PME, α, β, and γ ATP levels (left) and mean ATP (right) in Ctrl and NaHS treated kidney. (F) Representative transverse PAS-stained sections of kidneys at the indicated time in Ctrl and NaHS groups (left) and quantification of histological damages (score, right). Data expressed as mean ± SEM, n=4.

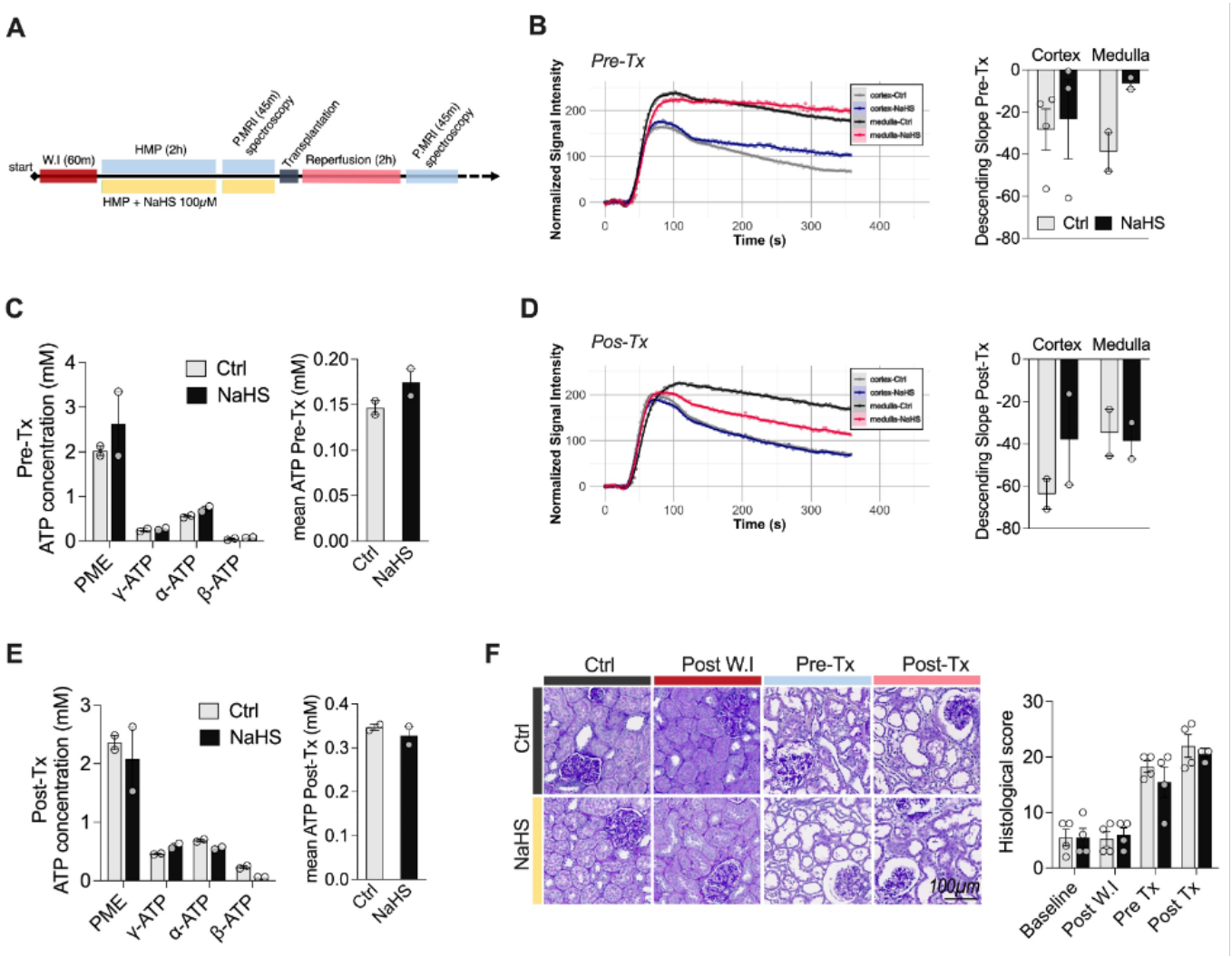

FIG. 2. Effects of Hydrogen Sulfide Supplementation during Hypothermic Machine Perfusion in a DCD model. (A) Experimental design. Pig kidneys underwent 60min of warm ischemia (WI) prior to 4 °C oxygenated (HMP) with Belzer MPS® UW with or without 100 μM NaHS for 2hrs during ^{31}P MRSI and prior to auto-transplantation (reperfusion) and post-transplant ^{31}P MRSI assessment. (B) Pre-transplant cortical and medullar Gd normalized signal intensity over time (right) and quantification (descending slopes, left) in the indicated groups. (C) Pre-transplant PME, α, β, and γ ATP levels (left) and mean ATP (right) in Ctrl and NaHS treated kidney. (D) Post-transplant cortical and medullar Gd normalized signal intensity over time (right) and quantification (descending slopes, left) in the indicated groups. (E) Post-transplant PME, α, β, and γ ATP levels (left) and mean ATP (right) in Ctrl and NaHS treated kidney. (F) Representative transverse PAS-stained sections of kidneys at the indicated time in Ctrl and NaHS groups (left) and quantification of histological damages (score, right) . Data expressed as mean ±SEM, n=3.

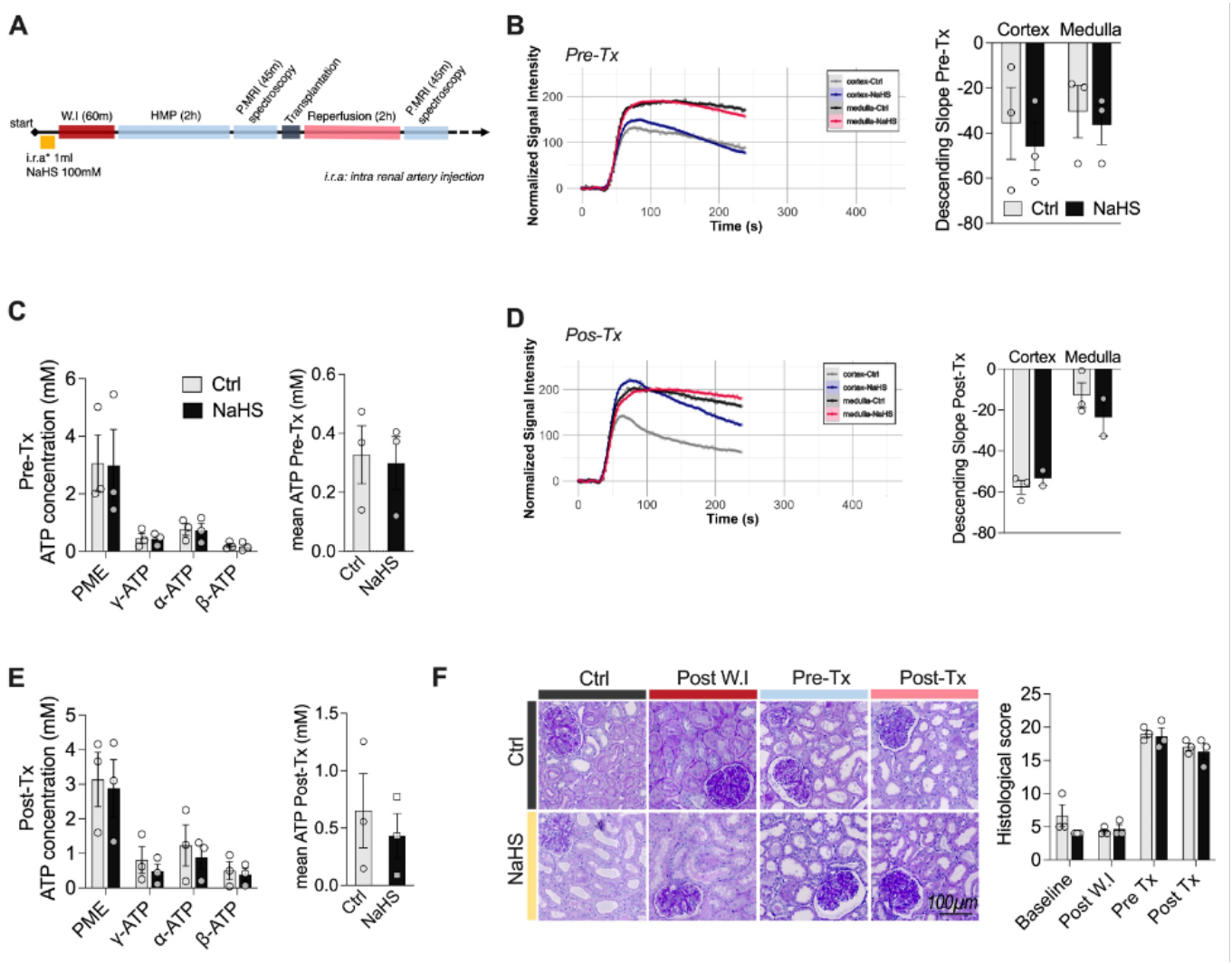

FIG. 3. Administration of Hydrogen Sulfide prior to Warm Ischemia in a DCD model. (A) Experimental design: Administration of 100 μM NaHS into the renal artery prior to 60min warm ischemia. Immediately after procurement, kideny were perfused at 4 °C with O_2, in Belzer MPS® UW for 2hrs and underwent ^{31}P MRSI, prior to auto-transplantation (reperfusion) and post-transplant ^{31}P MRSI assessment. (B) Pre-transplant cortical and medullar Gd normalized signal intensity over time (right) and quantification (descending slopes, left) in the indicated groups. (C) Pre-transplant PME, α, β, and γ ATP levels (left) and mean ATP (right) in Ctrl and NaHS treated kidney. (D) Post-transplant cortical and medullar Gd normalized signal intensity over time (right) and quantification (descending slopes, left) in the indicated groups. (E) Post-transplant PME, α, β, and γ ATP levels (left) and mean ATP (right) in Ctrl and NaHS treated kidney. (F) Representative transverse PAS-stained sections of kidneys at the indicated time in Ctrl and NaHS groups (left) and quantification of histological damages (score, right). Data expressed as mean ±SEM, n=3.

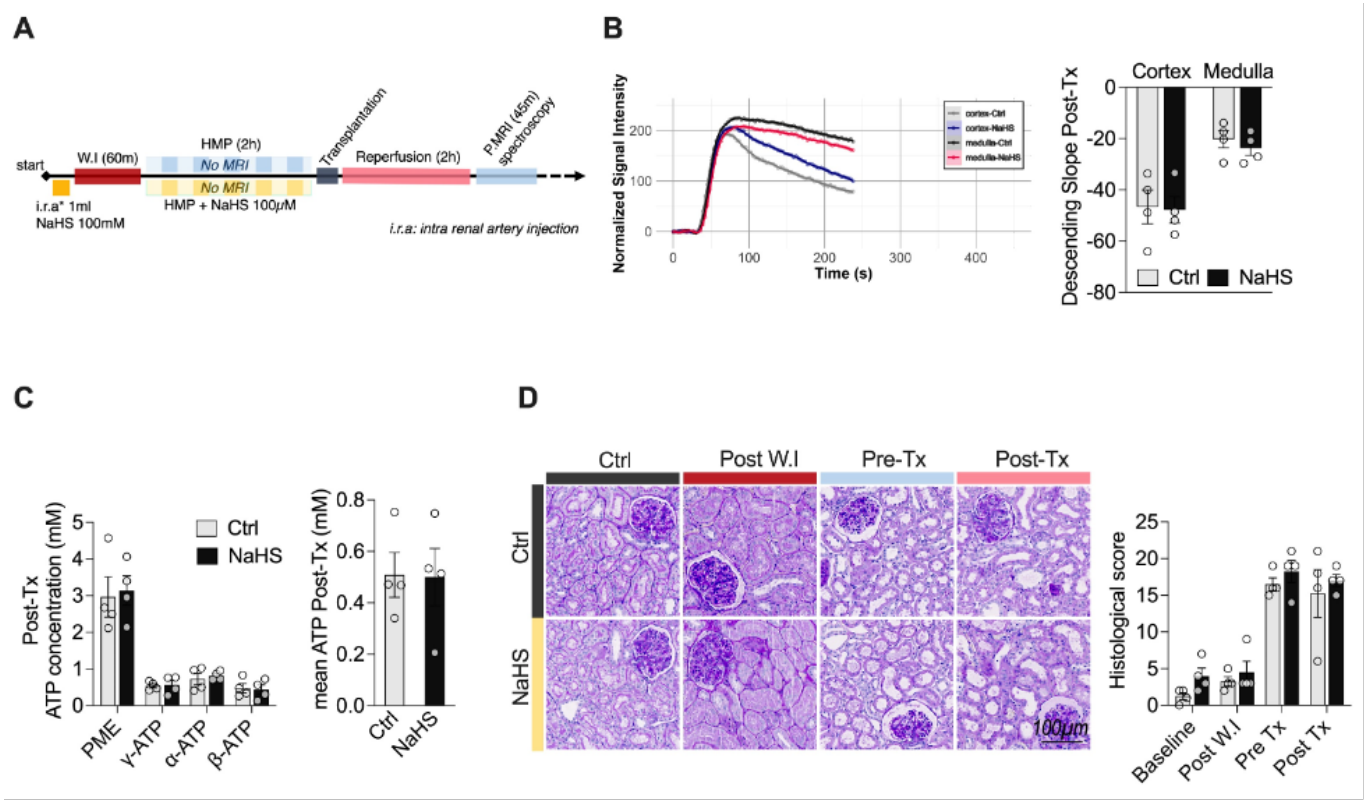

FIG. 4. Administration of Hydrogen Sulfide prior to Warm Ischemia and during HMP in a DCD model. (A) Experimental design. Administration of 100 μM NaHS into the renal artery prior to 60min warm ischemia. Immediately after procurement, kidney were perfused at 4 °C without O_2, in Belzer MPS® UW with or without NaHS as indicated for 2hrs, prior to auto-transplantation (reperfusion) and post-transplant ^{31}P MRSI assessment. (B) Post-transplant cortical and medullar Gd normalized signal intensity over time (right) and quantification (descending slopes, left) in the indicated groups. (C) Post-transplant PME, α, β, and γ ATP levels (left) and mean ATP (right) in Ctrl and NaHS treated kidney. (FD Representative transverse PAS-stained sections of kidneys at the indicated time in Ctrl and NaHS groups (left) and quantification of histological damages (score, right). Data expressed as mean ±SEM, n=4.

Part V

AT LAST, A CONCLUSION

13

CONCLUSION

"It's not for any one generation to see the completed picture. That's the point. The picture is never completed. There is always so much more that remains to be discovered."

- Ann Druyan, *Cosmos*

Contents

13.1 SUMMARY

Over the course of this thesis work, several tools were developed to enhance phosphorus spectroscopic imaging, and multiple investigations were conducted to assess organ viability and preservation techniques. In the following section, we recapitulate each topic with a summary of the main findings and primary contribution and possible future work to improve the findings or to continue the research.

13.2 DISCUSSION AND OUTLOOK

13.2.1 ^{31}*P-MRSI analysis with Artificial Intelligence*

In Chapter 6, we described the development of convolutional neural network-based deep learning methods to analyze, quantify, and reconstruct measured ^{31}P-MRSI spectra. While prior published works have integrated machine learning and deep learning for MRS analysis, our work is distinguished by several critical differences. Our approach employs a more comprehensive physical model, enabling the use of a larger number of training parameters to create a more diverse range of spectra for network training. Additionally, our approach shifts the traditional paradigm by aiming to evaluate the spectral parameters and metabolite quantification, which can be subsequently used to reconstruct the spectrum, rather than relying on fitting algorithms where residual minimization is the primary focus. Our methods have demonstrated favorable performance in comparison to fitting algorithms, even surpassing them in low SNR scenarios. The developed technique met the project's goal of achieving rapid computational analysis for potential use in clinical settings.

The methods developed in this study is primarily focused on analyzing the spectrum of the phosphorus nucleus, but the approach could be extended to analyze spectra from other nuclei as well. To enable this, the model would require modifications to account for variations in the chemical shift and J-coupling of the resonances, allowing for the creation of a dataset specific to the targeted nucleus. Moreover, the current model is based on the free induction decay (FID) signal, however, it can be adapted to other sequences as well.

Future work on the method should focus on implementing a confidence interval measurement, in a similar way than fitting algorithms like LCModel that provide an estimation of quantification along with confidence intervals. Additionally, an analysis on the impact of training

parameter ranges on SPAWNN's stability and robustness needs to be established. The model may benefit from an improved physical model that takes into account additional distortions, such as eddy current effects. The 31P-SPAWNN method is openly available on gitlab: https://gitlab.unige.ch/Julien.Songeon/31P-SPAWNN.

13.2.2 ^{31}P-MRSI Acceleration and Reconstruction with Compressed Sensing and Low Rank

In Chapter 8, we implemented of Compressed Sensing and Low Rank (CS-LR) acceleration and reconstruction techniques for ^{31}P-MRSI. The method involved the use of total generalized variation regularization and was adapted from previously published work on ^{1}H-MRSI. One unique aspect of our approach was the incorporation of different random undersampling patterns for each k-space average. This was of particular interest as the phosphorus nucleus is inherently less sensitive, requiring multiple averages for adequate SNR. By utilizing distinct undersampling patterns, we were able to achieve a greater k-space coverage while maintaining the desired acceleration factor. The findings demonstrated that the proposed method effectively enhanced the SNR while retaining high-quality spectral and spatial information, even under acceleration by a factor of three. The linewidth of the metabolite peaks remained unchanged at all acceleration factors, and anatomical details could still be extracted from the attenuated signals. This improvement also met the project's goal of achieving fast acquisition with reliable reconstruction to reduce the scan time of the transplantation viability assessment.

In order to make the CS-LR sequence available on the MRI for ^{31}P-MRSI, future work could include its development. Although a sequence for ^{31}P-MRSI has already been created, the incorporation of random undersampling patterns has not been developed yet. Currently, the study was performed on retrospective data, and analyzing accelerated in-vivo data to confirm the findings could be of interest.

13.2.3 *Assessment of Kidney viability with ^{31}P-MRSI*

In Chapter 10, we describe the experimental setup utilized for evaluating kidney viability. Our research team had fully developed a hypothermic pulsatile perfusion system (HPP), which is compatible with MRI technology and capable of perfusing kidneys. The HPP was also equipped with ^{31}P spectroscopic acquisition capability. This machine was utilized to evaluate porcine kidneys in an auto-transplantation setup model. The kidneys were subjected to warm ischemia for 30 or 60 minutes, and the results were compared to a control group without ischemia. Kidney function was assessed using measurements of ^{31}P-MRSI, gadolinium elimination, and histopathological scoring. The study successfully detected ischemia-reperfusion damage, which was observed with the three measurement methods. Notably, we established a correlation between the descending slope of gadolinium perfusion elimination and histological damage scores. This study achieved the project's objectives of assessing kidney viability with ^{31}P-MRSI and assessing mitochondrial functions ex-vivo.

The study encountered some limitations, and missed some of its objective. First and foremost, it was not possible to correlate the measurement of ATP from the ex-vivo mitochondrial functions with kidney function in-vivo or after transplantation, as legal authorization did not permit the survival of the animals. Long-term survival of the animals after transplant would be necessary for assessing the success or failure of the transplantation. Second, while the ischemia-reperfusion injury was observed and correlated with our measurements, the methodology does not cover the broad group of marginal donors (e.g., old donors, prolonged preservation, etc.). Therefore, an assessment of different organs from this group should be investigated. Thirdly, we concluded that the 45-minute scan time of ^{31}P-MRSI was too long to be a viable clinical

method. However, this limitation could be addressed with the improved ^{31}P-MRSI accelerated sequence. Fourthly, we intended to assess the two nicotinamide adenine dinucleotide metabolites (NAD+ and NADH) to measure the alteration of the redox state. This was not possible due to the low signal-to-noise ratio of the spectra at 3 T and the overlap of the resonances, which did not allow for the disentanglement and quantification of each metabolite.

13.2.4 *Sub-normothermic Preservation of Kidney*

In Chapter 11, we investigated the preservation of kidney grafts at a sub-normothermic temperature of 22 °C and compared the results with the current hypothermic preservation process at 4 °C. Our findings revealed that kidney grafts perfused at 22 °C exhibited increased ATP production and reduced ischemia-reperfusion injury (IRI) during transplantation, as compared to hypothermic preservation. The significant differences observed between the two groups were strongly correlated with histological scores and measurements of ATP and AMP pretransplanted. We concluded that perfusing kidney grafts at 22 °C may enhance the utilization of kidney allografts. Although the sub-normothermic project was not initially within the scope of the thesis, this study successfully met the objective of assessing organ preservation and viability using ^{31}P-MRSI.

This study also faced some limitations. Firstly, the research design did not allow for the assessment of metabolism with ^{31}P-MRSI or the performance of Gadolinium perfusion after transplantation. Additionally, as with the previous study, legal authorization did not permit the survival of the animals, limiting the post-transplantation assessment. Furthermore, this study did not cover the broad group of marginal donors, which should be investigated in future works.

13.2.5 *Preservationt of Kidney with Sodium Hydrosulfide (H_2S)*

In Chapter 12, we investigated the efficacy of hydrogen sulfide (H_2S) in reducing oxygen and ATP consumption in order to mitigate the effects of ischemia-reperfusion injury and improve renal function. Our results showed that ATP levels and kidney perfusion were inversely correlated with the severity of kidney histological injury. However, the administration of H_2S via NaHS did not result in significant reductions in IRI or improvements in kidney metabolism. Thus, we concluded that H_2S treatment does not significantly improve renal graft function in porcine kidneys. This study failed to demonstrate the potential benefits of using H_2S to preserve organs from ischemic injury for cold storage as part of our project objectives.

In addition to the aforementioned limitation, the outcome of this study was constrained by the uncontrolled delivery of H_2S via NaHS. To further investigate the effects of H_2S, future studies could be conducted under sub-normothermic preservation conditions, as higher temperatures would result in continuous oxygenation of the organ and could potentially enhance the effects of H_2S.

13.3 GENERAL CONCLUSION

All research projects were completed within the allocated timeframe. Although the original research plan aimed to translate H_2S preservation to clinical practice, the mitigated results led to a shift towards investigating sub-normothermic preservation. As with any research endeavor, we encountered several challenges. Few pigs died before completing the experiment, resulting in loss of data. In some cases, the kidneys were only partially or not perfused in the HPP machine. Additionally, the development of autosomal dominant polycystic kidney disease (ADPKD) in a few animals also resulted in loss of data. Issues with MRI were also faced, where some experi-

ments had to be prematurely terminated due to software issues, which impacted the amount of data collected.

On the other hand, we must acknowledge the exceptional facilities and support at our disposal for this research. The availability of a world-unique HPP system that is compatible with MRI, coupled with access to a research 3 T MRI with multi-nuclei spectroscopy capability, are significant advantages. These resources enabled us to perform the complex and necessary research outlined in this thesis. It is fair to say that this research would not have been possible without them.

In conclusion, we have developed a methodology that substantially enhances the sensitivity of our technique through the implementation of acceleration and reconstruction methods based on Low Rank and Compressed Sensing. We have also improved the spectral evaluation through the use of neural networks, enabling more efficient analysis of low signal-to-noise ratio and overlapping resonances. These advancements provide novel avenues for in vivo biochemistry studies, including the imaging of oxidative stress at ultra-high magnetic field strengths (7 T).

BIBLIOGRAPHY

[1] P. C. Lauterbur. "Image Formation by Induced Local Interactions: Examples Employing Nuclear Magnetic Resonance." In: *Nature* 242.5394 (Mar. 1973), pp. 190–191. DOI: 10.1038/242190a0.

[2] A N Garroway, P K Grannell, and P Mansfield. "Image formation in NMR by a selective irradiative process." In: *Journal of Physics C: Solid State Physics* 7.24 (Dec. 1974), pp. L457–L462. DOI: 10.1088/0022-3719/7/24/006.

[3] G. E. Uhlenbeck and S. Goudsmit. "Spinning Electrons and the Structure of Spectra." In: *Nature* 117.2938 (Feb. 1926), pp. 264–265. DOI: 10.1038/117264a0.

[4] Paul Dirac. *The principles of quantum mechanics*. en. 4th ed. International Series of Monographs on Physics. Oxford, England: Clarendon Press, Jan. 1981.

[5] E. M. Purcell, H. C. Torrey, and R. V. Pound. "Resonance Absorption by Nuclear Magnetic Moments in a Solid." In: *Phys. Rev.* 69 (1-2 1946), pp. 37–38. DOI: 10.1103/PhysRev.69.37.

[6] F. Bloch, W. W. Hansen, and Martin Packard. "Nuclear Induction." In: *Phys. Rev.* 69 (3-4 1946), pp. 127–127. DOI: 10.1103/PhysRev.69.127.

[7] F. Bloch, W. W. Hansen, and M. Packard. "The Nuclear Induction Experiment." In: *Phys. Rev.* 70 (7-8 1946), pp. 474–485. DOI: 10.1103/PhysRev.70.474.

[8] F. Bloch. "Nuclear Induction." In: *Phys. Rev.* 70 (7-8 1946), pp. 460–474. DOI: 10.1103/PhysRev.70.460.

[9] R. R. Ernst and W. A. Anderson. "Application of Fourier Transform Spectroscopy to Magnetic Resonance." In: *Review of Scientific Instruments* 37.1 (Jan. 1966), pp. 93–102. DOI: 10.1063/1.1719961.

[10] David J Griffiths. *Introduction to Quantum Mechanics*. 2nd ed. Upper Saddle River, NJ: Pearson, Mar. 2004.

[11] Claude Cohen-Tannoudji, Bernard Diu, and Frank Laloe. *Quantum Mechanics, Volume 1*. en. Quantum Mechanics. Nashville, TN: John Wiley & Sons, June 1977.

[12] W. G. Proctor and F. C. Yu. "The Dependence of a Nuclear Magnetic Resonance Frequency upon Chemical Compound." In: *Phys. Rev.* 77 (5 1950), pp. 717–717. DOI: 10.1103/PhysRev.77.717.

[13] P A Bottomley et al. "In vivo solvent-suppressed localized hydrogen nuclear magnetic resonance spectroscopy: a window to metabolism?" In: *Proceedings of the National Academy of Sciences* 82.7 (Apr. 1985), pp. 2148–2152. DOI: 10.1073/pnas.82.7.2148.

[14] G Androutsos, A Diamantis, and L Vladimiros. "The first leg transplant for the treatment of a cancer by Saints Cosmas and Damian." In: *J. BUON* 13.2 (Apr. 2008), pp. 297–304.

[15] Siddharth Pramod Dubhashi, B. M. Subnis, and Rajat Dinesh Sindwani. "Theodor E. Kocher." In: *Indian Journal of Surgery* 75.5 (Mar. 2012), pp. 383–384. DOI: 10.1007/s12262-012-0469-9.

[16] D.K.C. Cooper. "The First Transplant Surgeon: The Flawed Genius of Nobel Prize Winner, Alexis Carrel, edited by David Hamilton. World Scientific, London, 2017. 587 pages." In: *American Journal of Transplantation* 17.6 (June 2017), p. 1687. DOI: 10.1111/ajt.14264.

[17] Thomas Schlich. "The origins of organ transplantation." In: *The Lancet* 378.9800 (Oct. 2011), pp. 1372–1373. DOI: 10.1016/s0140-6736(11)61601-2.

[18] Judy Ozkan. "Peter Brian Medawar (1915-87) 1960 Nobel Prize for Medicine or Physiology." In: *European Heart Journal* 41.10 (Mar. 2020), pp. 1067–1068. DOI: 10.1093/eurheartj/ehaa090.

[19] Peter Morris. "Joseph E. Murray (1919-2012)." In: *Nature* 493.7431 (Jan. 2013), pp. 164–164. DOI: 10.1038/493164a.

[20] Gabriel M Danovitch, ed. *Handbook of kidney transplantation*. en. 5th ed. Lippincott Williams and Wilkins Handbook Series. Philadelphia, PA: Lippincott Williams and Wilkins, Oct. 2009.

[21] Luciana Assis-Borba et al. "Expanding the use of expanded criteria donors in kidney transplantation." In: *International Urology and Nephrology* 46.8 (Mar. 2014), pp. 1663–1671. DOI: 10.1007/s11255-014-0695-0.

[22] Swisstransplant. "Annual report 2022." In: (Jan. 2023).

[23] Robert S. Balaban. "Experimental Preparations and Models for MRS." In: *Investigative Radiology* 24.12 (Dec. 1989), pp. 948–950. DOI: 10.1097/00004424-198912000-00004.

[24] Miriam B. Niekisch et al. "Improved pretransplant assessment of renal quality by means of phosphorus-31 magnetic resonance spectroscopy using chemical shift imaging." In: *Transplantation* 77.7 (Apr. 2004), pp. 1041–1045. DOI: 10.1097/01.tp.0000120537.69074.5d.

[25] S D Taylor-Robinson et al. "In vivo and in vitro hepatic phosphorus-31 magnetic resonance spectroscopy and electron microscopy in chronic ductopenic rejection of human liver allografts." In: *Gut* 42.5 (May 1998), pp. 735–743. DOI: 10.1136/gut.42.5.735.

[26] Walther Gerlach and Otto Stern. "Der experimentelle Nachweis der Richtungsquantelung im Magnetfeld." In: *Zeitschrift für Physik* 9.1 (Dec. 1922), pp. 349–352. DOI: 10.1007/bf01326983.

[27] W. Pauli. "Über den Zusammenhang des Abschlusses der Elektronengruppen im Atom mit der Komplexstruktur der Spektren." In: *Zeitschrift für Physik* 31.1 (Feb. 1925), pp. 765–783. DOI: 10.1007/bf02980631.

[28] W. Pauli. "The Connection Between Spin and Statistics." In: *Physical Review* 58.8 (Oct. 1940), pp. 716–722. DOI: 10.1103/physrev.58.716.

[29] Steven Weinberg. *The Quantum Theory of Fields, Volume 1: Foundations*. Cambridge University Press, 2005. ISBN: 0521670535.

[30] Michele Maggiore. *A modern introduction to quantum field theory*. Oxford master series in statistical, computational, and theoretical physics. Oxford: Oxford Univ., 2005.

[31] Stephen G Gasiorowicz. *Quantum physics*. New York, NY: Wiley, 1974.

[32] Robert W. Brown et al., eds. *Magnetic Resonance Imaging*. John Wiley & Sons Ltd, Apr. 2014. DOI: 10.1002/9781118633953.

[33] Jeffrey Adam Kasten. "Superresolution Reconstruction for Magnetic Resonance Spectroscopic Imaging Exploiting Low-Rank Spatio-Spectral Structure." In: (2015). DOI: 10.5075/EPFL-THESIS-6546.

[34] Bernard Diu, Claudine Guthmann, and Lederer Danielle. *Physique statistique*. Collection enseignement des sciences. Hermann, 2001.

[35] Abhishek Gupta et al. "Dipolar relaxation revisited: A complete derivation for the two spin case." In: *Concepts in Magnetic Resonance Part A* 44.2 (Mar. 2015), pp. 74–113. DOI: 10.1002/cmr.a.21334.

[36] R.R. Ernst, G. Bodenhausen, and A. Wokaun. *Principles of nuclear magnetic resonance in one and two dimensions, p. 158-165*. Vol. 7. Oxford University Press 2. Wiley, June 1988, pp. 158–165.

[37] Assaf Tal. *Lecture notes in NMR Primer*. Weizmann Institute of Science, 2015.

[38] E. L. Hahn. "Spin Echoes." In: *Physical Review* 80.4 (Nov. 1950), pp. 580–594. DOI: 10.1103/physrev.80.580.

[39] E. M. Purcell, R. V. Pound, and N. Bloembergen. "Nuclear Magnetic Resonance Absorption in Hydrogen Gas." In: *Physical Review* 70.11-12 (Dec. 1946), pp. 986–987. DOI: 10.1103/physrev.70.986.

[40] Graham A. Webb, ed. *Chapter 3 - Methods and Applications of Phosphorus NMR Spectroscopy In Vivo*. Vol. 75. Annual Reports on NMR Spectroscopy. Academic Press, 2012, pp. 115 –160. DOI: 10.1016/b978-0-12-397018-3.00003-x.

[41] Jong-Hee Hwang and Cheol Soo Choi. "Use of in vivo magnetic resonance spectroscopy for studying metabolic diseases." In: *Experimental & Molecular Medicine* 47.2 (2015), e139–e139. DOI: 10.1038/emm.2014.101.

[42] M. Rudin, ed. *In-Vivo Magnetic Resonance Spectroscopy III: In-Vivo MR Spectroscopy: Potential and Limitations*. Springer Berlin Heidelberg, 1992. DOI: 10.1007/978-3-642-77218-4.

[43] Malcolm H Levitt. *Spin dynamics*. en. 2nd ed. Hoboken, NJ: Wiley-Blackwell, Mar. 2008.

[44] Anatole Abragam. *The principles of nuclear magnetism*. International Series of Monographs on Physics. Oxford, England: Clarendon Press, Oct. 1983.

[45] Hans J. Reich. *Lecture notes in NMR Spectroscopy*. University of Wisconsin, 2017.

[46] Robin A. Graaf. *In Vivo NMR Spectroscopy*. Wiley, Dec. 2018. DOI: 10.1002/9781119382461.

[47] R.J Ordidge, A Connelly, and J.A.B Lohman. "Image-selected in Vivo spectroscopy (ISIS). A new technique for spatially selective nmr spectroscopy." In: *Journal of Magnetic Resonance (1969)* 66.2 (Feb. 1986), pp. 283–294. DOI: 10.1016/0022-2364(86)90031-4.

[48] A Connelly et al. "Outer volume suppressed image related in vivo spectroscopy (OSIRIS), a high-sensitivity localization technique." In: *Journal of Magnetic Resonance (1969)* 78.3 (July 1988), pp. 519–525. DOI: 10.1016/0022-2364(88)90136-9.

[49] Roger J. Ordidge. "Random noise selective excitation pulses." In: *Magnetic Resonance in Medicine* 5.1 (July 1987), pp. 93–98. DOI: 10.1002/mrm.1910050113.

[50] J Frahm et al. "Stimulated echo imaging." In: *Journal of Magnetic Resonance (1969)* 64.1 (Aug. 1985), pp. 81–93. DOI: 10.1016/0022-2364(85)90033-2.

[51] Paul A. Bottomley. "Spatial Localization in NMR Spectroscopy in Vivo." In: *Annals of the New York Academy of Sciences* 508.1 Physiological (Nov. 1987), pp. 333–348. DOI: 10.1111/j.1749-6632.1987.tb32915.x.

[52] Michael Garwood and Lance DelaBarre. "The return of the frequency sweep: designing adiabatic pulses for contemporary NMR." In: *Journal of magnetic resonance* 153.2 (2001), pp. 155–177. DOI: 10.1006/jmre.2001.2340.

[53] Tom W. J. Scheenen et al. "Short echo time1H-MRSI of the human brain at 3T with minimal chemical shift displacement errors using adiabatic refocusing pulses." In: *Magnetic Resonance in Medicine* 59.1 (2007), pp. 1–6. DOI: 10.1002/mrm.21302.

[54] T R Brown, B M Kincaid, and K Ugurbil. "NMR chemical shift imaging in three dimensions." In: *Proceedings of the National Academy of Sciences* 79.11 (June 1982), pp. 3523–3526. DOI: 10.1073/pnas.79.11.3523.

[55] Lisa A Urry et al. *Campbell Biology*. 12th ed. Upper Saddle River, NJ: Pearson, Jan. 2020.

[56] Joseph F. Clark. "Creatine and phosphocreatine: a review of their use in exercise and sport." In: *Journal of Athletic Training* 32.1 (1997), pp. 45–51.

[57] B. K. Siesjo. "Brain energy metabolism." In: *Annals of Neurology* 5.3 (1979), pp. 308–308. DOI: 10.1002/ana.410050318.

[58] Yuchi Liu, Yuning Gu, and Xin Yu. "Assessing tissue metabolism by phosphorous-31 magnetic resonance spectroscopy and imaging: a methodology review." In: *Quantitative Imaging in Medicine and Surgery* 7.6 (Dec. 2017), pp. 707–716. DOI: 10.21037/qims.2017.11.03.

[59] Graham J. Kemp, Martin Meyerspeer, and Ewald Moser. "Absolute quantification of phosphorus metabolite concentrations in human muscle in vivo by ^{31}P MRS: a quantitative review." In: *NMR in Biomedicine* 20.6 (2007), pp. 555–565. DOI: 10.1002/nbm.1192.

[60] K. E. Conley et al. "Activation of glycolysis in human muscle in vivo." In: *American Journal of Physiology-Cell Physiology* 273.1 (1997). PMID: 9252469, pp. C306–C315. DOI: 10.1152/ajpcell.1997.273.1.C306.

[61] Philip Siekevitz. "Powerhouse of the Cell." In: *Scientific American* 197.1 (1957), pp. 131–144. ISSN: 00368733, 19467087. DOI: 10.1038/scientificamerican0757-131.

[62] Brian A Sparkes. *The red and the black*. en. London, England: Routledge, Mar. 1996.

[63] Ovid. *Metamorphoses : a new verse translation*. en. Penguin Clothbound Classics. London, England: Penguin Classics, Apr. 2014.

[64] Ian Goodfellow, Yoshua Bengio, and Aaron Courville. *Deep Learning*. MIT Press, 2016.

[65] Murray Campbell. "Knowledge discovery in deep blue." In: *Communications of the ACM* 42.11 (Nov. 1999), pp. 65–67. DOI: 10.1145/319382.319396.

[66] Charu C. Aggarwal. *Neural Networks and Deep Learning*. Springer International Publishing, 2018. DOI: 10.1007/978-3-319-94463-0.

[67] Thomas Mitchell. *Machine Learning*. New York, NY: McGraw-Hill Professional, July 1997, pp. 870–877.

[68] Janosh Riebesell. *janosh/tikz: v0.1.0*. 2022. DOI: 10.5281/ZENODO.7486911.

[69] Anna Choromanska et al. "The Loss Surfaces of Multilayer Networks." In: *Proceedings of the Eighteenth International Conference on Artificial Intelligence and Statistics*. Ed. by Guy Lebanon and S. V. N. Vishwanathan. Vol. 38. Proceedings of Machine Learning Research. San Diego, California, USA: PMLR, 2015, pp. 192–204. DOI: 10.48550/ARXIV.1412.0233.

[70] Shiv Ram Dubey, Satish Kumar Singh, and Bidyut Baran Chaudhuri. "Activation functions in deep learning: A comprehensive survey and benchmark." In: *Neurocomputing* 503 (Sept. 2022), pp. 92–108. DOI: 10.1016/j.neucom.2022.06.111.

[71] Leentje Vanhamme, Aad van den Boogaart, and Sabine Van Huffel. "Improved Method for Accurate and Efficient Quantification of MRS Data with Use of Prior Knowledge." In: *Journal of Magnetic Resonance* 129.1 (Nov. 1997), pp. 35–43. DOI: 10.1006/jmre.1997.1244.

[72] S. W. Provencher. "Automatic quantitation of localized in vivo ^{1}H spectra with LCModel." In: *NMR Biomed* 14.4 (2001), pp. 260–264. DOI: 10.1002/nbm.698.

[73] Alexander Selvikvåg Lundervold and Arvid Lundervold. "An overview of deep learning in medical imaging focusing on MRI." In: *Zeitschrift für Medizinische Physik* 29.2 (May 2019), pp. 102–127. DOI: 10.1016/j.zemedi.2018.11.002.

[74] Shanshan Wang et al. "Accelerating magnetic resonance imaging via deep learning." In: *2016 IEEE 13th International Symposium on Biomedical Imaging (ISBI)*. IEEE, Apr. 2016. DOI: 10.1109/isbi.2016.7493320.

[75] Chen Qin et al. "Convolutional Recurrent Neural Networks for Dynamic MR Image Reconstruction." In: *IEEE Transactions on Medical Imaging* 38.1 (Jan. 2019), pp. 280–290. DOI: 10.1109/tmi.2018.2863670.

[76] Jo Schlemper et al. "A Deep Cascade of Convolutional Neural Networks for Dynamic MR Image Reconstruction." In: *IEEE Transactions on Medical Imaging* 37.2 (Feb. 2018), pp. 491–503. DOI: 10.1109/tmi.2017.2760978.

[77] Steffen Bollmann et al. "DeepQSM - using deep learning to solve the dipole inversion for quantitative susceptibility mapping." In: *NeuroImage* 195 (July 2019), pp. 373–383. DOI: 10.1016/j.neuroimage.2019.03.060.

[78] Michael T. McCann, Kyong Hwan Jin, and Michael Unser. "Convolutional Neural Networks for Inverse Problems in Imaging: A Review." In: *IEEE Signal Processing Magazine* 34.6 (Nov. 2017), pp. 85–95. DOI: 10.1109/MSP.2017.2739299.

[79] Kyong Hwan Jin et al. "Deep Convolutional Neural Network for Inverse Problems in Imaging." In: *IEEE Transactions on Image Processing* 26.9 (Sept. 2017), pp. 4509–4522. DOI: 10.1109/tip.2017.2713099.

[80] Fabio Baselice et al. "Bayesian MRI denoising in complex domain." In: *Magnetic Resonance Imaging* 38 (May 2017), pp. 112–122. DOI: 10.1016/j.mri.2016.12.024.

[81] Ashish Phophalia and Suman K. Mitra. "3D MR image denoising using rough set and kernel PCA method." In: *Magnetic Resonance Imaging* 36 (Feb. 2017), pp. 135–145. DOI: 10.1016/j.mri.2016.10.010.

[82] Siyuan Shan et al. *Unsupervised End-to-end Learning for Deformable Medical Image Registration*. 2017. DOI: 10.48550/ARXIV.1711.08608.

[83] Bob D. de Vos et al. "A deep learning framework for unsupervised affine and deformable image registration." In: *Medical Image Analysis* 52 (Feb. 2019), pp. 128–143. DOI: 10.1016/j.media.2018.11.010.

[84] Jose Bernal et al. "Deep convolutional neural networks for brain image analysis on magnetic resonance imaging: a review." In: *Artificial Intelligence in Medicine* 95 (Apr. 2019), pp. 64–81. DOI: 10.1016/j.artmed.2018.08.008.

[85] Liang Chen, Paul Bentley, and Daniel Rueckert. "Fully automatic acute ischemic lesion segmentation in DWI using convolutional neural networks." In: *NeuroImage: Clinical* 15 (2017), pp. 633–643. DOI: 10.1016/j.nicl.2017.06.016.

[86] Dhritiman Das et al. "Quantification of Metabolites in Magnetic Resonance Spectroscopic Imaging Using Machine Learning." In: *Medical Image Computing and Computer Assisted Intervention - MICCAI 2017*. Springer International Publishing, 2017, pp. 462–470. DOI: 10.1007/978-3-319-66179-7_53.

[87] Nima Hatami, Michaël Sdika, and Hélène Ratiney. "Magnetic Resonance Spectroscopy Quantification Using Deep Learning." In: *Medical Image Computing and Computer Assisted Intervention - MICCAI 2018*. Springer International Publishing, 2018, pp. 467–475. DOI: 10.1007/978-3-030-00928-1_53.

[88] Y. Lecun et al. "Gradient-based learning applied to document recognition." In: *Proceedings of the IEEE* 86.11 (1998), pp. 2278–2324. DOI: 10.1109/5.726791.

[89] Olaf Ronneberger, Philipp Fischer, and Thomas Brox. "U-Net: Convolutional Networks for Biomedical Image Segmentation." In: 9351 (Oct. 2015), pp. 234–241. DOI: 10.1007/978-3-319-24574-4_28.

[90] P. Mansfield. "Spatial mapping of the chemical shift in NMR." In: *Magnetic Resonance in Medicine* 1.3 (Sept. 1984), pp. 370–386. DOI: 10.1002/mrm.1910010308.

[91] S Posse, C DeCarli, and D Le Bihan. "Three-dimensional echo-planar MR spectroscopic imaging at short echo times in the human brain." In: *Radiology* 192.3 (Sept. 1994), pp. 733–738. DOI: 10.1148/radiology.192.3.8058941.

[92] Ulrike Dydak et al. "Sensitivity-encoded spectroscopic imaging." In: *Magnetic Resonance in Medicine* 46.4 (Oct. 2001), pp. 713–722. DOI: 10.1002/mrm.1250.

[93] Ricardo Otazo et al. "Accelerated short-TE 3D proton echo-planar spectroscopic imaging using 2D-SENSE with a 32-channel array coil." In: *Magnetic Resonance in Medicine* 58.6 (2007), pp. 1107–1116. DOI: 10.1002/mrm.21426.

[94] Fa-Hsuan Lin et al. "Sensitivity-encoded (SENSE) proton echo-planar spectroscopic imaging (PEPSI) in the human brain." In: *Magnetic Resonance in Medicine* 57.2 (2007), pp. 249–257. DOI: 10.1002/mrm.21119.

[95] M. Lustig et al. "Compressed Sensing MRI." In: *IEEE Signal Processing Magazine* 25.2 (Mar. 2008), pp. 72–82. DOI: 10.1109/msp.2007.914728.

[96] Jeffrey Fessler. "Model-Based Image Reconstruction for MRI." In: *IEEE Signal Processing Magazine* 27.4 (July 2010), pp. 81–89. DOI: 10.1109/msp.2010.936726.

[97] Kai Tobias Block, Martin Uecker, and Jens Frahm. "Undersampled radial MRI with multiple coils. Iterative image reconstruction using a total variation constraint." In: *Magnetic Resonance in Medicine* 57.6 (2007), pp. 1086–1098. DOI: 10.1002/mrm.21236.

[98] Michael Lustig, David Donoho, and John M. Pauly. "Sparse MRI: The application of compressed sensing for rapid MR imaging." In: *Magnetic Resonance in Medicine* 58.6 (2007), pp. 1182–1195. DOI: 10.1002/mrm.21391.

[99] Lawrence Craig Evans and Ronald F. Gariepy. *Measure Theory and Fine Properties of Functions, Revised Edition*. Chapman and Hall/CRC, Apr. 2015. DOI: 10.1201/b18333.

[100] Florian Knoll et al. "Second order total generalized variation (TGV) for MRI." In: *Magnetic Resonance in Medicine* 65.2 (Dec. 2010), pp. 480–491. DOI: 10.1002/mrm.22595.

[101] In: (). DOI: 10.1137/090769521.

[102] Jeffrey Kasten, Franois Lazeyras, and Dimitri Van De Ville. "Data-Driven MRSI Spectral Localization Via Low-Rank Component Analysis." In: *IEEE Transactions on Medical Imaging* 32.10 (Oct. 2013), pp. 1853–1863. DOI: 10.1109/tmi.2013.2266259.

[103] D.L. Donoho. "Compressed sensing." In: *IEEE Transactions on Information Theory* 52.4 (Apr. 2006), pp. 1289–1306. DOI: 10.1109/tit.2006.871582.

[104] Sairam Geethanath et al. "Compressive Sensing Could Accelerate ^{1}H MR Metabolic Imaging in the Clinic." In: *Radiology* 262.3 (Mar. 2012), pp. 985–994. DOI: 10.1148/radiol.11111098.

[105] Itthi Chatnuntawech et al. "Accelerated ^{1}H MRSI using randomly undersampled spiral-based k-space trajectories." In: *Magnetic Resonance in Medicine* 74.1 (July 2014), pp. 13–24. DOI: 10.1002/mrm.25394.

[106] Neil E. Wilson et al. "Accelerated five-dimensional echo planar J-resolved spectroscopic imaging: Implementation and pilot validation in human brain." In: *Magnetic Resonance in Medicine* 75.1 (Jan. 2015), pp. 42–51. DOI: 10.1002/mrm.25605.

[107] Antoine Klauser et al. "Fast high-resolution brain metabolite mapping on a clinical 3T MRI by accelerated ^{1}H-FID-MRSI and low-rank constrained reconstruction." In: *Magnetic Resonance in Medicine* 81.5 (Dec. 2018), pp. 2841–2857. DOI: 10.1002/mrm.27623.

[108] Antoine Klauser et al. "Whole-brain high-resolution metabolite mapping with 3D compressed-sensing SENSE low-rank ^{1}H FID-MRSI." In: *NMR in Biomedicine* 35.1 (Oct. 2021). DOI: 10.1002/nbm.4615.

[109] Antoine Klauser et al. "Achieving high-resolution ^{1}H-MRSI of the human brain with compressed-sensing and low-rank reconstruction at 7 Tesla." In: *Journal of Magnetic Resonance* 331 (Oct. 2021), p. 107048. DOI: 10.1016/j.jmr.2021.107048.

[110] Hien M. Nguyen et al. "Denoising MR Spectroscopic Imaging Data With Low-Rank Approximations." In: *IEEE Transactions on Biomedical Engineering* 60.1 (Jan. 2013), pp. 78–89. DOI: 10.1109/tbme.2012.2223466.

[111] Yan Liu et al. "Improved Low-Rank Filtering of Magnetic Resonance Spectroscopic Imaging Data Corrupted by Noise and B_0Field Inhomogeneity." In: *IEEE Transactions on Biomedical Engineering* (2015), pp. 1–1. DOI: 10.1109/tbme.2015.2476499.

[112] Cara K. Black et al. "Solid organ transplantation in the 21st century." In: *Annals of Translational Medicine* 6.20 (Oct. 2018), pp. 409–409. DOI: 10.21037/atm.2018.09.68.

[113] C.H. Charles and I.R. Young. *MR Spectroscopy: Clinical applications and techniques*. Taylor & Francis, 1995. ISBN: 9781853170683.

[114] Stefan G. Tullius and Nicholas L. Tilney. "Both alloantigen-Dependent and -independent factors influence chronic allograft rejection." In: *Transplantation* 59.3 (Feb. 1995), pp. 313–318.

[115] Douglas Bastos Neves et al. "Primary graft dysfunction of the liver: definitions, diagnostic criteria and risk factors." In: *Einstein (São Paulo)* 14.4 (Oct. 2016), pp. 567–572. DOI: 10.1590/s1679-45082016rw3585.

[116] Laurence Le Moyec et al. "Proton Nuclear Magnetic Resonance Spectroscopy of Urine and Plasma in Renal Transplantation Follow-Up." In: *Nephron* 65.3 (1993), pp. 433–439. DOI: 10.1159/000187525.

[117] Nicolau Beckmann, Robert P. Hof, and Markus Rudin. "The role of magnetic resonance imaging and spectroscopy in transplantation: from animal models to man." In: *NMR in Biomedicine* 13.6 (2000), pp. 329–348. DOI: 10.1002/1099-1492(200010)13:6<329::aid-nbm653>3.0.co;2-w.

[118] Yi-Jen L Wu et al. "MRI Investigations of Graft Rejection Following Organ Transplantation Using Rodent Models." In: (2004), pp. 73–105. DOI: 10.1016/s0076-6879(04)86003-8.

[119] J. M. Grinyo. "Why Is Organ Transplantation Clinically Important?" In: *Cold Spring Harbor Perspectives in Medicine* 3.6 (June 2013), a014985–a014985. DOI: 10.1101/cshperspect.a014985.

[120] Marie Thuong et al. "New classification of donation after circulatory death donors definitions and terminology." In: *Transplant International* 29.7 (2016), pp. 749–759. DOI: 10.1111/tri.12776.

[121] Akinlolu O. Ojo et al. "Delayed Graft Function: Risk Factors And Implications For Renal Allograft Survival." In: *Transplantation* 63.7 (Apr. 1997), pp. 968–974. DOI: 10.1097/00007890-199704150-00011.

[122] Daniel A. Shoskes and Philip F. Halloran. "Delayed Graft Function in Renal Transplantation: Etiology, Management and Long-term Significance." In: *Journal of Urology* 155.6 (June 1996), pp. 1831–1840. DOI: 10.1016/s0022-5347(01)66023-3.

[123] Jerald P. Radich et al. "Second allogeneic transplantation after failure of first autologous transplantation." In: *Biology of Blood and Marrow Transplantation* 6.3 (May 2000), pp. 272–279. DOI: 10.1016/s1083-8791(00)70009-7.

[124] Peter Libby and Jordan S. Pober. "Chronic Rejection." In: *Immunity* 14.4 (Apr. 2001), pp. 387–397. DOI: 10.1016/s1074-7613(01)00119-4.

[125] Alessandro Poggi et al. "Human Gut-Associated Natural Killer Cells in Health and Disease." In: *Frontiers in Immunology* 10 (May 2019). DOI: 10.3389/fimmu.2019.00961.

[126] Arthue J. Matas et al. "The Impact Of An Acute Rejection Episode On Long-term Renal Allograft Survival." In: *Transplantation* 57.6 (Mar. 1994), pp. 857–859. DOI: 10.1097/00007890-199403270-00015.

[127] Johan W. de Fijter. "Rejection and function and chronic allograft dysfunction." In: *Kidney International* 78 (Dec. 2010), S38–S41. DOI: 10.1038/ki.2010.421.

[128] S. A. Lodhi and H.-U. Meier-Kriesche. "Kidney allograft survival: the long and short of it." In: *Nephrology Dialysis Transplantation* 26.1 (Dec. 2010), pp. 15–17. DOI: 10.1093/ndt/gfq730.

[129] Maria-Giulia Perrelli. "Ischemia/reperfusion injury and cardioprotective mechanisms: Role of mitochondria and reactive oxygen species." In: *World Journal of Cardiology* 3.6 (2011), p. 186. DOI: 10.4330/wjc.v3.i6.186.

[130] A Halestrap. "Mitochondrial permeability transition pore opening during myocardial reperfusion—a target for cardioprotection." In: *Cardiovascular Research* 61.3 (Feb. 2004), pp. 372–385. DOI: 10.1016/s0008-6363(03)00533-9.

[131] Vera G Grivennikova et al. "Interaction of the mitochondrial NADH-ubiquinone reductase with rotenone as related to the enzyme active/inactive transition." In: *Biochimica et Biophysica Acta (BBA) - Bioenergetics* 1319.2-3 (Apr. 1997), pp. 223–232. DOI: 10.1016/s0005-2728(96)00163-6.

[132] J. L. Zweier, J. T. Flaherty, and M. L. Weisfeldt. "Direct measurement of free radical generation following reperfusion of ischemic myocardium." In: *Proceedings of the National Academy of Sciences* 84.5 (Mar. 1987), pp. 1404–1407. DOI: 10.1073/pnas.84.5.1404.

[133] Masanori Kawaguchi et al. "Inflammasome Activation of Cardiac Fibroblasts Is Essential for Myocardial Ischemia/Reperfusion Injury." In: *Circulation* 123.6 (Feb. 2011), pp. 594–604. DOI: 10.1161/circulationaha.110.982777.

[134] Gabriel Loor et al. "Mitochondrial oxidant stress triggers cell death in simulated ischemia-reperfusion." In: *Biochimica et Biophysica Acta (BBA) - Molecular Cell Research* 1813.7 (July 2011), pp. 1382–1394. DOI: 10.1016/j.bbamcr.2010.12.008.

[135] Masayoshi Ito et al. "The Elephant Trunk Technique for Type A Dissection." In: *Journal of Cardiac Surgery* 15.3 (May 2000), pp. 163–166. DOI: 10.1111/j.1540-8191.2000.tb00451.x.

[136] Philip T. Thrush, Simon Urschel, and Elfriede Pahl. "Posttransplant Heart Failure." In: *Heart Failure in the Child and Young Adult*. Elsevier, 2018, pp. 625–638. DOI: 10.1016/b978-0-12-802393-8.00047-8.

[137] Kevin P. Daly et al. "Endomyocardial biopsy and selective coronary angiography are low-risk procedures in pediatric heart transplant recipients: Results of a multicenter experience." In: *The Journal of Heart and Lung Transplantation* 31.4 (Apr. 2012), pp. 398–409. DOI: 10.1016/j.healun.2011.11.019.

[138] Stephen G Pophal et al. "Complications of endomyocardial biopsy in children." In: *Journal of the American College of Cardiology* 34.7 (Dec. 1999), pp. 2105–2110. DOI: 10.1016/s0735-1097(99)00452-0.

[139] Philip F. Halloran, Konrad S. Famulski, and Jeff Reeve. "Molecular assessment of disease states in kidney transplant biopsy samples." In: *Nature Reviews Nephrology* 12.9 (June 2016), pp. 534–548.

[140] S. Feng et al. "Characteristics Associated with Liver Graft Failure: The Concept of a Donor Risk Index." In: *American Journal of Transplantation* 6.4 (Feb. 2006), pp. 783–790. DOI: 10.1111/j.1600-6143.2006.01242.x.

[141] Jan Pruim et al. "Selection criteria for liver donation: a review." In: *Transplant International* 6.4 (July 1993), pp. 226–235. DOI: 10.1111/j.1432-2277.1993.tb00653.x.

[142] New York State Department of Health Workgroup. "Workgroup on expanded criteria organs for liver transplantation." In: *Liver Transplantation* 11.10 (2005), pp. 1184–1192. DOI: 10.1002/lt.20569.

[143] Dronacharya Routh et al. "Changing Pattern of Donor Selection Criteria in Deceased Donor Liver Transplant: A Review of Literature." In: *Journal of Clinical and Experimental Hepatology* 3.4 (Dec. 2013), pp. 337–346. DOI: 10.1016/j.jceh.2013.11.007.

[144] S Studer and J Orens. "Cadaveric donor selection and management." In: *Respiratory Care Clinics* 10.4 (Dec. 2004), pp. 459–471. DOI: 10.1016/j.rcc.2004.06.006.

[145] Peter A. Sehr et al. "A model kidney transplant studied by phosphorus nuclear magnetic resonance." In: *Biochemical and Biophysical Research Communications* 77.1 (July 1977), pp. 195–202. DOI: 10.1016/s0006-291x(77)80182-4.

[146] P. A. Sehr et al. "Non-destructive measurement of metabolites and tissue pH in the kidney by 31P nuclear magnetic resonance." In: *Br J Exp Pathol* 60.6 (1979), pp. 632–641.

[147] Peter N. Bretan et al. "Pretbansplant assessment of renal viability by phosphorus-31 magnetic resonance spectroscopy." In: *Transplantation* 48.1 (July 1989), pp. 48–53. DOI: 10.1097/00007890-198907000-00011.

[148] Ronald J. Hené et al. "Pre-transplantation assessment of renal viability with ^{31}P magnetic resonance spectroscopy." In: *Kidney International* 46.6 (Dec. 1994), pp. 1694–1699. DOI: 10.1038/ki.1994.470.

[149] Juan José García Martínez and Karim Bendjelid. "Artificial liver support systems: what is new over the last decade?" In: *Annals of Intensive Care* 8.1 (Nov. 2018). DOI: 10.1186/s13613-018-0453-z.

[150] Jian-Da Lu and Jun Xue. "Chapter 101 - Poisoning: Kinetics to Therapeutics." In: *Critical Care Nephrology (Third Edition)*. Ed. by Claudio Ronco et al. Third Edition. Philadelphia: Content Repository Only! 2019, 600 –629.e7. ISBN: 978-0-323-44942-7.

[151] R. F. E. Wolf et al. "Noninvasive Metabolic Assessment Of Human Donor Livers." In: *Transplantation* 64.1 (July 1997), pp. 147–152. DOI: 10.1097/00007890-199707150-00025.

[152] Maciej Kosieradzki et al. "Progress in abdominal organ transplantation." In: *Medical Science Monitor* 17.12 (2011), RA282–RA291. DOI: 10.12659/msm.882119.

[153] J. I. Shapiro et al. "^{31}P nuclear magnetic resonance study of acute renal dysfunction in rat kidney transplants." In: *Magnetic Resonance in Medicine* 5.4 (Oct. 1987), pp. 346–352. DOI: 10.1002/mrm.1910050405.

[154] Michael D. Boska et al. "Image-guided ^{31}P magnetic resonance spectroscopy of normal and transplanted human kidneys." In: *Kidney International* 38.2 (Aug. 1990), pp. 294–300. DOI: 10.1038/ki.1990.199.

[155] T M Grist, H C Charles, and H D Sostman. "1990 ARRS Executive Council Award. Renal transplant rejection: diagnosis with ^{31}P MR spectroscopy." In: *American Journal of Roentgenology* 156.1 (Jan. 1991), pp. 105–112. DOI: 10.2214/ajr.156.1.1898541.

[156] Kazuo Sumimoto et al. "Reliable indices for the determination of viability of grafted liver immediately after orthotopic transplantation bile flow rate and cellular adenosine triphosphate level." In: *Transplantation* 46.4 (Oct. 1988), pp. 506–509. DOI: 10.1097/00007890-198810000-00007.

[157] Charles S. Landis et al. "Liver regeneration and energetic changes in rats following hepatic radiation therapy and hepatocyte transplantation by ^{31}P MRSI." In: *Liver International* 35.4 (Mar. 2014), pp. 1145–1151. DOI: 10.1111/liv.12507.

[158] Allan J. Collins et al. "US Renal Data System 2013 Annual Data Report." In: *American Journal of Kidney Diseases* 63.1 (Jan. 2014), A7. DOI: 10.1053/j.ajkd.2013.11.001.

[159] W. Kelly Wu et al. "Delayed graft function and the risk of acute rejection in the modern era of kidney transplantation." In: *Kidney International* 88.4 (Oct. 2015), pp. 851–858. DOI: 10.1038/ki.2015.190.

[160] Hailin Zhao et al. "Ischemia-Reperfusion Injury Reduces Long Term Renal Graft Survival: Mechanism and Beyond." In: *EBioMedicine* 28 (Feb. 2018), pp. 31–42. DOI: 10.1016/j.ebiom.2018.01.025.

[161] C. Ponticelli. "Ischaemia-reperfusion injury: a major protagonist in kidney transplantation." In: *Nephrology Dialysis Transplantation* 29.6 (Dec. 2013), pp. 1134–1140. DOI: 10.1093/ndt/gft488.

[162] Akinlolu O. Ojo. "Expanded Criteria Donors: Process and Outcomes." In: *Seminars in Dialysis* 18.6 (Nov. 2005), pp. 463–468. DOI: 10.1111/j.1525-139x.2005.00090.x.

[163] C. M. Lee. "Prolonged Cold Ischemia Time Obviates the Benefits of o HLA Mismatches in Renal Transplantation." In: *Archives of Surgery* 135.9 (Sept. 2000), pp. 1016–1019. DOI: 10.1001/archsurg.135.9.1016.

[164] Duska Dragun et al. "Prolonged cold preservation augments vascular injury independent of renal transplant immunogenicity and function." In: *Kidney International* 60.3 (Sept. 2001), pp. 1173–1181. DOI: 10.1046/j.1523-1755.2001.0600031173.x.

[165] Ronald F. Parsons and James V. Guarrera. "Preservation solutions for static cold storage of abdominal allografts." In: *Current Opinion in Organ Transplantation* 19.2 (Apr. 2014), pp. 100–107. DOI: 10.1097/mot.0000000000000063.

[166] L.K. Kayler et al. "Impact of Cold Ischemia Time on Graft Survival Among ECD Transplant Recipients: A Paired Kidney Analysis." In: *American Journal of Transplantation* 11.12 (Dec. 2011), pp. 2647–2656. DOI: 10.1111/j.1600-6143.2011.03741.x.

[167] Isabel Quiroga et al. "Major effects of delayed graft function and cold ischaemia time on renal allograft survival." In: *Nephrology Dialysis Transplantation* 21.6 (Feb. 2006), pp. 1689–1696. DOI: 10.1093/ndt/gfl042.

[168] Abdulla K. Salahudeen, Naeem Haider, and Warren May. "Cold ischemia and the reduced long-term survival of cadaveric renal allografts." In: *Kidney International* 65.2 (Feb. 2004), pp. 713–718. DOI: 10.1111/j.1523-1755.2004.00416.x.

[169] Victoria R. Pell et al. "Succinate metabolism: a new therapeutic target for myocardial reperfusion injury." In: *Cardiovascular Research* 111.2 (May 2016), pp. 134–141. DOI: 10.1093/cvr/cvw100.

[170] Edward T. Chouchani et al. "A Unifying Mechanism for Mitochondrial Superoxide Production during Ischemia-Reperfusion Injury." In: *Cell Metabolism* 23.2 (Feb. 2016), pp. 254–263. DOI: 10.1016/j.cmet.2015.12.009.

[171] Danielle Lê-Quôc and Khanh Lê-Quôc. "Relationships between the NAD(P) redox state, fatty acid oxidation, and inner membrane permeability in rat liver mitochondria." In: *Archives of Biochemistry and Biophysics* 273.2 (Sept. 1989), pp. 466–478. DOI: 10.1016/0003-9861(89)90506-7.

[172] Alexander B. Kotlyar and Andrei D. Vinogradov. "Slow active/inactive transition of the mitochondrial NADH-ubiquinone reductase." In: *Biochimica et Biophysica Acta (BBA) - Bioenergetics* 1019.2 (Aug. 1990), pp. 151–158. DOI: 10.1016/0005-2728(90)90137-s.

[173] Edward T. Chouchani et al. "Ischaemic accumulation of succinate controls reperfusion injury through mitochondrial ROS." In: *Nature* 515.7527 (Nov. 2014), pp. 431–435. DOI: 10.1038/nature13909.

[174] Fatih Arslan, Dominique P. de Kleijn, and Gerard Pasterkamp. "Innate immune signaling in cardiac ischemia." In: *Nature Reviews Cardiology* 8.5 (Mar. 2011), pp. 292–300. DOI: 10.1038/nrcardio.2011.38.

[175] Holger K Eltzschig and Tobias Eckle. "Ischemia and reperfusion-from mechanism to translation." In: *Nature Medicine* 17.11 (Nov. 2011), pp. 1391–1401. DOI: 10.1038/nm.2507.

[176] Ming Lu et al. "Intracellular redox state revealed by in vivo 31P MRS measurement of NAD+ and NADH contents in brains." In: *Magnetic Resonance in Medicine* 71.6 (July 2013), pp. 1959–1972. DOI: 10.1002/mrm.24859.

[177] Wayel Jassem et al. "The role of mitochondria in ischemia/reperfusion injury." In: *Transplantation* 73.4 (Feb. 2002), pp. 493–499. DOI: 10.1097/00007890-200202270-00001.

[178] Paola Costantini et al. "Modulation of the Mitochondrial Permeability Transition Pore by Pyridine Nucleotides and Dithiol Oxidation at Two Separate Sites." In: *Journal of Biological Chemistry* 271.12 (Mar. 1996), pp. 6746–6751. DOI: 10.1074/jbc.271.12.6746.

[179] Xiao-Hong Zhu et al. "In vivo NAD assay reveals the intracellular NAD contents and redox state in healthy human brain and their age dependences." In: *Proceedings of the National Academy of Sciences* 112.9 (Feb. 2015), pp. 2876–2881. DOI: 10.1073/pnas.1417921112.

[180] J. J. Nikken and G. P. Krestin. "MRI of the kidney-state of the art." In: *European Radiology* 17.11 (July 2007), pp. 2780–2793. DOI: 10.1007/s00330-007-0701-3.

[181] Nicolas Grenier, Michael Pedersen, and Olivier Hauger. "Contrast agents for functional and cellular MRI of the kidney." In: *European Journal of Radiology* 60.3 (Dec. 2006), pp. 341–352. DOI: 10.1016/j.ejrad.2006.06.024.

[182] Henry Rusinek, Manmeen Kaur, and Vivian S Lee. "Renal magnetic resonance imaging." In: *Current Opinion in Nephrology and Hypertension* 13.6 (Nov. 2004), pp. 667–673. DOI: 10.1097/00041552-200411000-00014.

[183] Jean-Pierre Laissy et al. "Functional evaluation of normal and ischemic kidney by means of gadolinium-DOTA enhanced TurboFLASH MR imaging: A preliminary comparison with 99mTc-MAG3 dynamic scintigraphy." In: *Magnetic Resonance Imaging* 12.3 (Jan. 1994), pp. 413–419. DOI: 10.1016/0730-725x(94)92534-8.

[184] Thomas L. Pallone, Zhong Zhang, and Kristie Rhinehart. "Physiology of the renal medullary microcirculation." In: *American Journal of Physiology-Renal Physiology* 284.2 (Feb. 2003), F253–F266. DOI: 10.1152/ajprenal.00304.2002.

[185] Jean-Bernard Buchs et al. "DCD Pigs' Kidneys Analyzed by MRI to Assess Ex Vivo Their Viability." In: *Transplantation* 97.2 (Jan. 2014), pp. 148–153. DOI: 10.1097/01.tp.0000438023.02751.22.

[186] Katarína Vajdová, Rolf Graf, and Pierre-Alain Clavien. "ATP-supplies in the cold-preserved liver: A long-neglected factor of organ viability." In: *Hepatology* 36.6 (Dec. 2002), pp. 1543–1552. DOI: 10.1002/hep.1840360633.

[187] Bote G. Bruinsma et al. "Metabolic profiling during ex vivo machine perfusion of the human liver." In: *Scientific Reports* 6.1 (Mar. 2016). DOI: 10.1038/srep22415.

[188] Shigehito Miyagi et al. "The Significance of Preserving the Energy Status and Microcirculation in Liver Grafts from Non-Heart-Beating Donor." In: *Cell Transplantation* 17.1-2 (Jan. 2008), pp. 173–178. DOI: 10.3727/000000008783906874.

[189] Rowan F. van Golen, Thomas M. van Gulik, and Michal Heger. "Mechanistic overview of reactive species-induced degradation of the endothelial glycocalyx during hepatic ischemia/reperfusion injury." In: *Free Radical Biology and Medicine* 52.8 (Apr. 2012), pp. 1382–1402. DOI: 10.1016/j.freeradbiomed.2012.01.013.

[190] Cyril Moers et al. "Machine Perfusion or Cold Storage in Deceased-Donor Kidney Transplantation." In: *New England Journal of Medicine* 360.1 (Jan. 2009), pp. 7–19. DOI: 10.1056/nejmoa0802289.

[191] Philipp Dutkowski et al. "First Comparison of Hypothermic Oxygenated PErfusion Versus Static Cold Storage of Human Donation After Cardiac Death Liver Transplants." In: *Annals of Surgery* 262.5 (Nov. 2015), pp. 764–771. DOI: 10.1097/sla.0000000000001473.

[192] Rabindra N. Bhattacharjee et al. "Subnormothermic Oxygenated Perfusion Optimally Preserves Donor Kidneys Ex Vivo." In: *Kidney International Reports* 4.9 (Sept. 2019), pp. 1323–1333. DOI: 10.1016/j.ekir.2019.05.013.

[193] T.A. Berendsen et al. "Hepatocyte Viability and Adenosine Triphosphate Content Decrease Linearly Over Time During Conventional Cold Storage of Rat Liver Grafts." In: *Transplantation Proceedings* 43.5 (June 2011), pp. 1484–1488. DOI: 10.1016/j.transproceed.2010.12.066.

[194] M.L. Nicholson and S.A. Hosgood. "Renal Transplantation After Ex Vivo Normothermic Perfusion: The First Clinical Study." In: *American Journal of Transplantation* 13.5 (May 2013), pp. 1246–1252. DOI: 10.1111/ajt.12179.

[195] Matyas Hamar and Markus Selzner. "Ex-vivo machine perfusion for kidney preservation." In: *Current Opinion in Organ Transplantation* 23.3 (June 2018), pp. 369–374. DOI: 10.1097/mot.0000000000000524.

[196] Yu-Ting Wang. "Functional assessment of transplanted kidneys with magnetic resonance imaging." In: *World Journal of Radiology* 7.10 (2015), p. 343. DOI: 10.4329/wjr.v7.i10.343.

[197] Humberto Morales-Loredo et al. "Hydrogen sulfide regulation of renal and mesenteric blood flow." In: *American Journal of Physiology-Heart and Circulatory Physiology* 317.5 (Nov. 2019), H1157–H1165. DOI: 10.1152/ajpheart.00303.2019.

[198] Guangdong Yang et al. "H_2S as a Physiologic Vasorelaxant: Hypertension in Mice with Deletion of Cystathionine γ-Lyase." In: *Science* 322.5901 (Oct. 2008), pp. 587–590. DOI: 10.1126/science.1162667.

[199] Bindu D. Paul and Solomon H. Snyder. "H2S signalling through protein sulfhydration and beyond." In: *Nature Reviews Molecular Cell Biology* 13.8 (July 2012), pp. 499–507. DOI: 10.1038/nrm3391.

[200] Alban Longchamp et al. "Amino Acid Restriction Triggers Angiogenesis via GCN2/ATF4 Regulation of VEGF and H2S Production." In: *Cell* 173.1 (Mar. 2018), 117–129.e14. DOI: 10.1016/j.cell.2018.03.001.

[201] John W. Elrod et al. "Hydrogen sulfide attenuates myocardial ischemia-reperfusion injury by preservation of mitochondrial function." In: *Proceedings of the National Academy of Sciences* 104.39 (Sept. 2007), pp. 15560–15565. DOI: 10.1073/pnas.0705891104.

[202] Eelke M. Bos et al. "Hydrogen Sulfide-Induced Hypometabolism Prevents Renal Ischemia/Reperfusion Injury." In: *Journal of the American Society of Nephrology* 20.9 (Sept. 2009), pp. 1901–1905. DOI: 10.1681/asn.2008121269.

Julien Songeon

PhD in Physics

Swiss - French
Rue Albert-Gos 18,
1206 Genève, Suisse

+41 79 561 59 05
julien@songeon.ch
julien-songeon

Education

2019 - 2023 Doctor of Philosophy (PhD) in Physics
University of Geneva, Switzerland
Thesis with Mention "très bien" (maximal grade)

2017 - 2019 Master of Science (MSc) in High Energy Physics | Final Grade: 5.8/6
University of Geneva and CERN, Switzerland
Thesis: 6/6, Thesis Defense: 6/6

2013 - 2017 Bachelor of Science (BSc) in Physics | Final Grade: 4.9/6
University of Geneva, Switzerland

Work Experience

February 2020 - June 2023 Teaching Assistant, University of Geneva
Part time job, teaching Assistant for the Classical Mechanics course, taught to first year students in physics (2020). Then General Physics taught to first year of chemistry and bio-chemistry (2020-2023).

September 2018 - August 2019 Technical Assistant, ECG Henry-Dunant
Part time job, assistance to laboratory experiments at a High School.

September 2016 - June 2018 Research and Teaching Assistant, University of Geneva
Part time job, instructor for the Physics Laboratories then for the General Physics B course, taught to students in biology and pharmaceutical sciences.

June - August 2017 Internship at DPNC, University of Geneva
TT-Pet project: study and computer simulations of new detectors for PET Scan.

June - August 2016 Internship at DQMP, University of Geneva
Studies of Vanadium DiSelenide (VSe_2) using STM/STS (Scanning Tunnelling Microscopy/Spectroscopy) and AFM (Atomic Force Microscope).

Academic Experience

PhD projects

Analysis of spectroscopic data.

- Development of a Deep Learning pipeline analysis tool in Python.
- Creation of a physics-based numerical model to create simulated datasets for supervised learning.
- Development of CNN architecture in Python using TensorFlow.

Development of MRI sequences

- Implementation of compressed sensing for spectroscopy data acquisition using C++.
- Development of a reconstruction algorithm using a Low-Rank approximation model in Matlab.

MSc project

Analysis of neutral particles at CERN.

- Development of a machine learning classifier, Boosted Decision Trees (BDTs), using Python and C++.

Languages

French :	Mother tongue
English :	Fluent, MSc and PhD followed in English

Computer Skills

Op. systems :	Unix/Linux (Ubuntu server), macOS, Windows 7 & 10
Analysis tools :	Mathematica, Matlab, Root, Geant4, Igor, Excel
Programming :	C++, Python, Bash
Tools :	Git, Docker
Certifications:	Machine Learning, Deep Learning, Convolutional Neural Network
Document processing :	Word, PowerPoint, LaTeX
Web tools :	PHP, HTML5, CSS3

Activities and Volunteer Experience

Student representative:	**Physics Section Council**, 2021-2023 Participation and vote on behalf of PhD students at the Physics section councils. **Quality office**, 2019-2023 Student representative in the quality office committee of the university. **Scientific Information Division**, 2018-2020 Student representative in the management and administration committee of the university libraries for the faculty of science. **Professor Nomination Committees**, 2016-2019 Student representative in nomination and renewal committees for professor.
Physics Student Association: (2015-2017)	**Treasurer** (2015-2016), **President** (2016-2017) Staff management, events, budget and communication planning.
Sciences Student Association: (2016-2019)	**Vice-President** (2016-2017), **President** (2017-2018), **Treasurer** (2018-2019) Transversality between the Dean office and the students, large scale events organisation, Nobel Prize conference organisation, staff management.
Outreach activity	**Nuit de la Science**, 2018 Event of the Department of Culture and Sport of the City of Geneva, organized by the Museum of History of Science.

Interests

Physics, Programmation, Motorsports, Chess